Material Solutions to Mitigate the Alkali Chloride-Induced High Temperature Corrosion

Kiamehr, Saeed

Publication date:
2014

Document Version
Publisher's PDF, also known as Version of record

Material Solutions to Mitigate the Alkali Chloride-Induced High Temperature Corrosion

PhD Thesis

$$(EIv'')''=q-\rho A\ddot{v}$$

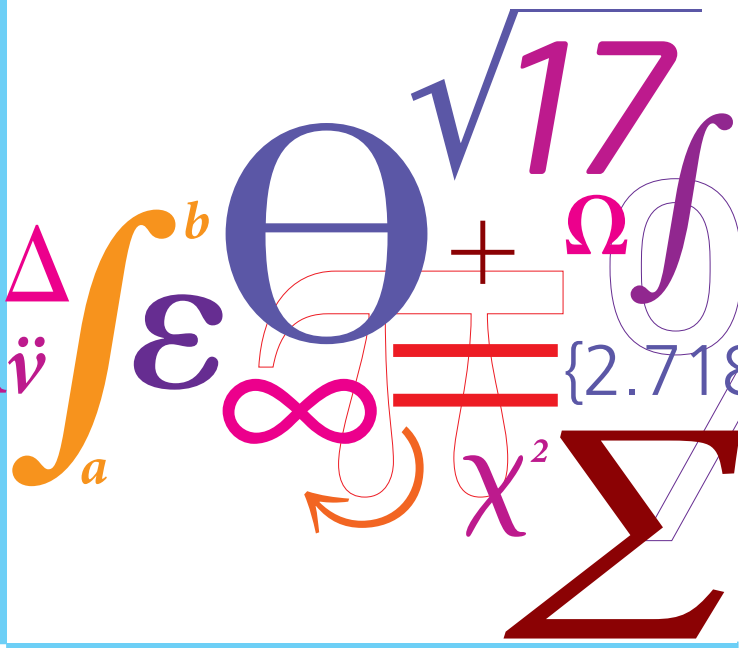

Saeed Kiamehr
November 2014

DTU Mechanical Engineering
Department of Mechanical Engineering

Technical University of Denmark (DTU)
Department of Mechanical Engineering
Section of Materials and Surface Engineering

Material Solutions to Mitigate the Alkali Chloride-Induced High Temperature Corrosion

Ph.D Thesis by

Saeed Kiamehr

Supervisors:

Marcel A.J. Somers

Kristian V. Dahl

Melanie Montgomery

November 2014

To my parents

Preface

This thesis is submitted as a partial fulfilment of the requirements for the Ph.D degree at the Technical University of Denmark (DTU), Department of Mechanical Engineering. The work has been conducted during the period September 2011 to November 2014 at the section of Materials and Surface Engineering under the supervision of Professor Marcel A.J. Somers. Dr. Kristian V. Dahl and Dr. Melanie Montgomery (COWI/Vattenfall) co-supervised the project. This work has been part of the project GREEN–Work Package 5 financially supported by the Danish Council for Strategic Research (DSF). Vattenfall and DONG Energy are appreciated for active participation in WP5.

Saeed Kiamehr

Kgs. Lyngby, November 2014

Acknowledgements

First and foremost I would like to express my sincere thanks to my supervisor Professor Marcel A.J. Somers whose help and support paved the way for me during the past years. Dr. Kristian V. Dahl (formerly DONG Energy, now DTU), Dr. Melanie Montgomery (formerly Vattenfall, now COWI) and Dr. Anette Hansson (formerly DONG Energy, now Haldor Topsøe) are appreciated for their useful guidance and consultations. I am grateful to the Danish Council for Strategic Research (DSF) for financially supporting my studies through the GREEN project.

I express my gratitude to my colleagues at the section of Materials and Surface Engineering for their kind companionship and providing a friendly environment for research. I specially thank the section's lab technicians Steffen Munch, Flemming Grumsen, Rolf Jensen, Peter Westermann, Lars Pedersen and John Troelsen for their help and support during the experimental part of the work. At the end I devote my ultimate appreciation to my parents. Without their care, love and encouragement it would have been impossible to reach this stage of life.

Abstract

High temperature corrosion induced by potassium chloride (KCl) is a major challenge for biomass-based power plants. The current study aims at identification or development of alloys or coatings that can yield a better performance at a target metal temperature of 600°C compared to austenitic stainless steels like TP347HFG. For this purpose theoretical and experimental investigations were performed, which can be divided into three major parts:

Part 1: Study of the reactivity between oxides and KCl

Calculation of the metal-oxygen-chlorine phase stability diagrams was performed for a large number of metals. This was aimed at identifying the constituent elements of a corrosion resistant alloy. Calculations suggested Al, Si, Cr, Ti, Y, Ce, Ta, Hf and Zr as suitable oxide-forming elements as well as Mo, Ni and Co as suitable matrix-forming elements. However, the presence of potassium in the environment necessitates that oxides of these elements should have a low affinity for reaction with KCl. Therefore the reactivity between oxides of these elements (except Mo) and KCl was experimentally investigated. Fe_2O_3 and Mn_3O_4 were also included as part of the experiments. Exposures were conducted at 650°C for 15h in flowing N_2(g)+5%O_2(g)+15%H_2O(g). Each exposed sample was a mixture of the metal oxide and KCl pressed into a tablet. Samples were examined with X-Ray Diffractometry (XRD) before and after the exposure. In addition, each exposed sample was further studied with Scanning Electron Microscopy (SEM) and Energy Dispersive X-Ray Spectroscopy (EDS). Investigations indicated that Cr_2O_3 and SiO_2 are reactive while no major reactivity was observed for Al_2O_3, CeO_2, Co_3O_4, Fe_2O_3, HfO_2, NiO, Ta_2O_5, TiO_2, Y_2O_3 and ZrO_2.

Part 2: Performance of commercial and model alloys

In order to rank currently available alloys and obtain further knowledge on the mechanism of high temperature corrosion induced by KCl, a wide range of commercial and model alloys were exposed under conditions relevant to high temperature corrosion in biomass-firing power plants. The exposures were conducted at 600°C for 168h in flowing N_2(g)+5%O_2(g)+15%H_2O(g). Samples were covered with a KCl deposit layer prior to the exposure. The alloys consisted of Fe-base and Ni-base chromia-formers as well as selected alumina-formers and silica-formers. In addition, complementary exposures in static lab air were performed to elucidate the contribution of chlorine in the course of corrosion as well as the role of potassium chloride vapor.

Results showed that while the majority of the alloys formed protective slow-growing oxides in the absence of KCl, they all suffered from significant attack when KCl was present. Thereby the inability of Cr to form a protective oxide when KCl is present was proven. No beneficial effect from the presence of Al (maximum 10.9 at.%) in the investigated alumina-formers could be observed. The Al in these alloys was either selectively removed along with Cr or was internally oxidized/nitrided. For Si (maximum 6.5 at.%) different effects were observed. For ferritic stainless steels internal oxidation/nitridation together with the detection of potassium in the inner oxide was found. For the investigated Ni-base silica former (alloy HR160), the extent of attack was relatively

small and no internal oxidation/nitridation was observed. However, potassium enrichment was found in the inner oxide along with Si and Cr. In summary, the measurement of the depth of attack on all the investigated alloys indicated that stainless steels EN1.4057 and Sanicro 28 along with the Ni-base alloys 625 and HR160 performed slightly better than the current materials solution TP347HFG in the laboratory exposures. Pure Ni incurred the least amount of damage.

Part 3: Performance of aluminum diffusion coatings

Among the suitable oxide-forming elements identified in part 1, Al is an obvious choice for further investigations. However, the results in part 2 suggested that high concentrations (at least more than 10.9at.%) of this element would be required to obtain a beneficial effect. Therefore the influence of diffusion enrichment of Al into the surface of selected substrates was investigated. Low temperature pack cementation (650˚C) was used for this purpose. The ferritic-martensitic steel P91 and pure Ni were used as substrates. Coatings produced consisted of $Fe_{1-x}Al$ on P91, Fe_2Al_5 on P91 and Ni_2Al_3 on pure Ni. Samples were exposed for 168h at 600^{o}C in static lab air with and without a KCl deposit. The salt-free exposure did not result in the formation of a fast-growing oxide on any of the samples. However, Fe_2Al_5 on P91 was extensively attacked when KCl was present. $Fe_{1-x}Al$ on P91 showed a passive behavior on large parts of the surface with only a few cases of localized attack. Ni_2Al_3 on Ni did not show any signs of attack anywhere on the sample.

Keywords: High temperature corrosion, deposit, potassium chloride, protective oxide breakdown, chlorine-induced volatilization, chromia-former, alumina-former, silica-former, diffusion coating.

Resume

Højtemperaturkorrosion induceret af kaliumklorid (KCl) er en stor udfordring for biomasse-fyrede kraftvarmeværker. Målet med dette studie er at identificere eller udvikle nye legeringer eller belægninger, som kan resultere i forbedrede egenskaber ved en metaltemperatur på 600˚C sammenlignet med austenitiske rustfrie stål såsom TP347HFG. Til dette formal er der udført teoretiske og eksperimentelle undersøgelser, som kan inddeles i tre dele:

Del 1: Studie af reaktivitet mellem oxider og KCl

Metal-oxygen-klor fase stabilitets diagrammer er blevet udregnet for at identificere metal-elementer, som potentielt kan udgøre grundelementerne i en korrosionsfast legering. Ifølge beregningsresultaterne er Al, Si, Cr, Ti, Y, Ce, Ta, Hf og Zr egnede som oxiddannere, mens Mo, Ni og Co vil være egnede som matrice-elementer. Eftersom der er KCl tilstede er der det yderligere krav, at oxiderne af de identificerede elementer ikke skal kunne reagere direkte med KCl. Derfor blev reaktiviteten mellem oxider af de identificerede elementer (med undtagelse af Mo) og KCl undersøgt eksperimentelt. Reaktiviteten af Fe_2O_3 og Mn_3O_4 blev også undersøgt. Eksponeringer blev foretaget ved 650^{o}C i 15 timer i strømmende N_2(g)+5%O_2(g)+15%H_2O(g). Test emnerne bestod af metaloxid- og KCl pulver presset til pille-form. Test emnerne blev karakteriseret med røntgen diffraktion (XRD) både før og efter eksponering. Efter eksponering blev testemnerne også undersøgt med scanning elektron mikroskop (SEM) og energi-dispersiv røntgen spektrometri (EDS). Undersøgelserne indikerede at Cr_2O_3 og SiO_2 var reaktive, mens der ikke var nogen målbar reaktivitet for Al_2O_3, CeO_2, Co_3O_4, Fe_2O_3, HfO_2, NiO, Ta_2O_5, TiO_2, Y_2O_3 og ZrO_2.

Del 2: Test af kommercielle legeringer og model-legeringer

For at evaluere opførslen af forskellige legeringer og opnå en øget viden om mekanismerne bag højtemperaturkorrosion induceret af KCl blev en bred række af kommercielt tilgængelige legeringer og model-legeringer testet under forsøgsbetingelser relevante for højtemperaturkorrosion i biomasse-fyrede værker. Eksponeringerne blev udført ved 600^{o}C i 168 timer i strømmende N_2(g)+5%O_2(g)+15%H_2O(g). Test-emnerne blev dækket med et lag af KCl inden eksponering. De testede legeringer inkluderer jernbaserede (stål) og nikkelbaserede kromoxiddannere samt udvalgte aluminiumoxid- og siliciumoxiddannere. Derudover udførtes dedikerede forsøg til at belyse rollerne af klor og KCl på gasform i den observerede korrosion.

Resultaterne viste at mens hovedparten af de undersøgte legeringer fremviste beskyttende opførsel (langsomt voksende oxidlag) når KCl ikke var tilstede, så var der betydeligt angreb på alle legeringer, når der tilførtes KCl. Derved blev det bevist, at et beskyttende oxidlag ikke kan baseres på Cr, når KCl er tilstede. Der blev ikke observeret nogen gavnlig effekt af aluminium (maks. indhold på 10.9 atom%) for de undersøgte aluminiumoxiddannende legeringer. Aluminium blev enten selektivt korroderet sammen med krom eller internt oxideret/nitreret. For silicium (maks. indhold på 6.5 atom%) blev der observeret forskellige effekter. For ferritiske rustfri stål blev der observeret intern oxidation/nitrering og kalium blev fundet i det indre oxid. For den undersøgte silicium-holdige nikkelbaserede legering (HR160) var der relativt lidt korrosionsangreb og der blev

ikke observeret intern oxidation/nitrering. Der blev dog fundet kalium opkoncentreret i det indre oxid sammen med silicium og krom. I sammendrag viste målingerne af korrosionsdybde på alle legeringerne, at de rustfrie stål EN1.4057 og Sanicro 28 samt de nikkelbaserede legeringer IN625 og HR160 klarede sig marginalt bedre i laboratorieforsøgene end stål TP347HFG, som er det stål som anvendes i kedler i dag. Rent nikkel den laveste korrosionsdybde af alle de testede materialer.

Del 3: Aluminiumsbaserede coatings

Iblandt de egnede oxiddannende elementer, som blev identificeret i del 1 er aluminium et oplagt valg for videre undersøgelser. Resultaterne i del 2 viste dog at indholdet af aluminium i så fald skulle være højere end 10.9 atom% for at opnå en gavnlig effekt. Derfor blev virkningen af at inddiffundere aluminium i overfladen af forskellige substrater undersøgt. Lavtemperatur pack-metoder (650˚C) blev anvendt til dette formal. Det martensitiske stål P91 og rent nickel blev anvendt som substrat-materialer. De producerede belægninger var $Fe_{1-x}Al$ på P91, Fe_2Al_5 på P91 og Ni_2Al_3 på rent nikkel. Test-emner blev eksponeret i 168 timer ved 600˚C i laboratorium-atmosfære både med og uden KCl. De salt-frie eksponeringer førte i ingen tilfælde til dannelse af et hurtigt voksende oxid. Derimod blev der observeret udbredt korrosion af Fe_2Al_5 på P91 når KCl var tilstede. $Fe_{1-x}Al$ på P91 udviste generelt en passiv opførsel men med enkelte lokale angreb. For Ni_2Al_3 på Ni var der ingen tegn på korrosion efter eksponering.

Nøgleord: Højtemperaturkorrosion, aflejringer, kaliumklorid, nedbrud af beskyttende oxid, klor-induceret volatilitet, kromoxid, aluminiumsoxid, siliciumoxid, diffusionsbelægning.

List of Publications

1. Saeed Kiamehr, Kristian V. Dahl, Trine N. Lomholt, Thomas L. Christiansen, Marcel A.J. Somers

High Temperature Corrosion due to Biomass Firing: A Study on the Reactivity between Potassium Chloride and Oxides

International Symposium on High Temperature Oxidation and Corrosion (ISHOC) 2014, Hakodate, Japan

2. Saeed Kiamehr, Kristian V. Dahl, Melanie Montgomery, Marcel A.J. Somers

KCl-Induced High Temperature Corrosion of Selected Commercial Alloys Part I: Chromia-formers

The manuscript is ready for submission

3. Saeed Kiamehr, Kristian V. Dahl, Melanie Montgomery, Marcel A.J. Somers

KCl-Induced High Temperature Corrosion of Selected Commercial Alloys Part II: Alumina and Silica-formers

The manuscript is ready for submission

4. Saeed Kiamehr, Sunday C. Okoro, Kristian V. Dahl, Melanie Montgomery, Marcel A.J. Somers

KCl-Induced High Temperature Corrosion Part III: Performance of Model Alloys and Argumentations on the Involved Mechanisms

The manuscript is under modification

5. Saeed Kiamehr, Trine N. Lomholt, Kristian V. Dahl, Marcel A. J. Somers

Application of Aluminum Diffusion Coatings to Mitigate the KCl-induced High Temperature Corrosion

The manuscript is under modification

6. Torbjörn Jönsson, Andreas Slomian, Trine N. Lomholt, Saeed Kiamehr, Kristian V. Dahl

Microstructural Investigations of Pure Nickel Exposed to KCl Induced High Temperature Corrosion

Accepted for publication in Materials at High Temperatures

Guidelines for the reader

The present thesis starts with an introduction regarding the importance of high temperature corrosion due to biomass firing and its implications for the energy conversion industry (Chapter 1).

Chapter 2 reviews the available literature regarding the corrosive effects of chlorine and alkali chlorides at high temperatures. Sections 2.1.3 and 2.2.2 are devoted to material performance reviews and contain a number of successful applications of metals and alloys in corrosive chlorine and alkali-chloride contaminated environments.

In Chapter 3 a critical review of the literature is presented based on the collation of the cited sources as well as complementary thermodynamic assessments by the author (section 3.1). This forms the basis of material design which is the subject of section 3.2.

Chapter 4 addresses the planning of the experimental investigation based on the results in Chapter 3. In addition, a number of experimental methods to evaluate the extent of high temperature corrosion are mentioned and the choice of method adopted in the current study is highlighted. At the end (section 4.3) a brief review of the analytical tools employed in this study is presented. This contains the fundamental concepts, implementation and limitations of Scanning Electron Microscopy (SEM), Energy Dispersive X-Ray Spectroscopy (EDS) and X-Ray Diffraction (XRD). Therefore if the reader is familiar with these concepts this section can be skipped.

Chapter 5 is a summary of the experimental investigations performed in this study along with the corresponding results. For details of the experimental parameters and results as well as the discussion, the reader is kindly asked to skip this chapter and refer to the appended papers (Chapter 9).

Finally, a number of appendices are included to provide complementary information regarding the details which were not directly addressed in different chapters. Appendix 1 contains chemical composition of the alloys mentioned in Chapter 2. Appendix 2 contains the X-Ray Diffractograms, Scanning Electron Micrographs and Energy Dispersive X-Ray Spectroscopy analysis associated with paper 1. Appendix 3 is a brief introduction on the computational thermodynamics as it forms the basis of the commercial packages (Thermo-Calc, FactSage and HSC Chemistry) employed in this study for thermodynamic calculations.

Table of Contents

1. Introduction

Due to the constantly increasing environmental concerns with regard to the greenhouse effect, utilization of CO_2-neutral fuels has become a point of focus over recent years. Among different options, biomass has shown to be an interesting fuel especially in countries with large forestry and agricultural resources. This is mainly due to the fact that biomass combustion, depending on the planting and consumption rate, has the potential of preserving the CO_2 balance in the atmosphere. However, combustion of biomass is not free from practical difficulties. Among the challenges, high temperature corrosion of heat exchangers is one of the most important negative factors when using biomass as a fuel. Efficiency of the power plant is closely coupled to the steam data, temperature and pressure, and as the temperature is raised an accelerated corrosion on hot section components such as superheater tubes is observed. This limits the output steam temperature of the current biomass-based power plants to a maximum of 540^{o}C [1] making them less efficient compared to the plants firing fossil fuels.

1.1 Description of the Problem

During biomass combustion, high corrosion rates are observed on the fireside of superheater tubes. The currently employed materials for such tubes are generally austenitic stainless steels such as TP347H (see appendix 1 for composition of alloys). This is due to their high temperature strength and creep resistance in addition to acceptable steamside oxidation rates. However, they lack adequate corrosion resistance on the fireside, which compels the industry to keep the steam temperature below 540^{o}C to maintain the corrosion rate at an acceptable level.

Mechanisms of fireside corrosion due to the biomass combustion are closely related to factors such as fuel composition, additives, temperature, combustion technology and plant design. Along with biomass combustion, deposits rich in potassium chloride (KCl) are formed on the superheater tubes [2]. Frandsen [2] described studies made in a number of Danish power plants dedicated to biomass firing. It was shown that the deposit contains about 80 wt.% KCl and the rest is mostly fly-ash particles composed of potassium calcium silicates. In some cases the inner layer of the deposit was almost pure KCl [3]. In addition, the flue gas contains HCl(g) and SO_2(g), which are known to be aggressive especially at high temperatures. Table 1.1 and Table 1.2 show typical compositions of fuel and flue gas from Danish power plants. As can be seen, potassium and chlorine form a large portion of the inorganic impurities of the fuel and the flue gas tends to show a large Cl/S ratio.

KCl has a strongly corrosive nature towards many metals and conventional alloys even in static lab air where the atmosphere lacks any HCl(g) and SO_2(g) [4]–[8]. However, even for well-controlled laboratory exposures, the exact mechanism of KCl-induced high temperature corrosion is not yet fully understood. In a power plant case, the situation is further complicated by the following factors:

- Co-existence of a number of corrosive compounds creates a complex aggressive environment (Figure 1.1) in which more than one mechanism may be responsible for degradation or there might even be synergy/antagonism between different phenomena.
- Involved mechanism(s) can change over time due to physical and chemical changes in the deposit layer such as change in composition, sintering, melting, or shedding of the deposit.
- Due to temperature variations (Figure 1.2), different mechanisms may be active over different periods of service, and at different locations in the plant.
- The temperature gradient between the flue gas and metal surface, which is of the order of several hundred degrees Celsius, may activate additional mechanisms which are not present under isothermal laboratory conditions.

Table 1.1: Fuel data for Danish cereal straw and wood chips [9].

Water content and heating value	unit	Straw		Wood chips	
		typical	variation	typical	variation
Water content	%(w/w)	14	8-23	45	20-60
Lower heating value (as received)	MJ/Kg	14.9	12.3-16.9	9.5	5.9-15.9
Lower heating value (water and ash free)	MJ/Kg	18.6	18-19	19.5	18.5-20.5
chemical composition (wt.% on a dry basis)					
Ash		4.5	2-7	1.0	0.3-6
Volatiles		78	75-81	81	70-85
Hydrogen, H		5.9	5.4-6.4	5.8	5.2-6.1
Carbon, C		47.5	47-48	50	49-52
Nitrogen, N		0.7	0.3-1.5	0.3	0.1-0.7
Sulfur, S		0.15	0.1-0.2	0.05	<0.1
Chlorine, Cl		0.4	0.1-1.1	0.02	<0.1
Silicon, Si		0.8	0.1-1.5	0.1	<1.1
Aluminum, Al		0.005	<0.03	0.015	<0.1
Iron, Fe		0.01	<0.03	0.015	<0.1
Calcium, Ca		0.4	0.2-0.5	0.2	0.1-0.9
Magnesium, Mg		0.07	0.04-0.13	0.04	<0.1
Sodium, Na		0.05	<0.3	0.015	<0.1
Potassium, K		1.0	0.2-1.9	0.1	0.05-0.4
Phosphorous, P		0.08	0.03-0.2	0.02	<0.1

Table 1.2: Flue gas composition due to straw firing (vol.%). Values marked with* are on dry basis.

O_2%	CO_2%	SO_2 (vppm)	HCl (vppm)	N_2%	H_2O%	Ref.
6*	12*	60*	400*	82*	2-3	[10]
6-8	4-18	20-30	15-900	bal.	2-11	cited in [11]

Therefore a sustainable material solution has to take many factors into account. The current study aims at obtaining further insight into the corrosion mechanism(s) as well as identifying or developing materials with improved performance compared to TP347HFG at a target metal temperature of 600^{o}C. For this purpose an extensive literature survey was performed, a summary of which is presented in Chapter 2. Subsequently literature reports were critically collated and evaluated with thermodynamic calculations employing the commercial software packages Thermo-

Calc [12], HSC Chemistry [13] and FactSage [14]. The in-depth discussion of literature reports and the corresponding calculations are given in Chapter 3. Based on these, material design guidelines are deduced which will be further examined in the experimental part of this work.

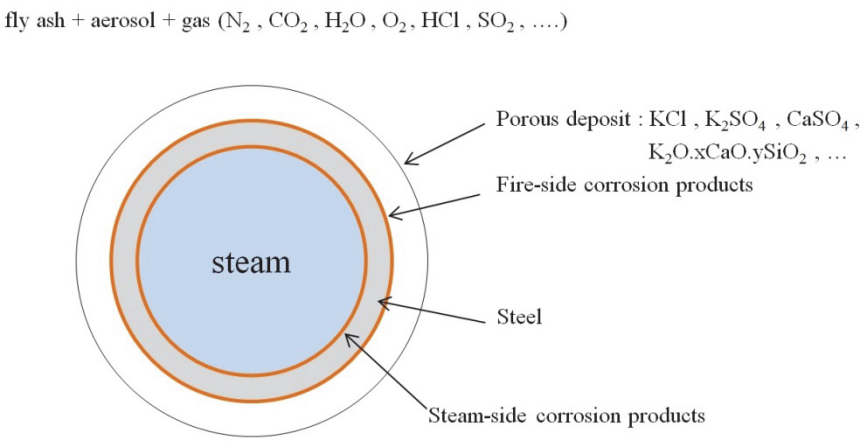

Figure 1.1: Schematic drawing of the cross section of a superheater tube with the deposit.

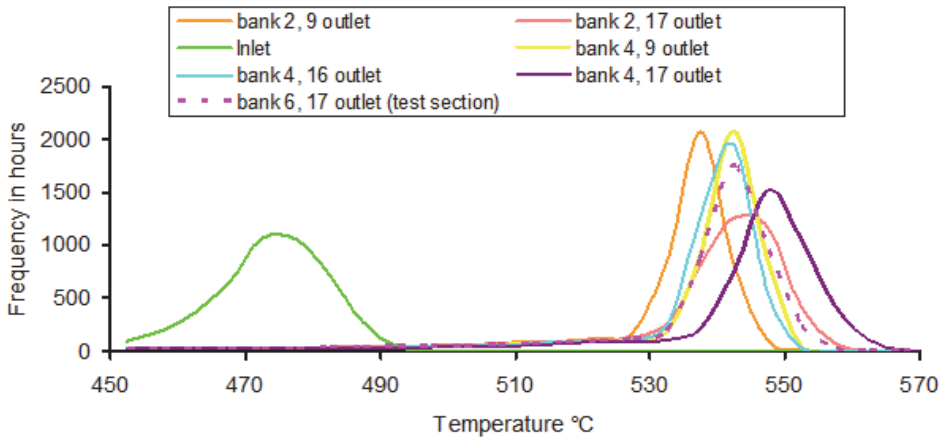

Figure 1.2: Example of steam temperature recorded at the inlet and outlet of superheater tubes at various positions in a Danish biomass-firing power plant. Exposure period has been 1 year [1].“Bank” refers to a bundle of tubes at a certain position in the boiler.

2. Synopsis of the Literature

This chapter summarizes the literature on the corrosive effects of gaseous chlorine-bearing species (HCl and Cl_2) as well as alkali chlorides (KCl and NaCl) at high temperature. Corrosion in biomass firing occurs primarily due to potassium and chlorine from the fuel. However, it is still debatable which of these two elements is the more important for the overall damage incurred by corrosion. This implies that robust materials design needs to consider both elements. Therefore the synopsis is subdivided in two sections; one part addressing the corrosion induced by gaseous Cl_2 and HCl and one part devoted to alkali chlorides, where the effects of the alkali component of the salt are addressed in detail.

2.1 High Temperature Corrosion Induced by Chlorine (Cl_2) and Hydrogen Chloride (HCl)

As a consequence of its high electronegativity, chlorine is one of the most reactive elements of the periodic table. This results in severe degradation of metals and alloys in chlorine containing environments, especially at elevated temperature. High temperature corrosion resulting from Cl_2(g) and HCl(g) is a key challenge in a variety of industrial processes such as polymer decomposition, processing of sewage sludge ashes and gasification of chlorine containing fuels [15]–[18]. In such cases the extent and rate of corrosion may be so high that the overall function of the unit becomes limited. To begin with, mechanisms of corrosion in the atmospheres containing only Cl_2(g) or HCl(g) are discussed and more complex environments will be addressed later.

2.1.1 Mechanisms: Oxygen-free atmospheres

Compared to the attack by species such as oxygen, sulfur and carbon, a characteristic feature of high temperature corrosion by chlorine is the development of volatile corrosion products [19]. Under such conditions, protection by formation of a dense and slow growing chloride layer is not possible because the corrosion product can be incorporated in the gas phase [17]. At low temperatures, chloride formation is typically the dominant reaction and consequently mass gain is the only observed effect (see Figure 2.1). As the temperature increases, sublimation of the metal chloride contributes to the mass change as well. At a specific temperature a steady state will be reached where the thickness of the chloride layer is constant over time and the amount of chloride formed is equal to the amount that sublimates. Kinetics of such reactions can be modeled [20], [21] by generalization of the Tedmon equation [22] which was originally derived to model the simultaneous formation and volatilization of chromium oxide in Fe-Cr alloys. At high enough temperatures sublimation becomes the dominant effect and a net mass loss is observed. In this case transfer of the Cl_2(g)/HCl(g) or volatile chlorides through the gas phase boundary layer is usually the rate controlling step [20] .

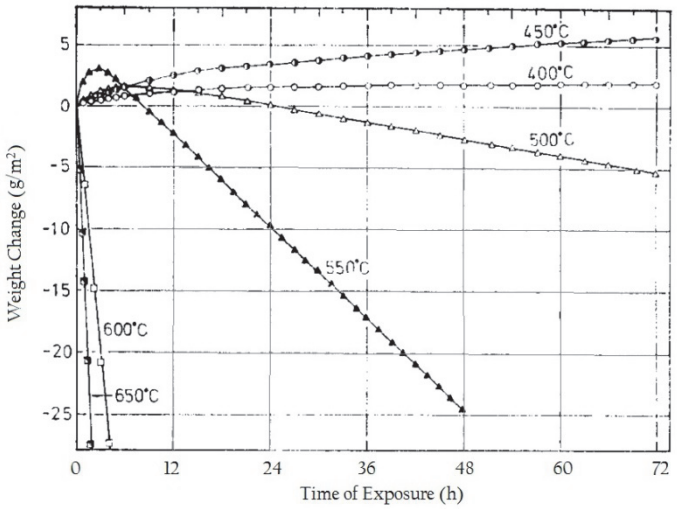

Figure 2.1: Mass change vs. time under stagnant HCl(g) for pure nickel [20]. The general trend is a parabolic mass gain at low temperatures and a paralinear mass loss at high temperatures.

2.1.2 Mechanisms: Oxidizing-Chlorinating atmospheres

Protection against corrosion at high temperatures is usually achieved through the formation of dense and adherent oxide layers. The addition of oxygen to a chlorine containing environment provides the possibility for protective oxide formation and consequently passivation of a metal surface. However, in practice with addition of oxygen or oxygen-bearing species to the system, it is observed that the corrosion rate may decrease or increase [21], [23]. The actual behavior depends on temperature, $P_{O2(g)}/P_{Cl2(g)}$ ratio, gas velocity and the reacting metal (Figure 2.2). Both oxides and chlorides can form and therefore a metal sample can undergo either mass gain or mass loss, as shown schematically in Figure 2.3. Corrosion under oxidizing-chlorinating conditions is a complex phenomenon and many different mechanisms can independently or simultaneously take place. A review on the suggested mechanisms is presented in the following sections.

2.1.2.1 Active Oxidation or Chlorine Cycle

To account for the acceleration of corrosion under conditions where oxides are the thermodynamically stable species, McNallan et al.[24] and Grabke et al.[25] suggested that chlorine penetrates the oxide layer and reacts with the underlying metal at the metal/oxide interface. At such locations, the oxygen partial pressure is low and chlorides are thermodynamically stable. However, as the metal chlorides are generally volatile at high temperatures, they sublime and diffuse out to reach the oxide/gas interface. Here the oxygen partial pressure is high and chlorides are unstable. Therefore, they react to form oxides and chlorine is released. The liberated chlorine can then diffuse through the oxide to the metal/oxide interface and hence a cycle is formed. In this model pores and cracks of the oxide layer are considered as the transport channels. Under such conditions no passivation is possible and the underlying material is actively consumed. Therefore this mechanism

is widely referred to as *"active oxidation"* in the literature. A schematic representation of this is given in Figure 2.4.

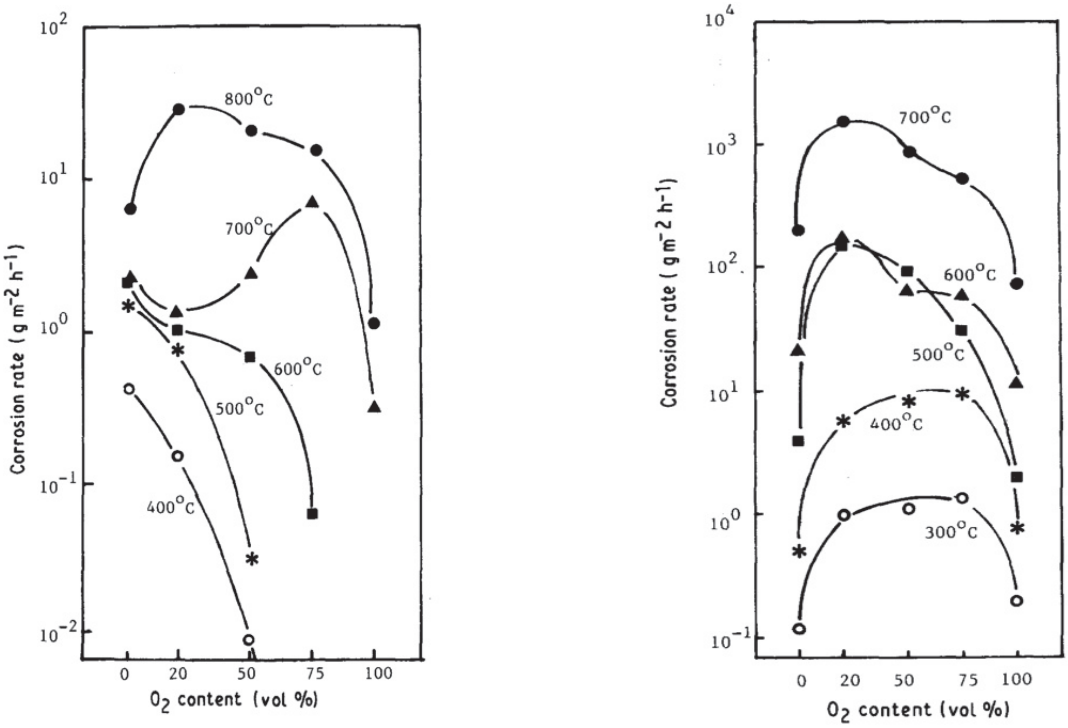

Figure 2.2: Change in the average corrosion rate of (a) pure chromium and (b) pure iron under mixtures of O_2(g) and HCl(g) after a 5h exposure. Rates were determined by mass change measurement after the removal of corrosion products [21][23].

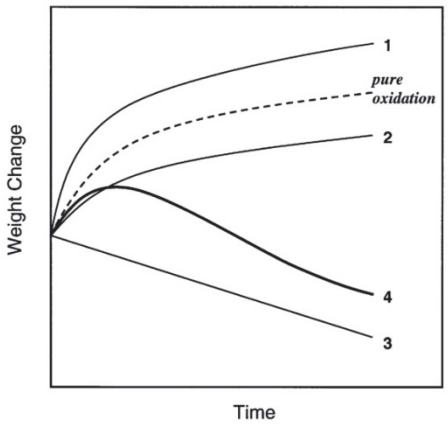

Figure 2.3: Four typical mass change curves in high temperature corrosion in O_2(g)+Cl_2(g)/HCl(g) atmospheres [26].

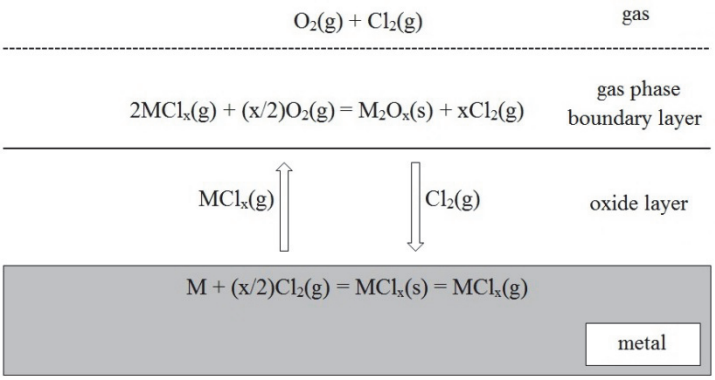

Figure 2.4: Schematic of the active oxidation mechanism.

Removal of alloying elements as volatile metal chlorides often accounts well for the microstructure of the alloys corroded in chlorine containing atmospheres (see Figure 2.5a-b). However, active oxidation cannot describe how the oxide layer is permeable to $Cl_2(g)$ and metal chlorides, while it is impermeable to $O_2(g)$, despite the smaller molecule [27], [28].

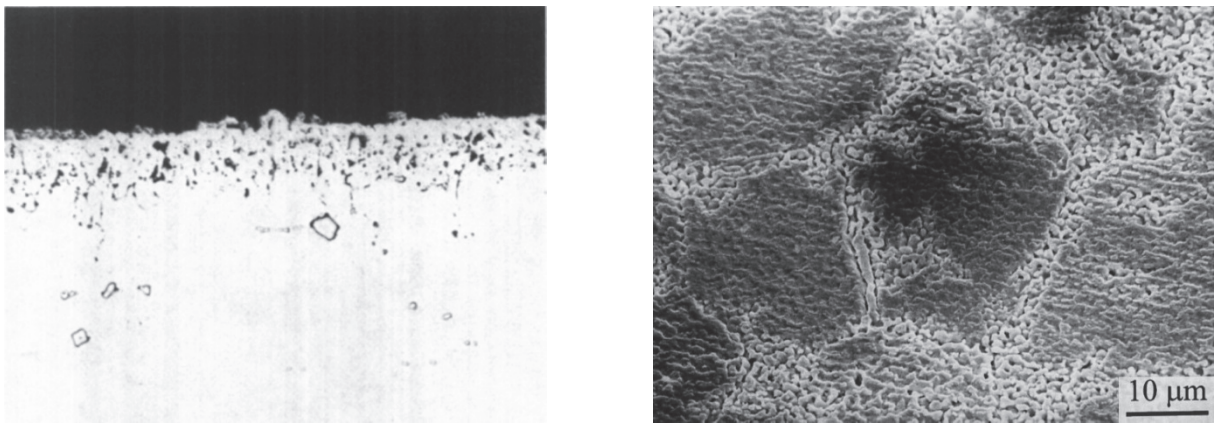

(a) (b)

Figure 2.5: (a) Cross section of alloy 800H exposed to Ar(g)+20%O_2(g)+2%Cl_2(g) at 900°C for 8h showing formation of porous nickel-rich areas depleted in Cr [29] (b) Surface of alloy 825 exposed to N_2(g)+5%O_2(g)+500vppm HCl(g) at 600°C for 139h. Image is taken at 45° tilt. Corrosion products are removed prior to the analysis. Image shows formation of porous Ni-rich areas (depleted in Cr) especially at the alloy grain boundaries [30].

2.1.2.2 Electrochemical Reaction Path

To avoid the abovementioned drawback of the active oxidation mechanism and to describe the mode by which chlorine migrates through the oxide layer, Folkesson et al.[28] suggested an electrochemical route for the reaction. In this model $Cl_2(g)$ or HCl(g) is assumed to be reduced at the oxide/gas interface to produce Cl^- ions. This cathodic reaction is coupled to the anodic reaction of metal oxidation at the metal/oxide interface. Subsequently Cl^- diffuses inward through the grain boundaries of the oxide layer while there is a countercurrent of metal cations diffusing outward. Metal chlorides will form wherever a metal cation meets a Cl^- anion. Therefore, depending on the

diffusivity of cations or anions, chlorides can form at the metal/oxide interface, within the oxide layer or at the oxide/gas interface. It has to be mentioned that in the latter case, chlorides are metastable and will be converted into oxides due to the locally high $P_{O2(g)}$ at the oxide/gas interface. Abels and Strehblow [31] showed that chlorine is even able to penetrate a pre-formed Cr-rich oxide layer on alloy IN600 (Figure 2.6).

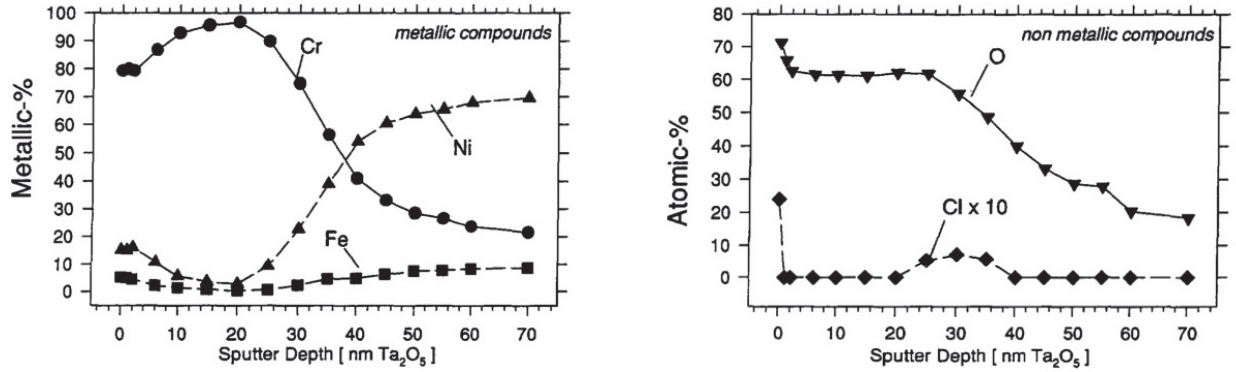

Figure 2.6: X-Ray Photoelectron Spectroscopy (XPS) depth profile of alloy IN600 after pre-oxidation at 700°C for 10min in Ar(g)+10%O_2(g) followed by exposure to Ar(g)+10%O_2(g)+500vppm HCl(g) for 30 min at the same temperature [31].

2.1.2.3 Mechanical Damage to the Oxide Layer

The presence of chlorine in the environment has a negative effect on the adherence of the oxide layer to the substrate. In fact, it has been widely observed [25], [26], [28], [30], [32]–[38] that the scales formed upon high temperature corrosion under oxidizing-chlorinating conditions are non-adherent and spall easily. Blistering of the oxide during exposure in O_2(g)+Cl_2(g) has been observed in-situ by McNallan et al.[39]. Zahs et al.[30] reported the formation of a multilayered highly wrinkled oxide on Fe-Cr alloys exposed to N_2(g)+5%O_2(g)+(500-1500) vppm HCl(g) at 600°C (Figure 2.7a). They observed that even pure Cr showed a thick multilayered oxide under similar conditions (Figure 2.7b) which was clearly reflected by serrations in the thermogravimetric curves. These findings strongly suggest that spallation of the oxide layer takes place during the exposure. Formation of multilayered oxide was ascribed to the growth stresses during the oxide formation, as well as formation of chlorides at the metal/oxide interface. Jonsson et al.[32] exposed alloy 310S to a similar atmosphere and observed formation of blisters (ridges) along the metal grain boundaries. Investigation of the sample showed that the oxide had buckled and had completely separated from the underlying metal on such locations. They attributed this to the stresses due to the large molar volume of transition metal chlorides formed at the metal/oxide interface (see Figure 2.7c-d for examples of blisters and ridges). Prescott and Stott [40] put forward the possibility for formation of liquid metal chlorides at the metal/oxide interface. Schwalm and Schutze [38] blamed the high vapor pressure of $FeCl_2$ formed at the metal/oxide interface, as a reason for the observed damage on stainless steel 10CrMo910 exposed to synthetic air+2%Cl_2(g) at 500°C. All in all, it appears that there is a general agreement in the literature with regard to the mechanical damage to the oxide layer caused by the presence of metal chlorides at the metal/oxide interface.

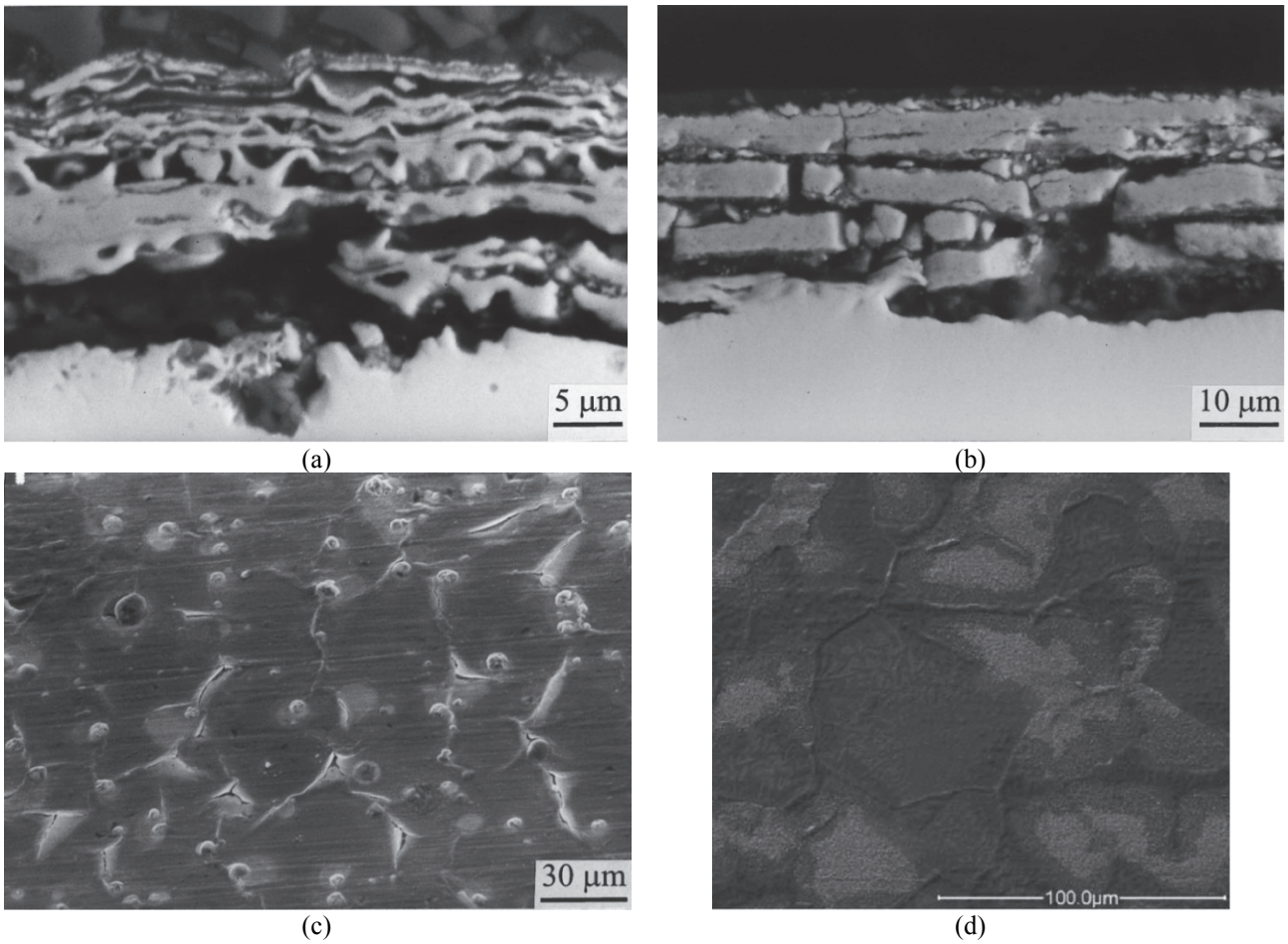

(a) (b) (c) (d)

Figure 2.7: (a) Fe-15wt.% Cr alloy exposed to N_2(g)-5%O_2(g)-500 vppm HCl(g) at 600°C for 168h [30](b) Pure Cr exposed to He(g)+5%O_2(g)+500 ppm HCl(g) at 600°C for 140h [30] (c) alloy 800 exposed to N_2(g)+5%O_2(g)+1500 vppm HCl(g) at 400°C for 168h [30] (d) alloy 310S exposed to N_2(g)+5%O_2(g)+500 vppm HCl(g) at 500°C for 1h [28].

2.1.2.4 Volatilization of the Oxide Layer

Maloney and McNallan [41] observed that exposure of pure Co at 927°C to oxidizing-chlorination atmospheres of high $P_{O2(g)}/P_{Cl2(g)}$ ratio resulted in steady state mass loss after a short period of mass gain (similar to Figure 2.1). They described the observed effect in terms of simultaneous oxide growth and oxide volatilization due to chlorination and subsequent evaporation (eq. 2.1)

$$CoO(s) + Cl_2(g) = CoCl_2(g) + (1/2)O_2(g) \quad ; \quad 2.1$$

Similar behavior was observed for pure Ni [42]. In addition, it was noted that on reducing the temperature from 927 to 827°C or 727°C, once the $P_{O2(g)}/P_{Cl2(g)}$ ratio drops below a critical value, an accelerated attack takes place. In fact, the rate of metal consumption was so high that the sample ignited (Figure 2.8a). No accelerated attack was observed when the temperature was decreased from 727 to 627°C. They attributed these effects to the thickness of the oxide layer formed at lower temperatures. In other words the oxide formed at lower temperatures is not an impermeable barrier

against $Cl_2(g)$ diffusion. Therefore $NiCl_2(s)$ formed at the metal/oxide interface and subsequently sublimed due to its high vapor pressure at the exposure temperature. This is schematically shown in Figure 2.8b.

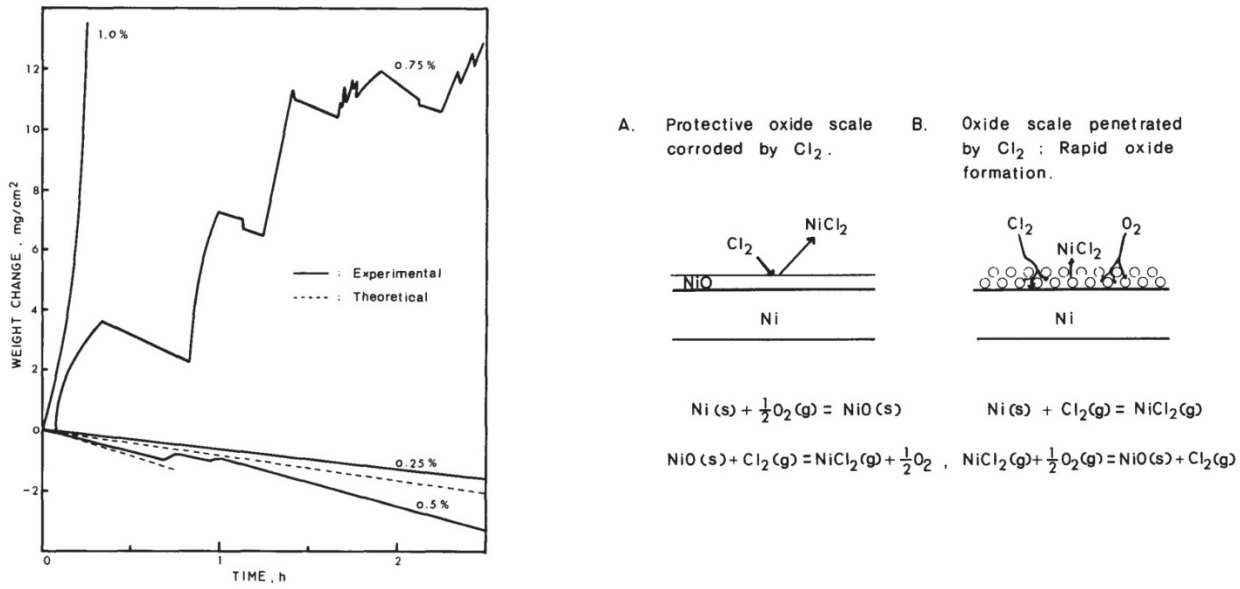

(a) (b)

Figure 2.8: (a) TG curves corresponding to Ni samples exposed to $Ar(g)+20\%O_2(g)+Cl_2(g)$ at 827°C. Values on the curves represent Cl_2 content of the gas (b) schematic of the change in corrosion mechanism [42].

Similar to Ni and Co, volatilization of the oxide formed on pure Cr has also been observed. However, under $O_2(g)+Cl_2(g)/HCl(g)$ atmospheres the vapor species is believed to be chromium oxychloride $CrO_2Cl_2(g)$[33], [43]. This is especially unfortunate as Cr is the crucial element for many high temperature alloys.

2.1.2.5 Modification of Transport Properties of the Oxide Layer

Entrapment or solubility of chloride ions in the oxide lattice, albeit in trace amounts, might play a role in changing the transport properties. Hossain and Saunders [44] suggested that chloride ions become incorporated in the close-packed oxide lattice which, in turn, increases the ionic mobility. Maloney and McNallan [41], [45] put forward the possibility for modification of transport properties in the oxide lattice due to an increase of the cation vacancy by incorporation of chloride ions (eq. 2.2). However, they mentioned that the effect should be small.

$$Cl_2(g) + O_o^{\cdot} = 2Cl_o^{\cdot} + V_M^{''} + (1/2)O_2(g) \quad ; \quad 2.2$$

Folkeson et al.[46] stated that incorporation of Cl^- into the oxide lattice is not expected due to its large size. Instead, they suggested that the presence of chloride ions (e.g. in the form of iron

chloride) at grain boundaries in the oxide facilitates the transport of ions across the oxide grain boundaries.

2.1.2.6 Internal Chlorination

There are a number of experimental investigations suggesting that the ingress of chlorine may not necessarily be limited to transport through the oxide layer. Stott et al.[47] studied a number of Fe-based and Ni-based alloys under air+2%Cl_2(g) at 900^{o}C and reported detection of chromium chloride within an internal corrosion zone. According to the authors, some internal chlorides even had a globular shape suggesting the presence of melt droplets at the exposure temperature (Figure 2.9a). Li and Rapp [48] embedded coupons of dilute Ni-Cr alloys in Ni+$NiCl_2$ mixture and exposed them at different temperatures for different durations. Subsequently they measured the solubility*diffusivity product ($N_x D_x$) and suggested that the chlorine atoms are not only adequately soluble but also have high diffusivity in the Ni matrix (Figure 2.9b). Elliott et al.[16] reported that the $N_x D_x$ product for chlorine in nickel at 750^{o}C is about two and a half times that for oxygen.

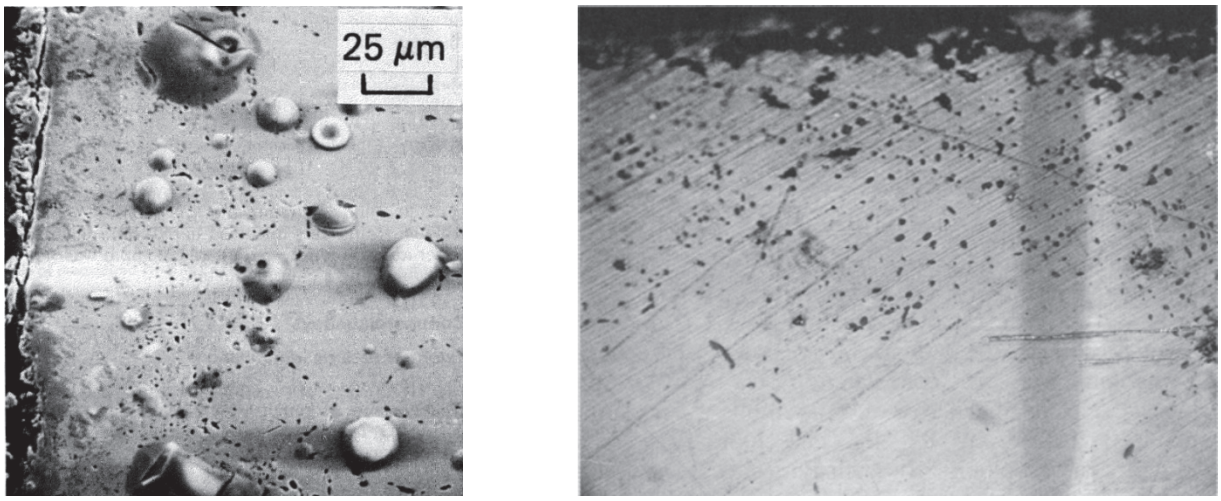

(a) (b)

Figure 2.9: (a) Morphology of the residual scale and internal corrosion zone of alloy 800H after 48h exposure to air+2%Cl_2(g) at 900^{o}C. Analysis shows that only chromium and chlorine are found in the globular areas [47]. Also note the grain boundary holes propagating deep into the alloy (b) Internal precipitation of $CrCl_2$ in Ni-0.56at.%Cr exposed at 900^{o}C while embedded in Ni+$NiCl_2$ powder mixture [48].

2.1.2.7 Competing Kinetics of Oxidation and Chlorination

Viklund and Pettersson [49] studied the behavior of a number of austenitic stainless steels under N_2(g)+10%O_2(g)+5%H_2O(g)+0.05%HCl(g) at 400 and 700^{o}C. Based on the significant amounts of the condensed metal chlorides at the cold parts of the furnace they suggested that the oxidation of sublimed metal chlorides is relatively slow. They also stated *"it seems that a kinetically favored formation of metastable chlorides has an important role in explaining high temperature corrosion in oxidizing-chlorinating environments, especially at lower temperatures"*. To the author's knowledge there is no direct comparison in the literature between the activation energies of oxidation and chlorination when the chemical reaction between metal and gas is the rate-controlling

step. However, the above-mentioned statement can have implications for material performance with decrease in temperature.

2.1.3 Mitigation of Corrosion

Although the abovementioned mechanisms portray a very aggressive image for chlorine, there are still materials that may render acceptable corrosion rates under chlorine-containing atmospheres at high temperatures. This section mentions these materials and presents a summary of the literature regarding the performance of commercial alloys.

As mentioned in section 2.1.2.4 due to the formation of volatile oxychloride, Cr is not necessarily a suitable oxide-forming element in an oxidizing-chlorinating atmosphere. In fact, depending on $P_{O2(g)}/P_{Cl2(g)}$ ratio, temperature and gas velocity, Cr may or may not be a beneficial element in the alloy. Stott and Shih [50] studied the corrosion behavior of a Fe-28wt.%Cr alloy in Ar(g)+20%O_2(g)+1%HCl(g) at 700^{o}C and reported that the mass gain of the sample was even larger than that of pure Fe. Kim an McNallan[51] investigated the performance of Fe-1wt.%Cr, Fe-5wt.%Cr, and Fe-20wt.%Cr in Ar(g)+50%O_2(g)+0.25%Cl_2(g) at 727^{o}C and found that all the alloys showed a similar corrosion extent. On the other hand, a later investigation within the same research group showed that 15wt.% (and more) Cr in Ni decreased the mass loss in Ar(g)+20%O_2(g)+0.25%Cl_2(g) at 927^{o}C [33]. Another study reporting a positive effect from Cr is the investigation by Viklund et al.[49]. They compared the corrosion resistance of a number of austenitic stainless steels under thermal cycling conditions at 700^{o}C in an atmosphere consisting of N_2(g)+10%O_2(g)+5%H_2O(g)+0.05%HCl(g). They reported improved performance with increase in Cr content of the alloys. Evidently, the effect of Cr depends on the actual experimental conditions. To compensate for this shortcoming, addition of Al or Si has sometimes been shown to be beneficial.

Elliott and Ansari [52] and Oh et al.[29] observed that under Ar(g)+20%O_2(g)+2%Cl_2(g) at 900^{o}C alloy 214, which contains 4.2wt.% Al, suffered only minor damage. This was while all the other alloys studied, which solely relied on Cr up to 30 wt.%, experienced significant attack due to the conversion of Cr_2O_3 to CrO_2Cl_2(g). The extent of corrosion was most pronounced for chromia-forming alloys containing refractory metals Mo and W. Rhee et al.[53] performed similar studies and found out that during long term (400h) exposures under Ar(g)+20%O_2(g)+0.25%Cl_2(g) at 900^{o}C, even with thermal cycling, alloy 214 showed least damage. Again all chromia-forming alloys, especially the W or Mo containing ones, showed significant mass loss due to the formation of volatile refractory metal oxychlorides. Analogous observations were reported by Stott et al.[47] based on experiments under Ar(g)+20%O_2(g)+2%Cl_2(g) at 900^{o}C. However, they report that although the Ni-Cr-Al alloys showed excellent performance, the Fe-Cr-Al alloy (FeCrAlloy) was completely corroded within 48h. Latreche et al.[54] reported satisfactory performance of alloys 214 and 602CA (the latter containing only 2wt.% Al) at 800^{o}C under synthetic air+0.1%Cl_2(g) atmosphere. Similar result was observed by Bender and Schutze [55] for alloy 602CA exposed under the same conditions. However, Schwalm and Schutze [56] reported that with increase in Cl_2(g) from 0.1 to 2% in synthetic air, at both 650^{o}C and 800^{o}C alloy 214 offers a similar corrosion performance to chromia-forming nickel-base alloys such as HR160 and alloy 59. Under reducing-

chlorinating conditions, Stott et al.[35] and Zheng et al.[57] reported a superior performance of alloy 214. However, this requires that the environment contains a sufficient amount of oxygen-bearing species such as $H_2O(g)$ or $CO_2(g)$.

The presence of Al in Fe-Cr alloys can also be beneficial under certain circumstances. Zahs et al.[58] studied the influence of alloying elements on the corrosion resistance of Fe-Cr alloys in $N_2(g)$+5%$O_2(g)$+500 vppm HCl(g) at 600^{o}C. They reported a positive effect of Al as the Fe-15Cr-5Al (wt.%) showed less mass gain compared to Fe-15wt.%Cr. However, this required that the surface was polished. The surface which was only ground showed a poor resistance leading to the formation of a multilayered, convoluted oxide scale. They attributed this effect to the physical effects (grinding marks and scratches) acting as a preferential site for the nucleation of chlorides. An interesting finding in their work was the effect of Si: Fe-15Cr-5Si (wt.%) showed a mass gain two orders of magnitude smaller than that of the Si-free alloy. The outstanding corrosion resistance was attributed to an increase in diffusivity of Cr due to the presence of Si. However, this result cannot be easily generalized as other researchers did not see an advantage of Si in chromia-forming alloys. Schwalm and Schutze [38], [59] studied the behavior of alloys 45TM and HR160 in synthetic air+2%$Cl_2(g)$ at temperatures ranging from 300-800^{o}C and did not observe a significant difference compared to the chromia-forming alloys. Bender and Schutze [55] studied alloy 45TM under synthetic air+(0.1-2)%$Cl_2(g)$ and reported corrosion performance analogous to the observations made by Schwalm and Schutze. In addition, they found the formation of internal chromium and silicon nitrides at 800^{o}C.

Another group of materials which has attracted attention for corrosion resistance concerns intermetallics, especially binary aluminides and silicides. Schwalm and Schutze [59] found that Fe_3Al has a satisfactory corrosion resistance against synthetic air+2%$Cl_2(g)$ at 800^{o}C. However, as the temperature is decreased to 650^{o}C this material is extensively attacked. They also mentioned that $MoSi_2$ suffered only from minor oxidation in the interior of the sample, which they attributed to the porosity of the original material. Latreche et al.[60] observed an outstanding corrosion resistance for bulk NiAl exposed to Ar(g)+0.2%$Cl_2(g)$+3vppm$O_2(g)$ at 600^{o}C. However, when the same material in the form of Atmospheric Plasma Sprayed (APS) coating was exposed at 800^{o}C, it was extensively attacked. Ni was removed due to volatilization by $Cl_2(g)$ and porous alumina was left behind. In another publication by the same author [61] it is reported that the addition of 9.5at.% Mo to NiAl significantly decreases the attack. The effect was ascribed to the formation of $(Mo,Ni)Al_2$ phase and its higher Al content as well as the relatively inert nature of α-Mo phase under such low $P_{O2(g)}$ conditions. Galetz et al.[62] studied the performance of bulk NiAl at 1000^{o}C in synthetic air+10%$Cl_2(g)$. They observed a significant attack of this material in the form of selective Al removal. However, they reported that additions of small amounts of Mo (e.g. 2 at.%) remarkably decreased the extent of attack. They argued that although Mo cannot be dissolved in NiAl its presence *"lowers the surface reaction rate"* and thereby less Al is lost to the gas in form of volatile chlorides.

Despite the successful cases of application of intermetallic phases in oxidizing-chlorinating atmospheres, this class of materials cannot be used as structural materials due to their inherent

brittleness. Therefore application of these materials as coatings has been conducted by several researchers. Bender and Schutze [55] produced an Al diffusion coating on alloy 602CA through the Pack Cementation (PC) process and report an excellent performance when the coated alloy was exposed in synthetic air+2%Cl_2(g) at 800^{o}C. Kalivodova et al.[63] reported a similar result when stainless steels P91 and HCM12 were diffusion-coated with Al and exposed at 600^{o}C in N_2(g)+5%O_2(g)+14%H_2O(g)+1.2%CO_2(g)+0.2%HCl(g).

In addition to the modification of alloy composition by elements such as Al or Si, another approach to reduce the chlorine-induced corrosion can be modification of the microstructure. With this aim, the effect of chromium-rich carbides has been addressed by a number of authors. Elliott and Ansari [52] exposed a number of commercial alloys at 900^{o}C in air+2%Cl_2(g). They observed internal attack in the form of void formation, most frequently along grain boundaries. They stated that this type of attack must be related to the precipitation hardening elements, carbides and especially dissociation of chromium carbides. McNallan et al.[19] exposed alloy 800H in an environment of 20%O_2(g)+0.25%Cl_2(g) at 850^{o}C and observed extensive grain boundary attack. They noticed an eightfold increase in the depth of internal attack when they replaced O_2(g) by CO_2(g). Therefore they attributed the attack to the presence or formation of chromium carbides. Berztiss et al.[64] performed systematic studies concerning the effect of carbides on the high temperature corrosion resistance in oxidizing-chlorinating atmospheres. Exposures were performed at 500 and 600^{o}C in N_2(g)+5%O_2(g)+(500-1500) vppm HCl(g) and both ferritic and austenitic stainless steels were considered in the study. They observed that Cr-rich carbides, irrespective of their size or type, were always preferentially attacked relative to both ferritic and austenitic matrices. In addition, it was revealed that Molybdenum-rich M_6C carbides were more stable compared to the matrix, while TiC did not show any preferential stability or susceptibility relative to the matrix. Therefore in chromia-forming alloys, in addition to the Cr content, the C content of the alloy is an important factor if internal attack should be avoided. To summarize, aluminides and silicides seem to be attractive options for corrosion resistance in oxidizing-chlorinating conditions. In addition, with the introduction of Al or Si to chromia-forming alloys and limiting the C content of the alloy, a suitable material may be developed. This will be further discussed in Chapter 3.

2.2 High Temperature Corrosion Induced by Alkali Chlorides

High temperature corrosion due to alkali chlorides is an important issue in a number of applications such as biomass firing, engine parts in service close to marine environments and waste incineration. Similar to the high temperature corrosion by $Cl_2(g)$ or HCl(g), there is no universal mechanism to account for the observed phenomena and depending on the temperature and gas phase chemistry, different degradation mechanisms can dominate. In the following sections a review on the literature is given.

2.2.1 Mechanisms

2.2.1.1 Chlorine-Induced Corrosion

Due to the aggressive nature of chlorine it has often been considered in the literature that the role of alkali chlorides in accelerating corrosion stems from the chlorine and not the alkali component of the salt. Gaseous $Cl_2(g)$ or HCl(g) evolves due to reaction between the alkali chloride and the oxide layer on metals [25]. Subsequently it contributes to the damage by one of the mechanisms mentioned in section 2.1.

Extraction of chlorine from alkali chlorides (and in general all chloride deposits) can also take place through other reactions depending on the gas phase chemistry. One of the most important reactions is the sulfation reaction (eq.2.3):

$$4KCl+O_2(g)+2SO_2(g)+2H_2O(g) =2K_2SO_4+4HCl(g) \quad ; \quad 2.3$$

This reaction has been mentioned by several authors as the main reason for the (assumed) chlorine-induced high temperature corrosion from the deposited chlorides[10], [65]–[68]. However, the effect of sulfur is still controversial as other authors believe that the presence of sulfur (SO_2 in an oxidizing environment) lessens the overall corrosion damage [69]–[73].

2.2.1.2 Alkali-Induced Corrosion

The role of alkali in accelerating corrosion has been addressed by Pettersson et al.[74][75]. They applied small amounts of KCl(s) on stainless steel 304L and studied the corrosion behavior in $N_2(g)+5\%O_2(g)+40\%H_2O(g)$ at 600^oC. Examination of the samples by X-Ray Diffractometry (XRD) and Auger Electron Spectroscopy (AES) revealed that potassium chromate (K_2CrO_4) was present among the corrosion products, while no significant amount of chlorine was detected. They argued that the formation of K_2CrO_4 acts as a sink for chromium in the oxide layer and observed that instead of a Cr-rich $(Fe,Cr)_2O_3$ oxide, which is known to be protective, a double layer non-protective oxide was formed (Figure 2.10). Thus, the role of KCl in high temperature corrosion of chromia-forming alloys resembles the role played by $H_2O(g)$, according to the mechanism proposed by Asteman et al. [76], [77] who suggested that in $H_2O(g)$-containing atmospheres the oxide layer is depleted in Cr due to the formation of volatile chromic acid $CrO_2(OH)_2(g)$ (see equations 2.4 and 2.5):

$$Cr_2O_3+(3/2)O_2(g)+2H_2O(g)=2CrO_2(OH)_2(g) \quad ; \quad 2.4$$
$$4KCl+Cr_2O_3+(3/2)O_2(g)+2H_2O = 2K_2CrO_4+4HCl(g) \quad ; \quad 2.5$$

In case of either KCl or $H_2O(g)$-induced attack on stainless steel 304L, the consequence is a fast-growing double layer oxide consisting of outward-growing Fe_2O_3 and inward-growing $(Fe,Cr,Ni)_3O_4$ [78]. To study the role of potassium further, Pettersson et al.[79], [80] conducted similar experiments with potassium carbonate (K_2CO_3) instead of KCl. Surprisingly, they found out that, for stainless steel 304L exposed to $N_2(g)+5\%O_2(g)+40\%H_2O(g)$, K_2CO_3 was equally corrosive as KCl (Figure 2.11a). Also Lehmusto et al.[81]–[83] and Pompe et al.[84] reported that the alkali component of the salt alone can cause corrosion on chromia-forming alloys. In addition, it has been shown that KCl vapor can cause breakdown of the protective oxide on Fe-Cr alloys [85]–[88].

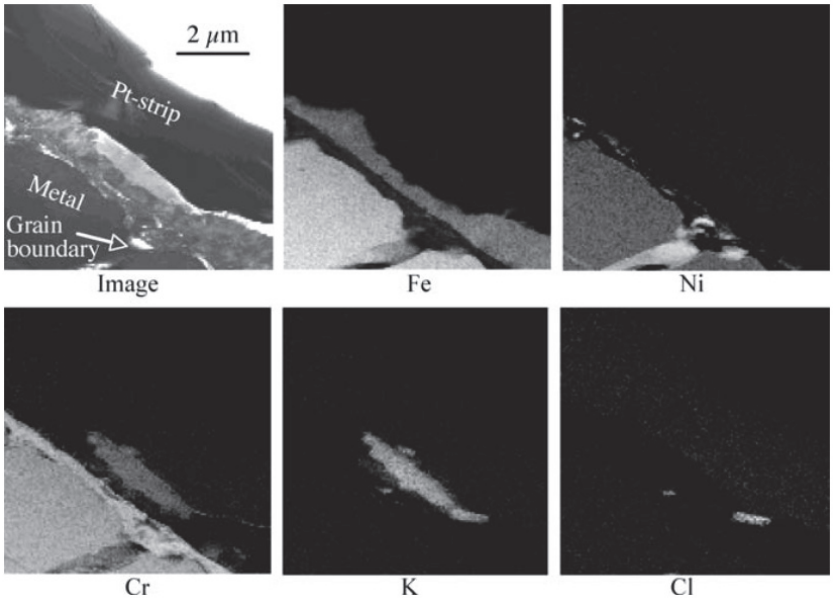

Figure 2.10: Transmission Electron Microscopy (TEM) and Energy Dispersive X-Ray Spectroscopy (EDS) maps of the oxide layer formed on stainless steel 304L exposed at 600°C under $N_2(g)+5\%O_2(g)+40\%H_2O(g)$ for 24h. 0.1 mg/cm^2. KCl has been applied on the sample surface prior to the exposure. Double layer configuration of the oxide layer, formed K_2CrO_4 and residual KCl can be seen in the maps. Note the Fe and Cr depletion at the metal grain boundary [78].

Another study that emphasizes the role of alkali is the investigation by Karlsson et al. [71], [89] where the effect of $SO_2(g)$ on KCl-induced corrosion of stainless steel 304L was examined. They found a beneficial effect of sulfur addition on the corrosion resistance (Figure 2.11b) and attributed this to the conversion of KCl to K_2SO_4, according to (eq.2.6). This species has a lower affinity to react with Cr_2O_3 than KCl [80].

$$2K_2SO_4+Cr_2O_3+(3/2)O_2(g)=2K_2CrO_4+2SO_3(g) \quad ; \quad 2.6$$

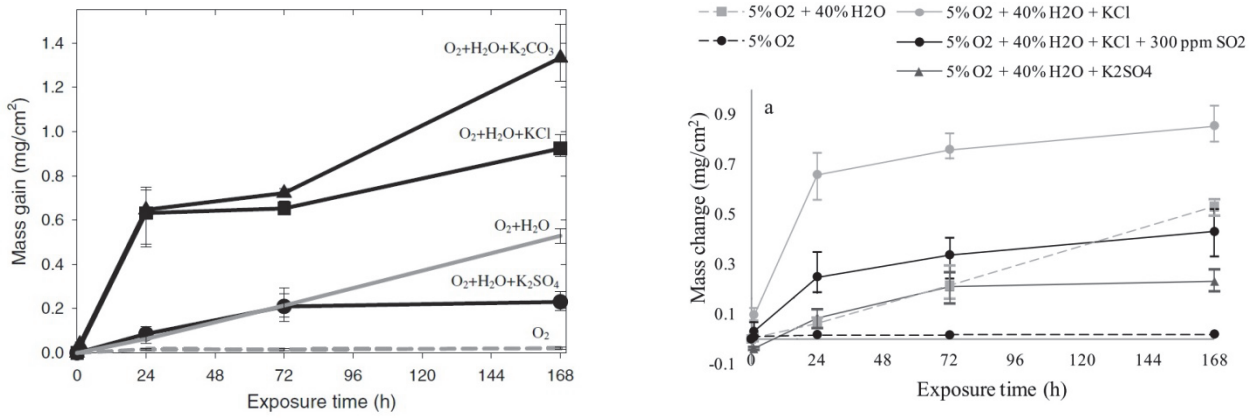

(a) (b)

Figure 2.11: Stainless steel 304L exposed to N_2(g)+5%O_2(g)+40%H_2O(g) at 600°C (a) effect of salt chemistry [79](b) effect of SO_2(g) [89].

According to the alkali-induced mechanism, it is expected that with an increase in Cr content of the alloy, its performance improves steadily. Pettersson et al.[90] compared the KCl-induced corrosion behavior of stainless steels 304L and Sanicro 28 coated with 0.1mg/cm^2 KCl(s) and exposed at 600°C in N_2(g)+5%O_2(g)+40%H_2O(g). They observed that Sanicro 28 suffered from significantly less damage and attributed this to the higher amount of Cr in Sanicro 28 compared to 304L. Similar behavior was observed by Pompe et al.[84] during studies on the corrosivity of K_2CO_3 at 800°C.

2.2.1.3 Alkali Chloride-Induced Corrosion

Although the alkali-induced mechanism can account for the initiation of attack, it does not address a continuation of corrosion. Based on the assumption that the corrosion is solely due to the alkali component of the salt, it is logically expected that pure Cr exposed to alkali chlorides passivates rapidly after a short initial attack. However, in practice the opposite is observed. Li et al. [88][8] exposed pure Cr under air+KCl deposit at 650°C and observed that a 2mm thick sample was completely consumed after 4h. Ceasing the exposure after 2h showed that a thick chromium chloride layer had formed in-between the residual chromium and porous Cr_2O_3 on top. Lehmusto et al. [83] studied the corrosion behavior of pure Cr powder mixed with KCl or K_2CO_3 under synthetic dry air. While there was no remarkable reaction between K_2CO_3 and Cr up to the maximum investigated temperature of 700°C, a significant attack by KCl was observed. In addition, starting with Cr_2O_3 instead of Cr, it was found that K_2CO_3 is reactive while KCl is not. Based on this they concluded that the reaction with K_2CO_3 starts, but does not continue, while the reaction with KCl sustains. Another study within the same research group revealed that, if the temperature is high enough, all the alkali chlorides are corrosive towards pure Cr while the alkali earth metals are not (Figure 2.12a-b) [91]. Accordingly, it was concluded that the presence of chloride ions alone does not explain the initiation of attack and that the properties of the cation are also important. Karlsson et al.[92] compared the effect of NaCl, KCl and $CaCl_2$ on the corrosion of stainless steel 304L. They found that the mechanisms of attack for NaCl and KCl were similar and both could accelerate

corrosion (Figure 2.12c). They reported that the amount of CrO_4^{2-} ion on the surface of NaCl- and KCl-affected samples was much higher than that on the $CaCl_2$-affected sample and attributed the

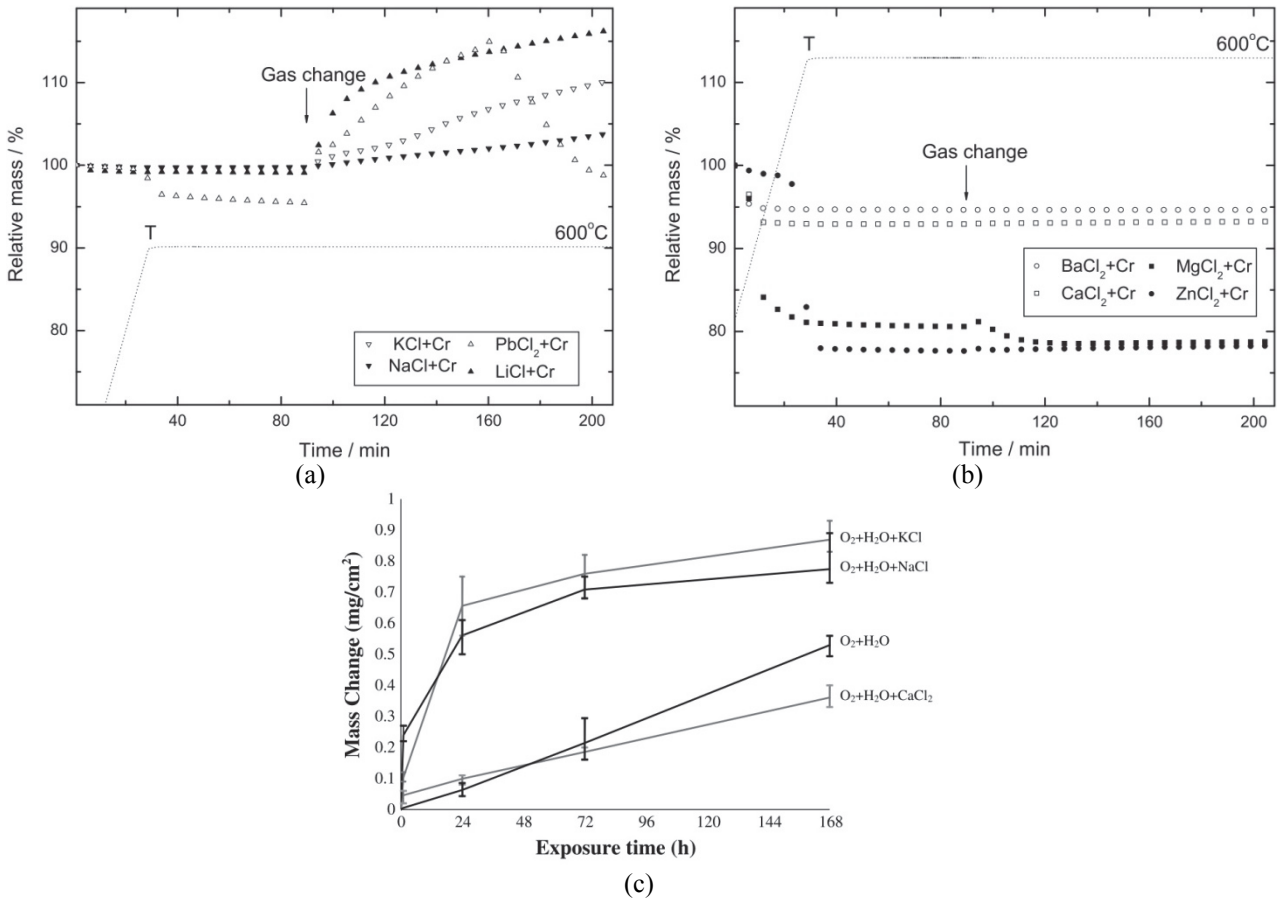

Figure 2.12 : (a) Mass change vs. time for mixtures of Cr powder and alkali chlorides (and lead chloride) exposed to dry synthetic air at 600°C. Heating was performed in nitrogen. The reactive gas was introduced after temperature was stabilized (b) same as (a) but with alkali earth metals (and zinc chloride). Mass loss due to evaporation ($ZnCl_2$), loss of absorbed water ($CaCl_2$ and $BaCl_2$) and oxidation ($MgCl_2$) is the only apparent effect [91]. (c) Stainless steel 304L exposed under $N_2(g)+5\%O_2(g)+40\%H_2O(g)$ for different times at 600°C. 1.35μmol/cm^2 of each salt has been deposited on the surface of the corresponding sample [92].

effect to the rapid conversion of $CaCl_2$ to CaO by H_2O. Shinata et al.[93]–[95] performed extensive studies on the chloride-induced high temperature corrosion of pure Cr and observed that, as long as the temperature is below the melting point of the pure salt, the corrosion by $BaCl_2$ and $CaCl_2$ initiated, but did not continue. On the other hand, a sustained attack was observed for NaCl well below its melting point (Figure 2.13a). The reaction rate was so fast that for a sample inserted into the furnace at 750°C, the temperature rose beyond 1300°C as a consequence of the evolved reaction heat (Figure 2.13b). These observations indicate that both the alkali and halogen component of the salt play a role in the corrosion and considering the alkali as the only aggressive agent is not sufficient. As mentioned before, if the attack was only induced by the alkali component of the salt, it would be possible to moderate the damage simply by increasing the Cr content of the alloy.

However, in agreement with the abovementioned fundamental studies on pure Cr, laboratory and field exposures often show that the corrosion of alloys can aggravate by enhancing the Cr content.

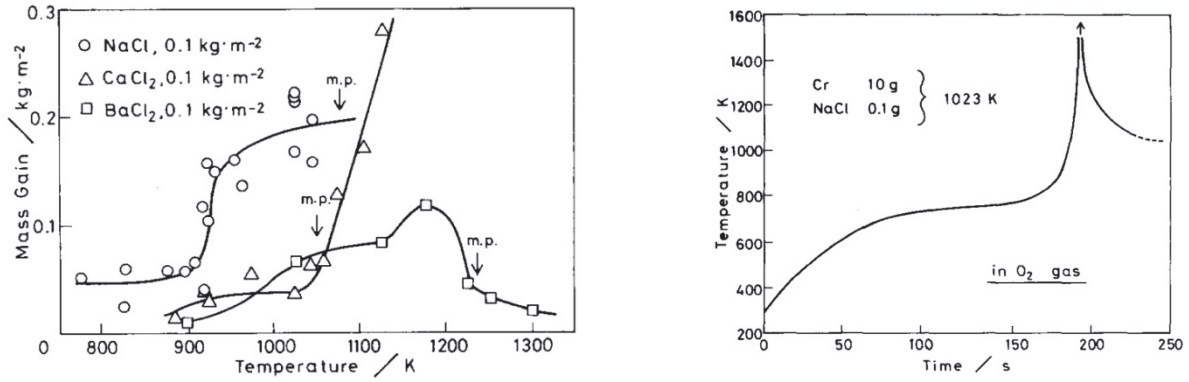

(a) (b)

Figure 2.13: (a) Mass gain vs temperature for pure Cr exposed to different chlorides for 2h under dry air. Notation m.p. denotes the melting point (b) Temperature rise due to the exposure of Cr(10g)+NaCl(0.1g) mixture at a furnace temperature of 750^{o}C [94].

Shinata et al.[96] reported that at 750^{o}C (i.e. ~50^{o}C below the melting point of NaCl) an increase in Cr content of the Ni-Cr binary alloys leads to more material loss by NaCl-induced corrosion. On the other hand, at 850 ^{o}C (i.e. ~50^{o}C above the melting point of NaCl) the corrosion resistance is independent of Cr content (see Figure 2.14). For Fe-Cr-(Ni) alloys a minimum was observed for both temperatures at intermediate Cr-contents (10-15wt%). Acceleration of the alkali chloride-induced corrosion of Fe-based alloys with a Cr content above an intermediate range of 10-15 wt%, is also observed in the work of Li et al. [88]. They found that a Fe-35wt%Cr alloy suffered more damage than an Fe-15wt%Cr alloy exposed underneath a KCl deposit in static lab air at 650^{o}C. An interesting observation in their study was that when the experiment was performed with KCl vapor instead, the alloy with the highest chromium content was most resistant. Similar observations were reported by Ma et al.[87] (see Figure 2.15a). Therefore, to reveal the mechanism of alkali chloride-induced attack, the effects from both the alkali and halogen component of the salt should be considered as well as the amount of the salt supplied to the system (see Figure 2.15b).

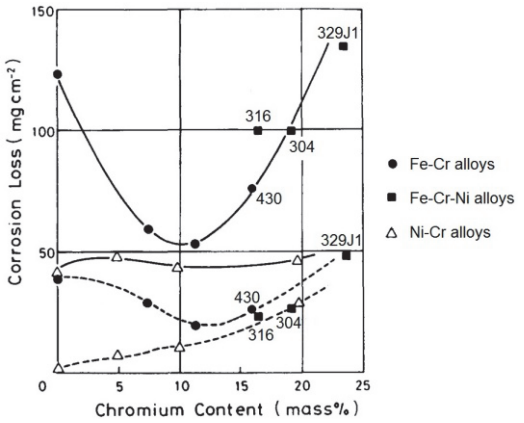

Figure 2.14: Corrosion extent vs Cr content for commercial stainless steels and Ni-Cr binary alloys coated with 20mg/cm^2 NaCl and exposed in flowing air at 750^{o}C (dashed line) and 850 ^{o}C (solid line) for 16h [96].

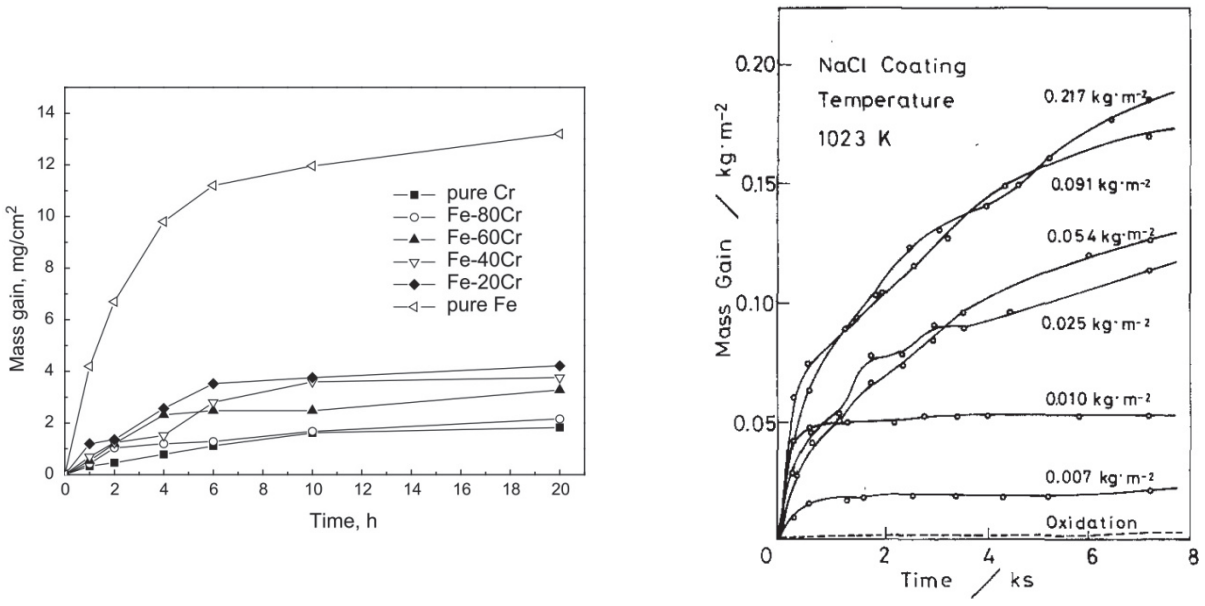

(a) (b)

Figure 2.15 : (a) Effect of chromium content in the binary Fe-Cr system on the corrosion extent due to the presence of 298ppm KCl(g) in flowing oxygen at 750^{o}C [87] (b) Effect of NaCl content on the corrosion of pure chromium at 750^{o}C in flowing dry air [94].

2.2.1.4 Electrochemical Reaction Path

From the argumentation given in section 2.2.1.2, it appears that the destructive effect of KCl should be limited to chromia-forming alloys. In this respect the experimentally observed acceleration of corrosion of Cr-free alloys [7], [97], [98] and pure iron [99] suggests that there might be complementary mechanisms. Cha and Spiegel [5], [6], [100] studied the interaction of KCl and an iron surface under N_2(g)+20%O_2(g) and observed reactivity already at 300^{o}C. Folkeson et al.[46] studied the KCl-induced corrosion behavior of low alloy steel T22 at 400 and 500^{o}C in N_2(g)+5%O_2(g)+40%H_2O(g) and observed accelerated corrosion already at 400^{o}C. They detected

chlorine without potassium at the metal/oxide interface. Therefore there must have been a reaction that extracts chlorine from KCl. They suggested the following cathodic and anodic reactions as the source for chlorine:

$$2KCl + (1/2)O_2(g) + H_2O(g) + 2e^- = 2KOH(g) + 2Cl^- \quad \text{cathode (oxide/gas interface)} \quad ; \quad 2.7$$

$$Fe = Fe^{2+} + 2e^- \quad \text{anode (metal/oxide interface)} \quad ; \quad 2.8$$

Subsequently wherever Fe^{2+} and Cl^- meet, $FeCl_2$ will form. Chloride ions are not expected to dissolve in the oxide lattice [28]. Accordingly, similar to the electrochemical mechanism in section 2.1.2.2, it was suggested that the transport of Cl^- takes place through the grain boundaries of the oxide. Finally, acceleration of corrosion was attributed to the presence of $FeCl_2$ at oxide grain boundaries, which facilitates transport of both iron and oxygen ions. In addition, the disappearance of K and Cl from the sample's surface was attributed to loss in the form of KOH(g) and $FeCl_2$(g)/HCl(g). In a similar study within the same research group, Jonsson et al.[101] investigated KCl-induced corrosion of low alloy steel T22. They observed similar corrosivity from KCl (see Figure 2.16a) and attributed the effects to an electrochemical interaction (equations 2.7 and 2.8). The mechanism is schematically shown in Figure 2.16b. The effect of KCl on the T22 steel was observed on a pre-oxidized sample as well, albeit to a lesser extent.

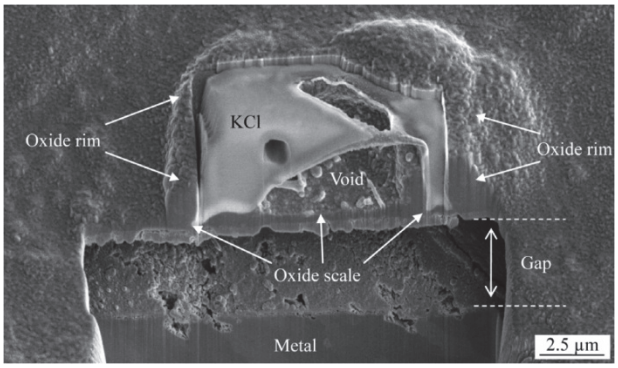

(a)

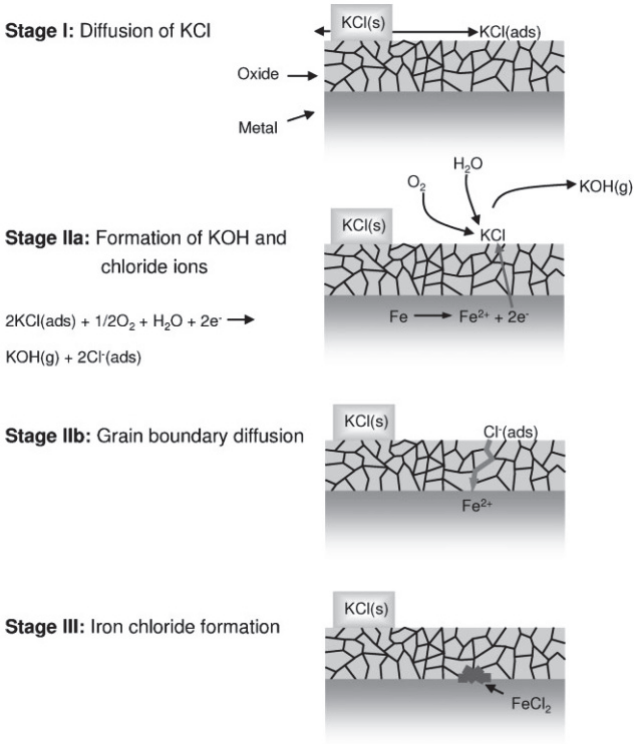

(b)

Figure 2.16: (a) Focused Ion Beam (FIB) milled cross section of a partly reacted KCl particle along with the oxide and the residual metal. Oxide rims are present all around the KCl particle. In addition, there is a submicron thick oxide beneath the KCl. The particle is hollow and the oxide layer is loose and non-adherent. Note the gap between the oxide and the underlying metal. [101] (b) Schematic representation of the mechanism proposed by Folkeson et al.[46].

2.2.1.5 Molten Salt Attack (Hot Corrosion)

Hot corrosion is a type of high temperature corrosion where a molten salt (or a liquid solution of salts) destroys a protective oxide by a fluxing mechanism [102]. There are a number of experimental observations that indicate the presence of a liquid phase when alkali chlorides are in contact with metals and alloys. Cha and Spiegel [5], [6] reported deformation and local spreading of KCl particles on the surface of Fe, exposed in N_2(g)+20%O_2(g), already at 300^{o}C. This temperature is well below the melting point of the salt (770^{o}C). Therefore the authors attributed the effect to the formation of a low temperature eutectic melt and reported that with the addition of 500vppm HCl(g) to the gas, the chlorine and oxygen content of the surface significantly increased. Similar results were obtained when KCl was replaced with NaCl [100]. Jonsson et al.[101] reported analogous observations during an in-situ study on the KCl-induced high temperature corrosion of low alloy steel T22. They reported that the KCl particles started to deform when the temperature reached around 355^{o}C; this was followed by a rapid distribution of K and Cl over the surface. These observations were explained from melt formation in KCl-$FeCl_2$ system. Table 2.1 contains the eutectic temperatures of several salt systems relevant to the KCl-induced corrosion. As can be seen the above-mentioned effects are consistent with the eutectic temperatures in KCl-$FeCl_3$ and KCl-$FeCl_2$ systems.

Table 2.1: Eutectic temperature data for several systems relevant to KCl-induced high temperature corrosion.

mixture	T_e(^{o}C)	ref.	mixture	T_e(^{o}C)	ref.
KCl-$FeCl_2$	355	[103]	KCl-K_2CrO_4	650	[104]
KCl-$FeCl_3$	202	[5]	KCl-$K_2Cr_2O_7$	367	[104]
KCl-$CrCl_2$	462	[103]	K_2CrO_4-$K_2Cr_2O_7$	393	[105]
KCl-$CrCl_3$	700	[5]	KCl-K_2SO_4	694	[15]
KCl-$NiCl_2$	508	[5]			

Formation of KCl-$FeCl_2$ eutectic melt was also reported by Nielsen et al.[10] and van Lith et al.[66], [106]. They exposed a ferritic-martensitic (X20CrMoV121) and an austenitic stainless steel (TP347HFG) at 550-560^{o}C to the KCl deposit and the flue gas composition mentioned in Table 1.2. It was observed that the outermost corrosion product was always a uniform layer of K_2SO_4 with threads of iron oxide embedded in it (see Figure 2.17a). The morphology of this layer was characteristic for a result of eutectic solidification (Figure 2.17b). The exposure temperature is well below the eutectic temperature of the KCl-K_2SO_4 system (694^{o}C). Therefore the possibility of melt formation solely due to KCl and K_2SO_4 was ruled out. Instead, the authors attributed this effect to the formation of a KCl-$FeCl_2$ molten mixture. This mixture was suggested to be converted to K_2SO_4+Fe_xO_y due to sulfation and oxidation respectively.

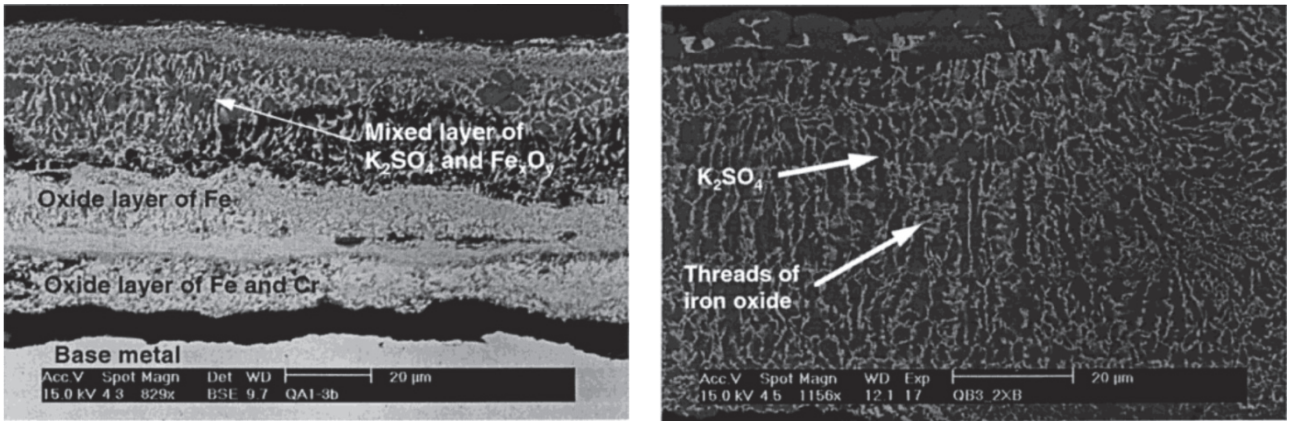

(a) (b)

Figure 2.17: (a) Morphology of corrosion products on stainless steel X20CrMoV121 exposed at 560°C for 72h under the KCl(s) deposit and gas composition listed in Table 1.2. (b) Outermost corrosion product in (a) shown at higher magnification: Threads of iron oxide within the K_2SO_4 layer resembling a eutectic structure [10].

Table 2.1 shows that in addition to the melt formation in KCl-metal chloride system, formation of potassium dichromate ($K_2Cr_2O_7$) can also contribute to melt formation. However, this species has shown itself to be difficult to detect. Lehmusto et al.[105] reported visual detection of trace amounts of an orange compound when a Cr+KCl powder mixture was exposed in dry air upon slow heating to 700°C. They attributed this to the characteristic color of $K_2Cr_2O_7$. Li et al.[8] studied the corrosion behavior of pure Cr exposed to KCl(g) at 650°C and reported detection of $K_2Cr_2O_7$ by means of XRD. Ma et al.[87] obtained similar results when exposing binary Fe-Cr alloys to O_2(g)+KCl(g) (Figure 2.18). If $K_2Cr_2O_7$ is present, it can play an important role in sustaining the attack on pure Cr, in addition to chlorine.

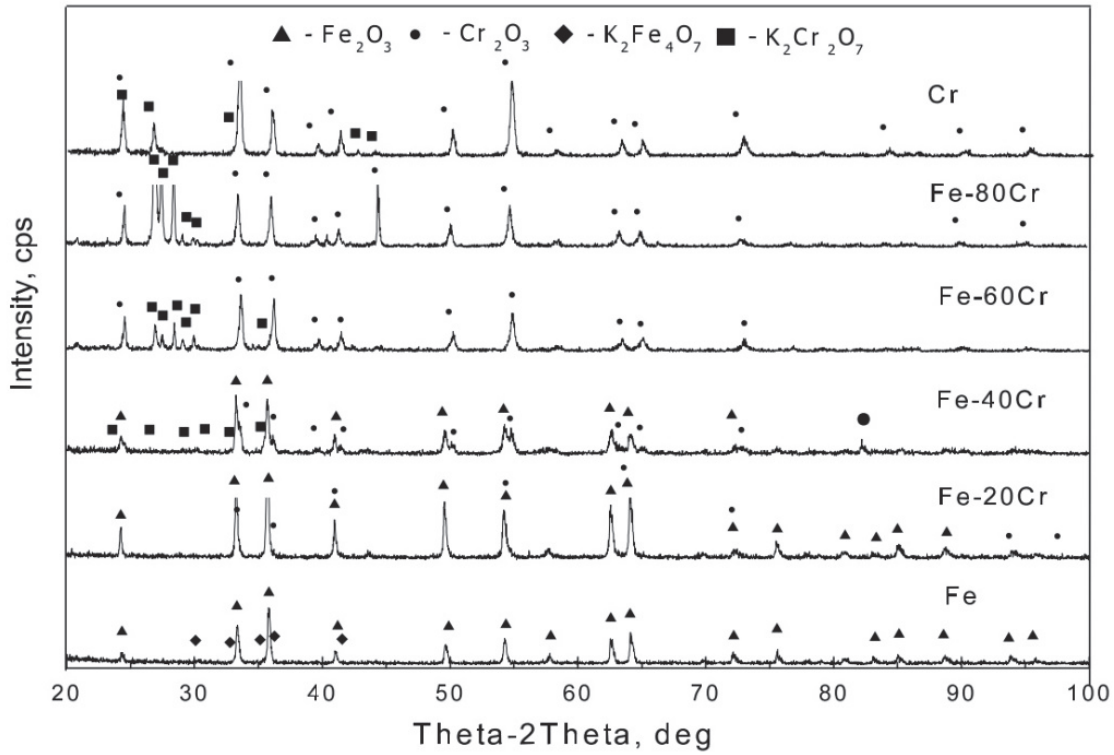

Figure 2.18 : Phase analysis of the corrosion products on a number of binary Fe-Cr alloys exposed to O_2(g)+298vppm KCl(g) at 750°C for 20h [87]. CuK_α has been used as the incident radiation.

2.2.2 Mitigation of Corrosion

In spite of the wealth of corrosion mechanisms involving alkali chlorides, several metals and alloys with sufficient corrosion resistance have been reported in the literature. This section mentions such materials and presents a brief review of selected material performance studies.

Similar to the oxidizing-chlorinating atmospheres, iron and nickel aluminides have often shown satisfactory corrosion resistance against KCl provided that the content of Al is high enough. Li and Spiegel [7] studied the corrosion of a series of Fe-Al binary alloys along with NiAl under air+KCl deposit at 650°C. They reported an outstanding performance of NiAl (see Figure 2.19a) but Fe-10at.%Al and Fe-20at.%Al showed deep internal attack in addition to the formation of thick external oxides. For the Fe-45at.%Al alloy, the surface was partly covered with a protective Al_2O_3 scale and partly with non-protective oxide beneath which Al-depleted zones were detected (Figure 2.19b). Without a KCl deposit, the studied Fe-Al alloys showed significantly lower mass gain values. Vokal et al.[107] studied the corrosion behavior of the alloys P91, 17Cr/13Ni, 800 and IN617 along with their aluminide diffusion coatings. Exposure was performed under air+KCl-50mol%K_2SO_4 deposit at 650°C for 300h. They observed that the presence of Fe_2Al_5, (Fe,Ni)Al and Ni_2Al_3 coatings prevented excessive metal loss for all the alloys studied. In addition, they reported a negative effect from the Cr-rich phases within the coating. Li et al.[97] exposed Fe-35wt.%Cr and Fe-21Cr-5Al(wt.%) along with NiAl and Fe-45at.%Al under a molten KCl-NaCl mixture at 670°C for 48h. They reported superior performance for the aluminides compared to the two Cr-containing alloys.

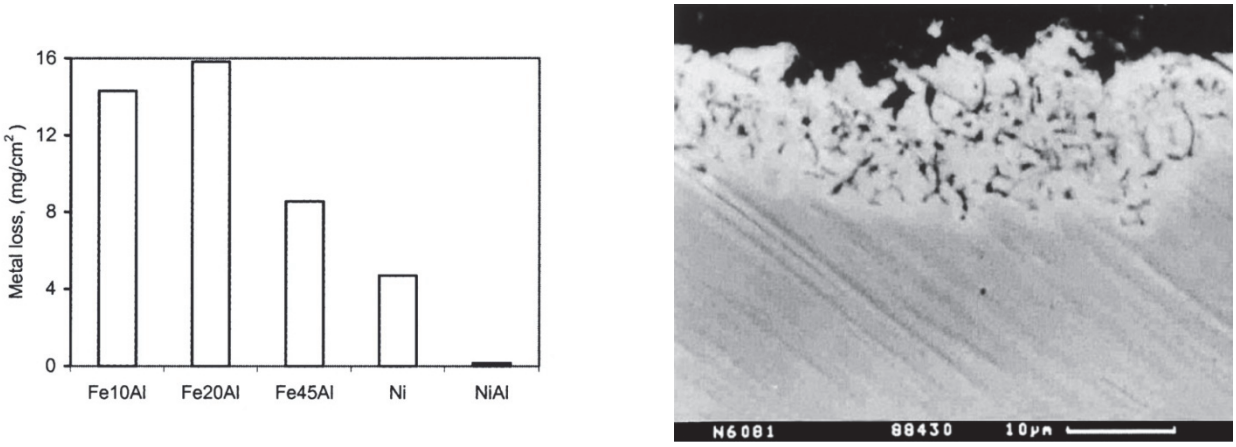

(a) (b)

Figure 2.19: (a) Mass change of the alloys (b) Al-depleted zone observed on parts of the surface of Fe-45at.%Al. Exposure performed at 650°C under air+KCl deposit for 48h [7].

Sato et al.[99] reported that no interaction took place between pure Si powder mixed with equimolar NaCl-KCl powder, heated in air at 600°C for 3h. On the other hand, pure Cr powder was extremely reactive under these conditions (see Figure 2.20). Yasuda et al.[108] studied the influence of siliconizing (formation of a Si diffusion coating) on the corrosion performance of stainless steels 304 and 430 covered with 5mg/cm^2 KCl-NaCl-Na_2SO_4 mixture. The exposure was performed at 900°C for different times in N_2(g)+18.4%O_2(g)+20%H_2O(g)+1348 vppm HCl(g). They observed that the siliconized alloys showed significantly lower mass gain compared to the bare alloys. Sato et al.[99] obtained similar results with alloy 304 siliconized and exposed to KCl-NaCl-Na_2SO_4 under air at 600°C. They reported an improved performance compared to the untreated alloy. However, although the siliconized alloy showed less mass gain, formation of internal silica was observed. To summarize there is a positive sense in the literature towards formation of Al or Si diffusion coatings to mitigate the alkali chloride-induced attack.

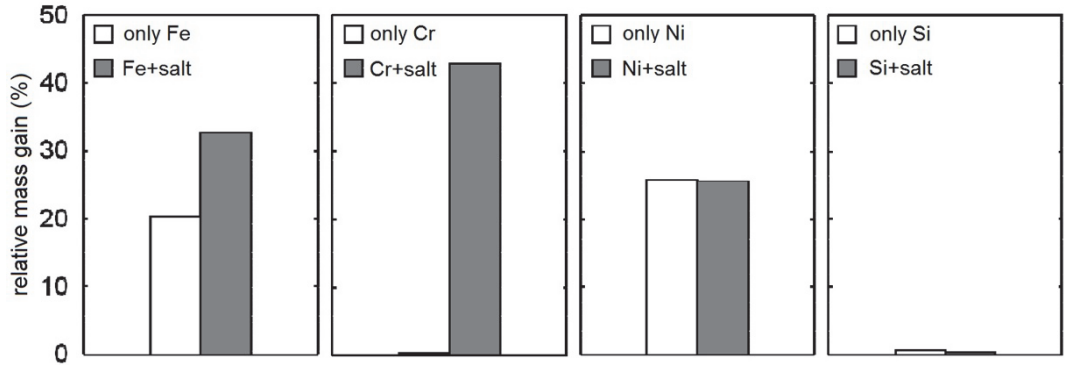

Figure 2.20 : The effect of alkali salts on the oxidation of pure Fe, Cr, Ni and Si. Exposure performed at 600°C under air for 3h. Metal powder was mixed with equimolar KCl-NaCl powder [99].

The positive effect of Al or Si is not limited to the surface phases rich in these elements. Several investigations suggest that the addition of these elements to Fe-Cr-(Ni) alloys improves the corrosion resistance against alkali chlorides. Hiramatsu et al.[109] reported a positive effect of the

addition of Al or Si to ferritic and austenitic stainless steels on their corrosion resistance to NaCl-induced attack under air and cyclic temperature conditions. An interesting observation in their study was that the Si-modified alloy showed its superior performance only after thermal cycling. Fujikawa and Maruyama [110] investigated the effect of Si content and aging on the corrosion resistance of austenitic stainless steels. They reported a positive effect of Si and a negative effect of aging due to the formation of chromium carbides. It was shown that the extent of intergranular attack increased with increase in C content of the alloy. Li et al.[111] studied the effect of Al and/or Si addition to 9wt% chromium steel P91 on its resistance against KCl-induced corrosion. They modified the steel composition with 2.2 wt.% Al and/or Si and exposed it to air+KCl vapor at 650^{o}C for 96h. Both elements showed a positive effect in reducing the extent of corrosion, with Si showing a superior beneficial effect compared to Al (Figure 2.21a). In a similar study from the

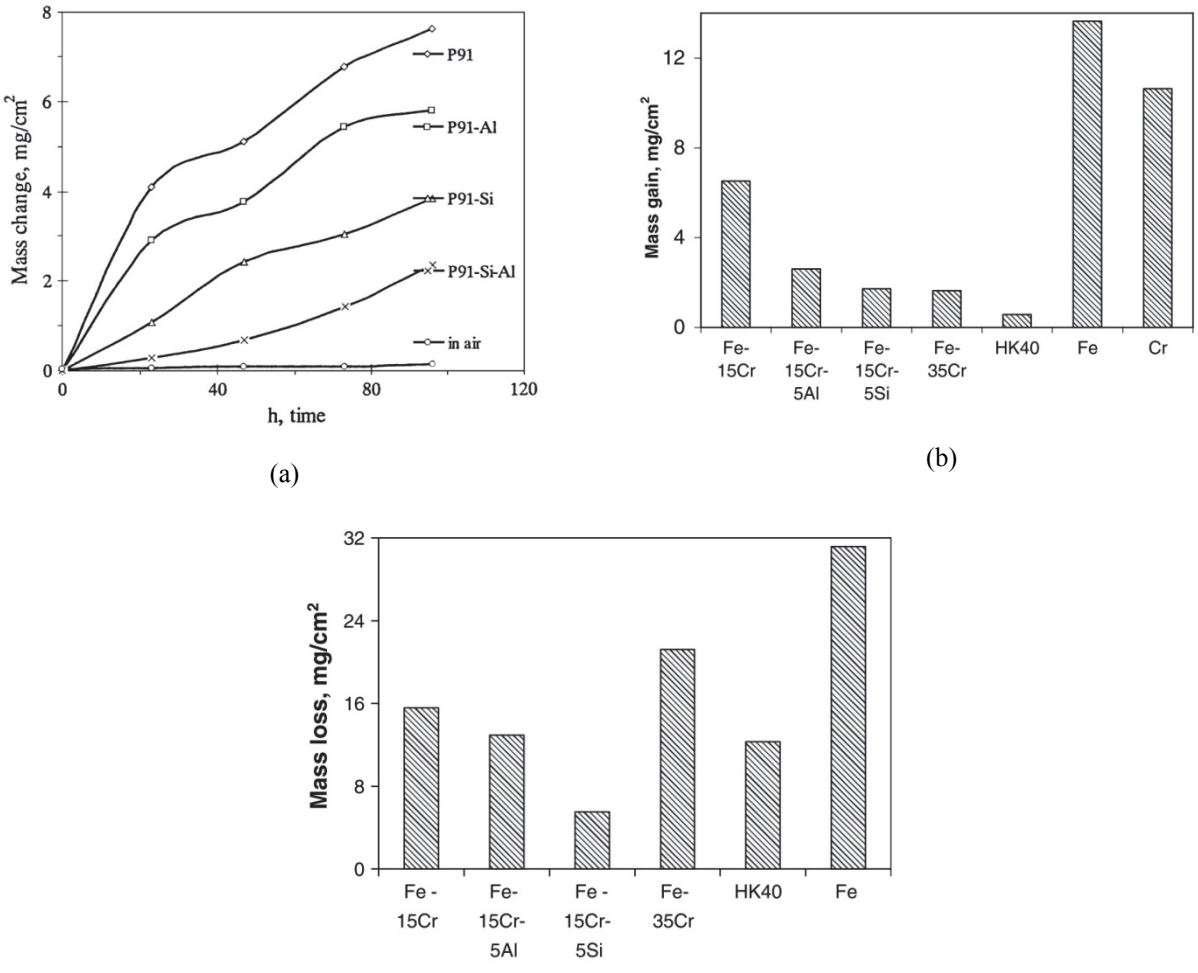

Figure 2.21: (a) Effect of Al and/or Si addition to the performance of low Cr steel P91 under air+KCl vapor at 650^{o}C [111] (b) Comparison between the corrosion resistance of Fe, Cr, Fe-Cr alloys and two alloys modified with Al/Si. Exposure under air+KCl vapor at 650^{o}C for 48h. (c) The same alloys exposed under air+KCl deposit at 650^{o}C for 48h. Mass loss has been measured after removal of the corrosion products by chemical etching in an alkoxide solution of $KMnO_4$ at 80^{o}C with HCl as inhibitor [88].

same research group, Fe, Cr and a number of Fe-Cr alloys along with their Al/Si modifications were evaluated [88]. Exposures were performed in air+KCl vapor and also air+KCl deposit (60mg/cm^2) at 650^{o}C for 48h. Results are shown in Figure 2.21b-c. Evidently, Al and/or Si additions have a beneficial effect. Moreover, similar to the effect shown in Figure 2.15a-b, the presence of solid salt is necessary to result in higher corrosion rates for Cr. It is reported that the pure Cr sample was completely consumed under the deposit while under the vapor it was only partly corroded.

Finally it is worth mentioning that the influence of the Cr content depends on several factors, and under certain conditions it might be the case that alloys with higher chromium content perform better. According to Lehmusto et al.[105] interaction between pure Cr and KCl starts between 500-550^{o}C. Therefore at lower temperatures a negative effect from Cr is not expected. Gas phase chemistry such as presence and content of H_2O(g) and SO_2(g) also plays a significant role on the effect of Cr content. A positive effect from H_2O(g) in mitigating the chlorine-induced corrosion is reported in the review paper by Chang and Wei [112]. In addition Lehmusto et al.[81], [82] reported that the KCl-induced attack on alloys 304L and IN625 was much less pronounced in wet air (30vol.% water vapor) as compared to dry conditions. Proff et al.[113] and Pettersson et al.[114] reported that corrosion of alloy Sanicro 28 by KCl was more severe in dry N_2(g)+5%O_2(g) compared to that with 40 vol.% water vapor. SO_2(g) is also believed to have a positive effect on the alkali chloride-induced corrosion by a number of researchers [70]–[72], [92] therefore SO_2 content of gas and/or sulfate content of deposit can play an important role on the effect of Cr. As an example the investigations by Gotthjælp et al.[115] can be mentioned. They exposed alloys Sanicro 28 and Sandvik 8LR30 at 600^{o}C under a deposit composed of 25wt%KCl+65wt%K_2SO_4 (+10wt%silicate). The exposure lasted for 310h and the flue gas was N_2(g)+8%O_2(g)+ 7.3%H_2O(g)+19%CO_2(g)+300vppmSO_2(g)+200vppmHCl(g). In their study, Sanicro 28 had the best corrosion resistance. Montgomery and Maahn [4] performed a similar test with the same alloys and deposit, but in static lab air. Again the alloy with the highest Cr content performed best, which is in contrast with field test exposures in Danish power plants, where a Cr content above 15-18wt% was reported to be detrimental [116]. .

3. Materials Design Strategy

In the previous chapter several mechanisms were described to account for the corrosive effects of chlorine and alkali chlorides. The mechanisms proposed by different authors were put forward to explain observations under different experimental conditions and none of the mechanisms provides a comprehensive description of all observed effects. In this chapter the literature reports are collated and further discussed in light of thermodynamic calculations. Accordingly interpretations will be drawn, based on which, materials design strategies will be proposed

3.1 Critical Review of the Literature Reports

3.1.1 Effects of Cl_2(g) and HCl(g)

The studies by Maloney and McNallan[41] on pure Co as well as Lee and McNallan[42] on pure Ni show that at temperatures as high as 900°C, volatilization of the oxide layer, by conversion to volatile chlorides, is the dominant corrosion mechanism if the $P_{O2(g)}/P_{Cl2(g)}$ ratio is large enough. In addition, there is experimental evidence suggesting that the same mechanism is valid for other metals as well. Excellent performance of alumina-forming alloys under oxidizing-chlorinating conditions at temperatures as high as 900°C [29], [47], [52], [53] can probably be explained by the low partial pressure of aluminum oxychloride (AlOCl) and aluminum chloride ($AlCl_3$) in equilibrium with Al_2O_3 and atmosphere [29], [47]. Similarly, poor performance of chromia-forming alloys can be attributed to the high partial pressure of CrO_2Cl_2(g) in equilibrium with Cr_2O_3 and atmosphere [29], [47]. On the other hand, acceleration of the corrosion rate of Co[41] and Ni[42] with a decrease in temperature (827 to 727°C for Co and 927 to 827°C for Ni) indicates that other mechanisms than volatilization of oxide are important too [41]. Chlorine comes into contact with metal and produces significant damage that in the worst case can cause ignition of the sample. A pertinent question is why the oxide layer is permeable to chlorine at lower temperatures. Lee and McNallan[42] attribute this to the "*slow kinetics"* of oxidation at lower temperatures. This leads to the formation of a relatively thin oxide layer. Subsequently the slightest volatilization of the oxide, e.g. by the formation of local pits in the oxide, exposes the underlying alloy to the chlorine-containing gas. However, in their results it is shown that a preoxidized sample is also attacked, albeit after an incubation time (Figure 3.1a). Lack of a significant mass loss during incubation may indicate that volatilization of the oxide layer is negligible. Therefore, prior to the initiation of corrosive attack on the pre-oxidized sample, another mode of transport of chlorine appears to be in action. One conceivable possibility is ionic transport of chlorine through the grain boundaries of the oxide as proposed by Folkeson et al.[28]. As metal chlorides form at the metal/oxide interface the oxide can become cracked open (mechanical damage to the oxide) and the underlying metal is exposed to the gas atmosphere. Such effect, depending on the gas chemistry and temperature, may lead to the ignition type attack for a metal like Ni; however for a metal like Cr it is more likely that a new oxide layer forms. This oxide layer is subsequently penetrated by chlorine and a formation-

spallation-reformation sequence drives the continuation of damage (see the serrated TG curve in Figure 3.1b).

Another mechanism that appears to be more important at lower temperatures is the change in the transport properties of the oxide layer. A close look at Figure 2.7b shows that in addition to the multilayered morphology of the chromium oxide, each layer is quite thick. Chromium oxide is known to be a slow growing oxide at least at a relatively low temperature of 600°C. For illustration, the investigations by Pujilaksono et al.[117] can be mentioned. According to their results, mass gain of pure Cr exposed to 100% O_2(g) at 600°C after 24h is only about 0.03mg/cm^2. In comparison, the value in Figure 3.1b, with only 5% O_2(g), is about 0.4mg/cm^2 after 24h. Thus the observation of a thick chromium oxide could be an indication that the transport properties of the oxide lattice (defect chemistry) or oxide grain boundaries are changed due to the presence of chlorine. This hypothesis is supported by the observation that the mass change curve between the serrations is smooth (Figure 3.1b). In other words, between two consecutive serrations a small region with parabolic growth takes place where the parabolic rate constant is higher than that for oxidation in pure O_2(g).

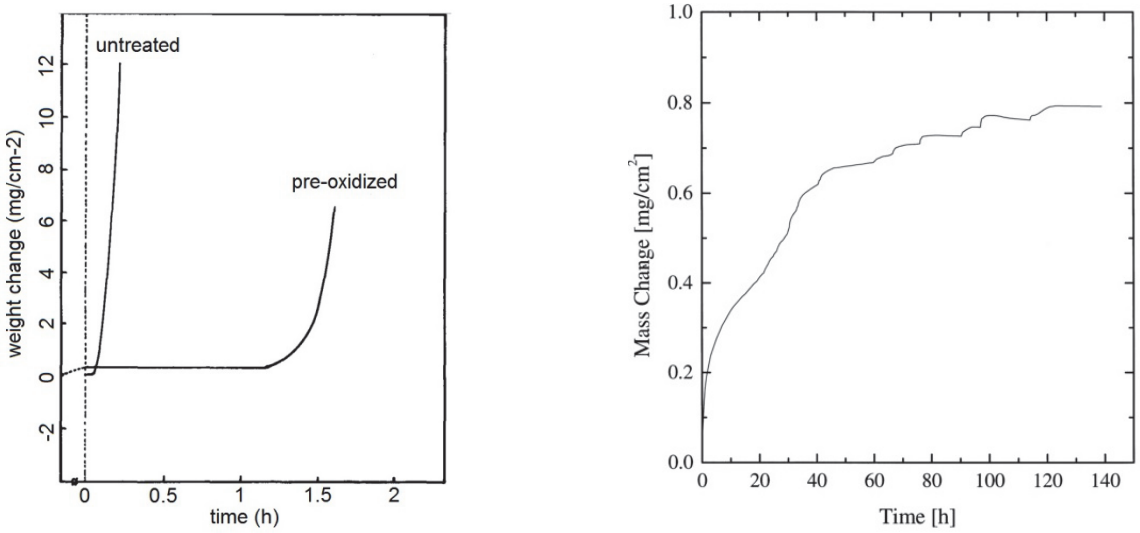

(a) (b)

Figure 3.1: (a) Pure Ni exposed to Ar(g)+50%O_2(g)+1.25%Cl_2(g) at 727°C. The sample has been preoxidized for 24h in pure O_2(g). After this period the gas has been switched to the experimental atmosphere. Sample without preoxidation is also shown in the diagram for comparison. Image reproduced from [42]. (b) Pure Cr exposed in He(g)+5%O_2(g)+500 vppm HCl(g) at 600°C [30].

The above-mentioned mechanisms are not the only mechanisms by which chlorine degrades metals and alloys. In chlorine-induced high temperature corrosion of austenitic stainless steels and Ni-base alloys, formation of porous Ni-rich areas at the metal/oxide interface is often observed. As mentioned in section 2.1.2.1, removal of the alloying elements in the form of subliming (or evaporating) molecular chlorides accounts well for the formation of these regions. However, Smeggil et al.[27] and Pettersson et al.[74] put forward the question that any channel that is open for Cl_2(g) ingress and metal chloride sublimation will be open to O_2(g) as well. In other words, it is still unclear how the oxide layer is permeable to large Cl_2(g)/metal chloride molecules while it is a

barrier for the smaller $O_2(g)$ molecules. Jonsson et al.[32] studied the corrosion of alloy 310S in $N_2(g)$+95%$O_2(g)$+500vppm HCl(g) at 500°C and observed discrete Ni-rich areas as well as chlorine at the metal/oxide interface. They reported that initial chlorides were formed in accordance with the metallic composition of the alloy, but enrichment of Cr chloride and depletion of Ni chloride took place over time. They attributed this to a displacement reaction which *"plates out"* the Ni (eq. 3.1).

$$NiCl_2(s) + Cr = Ni + CrCl_2(s) \quad ; \quad 3.1$$

However, considering the low diffusivity of alloying elements at temperatures as low as 500 and 600°C, other mechanisms seem to apply as well.

During high temperature oxidation of metals, voids can form at the metal/oxide interface. Jonsson et al.[32] and Pettersson et al.[118] studied the oxidation of austenitic stainless steels 310 and Sanicro 28 in dry and wet $O_2(g)$ and observed the formation of voids, which they explained as Kirkendall voids, formed due to the preferential oxidation of Cr and Fe. Accordingly Ni enrichment was observed due to the depletion of Cr and Fe. Considering the presence of sub-surface voids and inspired by eq. 3.1 as well as the electrochemical model [28], a number of hypotheses can be put forward to account for the selective corrosion. For simplicity, consider the case for a Ni-Cr binary alloy at 600°C:

Hypothesis A: As the Cl^- penetrates the oxide layer (e.g. through the grain boundaries of oxide) $NiCl_2(s)$ can form at the metal/oxide/void interface where Ni enrichment has taken place due to a preferential oxidation of Cr. This would lead to the presence of $Cl_2(g)$ within the void as the $NiCl_2(s)=Ni+Cl_2(g)$ equilibrium is reached. A calculation with Thermo-Calc (TAB module)[12] shows that equilibrium $P_{Cl2(g)}$ for this reaction at 600°C is 10^{-10} atm. This partial pressure is significantly larger than the similarly calculated equilibrium $P_{Cl2(g)}$ for $CrCl_2(s)=Cr+Cl_2(g)$ at 600°C, which is 10^{-17} atm. Subsequently chlorination of Cr will take place wherever $Cl_2(g)$ comes into contact with Cr on the void surface. Since the vapor pressure of $CrCl_2(s)$ at 600°C is not negligible (10^{-7} atm calculated using the TAB module) volatilization of Cr as $CrCl_2(g)$ takes place (this can be $CrCl_3(g)$ if the $P_{Cl2(g)}$ of the gas is sufficiently large). However, upon reaching the void/oxide interface $CrCl_2(g)$ can dissociate according to $CrCl_2(g)=Cr^{3+}+Cl_2(g)+3e^-$ and $Cl_2(g)$ is released to repeat the cycle. Oxidation of $CrCl_2(g)$ at the oxide/void interface is coupled to a reduction of $O_2(g)$ at the gas/oxide interface. Subsequently Cr_2O_3 will form wherever Cr^{3+} and O^{2-} meet (see the schematic representation in Figure 3.2a).

Hypothesis B: As the calculated vapor pressure of $NiCl_2(s)$ at 600°C is significant ($1.28*10^{-4}$ atm using TAB module) it will sublime if $NiCl_2(s)$ forms at the metal/oxide/void interface. When $NiCl_2(g)$ comes into contact with Cr on the void surface the displacement reaction $NiCl_2(g)+Cr=Ni+CrCl_2(g)$ will take place. Subsequently when the sublimed $CrCl_2(g)$ comes into contact with a Ni atom at the metal/oxide/void interface the reaction $CrCl_2(g)+Ni=Cr^{3+}+2NiCl_2(g)+3e^-$ will take place restoring the $NiCl_2(g)$ to repeat the cycle (see the schematic representation in Figure 3.2b). It is also possible that the reactions according to hypothesis A and hypothesis B could occur simultaneously. In that case, due to the higher vapor

pressure of $NiCl_2(g)$ compared to $P_{Cl2(g)}$ in equilibrium with Ni-$NiCl_2(s)$ it would seem that the contribution from hypothesis B would be larger. In addition, if the oxide layer contains any Ni^{2+}, the displacement reactions $CrCl_2(g)+Ni^{2+}=Cr^{3+}+NiCl_2(g)+3e^-$ (void/oxide interface) and $NiCl_2(g)+Cr=Ni+CrCl_2(g)$ (void/metal interface) could return the Ni into the metal lattice. It is also possible that after $CrCl_2(g)$ is formed due to $NiCl_2(g)+Cr=Ni+CrCl_2(g)$ it will continue the reaction path according to hypothesis A. In this case the $NiCl_2(g)$ acts only as an initiator.

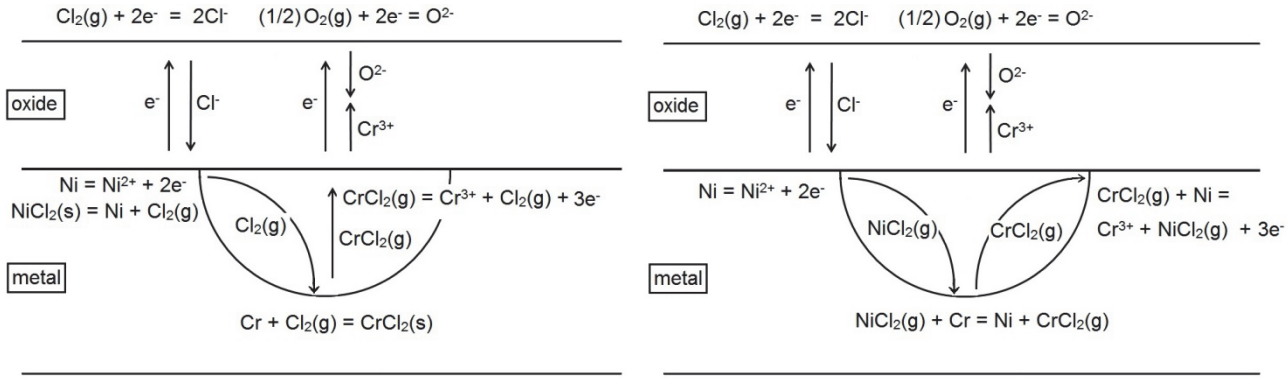

(a) (b)

Figure 3.2 : Schematic of the hypothetical models to explain the selective corrosion in a Ni-Cr alloy when (a) $Cl_2(g)$ and (b) $NiCl_2(g)$ accelerate Cr transport across a void at the metal/oxide interface (half-circles represent the voids). For simplicity the oxide and metal grain boundaries are not shown in the figures. Transport of Cl^- is suggested [46] to take place through the oxide grain boundaries.

The above-mentioned hypotheses can explain the formation of porous Ni-rich regions as Cr leaves the alloy and Ni is left behind. In addition, they do not require that $CrCl_2(g)$ travels through the oxide layer to reach regions of higher $P_{O2(g)}$. As mentioned before the supposed channels through which molecular chlorides, such as $CrCl_2(g)$, are transported will be open to $O_2(g)$ as well and therefore reducing conditions at the metal/oxide interface cannot be established. In other words, active oxidation cannot describe the selective corrosion when the $P_{O2(g)}/P_{Cl2(g)}$ is substantially large. This can be illustrated by considering the case shown in Figure 2.5b. In this case $P_{O2(g)}/P_{HCl(g)}$ is equal to 100 meaning that for each hundred $O_2(g)$ molecules, there is only one HCl(g) molecule. Although the chlorination reactions are quite fast, it is far from expectation that the first reaction product for metals like Cr and Fe in this environment, 100 $O_2(g)$ molecule vs. only one HCl(g) molecule, is their chlorides. This is further supported by considering that there is always a thin layer of protective oxide present at the surface of metals like Cr and Cr-containing alloys. Instead it is more likely that chlorine is transported through the oxide by an electrochemical mechanism. Subsequently gas phase transport within the voids (at the metal/oxide interface) coupled to the modified transport properties of the oxide layer can account for the formation of a fast growing oxide on top of a porous Ni-rich alloy. To distinguish such hypothetical description from the classic active oxidation model it will be referred to as *"modified active oxidation"* throughout the rest of this report. It is worth mentioning that when the alloy contains Fe (e.g. alloy 825 in Figure 2.5b) or for austenitic stainless steels, depending on the $P_{Cl2(g)}$ of the atmosphere, Fe can also be volatized along with Cr. However, for ferritic stainless steels the mechanical effects of chlorine appear to be

more important (see Figure 2.7b) as vacancy injection due to preferential oxidation is not generally the case for these alloys.

To summarize, based on the previous chapter and discussions in the current chapter, a tentative categorization of dominant corrosion mechanisms in $O_2(g)+Cl_2(g)/HCl(g)$ atmospheres is inferred and is schematically shown in Figure 3.3. For further exemplification of this diagram the case shown in Figure 2.8a is represented in Figure 3.4 where the occurrence of each mechanism is designated. For $0.25\%Cl_2(g)$ in $Ar(g)+20\%O_2(g)$ it is the volatilization of oxide, i.e. conversion of $NiO(s)$ to $NiCl_2(g)$, which is the dominating mechanism. When $Cl_2(g)$ content is increased to 0.5%, serrations on the curve start to appear coupled to a sharp jump which is followed by volatilization again. This behavior is more pronounced when $Cl_2(g)$ content is increased to $0.75\%Cl_2(g)$. Such behavior strongly suggests that mechanical damage to the oxide layer exposed the alloy to the gas. However, as the $P_{O2(g)}/P_{Cl2(g)}$ was not low enough, active oxidation did not take place and after some time, volatilization of the newly formed oxide became the dominant mechanism. Finally when $Cl_2(g)$ content is 1%, active oxidation dominates. In this case the rate of oxidation, due to the catalysis by $Cl_2(g)$, is so high that the sample ignites.

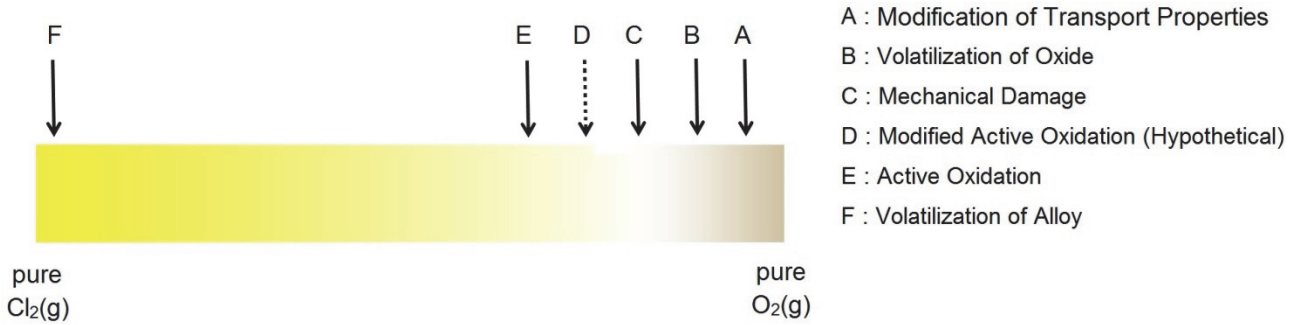

Figure 3.3 : Schematic presentation of the domination realm of corrosion mechanisms in chlorine-containing environments.

It is necessary to mention that the occurrence and the realm of domination of each mechanism depends on the temperature and chemical element in question. At low enough temperatures, no volatilization of oxide can be involved. In addition, different mechanisms often overlap or have synergy. For instance, occurrence of both volatilization of oxide and mechanical damage (the case for 0.5 and 0.75% $Cl_2(g)$ in Figure 3.4) or occurrence of both mechanical damage and change in the transport properties of the oxide (the case in Figure 3.1b) can be mentioned. The practical implication of such a diagram is that the alloy design strategy, which is determined by the dominant corrosion mechanism(s), changes with the $P_{O2(g)}/P_{Cl2(g)}$ of the environment as well as the temperature.

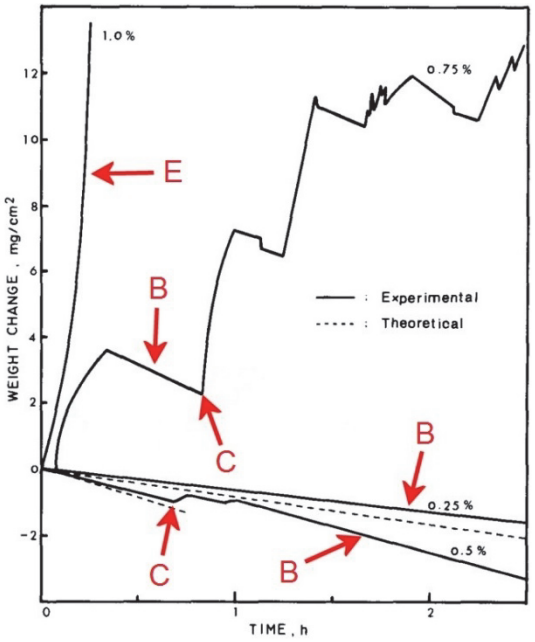

Figure 3.4 : Representation of Figure 2.8a where the incidence of each mechanism (or several mechanisms at the same time) is designated. See the legends in Figure 3.3 for description of letters B,C and E.

3.1.2 Effects of Alkali Chlorides

A distinctive aspect of high temperature corrosion by alkali chlorides compared to that by $Cl_2(g)$ or HCl(g) is the contribution from the alkali element. As shown by Pettersson et al.[74] the KCl-induced attack on chromia-forming alloys initiates due to K_2CrO_4 formation. K acts as a chromium-sink similar to the effect of water vapor reported by Asteman et al.[76], [77]. Equilibrium calculations with Thermo-Calc (using TAB module) shows that the change in the standard Gibbs energy for reactions 2.4 and 2.5 is positive (see equations 3.2 and 3.3).

$$Cr_2O_3+(3/2)O_2(g)+2H_2O(g)=2CrO_2(OH)_2(g) \quad ; \quad \Delta G^o(600^oC)=+254 \text{ KJ}$$
$$P_{CrO2(OH)2(g)}=4*10^{-10} \text{ atm for } P_{O2(g)}=0.05 \text{ atm and } P_{H2O(g)}=0.15 \text{ atm} \quad ; \quad 3.2$$

$$4KCl+Cr_2O_3+(3/2)O_2(g)+2H_2O = 2K_2CrO_4+4HCl(g) \quad ; \quad \Delta G^o(600^oC)=+151 \text{ KJ}$$
$$P_{HCl(g)}=7*10^{-4} \text{ atm for } P_{O2(g)}=0.05 \text{ atm and } P_{H2O(g)}=0.15 \text{ atm} \quad ; \quad 3.3$$

However, detection of K_2CrO_4 and $CrO_2(OH)_2(g)$ in the abovementioned studies shows that the reaction progress is sufficient to deplete the original oxide in Cr. This is likely due to the small thickness of the oxide formed during the initial stages at a relatively low temperature of 600°C. As an example the study by Jonsson et al.[78] can be mentioned. They exposed KCl-coated stainless steel 304L at 600°C in $N_2(g)+5\%O_2(g)+40\%H_2O(g)$ and observed that after one hour, in the regions where the oxide is still protective, its thickness is only (around) 70nm. This implies that a preformed oxide can delay the onset of breakdown. For alloys without preoxidation the course of events taking place after the breakdown of the initial thin oxide determines how much damage is

eventually incurred. At this point an important issue is the contribution from chlorine. Of course the $Cl_2(g)$ or HCl(g) evolved due to the reaction between the original oxide and the alkali chloride (see eq. 3.3) can contribute to the corrosion if it is not effectively dissipated. However, the chlorine evolved due to the oxide and alkali chloride interaction cannot always account for the corrosion acceleration after an initial stage. A pertinent example can be the KCl-induced high temperature corrosion of pure iron (Figure 2.20) and low alloy steels (Figure 2.16). Thermo-Calc[12] calculations, using the TAB module, shows that the $P_{Cl2(g)}$ generated due to the reaction between KCl and Fe_2O_3 is too low to allow chlorination of Fe (Figure 3.5). Nevertheless, in the studies by Jonsson et al.[101] and Folkeson et al.[46] chlorine was observed at the metal/oxide interface when KCl-coated low alloy steel (T22) was exposed at 400°C. The study by Jonsson et al.[101] was performed in an Environmental Scanning Electron Microscope (ESEM) at a pressure of 2.5Torr. Consequently, the slightest amount of $Cl_2(g)$ or HCl(g) that has evolved from the reaction between oxide and KCl would be removed by the microscope's pumping system. These circumstances and the low $P_{Cl2(g)}$ value for interaction between KCl and Fe_2O_3 (10^{-25}-10^{-20} atm at 400°C according to Figure 3.5), support the electrochemical mechanism for extraction of chlorine from KCl; hence the mechanism by Folkeson et al.[46] appears plausible. Such a mechanism is also consistent with similar observations on a preoxidized sample in the study by Jonsson et al.[101] .

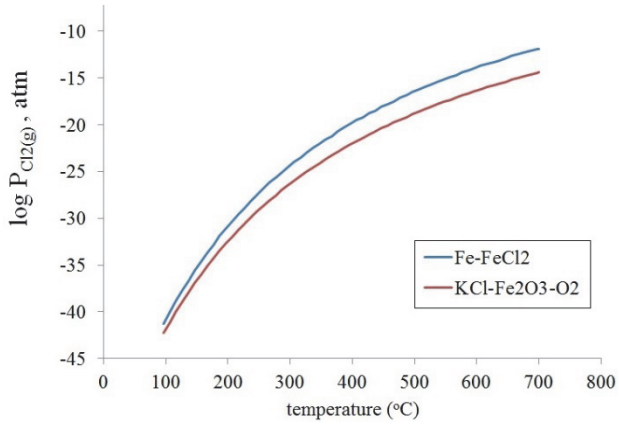

Figure 3.5 : $P_{Cl2(g)}$ due to Fe-$FeCl_2$ equilibrium compared with that due to the reaction between KCl and Fe_2O_3 to form $KFeO_2$ ($P_{O2(g)=0.05atm}$).

Unlike the electrochemical path suggested for the attack by HCl(g)[28] the mechanism proposed for KCl-induced attack of iron is, at first glance, not consistent with thermodynamics (compare equations 3.4 and 3.5). One way that it could be thermodynamically favored is to use the heat released by oxidation of Fe to break the bond between K and Cl. Then the total reaction in the presence of water vapor would be according to eq.3.6 leading to the formation of $FeCl_2$ wherever Fe^{2+} and Cl^- meet. This could be at the oxide/gas interface where the $FeCl_2$ is metastable [46], [101]. In this case, oxidation of $FeCl_2$ will release HCl(g) (eq.3.7). The liberated KOH(g) (eq.3.6) and HCl(g) (eq.3.7) may react with each other and reform KCl. In this way KCl would partly act as a catalyst. Ionic transport of chlorine has been suggested to occur on the chromia-forming alloys as well [114]. However, this happens only if there is residual KCl(s) after the chromate formation reaction is complete [114]. Such condition is promoted with increase in the amount of the deposited salt.

$$Fe + (1/2)O_2(g) + 2HCl(g) = FeCl_2 + H_2O(g) \;;\; \Delta G^o(500^oC) = -231\ KJ \quad ; \quad 3.4$$

$$Fe + 2KCl + (1/2)O_2(g) + H_2O(g) = 2KOH(g) + FeCl_2 \;;\; \Delta G^o(500^oC) = +214\ KJ \quad ; \quad 3.5$$

$$4Fe + 4KCl + (5/2)O_2(g) + 2H_2O(g) = 2FeCl_2 + Fe_2O_3 + 4KOH(g) \quad ; \quad 3.6$$

$$\Delta G^o(500^oC) = -168\ KJ$$

$$4FeCl_2 + O_2(g) + 4H_2O(g) = 2Fe_2O_3 + 8HCl(g) \;;\; \Delta G^o(500^oC) = -236\ KJ \quad ; \quad 3.7$$

From the literature reports and argumentations mentioned so far, it appears that alkali chlorides play a dual role in the damage to the chromia-forming alloys. The first role is in breaking down the protective chromium-rich oxide, which renders the alloy unprotected. The second role is in supplying chlorine to the alloy, which causes further damage according to one (or more) of the mechanisms mentioned in the previous chapter. Similar to the chlorine-induced corrosion, porous Ni-rich regions are often observed in alkali-chloride induced corrosion of austenitic stainless steels and Ni-based alloys as well (Figure 3.6). Therefore removal of alloying elements in the form of volatile metal chlorides also takes place due to the alkali chlorides. Analogous to chlorine-induced corrosion, active oxidation or modified active oxidation can be applied to describe the formation of Ni-rich regions. However, unlike the corrosion by $Cl_2(g)$ or HCl(g) the value of $P_{O2(g)}/P_{Cl2(g)}$ is not clear, because part of the chlorine that contributes to the corrosion will come from the electrochemical interaction between the alloy and the salt. This means that the $P_{O2(g)}/P_{Cl2(g)}$ for a certain case of alkali chloride-induced corrosion will depend on the metallic element in question as well as size and contact situation of particles with the surface. In addition as the solid salt in contact with the oxide layer is consumed over time, the $P_{O2(g)}/P_{Cl2(g)}$ ratio will change.

Another important issue regarding the alkali-chloride induced corrosion is the contribution from molten salts. As mentioned in the previous chapter in many articles [5], [6], [10], [46], [66], [100], [101], [106] a strong belief exists that for exposure of Fe and Fe-based alloys to alkali chlorides an alkali chloride-iron chloride molten mixture is formed. This melt is thought to be responsible for fast distribution of species over the surface [101]. However, the presence of a thick iron-rich oxide underneath it (see Figure 2.17a) indicates that its role is different from the role of molten salts in classic hot corrosion, i.e. fluxing the oxide layer. It appears that after the breakdown of the original protective oxide, the thick Fe-rich oxide acts as a barrier between the molten salt and the alloy. However, this beneficial effect from a thick non-protective oxide layer seems to be composition dependent. According to Ma et al.[87] with an increase in Cr content in the Fe-Cr binary system the formation of $K_2Cr_2O_7$ is promoted (see Figure 2.18). It appears that by increasing the Cr content of the alloy, there is enhanced probability for involvement of a fluxing mechanism. This may be ascribed to the low melting point of $K_2Cr_2O_7$ (396^{o}C according to [13]) and the low eutectic temperature in the KCl-$K_2Cr_2O_7$ system (see Table 2.1). The ignition type attack on pure Cr mixed with NaCl[94] (temperature increase to beyond 1300^{o}C) suggests that the protective oxide was destroyed and a direct contact between Cr and Cl^- was stablished. This is somewhat similar to the ignition type attack on pure Ni observed by Lee and McNallan[42] where NiO was damaged by volatilization and a direct contact between Ni and $Cl_2(g)$ became possible resulting in the release of

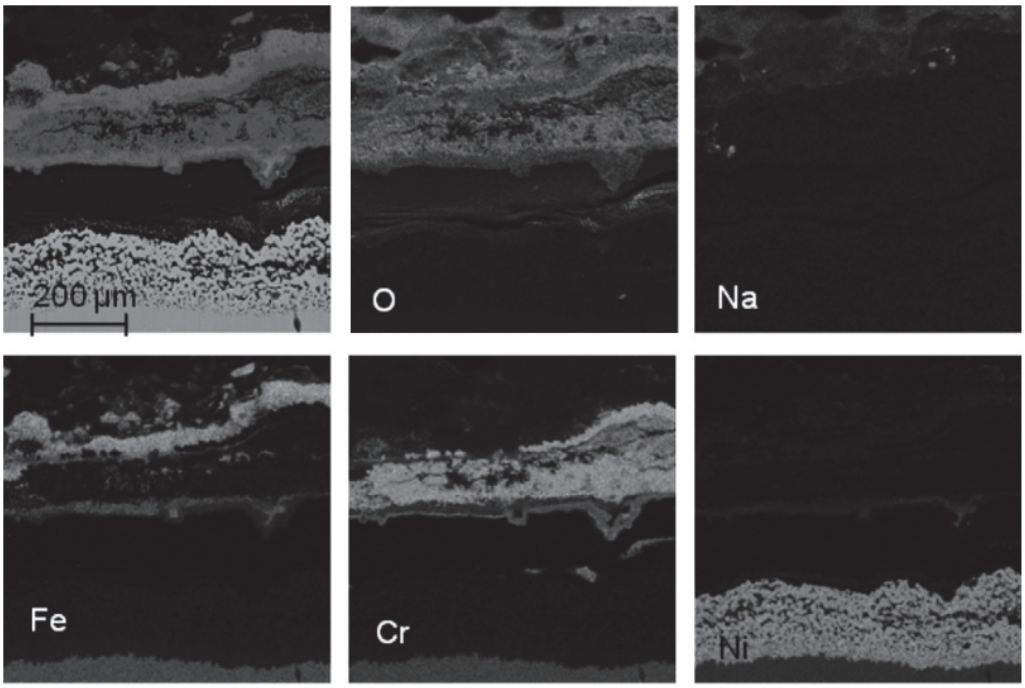

Figure 3.6 : Corrosion morphology and distribution of alloying elements throughout the corrosion products on Sanicro 28 exposed at 600°C for 168h in air. Sample was covered with NaCl(s) deposit[119]. Note the formation of porous Ni-rich areas. According to the reference no chlorine could be clearly found on the analyzed location.

a large amount of heat due to the subsequent oxidation of $NiCl_2(g)$. Extreme reactivity between pure Cr and alkali chlorides has implications for Cr-rich phases in the alloys as well.

So far the discussion of the role of molten salts involved gas atmospheres containing only $O_2(g)$ or $O_2(g)+H_2O(g)$. The situation changes when $Cl_2(g)$ or $HCl(g)$ are present in the gas. First and foremost, the presence of these species, depending on their concentrations, can displace the oxide-alkali chloride reactions to the left. As an example, if the gas phase contains more than 700vppm $HCl(g)$ the chromate formation reaction, eq. 3.3, is not spontaneous according to the calculation. In such cases a possible corrosion-initiating mechanism can be fluxing of the original protective oxide by a molten alkali chloride-metal chloride mixture.

3.2 Design Strategy

Based on the mechanisms mentioned in the previous chapter and the argumentations in the current chapter, a number of guidelines can be adopted for designing materials that can withstand high temperature corrosion due to chlorine and alkali chlorides. This section lists the important parameters to consider in the design of corrosion-resistant materials. Similar to the previous sections, gaseous chlorine and alkali chlorides are discussed separately to present a clearer picture of the different factors.

3.2.1 High Temperature Corrosion Induced by Cl_2(g) and HCl(g)

In oxygen-free chlorinating atmospheres, metals and alloys often suffer significant damage as a consequence of volatile metal chlorides at high temperatures. However, if $P_{Cl2(g)}$, temperature and gas velocity are low enough, there are metallic elements that can give acceptable corrosion rates. A meticulous evaluation requires availability of many kinetic constants for each element (rate constants for chlorination, mass transport coefficient in the gas phase etc.). However, thermodynamics can provide useful data to assess which elements would potentially be most corrosion resistant. Thus the vapor pressure of metal chlorides can be used to compare different elements. Usually the temperature at which the vapor pressure of a metal chloride reaches a value of 10^{-4} atm is employed as the criterion for volatility of metal chlorides [19]. This temperature is often referred to as T_4; hence an element with higher T_4 forms a less volatile chloride. Table 3.1 shows the calculated (and literature) values of T_4 along with sublimation, melting and boiling points for chlorides of several common alloying elements. As can be seen Ce and Y form the least volatile chlorides. Chevalier et al. [120] studied corrosion of several alloys under Ar(g)+2%Cl_2(g) at 850°C and found that the low chromium Ni-base alloys showed a better performance compared to the high-chromium Ni-base alloys. In addition, Fe-base alloys were damaged most of all. This result can be explained in light of the values given in Table 3.1. As $CrCl_3$ and especially $FeCl_3$ are more volatile chlorides compared to $NiCl_2$, the presence of Cr and Fe in Ni leads to larger material loss under this condition.

Table 3.1: Some physical properties of a number of transition metal chlorides. Values are calculated with Thermo-Calc [121] (using modules TAB and POLY3) unless mentioned otherwise. T_s: sublimation point, T_m: melting point, T_b: boiling point.

chloride	T_s(°C)	T_m(°C)	T_b(°C)	T_4(°C)	chloride	T_s(°C)	T_m(°C)	T_b(°C)	T_4(°C)
$FeCl_2$		677	1026	520	$TiCl_3$		730[122]	750[122]	432*
$FeCl_3$		308	392*	170*	$TiCl_4$		-25[13]	95	-38[122]
$CrCl_2$		824	1699	814	$ZrCl_4$	332			146[122]
$CrCl_3$		827	846	532	$HfCl_4$	319[123]			132[122]
$NiCl_2$	970			593	$CeCl_3$		807	1812	931
$MoCl_3$		1027[13]	1027[13]	388[13]	YCl_3		721	1400	814
$MoCl_4$		317	405	139	$CoCl_2$		737	1085	573
$AlCl_3$	181*			74*	$TaCl_2$		937[13]	1377[13]	
$SiCl_4$		-70[123]	58	-87[122]	$TaCl_5$		216[123]	242[123]	80[122]

* Transformation to gas phase takes place in dimer molecules i.e. in form of $(MCl_x)_2$.

Under oxidizing-chlorinating conditions, the protection depends on the rapid formation and stability of a slow-growing oxide. To achieve this, the following factors need to be considered:

1- The oxide-forming element of the alloy should have a large affinity for oxygen in the presence of chlorine. This means a large oxide stability area in a metal-oxygen-chlorine, M-O_2(g)-Cl_2(g), phase diagram at constant temperature.
2- The chloride and oxychloride of the oxide-forming element should have a very low partial pressure in equilibrium with the metal oxide and the gas phase. This guarantees that volatilization of oxide (conversion to volatile chlorides or oxychlorides) cannot break the original protective oxide. This factor becomes increasingly important with increase in temperature.

3- The oxide layer should be dense and slow growing. This guarantees that chlorine cannot be transferred in molecular form i.e. $Cl_2(g)$ and HCl(g). However, since Cl^- may be transported through the oxide grain boundaries, complete suppression of chlorine ingress requires modification of oxide grain boundaries. Presence of reactive elements such as Y may be beneficial [37], [50]. However, the effect is not fully understood and in some cases due to Y addition grain boundary attack (in the metal) has been shown to aggravate corrosion [37], [124].
4- Concentration, activity and mobility of the oxide-forming element in the alloy should be large enough to result in rapid formation of the oxide layer. This is especially a limiting factor at lower temperatures. In addition, factors such as grain size and plastic deformation that affect the diffusivity of the oxide-forming element are also important.
5- Presence of refractory metals such as Mo or W or susceptible phases such as Cr carbides should be avoided. However, this factor is important only if the protective oxide breaks. In the absence of a protective oxide, Mo or W can be attacked by oxygen, chlorine or both. As all of the resultant compounds (oxide, chloride, oxychloride) are volatile at high enough temperatures an accelerated mass loss will take place if these elements are present in the alloy.
6- The element that forms the matrix of the alloy should have a low affinity to chlorine under low $P_{O2(g)}$ (i.e. reducing) conditions. Again, this factor is important in the event of breakdown of the protective oxide.

Similar to the discussion on oxygen-free atmospheres, again a full evaluation of suitable materials would require comprehensive data regarding the kinetics of oxidation and chlorination as well as diffusion in the alloys. However, as the first step of analysis, thermodynamics of the M-$O_2(g)$-$Cl_2(g)$ system need to be investigated. For this purpose the M-$O_2(g)$-$Cl_2(g)$ phase stability (predominance) diagrams for a large number of metallic elements of the periodic table were calculated with Thermo-Calc (SSUB3 database)[12]. Subsequently elements with large oxide stability area were selected and considered as candidate oxide-forming elements. In addition, elements with a large metal stability area under reducing conditions (low $P_{O2(g)}$) could be considered as candidate matrix-forming elements. The boundary between reducing and oxidizing conditions for each element is considered as the $P_{O2(g)}$ in equilibrium with metal and oxide. It is worth mentioning that under the conditions where the conversion of oxide to chloride or oxychloride is the dominant mechanism (usually at temperatures as high as 800°C and above) the M-$O_2(g)$-$Cl_2(g)$ phase diagrams need to be modified to consider the volatility of chlorides or oxychlorides. This is implemented by considering the partial pressure of chlorides or oxychlorides, instead of using an activity of one for calculation of oxide/chloride or oxide/oxychloride phase boundary. Bender and Schutze [36] calculated the M-$O_2(g)$-$Cl_2(g)$ diagrams assuming a partial pressure of 10^{-4} atm for chlorides and oxychlorides and called it *"quasi-stability diagrams"*. However, as the target temperature of this study (600°C) is relatively low, the classic M-$O_2(g)$-$Cl_2(g)$ phase diagrams (i.e. assuming an activity of one for chlorides and oxychlorides) were considered.

Taking into account the criteria 1 and 6 as the first step, calculations showed that Al, Si, Cr, Ti, Y, Ce, Ta, Hf and Zr are suitable oxide-formers among the common alloying elements. In addition,

Mo, Ni and Co are desirable as the matrix-forming elements. The corresponding phase diagrams for the candidate elements are shown in Figure 3.7 and Figure 3.8.

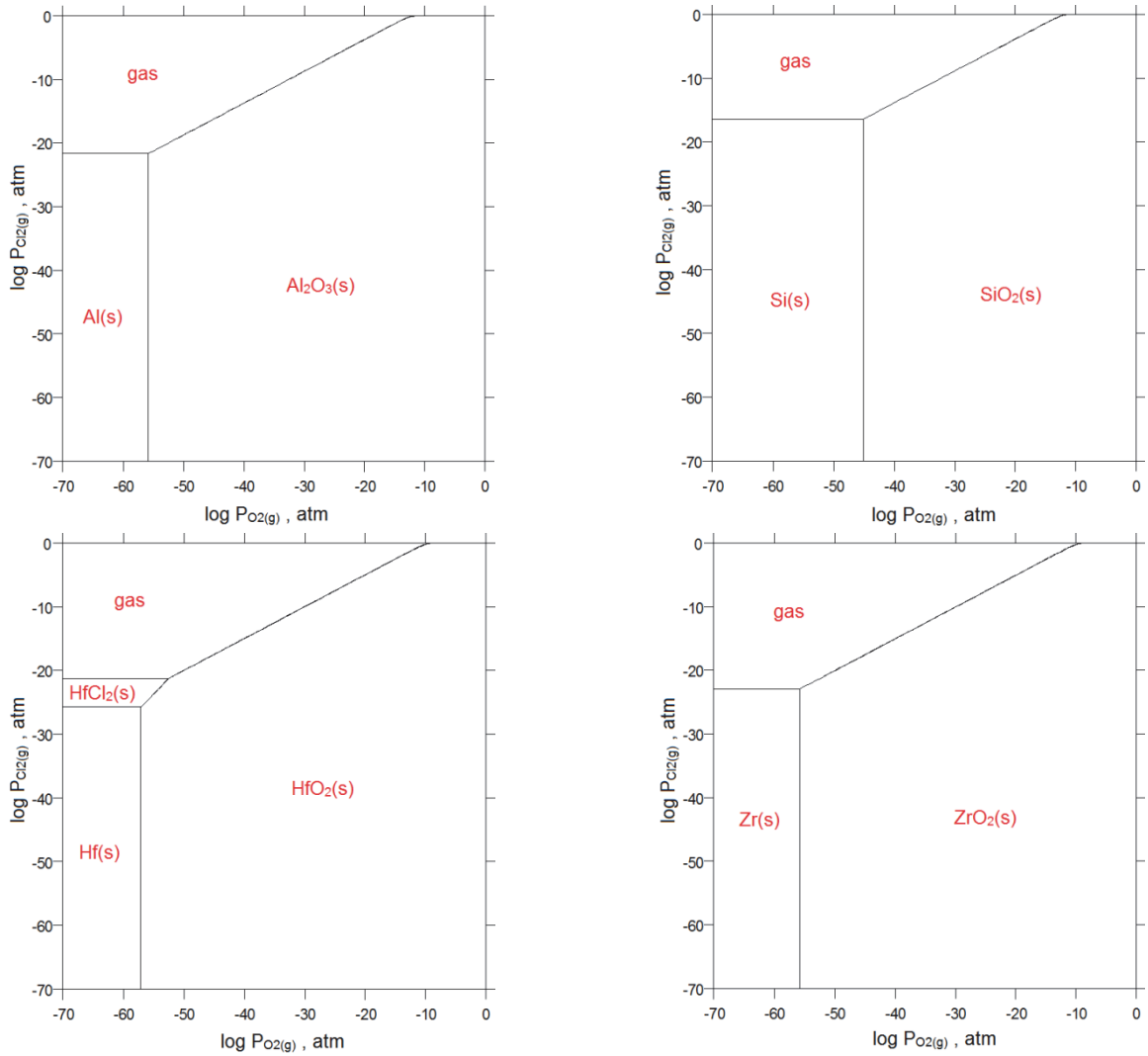

Figure 3.7: Calculated M-O_2(g)-Cl_2(g) phase stability diagrams at 600°C for elements with large oxide stability area. Calculations with Thermo-Calc[12] using database SSUB3. 1 mole of metal and 10^{-6} mole Ar(g) (as inert gas) were considered for calculations.

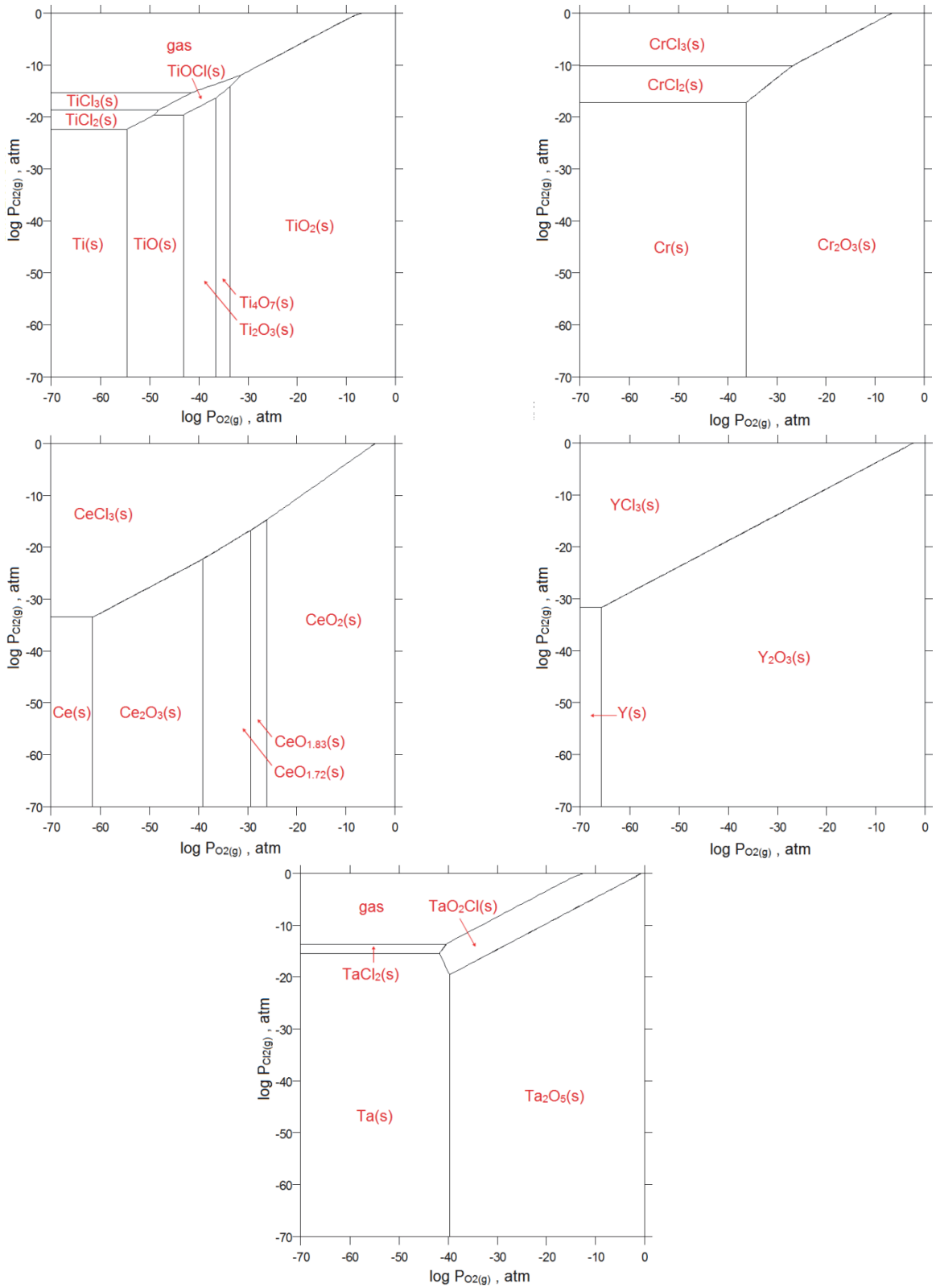

Figure 3.7 (cont.)

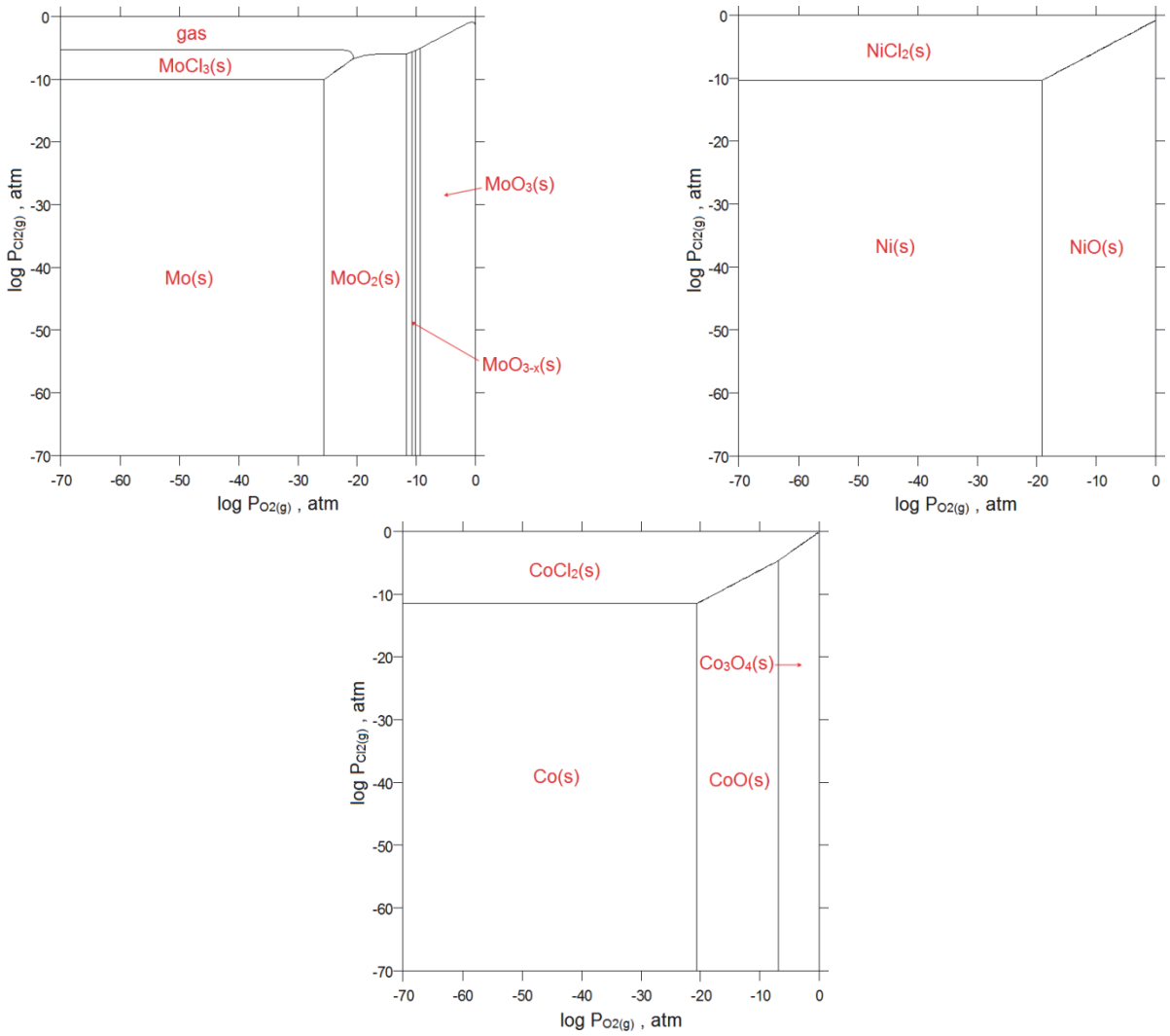

Figure 3.8: Calculated M-O_2(g)-Cl_2(g) phase stability diagrams at 600°C for elements with large metal stability area under reducing conditions. Calculations with Thermo-Calc[12] using database SSUB3. 1 mole of metal and 10^{-6} mole Ar(g) (as inert gas) was considered for calculations.

3.2.2 High Temperature Corrosion Induced by Alkali Chlorides

As mentioned in the previous sections, in alkali chloride-induced high temperature corrosion the alkali component of the salt is contributing to the corrosion as well. This means that in addition to the factors important for chlorine-induced corrosion, additional points need to be considered to mitigate corrosion. According to the previous discussions these factors are as follows:

1- Reactivity between protective oxide and the alkali chloride: Such reactions (e.g. eq.3.3) break down the original protective oxide and also evolve Cl_2(g) or HCl(g).

2- A more noble nature for the matrix-forming element in the alloy: This is important as the breakdown of the protective oxide can pave the way for electrochemical interaction between the elements in the alloy and the alkali chloride (see eq.3.6). In the event of breakdown of the protective oxide, a reactive matrix element will then cause evolution of more Cl^-. In addition, a low reactivity between the oxide of the matrix-forming element and the alkali chloride appears to be favorable as less Cl_2(g) or HCl(g) would be evolved in case of a

reaction. However, if a protective oxide is rapidly established and maintained this factor becomes less important.

3- The lowest melting point in the alkali oxide-metal oxide(s) system should be as high as possible: Formation of molten phases in high temperature corrosion generally needs to be avoided as it leads to a fast distribution of corrosive species and also has the potential to flux any underlying oxide layer.

4- Low solubility of the protective oxide in the alkali chloride-metal chloride molten mixture: This factor is more important when the gas atmosphere contains Cl_2(g) or HCl(g) in addition to other species. In such a case metal chlorides can form on the surface and together with the alkali chlorides, can form a low melting point eutectic that can flux the underlying oxide (see Table 2.1).

Considering the abovementioned factors and also the candidate oxide-forming and matrix-forming elements (mentioned in section 3.2.1) complementary thermodynamic calculations were performed to further narrow down the range of suitable elements.

Table 3.2 shows the calculated standard Gibbs energy changes due to a number of possible reactions between different oxides and KCl. The reason for considering KCl and a temperature of 600^{o}C is based on the prevalence of KCl (and not other alkali chlorides) in biomass combustion and the target temperature of this study. Unfortunately the thermochemical data for possible reaction products ($K_2O.M_2O_x$ type oxides) were not available for all the oxides in the databases of the adopted commercial softwares. Therefore the investigation was limited to the tabulated reactions. Reactions between Fe_2O_3 and KCl as well as Fe_3O_4 and KCl were also tabulated due to the importance of Fe as the basis of the entire stainless steel family. As can be seen, surprisingly Fe oxides (Fe_2O_3 and Fe_3O_4) have the lowest affinity for KCl. On the other hand Mo and Cr develop oxides which are more prone to react with KCl compared to the other oxides. For TiO_2 the discrepancy in the data between different sources is significant therefore no conclusion can be made based on the calculated values.

In the absence of a protective oxide there will be the possibility for electrochemical interactions between the matrix element and the salt as well (see equations 2.7 and 2.8). Therefore to evaluate which of the candidate matrix-forming elements is more susceptible to undergo such interaction, the standard Gibbs energy change for the relevant reactions was calculated with Thermo-Calc[12](using TAB module). The corresponding data is given in equations 3.8 to 3.10. The results indicate that Mo is highly reactive, while Ni and Co show a rather inert behavior with Ni being superior to Co.

$$Mo + (5/4)O_2(g) + (1/2)H_2O(g) + KCl = (1/3)MoCl_3 + (2/3)MoO_3 + KOH(g) \quad ; \quad \Delta G^{o}(600^{o}C) = -210.5KJ \quad ; \quad 3.8$$

$$Ni + (1/2)O_2(g) + (1/2)H_2O(g) + KCl = (1/2)NiCl_2 + (1/2)NiO + KOH(g) \quad ; \quad \Delta G^{o}(600^{o}C) = +55.8KJ \quad ; \quad 3.9$$

$$Co + (7/12)O_2(g) + (1/2)H_2O(g) + KCl = (1/2)CoCl_2 + (1/6)Co_3O_4 + KOH(g) \quad ; \quad \Delta G^{o}(600^{o}C) = +31KJ \quad ; \quad 3.10$$

Table 3.2: Affinity of a number of oxides to KCl at 600°C. Reactions are balanced for 1 mole of KCl. ΔG^o values are calculated with Thermo-Calc (database SSUB3) [12], FactSage (database FactPS) [14] and HSC Chemistry [13] depending on the availability of the thermochemical data. Value of ΔG^o (600°C) for KCl=KCl(g) varies between +91.4-+91.6 from [12]–[14]. This value can be used to estimate the reactivity of the salt vapor and oxides.

oxide	reaction equation	ΔG^o (600°C), KJ
Al_2O_3	$(1/2)Al_2O_3 + KCl + (1/2)H_2O(g) = KAlO_2 + HCl(g)$	+112.3[12], +124.5[14], +112.5[13]
	$3Al_2O_3 + KCl + (1/2)H_2O(g) = (1/2)K_2Al_{12}O_{19} + HCl(g)$	+59[14]
	$(9/2)Al_2O_3 + KCl + (1/2)H_2O(g) = KAl_9O_{14} + HCl(g)$	+48.5[14]
Cr_2O_3	$(1/2)Cr_2O_3 + KCl + (1/2)H_2O(g) = KCrO_2 + HCl(g)$	+95.4[12], +95.6[13]
	$(1/4)Cr_2O_3 + KCl + (3/8)O_2(g) + (1/2)H_2O(g) = (1/2)K_2CrO_4 + HCl(g)$	+37.8[12], +37.5[14], +38.0[13]
	$(1/2)Cr_2O_3 + KCl + (3/4)O_2(g) + (1/2)H_2O(g) = (1/2)K_2Cr_2O_7(l) + HCl(g)$	+29.9[13]
Fe_2O_3	$(1/2)Fe_2O_3 + KCl + (1/2)H_2O(g) = KFeO_2 + HCl(g)$	+131.0[12], +131.8[13]
Fe_3O_4	$(1/3)Fe_3O_4 + KCl + (1/12)O_2(g) + (1/2)H_2O(g) = KFeO_2 + HCl(g)$	+111.6[12], +110.5[13]
SiO_2	$SiO_2 + KCl + (1/2)H_2O(g) = (1/2)K_2Si_2O_5 + HCl(g)$	+68.7[12], +78.5[14], +69.1[13]
	$2SiO_2 + KCl + (1/2)H_2O(g) = (1/2)K_2Si_4O_9 + HCl(g)$	+73.3[12],+108[14], +74.5[13]
	$(1/2)SiO_2 + KCl + (1/2)H_2O(g) = (1/2)K_2SiO_3 + HCl(g)$	+96.2[12], +113[14], +96.5[13]
TiO_2	$TiO_2 + KCl + (1/2)H_2O(g) = (1/2)K_2Ti_2O_5 + HCl(g)$	+134.5[14]
	$(3/2)TiO_2 + KCl + (1/2)H_2O(g) = (1/2)K_2Ti_3O_7 + HCl(g)$	+131.5[14]
	$3TiO_2 + KCl + (1/2)H_2O(g) = (1/2)K_2Ti_6O_{13} + HCl(g)$	+134[14]
	$(1/2)TiO_2 + KCl + (1/2)H_2O(g) = (1/2)K_2TiO_3 + HCl(g)$	-56.2[13], +136[14]
	$(1/4)TiO_2 + KCl + (1/2)H_2O(g) = (1/4)K_4TiO_4 + HCl(g)$	+301[14]
	$(5/8)TiO_2 + KCl + (1/2)H_2O(g) = (1/8)K_8Ti_5O_{14} + HCl(g)$	+560[14]
Ta_2O_5	$(1/2)Ta_2O_5 + KCl + (1/2)H_2O(g) = (1/2)KTaO_3 + HCl(g)$	+58.5[13]
MoO_3	$(1/2)MoO_3 + KCl + (1/2)H_2O(g) = (1/2)K_2MoO_4 + HCl(g)$	+33.6[13]
	$MoO_3 + KCl + 0.5H_2O(g) = 0.5K_2Mo_2O_7 + HCl(g)$	+14.3[13]
	$1.5MoO_3 + KCl + 0.5H_2O(g) = 0.5K_2Mo_3O_{10} + HCl(g)$	+10.5[13]
	$2MoO_3 + KCl + 0.5H_2O(g) = 0.5K_2Mo_4O_{13} + HCl(g)$	-0.7[13]
	$4MoO_3 + KCl + 0.5H_2O(g) = 0.5K_2Mo_8O_{25} + HCl(g)$	-4.4[13]

Regarding the formation of a liquid phase, due to the reaction between oxides and KCl, a literature survey was performed and the results are shown in Table 3.3. Unfortunately the data was available only for a limited number of systems. The collected information showed a similar trend to the reactivity between oxides and KCl i.e. Mo and Cr oxides were the ones most disposed to form a low melting point eutectic mixture with K_2O.

Table 3.3: The lowest melting point found in the literature regarding the K_2O-M_2O_x pseudobinary system (M stands for the metal).

system	K_2O-Al_2O_3	K_2O-SiO_2	$K_2Cr_2O_7$-K_2CrO_4	K_2O-TiO_2	K_2O-Ta_2O_5	K_2MoO_4-MoO_3
temperature (°C)	740[125]	655[126]	393[127]	633[128]	800[127]	<500[127]

To summarize, the results of calculations suggest that Ni and Co are suitable matrix-forming elements. In addition, Al, Si, Ta and probably Ti are better oxide-formers compared to Cr. However, this result is incomplete due to the lack of experimental information for the interaction of

KCl and oxides of the candidate elements. Finally, it is important to remember that these results are based only on thermodynamics and do not take into account kinetic aspects.

4. Planning, Method and Tools of the Experimental Investigations

In this chapter, based on the discussion and calculations mentioned in Chapter 3, the framework of the experimental investigation is defined. In addition, the experimental set up and corrosion evaluation method are described. Finally, a concise review on the analytical techniques employed in this study is presented.

4.1 Experiment Design

In Chapter 3, a number of candidate elements for design of an alloy resistant to chlorine and alkali chloride-induced corrosion were identified. However, due to the lack of thermochemical data for several potassium-metal-oxygen compounds, it is not clear whether certain elements (Ni, Co, Hf, Zr, Ce, Y, and Ta) can be used to reduce the alkali chloride-induced corrosion. In addition, the literature reports were not in agreement as to the dominant corrosion mechanism for the currently used materials. Therefore, the following sequence of investigations was considered as the research strategy in this study:

1- Reactivity between oxides and KCl to identify the suitable oxide-forming and matrix-forming elements.
2- Performance of selected chromia-forming conventional alloys under controlled laboratory conditions to gain further knowledge about the dominant corrosion mechanism(s).
3- Influence of the presence of additional oxide-forming elements on the performance of chromia-forming alloys (both commercial and model alloys). The additional elements are chosen based on thermodynamic considerations and the results from the reactivity between oxides and KCl.
4- Performance of coatings based on the suitable oxide-forming elements.

The exact experimental parameters for each series of investigations will be mentioned in Chapters 5 and 9. However, some general aspects of experimental procedure and assessment of the corrosion is given in section 4.2.

4.2 Experimental Set-Up and Corrosion Assessment Method

High temperature corrosion experiments require exposure of samples to high temperatures under controlled atmospheres. The chemistry of the gas can be adjusted by controlling the flow rate of individual gas components. This is usually achieved by employing a suitable flow measuring device such as a rotameter or a mass flow controller for each component of the gas. If the desired gas atmosphere requires a specific $H_2O(g)$ content, a common method is to pass the inlet gas through a humidifier. Figure 4.1 shows a schematic of the experimental set-up used in the current study. $N_2(g)$

and $O_2(g)$ are supplied from different gas cylinders and their corresponding flowrates are adjusted by means of thermal mass flow controllers. They are mixed and led through the humidifier, which is a water bath equipped with a thermostat. By adjusting the temperature of the water bath, it is possible to adjust the $H_2O(g)$ content of the inlet gas. In this way the required gas mixture of $N_2(g)+O_2(g)+H_2O(g)$ can be supplied to the reaction tube.

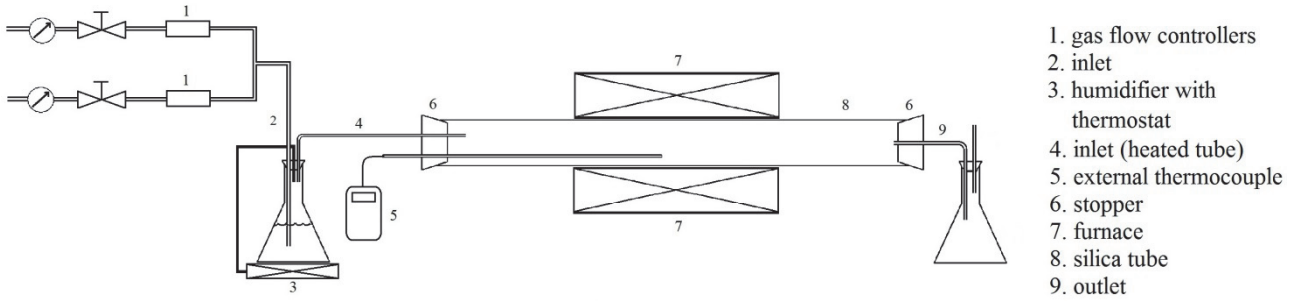

Figure 4.1: schematic of the experimental set-up used in this study.

Assessment of the extent of high temperature corrosion due to solid salts can be performed by several different methods depending on the type of corrosive species, extent of damage and the morphology of corrosion. A common method is to follow the mass change as the sample is being exposed. This technique is referred to as Thermogravimetry Analysis (TGA) and is quite common for the study of many types of corrosion e.g. oxidation, sulfidation etc. In fact, when the corrosion leads to either mass gain or mass loss, TGA is a very accurate and reliable method to follow the course of reactions and study the kinetics. However, if both mass loss and mass gain are simultaneously involved, interpretation of mass change data is difficult. As an example, high temperature corrosion in oxidizing-chlorinating environments can be mentioned. Under such conditions formation of oxides leads to mass gain while formation of chlorides and oxychlorides may lead to mass loss due to sublimation. To compensate for such shortcomings, a widely practiced method is to measure the mass loss after removal of the residual corrosion products. This can be done by mechanical methods such as blasting glass beads on the sample surface (see e.g. [109]) or pickling the corrosion products by suitable chemical solutions (see e.g. [30]). However, this technique is not accurate if internal corrosion products are present. Another approach to evaluate the extent of attack is measurement of oxide layer thickness (see e.g.[82]). As with the previous methods, application of this method is not free from difficulties. The first challenge is due to the fact that oxide layers of different alloys do not necessarily have the same density. Therefore the thickness of the oxide layer is not an accurate method for comparison between different alloys. Another difficulty with this method is that in some corrosion scenarios such as chloride deposit-induced corrosion, the oxide layer is porous and often incorporated into the deposit residues. In addition, the oxide layer can spall from the surface during or after exposure. For such cases it is not easy to define the boundaries of the oxide layer when measuring its thickness. Therefore to avoid these deficiencies, decrease in the metal thickness was employed in the present study. Pre-exposure measurements are conducted, and residual metal thickness can be measured after exposure and therefore the metal thickness loss can be calculated. Similar to many of the above-mentioned techniques, measuring the decrease in metal thickness is also an ex-situ method and does not

provide information regarding the course of corrosion unless a large number of time-resolved exposures are carried out. In addition, a sufficiently large number of measurements need to be madeto have acceptable statistics. However, a distinct advantage of this method is that it is possible to take into account the specific corrosion morphology. In fact, measurement of mass change or thickness of the oxide layer does not reveal adequate information about the incidence or depth of localized attack. The importance of corrosion morphology is prominent for pressurized vessels or tubes. In such cases a single deep local attack, e.g. in the form of void or grain boundary corrosion, may be able to decrease the load-bearing cross section below a critical value and cause an early breakdown of the whole component.

4.3 Analytical Techniques

In high temperature corrosion, a variety of analytical techniques are used to study the mechanism(s) of corrosion. These techniques provide information regarding the morphology of corrosion as well as elemental and phase composition of the corrosion products. Hence it becomes possible to understand how different species have formed and have been transported due to the corrosion. Such knowledge can unveil the mechanism(s) of attack and accordingly a suitable materials strategy to reduce corrosion can be implemented. The following paragraphs present a brief description of the analytical methods employed in this study.

4.3.1 Scanning Electron Microscopy (SEM) [129]

Interactions due to the collision of accelerated electrons and surface of solid matter constitute the basis for image formation and analysis in electron microscopy. Figure 4.2a shows the different components of a typical Scanning Electron Microscope (SEM). Electrons are extracted from a source located at the top part of the instrument. Common sources are either based on the thermionic effect (e.g. tungsten filament gun) or field evaporation effect (field emission gun). Subsequently electrons are accelerated by application of a large electric field. Typical accelerating voltage rates are between 5-30 KV. By employing electromagnetic lenses, a focused electron beam is formed which, by means of additional electromagnetic coils, is scanned across the sample surface.

As high velocity electrons hit the surface, a number of physical effects occur which are outlined in Figure 4.2b. Among these, emission of secondary electrons (SE), backscattered electrons (BSE) and characteristic X-rays are the most commonly utilized effects in SEMs for the purpose of microscopy and chemical analysis. A SE is created when a high energy Incident Electron (IE) collides with one of the electrons of the inner electronic shells of the matter and, due to its high energy, grazes the electron out of the atom. Alternatively it is possible that the IE is only scattered upon collision with the atoms. A BSE is generated when such scattering, or sequence of scatterings, causes the electron to leave the surface while still conserving most of its original kinetic energy, i.e. it is elastically scattered. At a constant acceleration voltage and beam current, the portion (i.e. number of the electrons emitted per incident electron) of the SE and BSE increases with sample tilt. This means that regions of geometric irregularity, i.e. local tilt relative to the incident electron

beam, will emit larger numbers of SE and BSE. Such effect is the basis of topographic contrast formation in the SEM. Such contrast can be obtained with both SE and BSE. However, compared to the SE, BSE have larger energies and can therefore escape from a larger volume in the sample (Figure 4.2c). Consequently spatial resolution in obtaining topographic images with BSE is poorer compared to the SE. In fact, as the SE have lower energies and come from shallower volumes of the surface, topographic images are usually taken in the SE mode. Unlike SE, the BSE is closely dependent on the atomic number (Z) of the target atoms and increases monotonically as the average Z of the target material increases. This means that in a completely flat sample with chemical heterogeneity, regions with different compositions emit different numbers of BSEs per unit time. This effect is the basis of the compositional contrast. In the current study, due to the importance of distribution of elements throughout the corrosion products, chemical composition contrast is of utmost importance. Therefore imaging was always performed in the BSE mode unless otherwise mentioned.

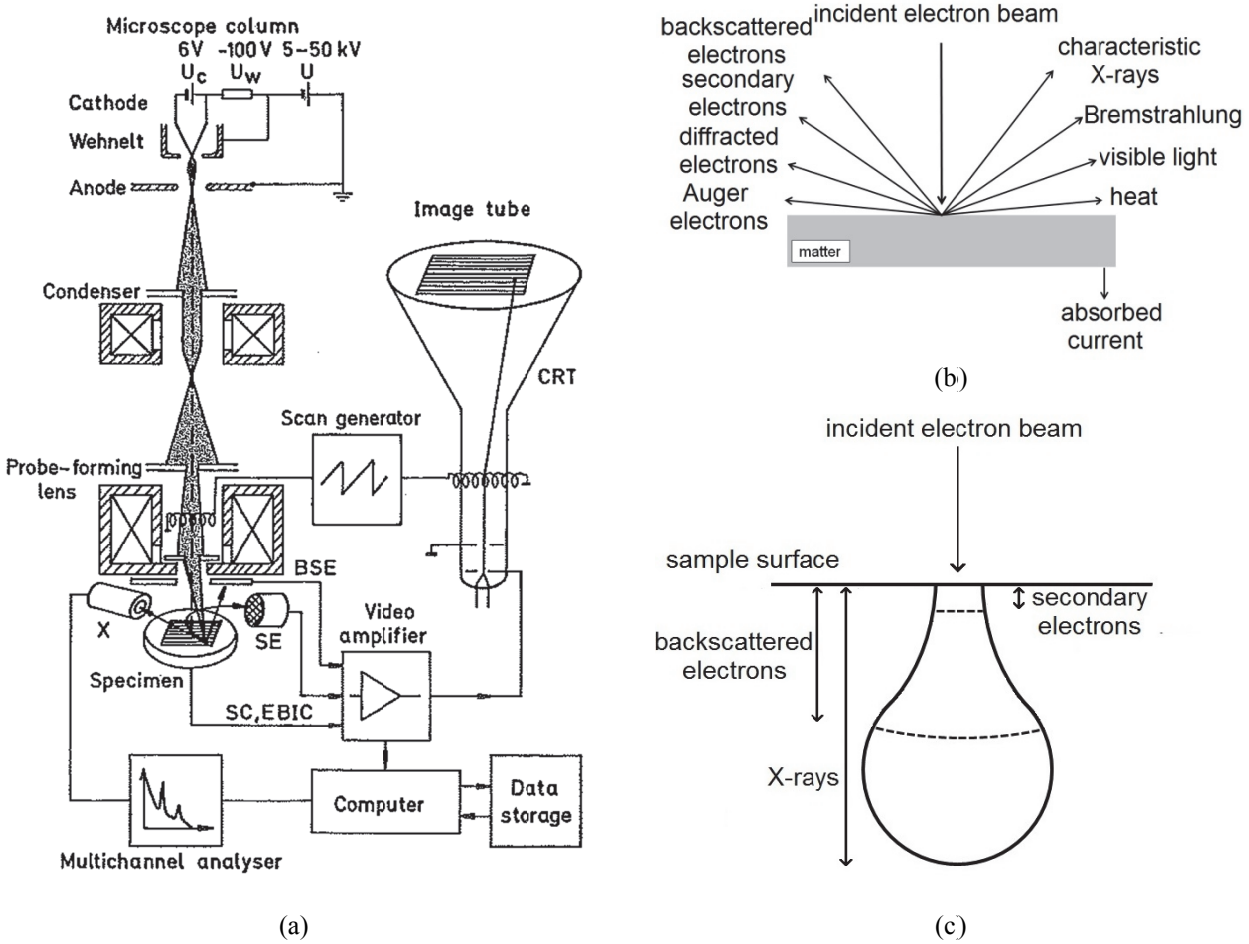

Figure 4.2 : (a) Schematic of a SEM unit [130]. (b) Possible effects due to the interaction between accelerated electrons and solid matter. Reproduced from [131]. For thick samples electrons will eventually stop within the matter while for the sufficiently thin samples they might be transmitted as well. (c): Schematic of the interaction volume i.e. the volume within which 95% of the incident electrons will finally rest. As can be seen BSE come from larger volume compared to SE. Reproduced from [129].

4.3.2 Energy Dispersive X-Ray Spectroscopy (EDS)[129]

As mentioned in the previous section, one of the consequences of bombarding the solid matter with high velocity electrons is the emission of characteristic X-rays. As the electrons with high kinetic energy strike the atoms of the target material, they can induce electron transitions between the electronic shells of the target atom. As an example an electron in the K shell (innermost layer) might jump to the L shell, which has a higher potential energy (Figure 4.3a). Once this electron jumps back to its original shell, an X-ray photon is emitted. The energy of such a photon corresponds to the energy difference between the K and L shells of the target atom. As the energy difference between electronic shells of an atom is element-specific, measurement of the energy of these X-rays enables chemical identification (elemental analysis) of the target material. In addition, counting the number of emitted X-ray photons of the same energy provides information about the concentration of elements present. Such possibilities form the basis of the EDS method and are implemented by mounting an X-ray detector into the SEM chamber (denoted by X in Figure 4.2a). A typical EDS detector is composed of a gold-coated piece of Si with a protective Be window in front of it. Through the Au films a bias is applied across the Si and as the X-rays are absorbed by the detector a short-lasting current, referred to as a pulse, is established due to the semiconducting property of Si. These pulses are transferred to a multichannel analyzer (MCA) and subsequently recorded by a computer as histograms of intensity (number of counts) versus energy. The intensity measurements are directly converted by the EDS software into composition data by application of matrix corrections taking into account atomic number, absorption and fluorescence effects.

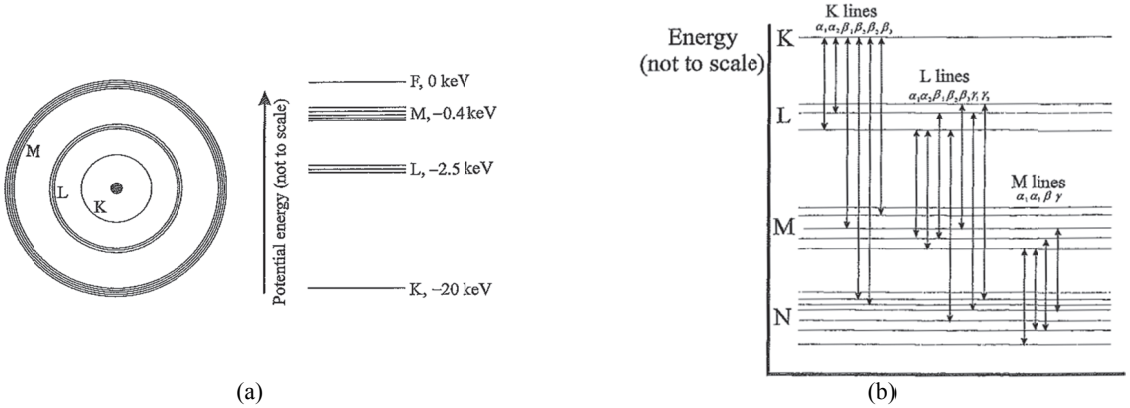

Figure 4.3 : (a) First three electron shells of Mo. Electrons of K shell are most tightly bound to the nucleus. To excite a single K electron to jump to the L shell, 20-2.5=17.5 KeV energy is needed [129](b) Designations to specify electronic transitions between shells. K_α denotes transition between K and L while K_β corresponds to that between K and M. The energy of the X-ray photons will also depend on which electronic orbitals are involved in the transition. Values of transition energies between different shells and for different elements are available in the literature [129].

Among the large number of possible electronic transitions $K_{\alpha 1}$ and $K_{\alpha 2}$ have the highest intensities (for typical beam energy of 25KeV) and are therefore most widely used for characterization. As the energy required to excite K electrons increases with increasing the atomic number, characterization of heavier elements involves application of higher accelerating voltages

(higher beam energies). However, in such cases it is usually preferred to employ other transitions (L and M series) rather than increasing the accelerating voltage.

Although at a first glance quantitative determination of composition by EDS does not seem difficult, there are in fact a number of effects which introduce uncertainties in a concentration measurement by EDS. A number of such difficulties are listed as follows:

- Absorption of X-rays of light elements, such as carbon and oxygen, by the heavier elements in the alloy as well as the Be window which results in erroneous quantification of such elements by EDS. In fact, accurate quantitative measurement of elements lighter than sodium by conventional EDS detectors is impossible.
- Large sampling volume: The volume from which X-rays originate (sampling volume) also plays an important role in defining the resolution of the analysis (see Figure 4.2c). The volume is in the order of $1\mu m^3$ for a typical accelerating voltage of 20KV for a metallic material. Therefore if finer resolutions are required, the accelerating voltage needs to be lowered. This, in turn, will lower the chance for exciting desired electron transitions. Accordingly, the spatial resolution of EDS is practically limited to about 1μm. In addition, as the electron energy drops during its travel through the matter, elements having higher energy transitions will stop emitting X-rays at shallower depths. This means that, the depth of analysis is not the same for all the alloying elements.
- Poor energy resolution of the detector: A typical detector cannot resolve energy peaks closer than 100-200eV. Therefore distinction between closely spaced lines such as S K_α and Mo L_α is difficult.
- Sum peak: When two identical X-ray photons enter the detector at the same time this would be registered as one photon with twice as much energy as the original ones.
- Si escape peak: X-rays having energies higher than Si K_α (1.74KeV) induce X-ray emissions by the detector's Si itself. Therefore a Si K_α peak might be imposed to the EDS spectrum as well.
- Fluorescence: as the X-rays produced by electron transitions in an element travel through the material they might induce electronic transitions of lower energies in the other elements. Thus the number of characteristic X-rays emitted from the element(s) having lower energy transitions will show higher than the actual value. An example can be a Cu-30%Zn alloy where Zn K_α radiation (8.64KeV) leads to additional emission of Cu K_α (8.05KeV). Fortunately modern EDS software automatically perform the necessary corrections for this effect.

Despite the above-mentioned limitations, EDS has the major advantage of being a fast semi-quantitative analysis which makes it a quite common analytical method. An EDS detector in an SEM can be placed close to the specimen and therefore efficiently collect a large number of X-rays of different energies simultaneously. Thus obtaining a complete spectrum takes only a few minutes. Consequently acquisition of compositional maps (extension of spot analysis in one or two dimensions) can be achieved in a reasonable period of time [129].

4.3.3 X-Ray Diffractometry (XRD)

Although elemental composition provided by the EDS method is a necessary component of analysis, often it is required to know in which phase(s) the detected elements are present. As an example, although detection of Fe and O peaks in the EDS spectra of an oxidized sample proves that these elements are present it cannot distinguish which iron oxide (wustite, magnetite or hematite) has formed. To obtain such information a phase analysis technique such as XRD should be employed. This method is based on the interaction of X-rays and crystalline planes. When an X-ray beam is irradiated on the surface of matter, one of the consequences is the scattering of the beam. When the scattered X-rays interfere constructively, diffraction takes place (Figure 4.4). The relationship between the X-ray wavelength, distance between the crystalline planes of hkl index (d_{hkl}) and the incidence angle is known as the Bragg's law (equation 4.1). In this relationship n is an integer representing the order of scattering [132].

$$n\lambda = 2d_{hkl} \cdot \sin\theta \quad ; \quad 4.1$$

Equation 4.1 shows that if the X-ray beam is scanned over an angular range and an X-ray detector is employed to detect the scattered beam, a spectrum of intensity versus angle will form. In such a spectrum, for a certain crystalline matter, intensity peaks occur only at certain angles with each peak belonging to a certain group of crystalline planes (d_{hkl}). Therefore the obtained spectrum of diffracted X-rays can be used as the fingerprint for a certain crystalline compound. However, due to the large number of natural and synthetic compounds, there is possibility for overlap of the peaks. This can make phase analysis difficult if more than one crystalline compound is present in the studied sample. Therefore XRD is often coupled with an elemental analysis method such as EDS to narrow down the number of possible phases.

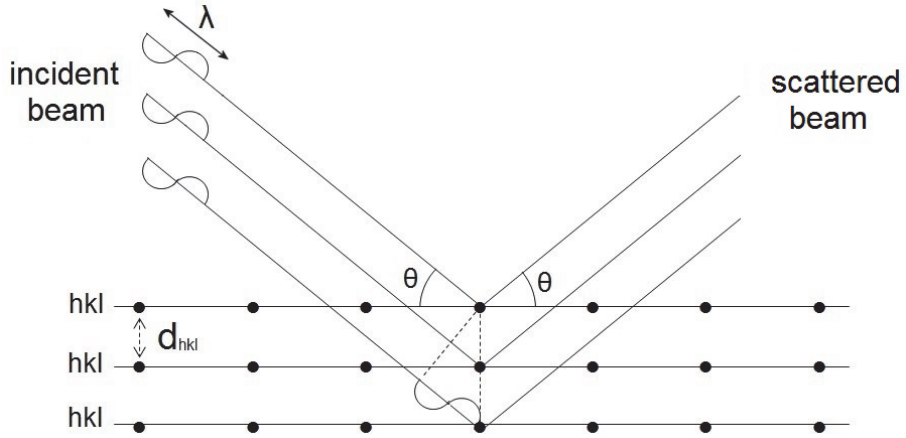

Figure 4.4: Schematic representation of the diffraction of X-ray beams in a crystalline lattice. When the values of λ, d_{hkl} and θ satisfy the Bragg's law condition, scattered X-rays interfere constructively and diffraction occurs. Figure reproduced from [133].

Figure 4.5a shows a simplified schematic of implementation of the XRD method. As can be seen the source is moved along a circular path to scan a certain angular range. Meanwhile the detector is

also rotated in a way that it mirrors the rotation of the source. This mode is usually referred to as the Bragg-Brentano configuration and is used for general phase analysis when the phase composition of the surface is the same as that of the bulk. If the phase analysis of thin films or surface compounds is desired, to avoid penetration of X-rays deep into the bulk, the source can be fixed at a very acute angle (e.g. 1^{o}) and only the detector rotates (Figure 4.5b). This mode is referred to as Grazing Incidence (GI) configuration and is especially important in corrosion science where the composition of surface compounds (e.g. oxide) can be different from the bulk.

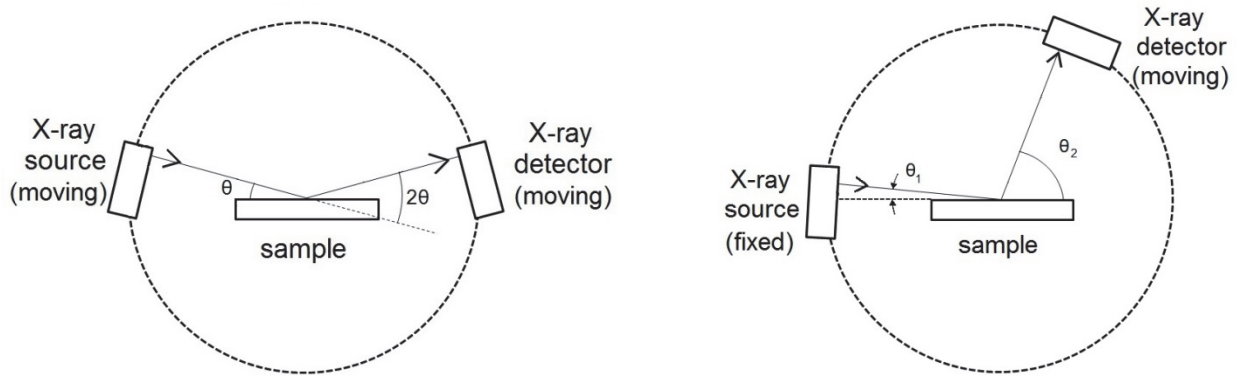

(a) (b)

Figure 4.5: (a) XRD analysis in Bragg-Brentano mode. Figure reproduced from [134] (b) XRD analysis in Grazing Incidence (GI) mode. Note that in this mode the scattering angle is $\theta=(\theta_1+\theta_2)/2$. Figure reproduced based on [134], [135].

5. Summary of the Experimental Investigations

The experimental investigations in this study were divided to three parts. Summary of the experimental procedure, results and conclusions in each part is given in the following sections.

5.1 Investigation of the Reactivity between Oxides and KCl

The choice of oxides was based on the calculations mentioned in section 3.2.1. However, molybdenum oxide was excluded from the study due to concerns about the development of volatile reaction products. In addition, Fe_2O_3 and Mn_3O_4 were added to the experimental batch as iron and manganese are abundant elements and widely employed in many industrial alloys. The rest of the studied oxides consisted of ZrO_2, TiO_2 (both rutile and anatase), Y_2O_3, SiO_2, Ta_2O_5, Cr_2O_3, HfO_2, CeO_2, Al_2O_3, NiO and Co_3O_4. Except Ta_2O_5, Mn_3O_4 and TiO_2(rutile), which had unspecified particle sizes, the rest of the oxides had particle sizes ranging from 20 to 200nm. In addition, KCl had a particle size of 63-90μm. Assuming that the condensed reaction product consists of 1 mole of K_2O and 1 mole of oxide (i.e. with the general formula $K_2O.M_2O_x$) the reaction equations were balanced and subsequently each oxide was mixed with KCl according to this stoichiometry. Mixing was done using an agate mortar. Thereafter, part of the mixture was transferred to a mold and pressed manually to produce cylindrical tablets of 17mm diameter. Subsequently the composite oxide-KCl tablets were separately exposed at 650^oC for 15h in a flowing $N_2(g)+5\%O_2(g)+15\%H_2O(g)$ atmosphere. Prior to and after the exposures samples were studied with X-Ray Diffraction (XRD) using a Bruker D8 Discover diffractometer. In addition, morphology of the exposed samples were examined with a FEI Inspect S Scanning Electron Microscope (SEM) equipped with an Energy Dispersive X-Ray Spectroscopy (EDS) detector. The results suggested that Cr_2O_3 and SiO_2 were reactive with KCl under the applied experimental condition. For Cr_2O_3 the reaction product was identified as K_2CrO_4. For SiO_2, XRD did not clarify whether a reaction has taken place. However, study of the exposed sample with SEM/EDS strongly suggested a reaction had occurred. Formation of an amorphous reaction product on SiO_2-KCl tablet was not surprising because the original SiO_2 was amorphous. For Mn_3O_4, XRD could not give an indication whether this oxide is reactive with KCl due to possible peak overlaps. However, examination of the sample with SEM/EDS suggested lack of a major reactivity. For ZrO_2, TiO_2, Y_2O_3, Ta_2O_5, Fe_2O_3, HfO_2, CeO_2, Al_2O_3, NiO and Co_3O_4 results from XRD as well as investigation with SEM/EDS indicated lack of a major reaction between these oxides and the salt under the applied experimental condition.

5.2 Investigation of the Performance of Commercial and Model Alloys

The second part of the investigations was devoted to the evaluation of the corrosion resistance of a wide range of alloys including both commercial and model alloys. This was aimed at ranking the materials as well as obtaining further insight into the corrosion mechanism(s). Choice of alloys was aimed at clarifying the effect of chromium content as well as influence of the presence of an extra oxide-forming element in the alloy. Such elements were limited to aluminum and silicon in this study. This was based on:

- results from oxide-KCl reactivity
- thermodynamic considerations in Table 3.2 showing that in presence of Cr_2O_3 , SiO_2 should not react with KCl
- solubility of the extra oxide-forming element in iron or nickel (as the basis of many high temperature alloys) and
- literature reports suggesting a beneficial effect in the addition of aluminum or silicon to the chromia-forming alloys.

The chemical composition of the studied alloys is given in Table 5.1. Pure nickel (99.99% purity) was also included in the studies for comparison. Samples were coupons (7-8 mm x 17-20 mm) cut with a precision cutter to a thickness within the range 250-340 μm. A ~1 mm thick layer of KCl powder (particle size of 63-90 μm) was applied to about 2/3 of the sample length. Samples were placed on flat alumina coupons and loaded into a multi-channel alumina sample holder with the KCl-free part of the samples towards the gas stream. The sample holder itself was placed in the even temperature zone of a horizontal furnace equipped with a silica tube. A schematic representation of the experimental set-up can be found in the previous chapter (Figure 4.1).

The samples were exposed for 168h at 600^{o}C to flowing N_2(g)+5%O_2(g)+15%H_2O(g) with a velocity of 0.25cm/s at the inlet temperature. As a reference, a salt-free exposure was carried out for all the commercial alloys. In addition to the above-mentioned exposures, two additional tests were performed for further clarification of the corrosion mechanism(s). The first test was aimed at understanding the role played by the salt vapor. For this purpose, coupons of alloys 263 and 625 as well as Sanicro 28 were placed on top of an alumina boat containing KCl powder. The surface of the salt in the boat was flattened to give a uniform distance of ~2 mm between the salt and the samples. Exposure was performed at 600^{o}C for 168h in static lab air. The second complementary test addressed the role of chlorine in high temperature corrosion due to KCl. For this test two samples of alloy Nimonic 80A were covered with either of KCl or K_2CO_3 deposits and were separately exposed at 600^{o}C for 168h in static lab air.

Samples subjected to salt-free exposure were studied with X-Ray Diffraction (XRD) using a Bruker D8 Discover diffractometer in grazing incidence (GI) mode. However, for salt-affected samples it was not possible to perform XRD. This was due to the sintering of KCl and incorporation of the corrosion products into the deposit. Consequently mechanical removal of KCl without removing some of the corrosion products proved challenging.

Table 5.1: Chemical composition of the investigated alloys. Carbon and nitrogen contents were measured with Fusion Thermal Conductivity Detection units LECO CS230 and LECO TN500 respectively. Other elements were determined with EDS. All the alloys are commercial except the last three which are model alloys. Composition of the model alloys is according to the supplier's certificate. All values are in wt% (values in parentheses are in at%). Elements without a value in the last column were present in trace amounts.

alloy	Fe	Cr	Ni	Al	Si	Mo	Co	Mn	Ti	C	N	other
TP347HFG[a]	bal.	19.1 (20.1)	10.0 (9.3)		1.0 (1.9)			1.7 (1.7)		0.057	0.019	Nb
TP347H	bal.	19.1 (20.2)	10.0 (9.4)		0.6 (1.1)			1.9 (1.9)		0.047	0.019	Nb
Sanicro 28	35.1 (35.3)	28.2 (30.5)	29.6 (28.2)		0.5 (1.1)	3.8 (2.2)		1.8 (1.8)		0.021	0.058	Cu 1.0 (0.9), Al
EN1.4021	bal.	13.9 (14.7)			0.5 (0.9)					0.192	0.022	Mn
EN1.4057	bal.	18.4 (19.4)	1.9 (1.8)		0.3 (0.6)			0.7 (0.7)		0.179	0.039	Al
EN1.4521	bal.	19.4 (20.5)			0.6 (1.2)	1.9 (1.1)		0.4 (0.4)	0.2 (0.3)	0.024	0.024	Cu,Nb
263	0.4 (0.4)	21.8 (24.2)	bal.	0.6 (1.2)	0.2 (0.4)	6.3 (3.8)	19.7 (19.3)		2.1 (2.6)	0.059	0.004	
625	4.1 (4.4)	23.4 (26.8)	bal.	0.2 (0.4)	0.3 (0.6)	9.5 (5.9)				0.033	0.044	Nb3.5 (2.2), Ti
C276	6.3 (7.1)	16.6 (20.0)	bal.	0.3 (0.6)		16.4 (10.8)	1.2 (1.3)	0.6 (0.7)		0.007	0.022	W4.1 (1.4), V
FeCrAlY	bal.	23.2 (23.2)		5.1 (9.8)						0.040	0.018	Si,Ti, Zr
Kanthal APM	bal.	23.1 (22.9)		5.7 (10.9)	0.6 (1.1)					0.032	0.017	Ti,Zr
Nimonic 80A	0.8 (0.8)	20.7 (22.2)	bal.	1.4 (2.9)	0.4 (0.8)				2.3 (2.7)	0.070	0.014	
214	3.6 (3.5)	17.2 (18.0)	bal.	4.8 (9.7)						0.038	0.002	Zr
HR160	0.3 (0.3)	29.3 (30.8)	bal.		3.3 (6.5)	0.2 (0.1)	29.2 (27.1)		0.4 (0.5)	0.052	0.007	Al
153MA	bal.	20.4 (21.3)	10.0 (9.2)		1.6 (3.1)					0.048	0.15	Ce,La,Ti, Mn
Fe14Cr3Si[b]	bal.	14.1 (14.5)			3.1 (6.0)					0.008	0.007	Ni
Fe19Cr3Si2Ni[b]	bal.	19.0 (19.5)	2.0 (1.8)		3.1 (5.8)					0.007	0.009	
Ni45Cr4Nb[c]		44.80 (48.4)	bal.		(0.1)				0.5 (0.6)	0.013	0.001	Nb4.06 (2.45) Si

[a] Fine-grain TP347H
[b] Cast alloys (exposed in as-cast condition)
[c] Powder metallurgical alloy

After the exposures, samples were mounted in epoxy resin in an upright position without removing the salt layer. Subsequently their cross sections were prepared with grinding/polishing using water as lubricant for the samples of the salt-free test and ethanol for the salt-affected samples. The decrease in metal thickness for the salt-affected samples was measured in a Reflective Light Microscope (RLM) equipped with a travelling stage. Twenty measurements were undertaken

at intervals of 0.5 mm and average and standard deviation were calculated for each sample. Thereafter the surface was re-scanned to find the location with the deepest penetrating damage. Average and worst case values less than 5µm were considered insignificant with respect to the accuracy achieved with pre-exposure micrometer measurements of the sample thickness. For pure nickel, as boundaries of the oxide were well defined, SEM images were used to obtain the thickness loss. Finally, morphology of the corrosion products was studied with an FEI Inspect S Scanning Electron Microscope (SEM) equipped with an Energy Dispersive X-Ray Spectroscopy (EDS) detector.

It was observed that stainless steels TP347H, EN1.4521 and 153MA formed fast-growing oxides even without the KCl. The rest of the alloys showed a passive behavior in the salt-free exposure. Apparently the original protective oxide on TP347H, EN1.4521 and 153MA breaks down within 168h of exposure in N_2(g)+5%O_2(g)+15H_2O. Despite the satisfactory performance of the majority of alloys in the salt-free exposure, they all suffered from significant attack when KCl was present. Figure 5.1 shows the extent of attack on all the investigated alloys. As can be seen compared to TP347HFG, which is the current state of the art material, stainless steels EN1.4057 and Sanicro 28 as well as nickel-base alloys 625 and HR160 showed indications of a better performance. Surprisingly pure nickel was damaged least of all.

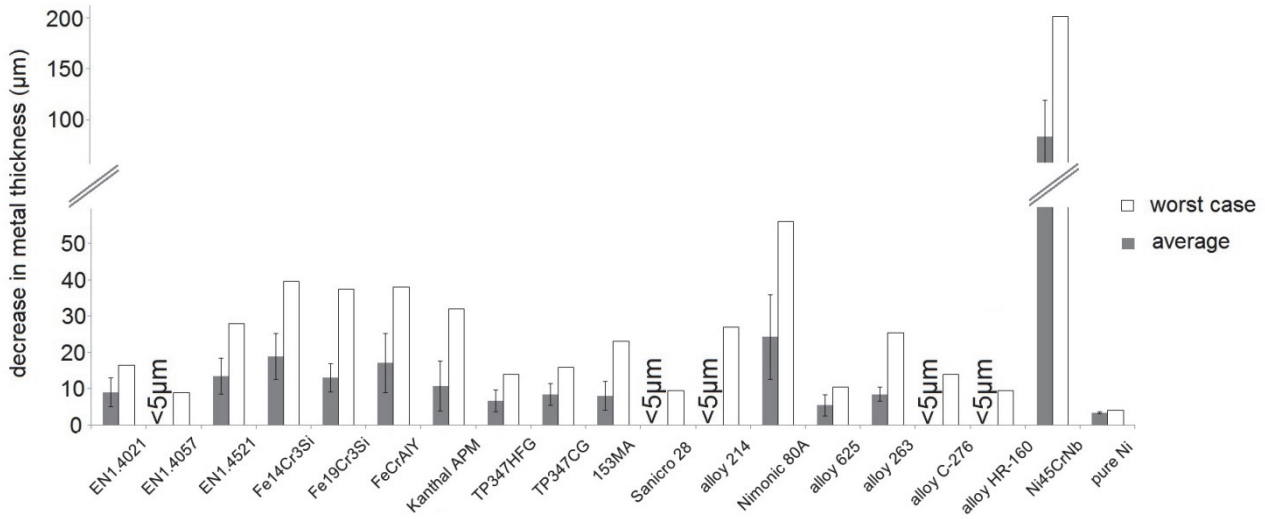

Figure 5.1: Extent of corrosion observed on all the alloys (and pure nickel) exposed at 600°C for 168h in N_2(g)+5%O_2(g)+15%H_2O(g) under a KCl deposit.

It was observed that among the commercial stainless steels a general improvement with increase in the chromium content of the alloy took place. This improved performance was for the investigated range of 14-19 at% chromium for ferritic stainless steels and 19-28 at% for the austenitic grades. The only exception was EN1.4521 which showed a poor performance compared to the alloys with similar (and even lower) chromium contents. Poor performance of this alloy was attributed to the formation of a molybdenum-rich phase along the grain boundaries and within the grains of this alloy. It is suspected that presence of such phase decreases the chromium diffusion flux through the grain boundaries. No trend could be seen regarding the dependence of corrosion

extent on chromium content of the commercial nickel-base alloys. However, it was found that under the applied experimental condition pure nickel performed better than all of its chromium containing alloys.

The presence of aluminum in FeCrAlY and Kanthal APM did not lead to the formation of a protective oxide as internal oxidation/nitridation took place on these alloys. In addition, the nickel-base alumina-forming alloys 214 and Nimonic 80A showed selective corrosion. For these alloys chromium, and aluminum (and titanium in case of Nimonic80A) were selectively removed from the alloy and formed thick non-protective oxides outside of the alloy. The attack on Nimonic 80A was more extensive compared to alloy 214.

Presence of 3.1 at.% silicon in alloy 153 did not lead to a significant difference in corrosion performance of this alloy compared to the low-silicon austenitic stainless steels of similar chromium and nickel contents. On the ferritic model alloys Fe14Cr3Si and Fe19Cr3Si2Ni presence of up to 6 at.% silicon did not lead to the formation of a protective silica layer. Potassium could be found along with the silicon in the inner oxide and internal oxidation/nitridation took place under the inner oxide. However, it is still unclear whether this is due to the lack of enough diffusivity of silicon in the alloys or the presence of a chromium-rich phase, suspected to be chromium carbide, along the grain boundaries of the two alloys. On alloy HR160 a chromium-silicon-potassium-oxygen compound (or mixture of compounds) could be detected as the inner corrosion product. This compound seems to retard the corrosion as this alloy showed a relatively small corrosion extent and no internal oxidation/nitridation of silicon was observed. However, it requires further investigation to clarify whether this effect is due to higher chromium content of the alloy or it originates in the presence of silicon.

Nickel-base alloys with chromium-rich phases (Nimonic 80A, 214 and Ni45Cr4Nb) were especially susceptible to the selective corrosion attack. This type of attack led to the formation of deep porous nickel-rich regions in the alloy. On the rest of the alloys selective corrosion was less pronounced. In addition, comparison between the effects of KCl and K_2CO_3 on Nimonic 80A showed that both potassium and chlorine can play a role in the alkali-chloride induced high temperature corrosion. While for K_2CO_3-induced attack inner and outer corrosion products could be observed, for KCl-induced attack only outer corrosion products could be detected. In the former case nickel had left the alloy and chromium was enriched close to the surface while in the latter case chromium had left the alloy and nickel was enriched close to the surface. This shows that although potassium can damage the chromium-rich protective oxides and initiate the attack, presence of chlorine is necessary to incur the selective corrosion. Hence formation of deep porous nickel-rich areas was attributed to the selective removal of alloying elements due to the chlorine.

Exposure of alloys (Sanicro 28, 263 and 625) to potassium chloride vapor revealed that even a small amount of salt vapor is highly corrosive towards alloys at a temperature of 600^{o}C as none of this high chromium alloys showed the formation of a slow growing oxide. This has implications for corrosion continuation when the solid salt in direct contact with the sample is consumed or the distance between the unreacted KCl and the metal surface is large due to the formation of

voluminous and porous corrosion products. On Sanicro 28 deep grain boundary attack in form of selective corrosion was observed. The extent of attack was at least one order of magnitude larger than the attack in flowing N_2(g)+5%O_2(g)+15%H_2O(g). This shows the importance of the gas phase composition and dynamics in high temperature corrosion induced by KCl.

5.3 Investigation of the Performance of Coatings

Among the suitable oxide-forming elements identified in section 5.1, Al is the most abundant option. However, the results in section 5.2 suggested that high concentrations (at least more than 10.9 at.%) of this element are required to show a (possible) beneficial effect. Therefore the influence of enrichment of this element in the surface of selected substrates was investigated. Low temperature Pack Cementation was employed for this purpose. In this process the substrate alloy is embedded in a powder pack consisting of the metal source (e.g. aluminum), an inactive filler material (e.g. alumina) and a halide activator (e.g. ammonium chloride or aluminum chloride). Heating the mixture up to a sufficiently high temperature in an inert atmosphere (e.g. argon) activates the surface and initiates deposition. The halogen forms volatile metal chlorides that decompose at the sample surface leaving behind a metallic deposit. Reactive diffusion of the deposited metal atoms and compounds in the alloy leads to the formation of the intermetallic phases [18], [136]. Parameters of the performed process are shown in Table 5.2. Pure nickel (99.99 wt%) and ferritic-martensitic stainless steel P91 (Fe-9Cr-1Mo-0.5Si-0.2V wt%) were chosen as the substrate materials to be aluminized.

Table 5.2: Parameters of the pack cementation process

pack component (wt%)	specification	phase to be formed		
		$Fe_{1-x}Al$	Fe_2Al_5	Ni_2Al_3
Al	99.9%purity, max 60µm	10	10	10
Fe		10	0	0
$AlCl_3$	anhydrous	6	6	6
Al_2O_3		74	84	84
Duration (h)		20	6	8

After the coating, samples were separated from the residues and cleaned in an ultrasonic bath of ethanol. Subsequently one sample of each aluminide phase was partly (2/3 of length) covered with a ~1mm thick layer of KCl powder (particle size 63-90µm) and was exposed for 168h at 600°C in static lab air. A salt-free exposure was also performed for comparison. The as-coated and exposed samples were investigated with XRD to determine their phase composition. For this purpose a Bruker D8 Discover X-Ray diffractometer was used and the analysis for each sample was performed under both grazing-incidence and Bragg-Brentano configurations. Thereafter cross sections of the samples were prepared by embedding them in epoxy resin and grinding/polishing using ethanol as lubricant. The microstructure of the samples was studied using an Inspect S SEM equipped with an EDS detector. XRD confirmed that the coatings produced consisted of $Fe_{1-x}Al$ on P91, Fe_2Al_5 on P91 and Ni_2Al_3 on pure Ni. In addition, SEM/EDS investigations revealed the presence of a Cr-rich phase within the Fe_2Al_5 coated P91as well as a Cr and Si rich phase close to

the surface of this coating. This latter phase was identified as Cr_3Si according to XRD. The as-coated Fe_2Al_5 often showed presence of deep cracks extending all the way through the coating. However, the other two coatings did not show such defect.

The salt-free exposure did not result in the formation of a fast-growing oxide on any of the samples. The interdiffusion between the coating and the substrate was the only apparent effect. However, Fe_2Al_5 on P91 was extensively attacked when KCl was present. The dominant corrosion morphology was selective removal of Al from the coating resulting in the enrichment of Fe and Cr. Thick and highly porous Al-rich oxide was observed on top of the coating. XRD identified this thick oxide as (corundum) Al_2O_3. $Fe_{1-x}Al$ on P91 showed a passive behavior on large parts of the surface. Only few cases of localized attack were observed for this coating. SEM/EDS investigation on the location of a well-developed localized attack revealed the presence of a double layer oxide rich in Fe on the outer parts and Cr in the inner parts. XRD confirmed the presence of Fe_2O_3. Ni_2Al_3 on pure Ni did not show any sign of attack anywhere on the sample.

6. Conclusions

Following conclusions can be drawn based on the investigations performed in this study:

1- Reactivity of a number of oxides with KCl was studied at 650°C in flowing N_2(g)+5%O_2(g)+15%H_2O(g) gas atmosphere. Exposure duration was 15h and the investigated oxides consisted of SiO_2, Cr_2O_3, ZrO_2, TiO_2 (both rutile and anatase), Y_2O_3, Ta_2O_5, Fe_2O_3, HfO_2, CeO_2, Al_2O_3, NiO, Mn_3O_4 and Co_3O_4. It was observed that Cr_2O_3 and SiO_2 are reactive with KCl. For Cr_2O_3 the reaction product is K_2CrO_4. For SiO_2 the exact stoichiometry of the product cannot be determined with XRD due to the amorphous nature of the silicate formed. For Mn_3O_4, XRD cannot give an indication whether this oxide is reactive with KCl due to peak overlap. However observation of the sample under SEM suggests lack of a major reactivity. For ZrO_2, TiO_2, Y_2O_3, Ta_2O_5, Fe_2O_3, HfO_2, CeO_2, Al_2O_3, NiO and Co_3O_4 results from XRD as well as observation under SEM suggest lack of a major reaction between these oxides and the salt.

2- A wide range of commercial chromia-forming alloys along with selected alumina and silica-forming alloys were exposed at 600°C for 168h with and without a KCl deposit. The exposure atmosphere was flowing N_2(g)+5%O_2(g)+15%H_2O(g). This was aimed at ranking the materials as well as obtaining further knowledge about the reaction mechanism(s). The investigated alloys consisted of stainless steels (TP347HFG, TP347H, Sanicro28, 153MA, EN1.4021, EN1.4057, EN1.4521, FeCrAlY and Kanthal APM) and Ni-base alloys (263, 625, C276, 214, Nimonic 80A and HR160).

3- Among the investigated alloys only stainless steels TP347H, EN1.4521 and 153MA developed fast-growing oxides in the salt-free exposure. The original chromium-rich oxide on these alloys breaks down within 168h in N_2(g)+5%O_2(g)+15%H_2O(g) at 600°C. In addition, it is indicated that the presence of a molybdenum-rich phase along the grain boundaries (observed in stainless steel EN1.4521) is detrimental for the oxidation resistance. Although majority of the alloys showed a passive behavior in the salt-free exposure, when KCl was present none of them could form a slow growing protective oxide and they were all damaged. However the extent of this damage was different on different alloys.

4- Two distinct corrosion morphologies could often be observed on the alloys attacked by KCl. An outer highly porous morphology referred to as type A oxide and an inner denser morphology referred to as type B oxide. On Ni-base alloys pitting and selective corrosion were sometimes observed.

5- Compared to the currently widely used austenitic stainless steel TP347HFG, the following materials indicated slightly less corrosion damage: EN1.4057, Sanicro 28, alloy 625 and alloy HR160.

6- On iron-base alloys, generally an improved corrosion performance was observed for a higher chromium content. This improved performance was for the investigated range of 14-19 at% chromium for ferritic stainless steels and 19-28 at% for the austenitic grades. For the nickel-based alloys no clear trend was observed.

7- The presence of aluminum did not lead to the formation of a protective alumina layer on any of the investigated alumina-forming alloys (FeCrAlY, Kanthal APM, Nimonic80A and alloy 214). Based on a worst case criterion, under the applied experimental conditions, none of the alumina-forming alloys showed less damage than the currently widely used material TP347HFG.
8- The failure of aluminum to form a protective oxide on the iron-chromium and nickel-chromium alloys under the investigated conditions is believed to be a result of a) aluminum chlorination and subsequent formation of alumina from oxidation of its chloride (alumina in type A oxide) and b) internal oxidation of aluminum (alumina under the type B oxide).
9- The presence of 3.1 at% (1.6wt.%) silicon in the austenitic stainless steel 153MA did not lead to a significant difference in performance compared to the low-silicon austenitic stainless steels of similar chromium and nickel contents.
10- On the Ni-base silica-former (alloy HR160) a compound (or mixture of compounds) containing potassium-chromium-silicon-oxygen was formed as the inner corrosion product which seems to have a barrier effect against the continuation of corrosion.
11- Exposure of alloys 263, 625 and Sanicro28 to KCl vapor at 600^{o}C in static lab air revealed that the generated vapor pressure of KCl(g) is enough to breakdown the initial chromium-rich oxide on the alloys that rely on chromia for protection. In addition, even with the small concentration of chlorine-bearing species a remarkable effect from chlorine could be observed. The observed role of KCl(g) has implications for corrosion continuation when the solid KCl in direct contact with the metal is consumed.
12- Sanicro 28 exposed to KCl(g) in static lab air had much deeper attack than when it was exposed under solid KCl in flowing N_2(g)+5%O_2(g)+15%H_2O(g). This shows that gas phase composition and dynamics play a significant role in the extent of damage due to KCl-induced high temperature corrosion.
13- Exposure of Nimonic 80A to either KCl or K_2CO_3 (600^{o}C, static lab air) showed that both K and Cl can play a role in KCl-induced corrosion. The K_2CO_3-affected sample suffered from the breakdown of the original chromium-rich protective oxide and showed double layer corrosion morphology with Ni-enrichment out of the alloy and Cr-enrichment inside the alloy. The KCl affected sample could not form a protective oxide either. However, morphology of the corrosion product was the opposite of what was observed for the K_2CO_3-affected sample; Cr was enriched out of the alloy and Ni was enriched inside the alloy forming a porous Ni-rich zone all over the surface. This shows that although the protective oxide breaks due to the potassium effect, selective removal of the alloying elements is caused by the chlorine.
14- The presence of up to 6 at.% (3wt.%) silicon in ferritic stainless steels did not lead to the formation of a protective silica layer for the investigated model alloys exposed to N_2(g)+5%O_2(g)+15%H_2O(g) under a KCl deposit. Potassium could be found together with silicon in the inner oxide and internal oxidation/nitridation took place.
15- Ni-45Cr-4Nb (wt.%) model alloy showed the worst performance among all the investigated alloys exposed to N_2(g)+5%O_2(g)+15%H_2O(g) under a KCl deposit. This is attributed to the presence of a large fraction of chromium-rich phase (α-Cr) in the microstructure. Substantial

selective removal of chromium took place which was attributed to the volatilization of chromium in form of chromium chloride(s).

16- On pure nickel, exposed to $N_2(g)+5\%O_2(g)+15\%H_2O(g)$ under a KCl deposit, the presence of KCl only led to a slight increase in the oxide porosity. However, the change in the extent of oxidation was insignificant. In fact, pure nickel showed a better performance compared to all of the investigated alloys. This was attributed to the lack of reactivity between nickel oxide and KCl as well as small thermodynamic driving force for any electrochemical interaction between the salt and pure nickel.

17- A hypothetical model was proposed to account for the selective corrosion induced by chlorine and alkali chlorides. This model attributes the selective corrosion to the formation of oxidation-induced subsurface voids. It was suggested that formation of volatile metal chlorides at the metal/oxide interface leads to the gas phase transport across such voids and accelerates the selective removal of more reactive elements from the alloy.

18- Pack cementation process was employed to produce $Fe_{1-x}Al$ and Fe_2Al_5 phases on the ferritic-martensitic stainless steel P91 and Ni_2Al_3 on pure Ni. The samples were exposed at 600^{o}C for 168h in static lab air with and without a KCl deposit. These coatings showed excellent performance against air-oxidation at 600^{o}C when KCl was absent.

19- $Fe_{1-x}Al$ coated on P91 formed a passivating layer on large parts of the surface when exposed to KCl. Local failures were observed on this coating which were always associated with depletion/dilution of aluminum. Double layer corrosion morphology was found on the location of local attack on the sample. The location of attack showed an outer Fe-rich part and an inner Cr-rich part.

20- Fe_2Al_5 coated on P91 was attacked all over the surface when KCl was present. The attack was generally in form of selective aluminum removal. On large parts of the surface the attack does not seem to have continued upon the formation of $Fe_{1-x}Al$. In a few cases, the coating was completely consumed and voluminous corrosion products had formed.

21- Ni_2Al_3 coated on pure Ni formed a passivating layer all over the surface when exposed to KCl. No sign of attack could be detected on this coating.

7. Outlook

During the course of literature survey and experimental investigations the following items appeared to be interesting topics worth of further investigations:

1- Study of the reactivity between oxides and KCl based on the analysis of the off-gas by an accurate instrument such as mass-spectrometer. Unlike XRD which cannot detect amorphous/minor phases or Thermogravimetry which can be inaccurate when several evaporating species are evolved, detection of HCl(g) in the off-gas pinpoints that a reaction between the oxide and KCl has taken place.
2- Application of Ti, Y, Ce, Ta, Hf and Zr as diffusion coatings on pure Ni. Study of the reactivity between oxides and KCl suggests that oxides of these elements do not significantly react with KCl.
3- Systematic investigation of the influence of presence of SO_2(g), HCl(g) and CO_2(g) on the KCl-induced high temperature corrosion. For SO_2(g) the effect of gas stream direction (parallel or perpendicular to the surface) is especially interesting as it will clarify the contribution of evolved chlorine due to sulfation.
4- Influence of deposit removal and re-coating on the corrosion morphology and extent.
5- Investigation of the performance of alloys EN1.4057, Sanicro28, 625, HR160 as well as pure Ni in a real boiler and comparison of the behavior of these alloys compared to TP347HFG. This is especially important since the effect of temperature gradient between the gas and metal, thermal cycling as well as CO_2 and minor contaminants in the flue gas (HCl and SO_2) were not addressed in this study.
6- Investigation of the performance of Al diffusion coatings especially Ni_2Al_3 on Ni-base alloys in a real boiler application.
7- Influence of solutionizing heat treatment on the performance of Nimonic 80A and alloy 214.
8- Investigation of performance of TiN in chlorinating atmospheres as this phase appeared to be unaffected in the selective corrosion region observed on Nimonic 80A.
9- Effect of surface quality (coarse ground vs well-polished surface) on the performance of materials under oxidizing-chlorinating conditions.
10- Influence of higher Si content on the performance of alloy 153MA. In addition comparison between the performance of alloy HR160 with a Si-free Ni-base alloy of similar Cr content will reveal if the relatively low damage observed on this alloy is due to Si or not.
11- Effect of presence of carbide-stabilizing elements such as Nb in the Si-containing model alloys to see if the poor performance of these alloys is due to low diffusivity of Si at 600^{o}C in the alloys or it is a result of sensitization. In addition, the influence of grain size on the performance of such a carbide-stabilized silica-former would be interesting.
12- Investigating the performance of Cr-free Fe_2Al_5 to see if the catastrophic attack on this compound is a result of a Cr-rich phase in the alloy. In addition, it would be interesting to intentionally dope Ni_2Al_3 with Cr to see if any attack would follow.

8. References

[1] M. Montgomery, S. A. Jensen, U. Borg, O. Biede, and T. Vilhelmsen, "Experiences with high temperature corrosion at straw-firing power plants in Denmark," *Mater. Corros.*, vol. 62, no. 7, pp. 593–605, Jul. 2011.

[2] F. J. Frandsen, "Ash Formation, Deposition and Corrosion When Utilizing Straw for Heat and Power Production," Technical University of Denmark, 2011.

[3] H. P. Michelsen, F. Frandsen, K. Dam-Johansen, and O. H. Larsen, "Deposition and high temperature corrosion in a 10 MW straw fired boiler," *Fuel Process. Technol.*, vol. 54, no. 1–3, pp. 95–108, Mar. 1998.

[4] M. Montgomery and E. Maahn, "High Temperature Corrosion of Stainless Steel under Fly-ash Deposits, Supplementary Experiments for EFP 94 , J. Nr. 1323/94-0006," 1994.

[5] S. C. Cha and M. Spiegel, "Local reactions of KCl particles with iron, nickel and chromium surfaces," *Mater. Corros.*, vol. 57, no. 2, pp. 159–164, Feb. 2006.

[6] S. Cha and M. Spiegel, "Fundamental studies on alkali chloride induced corrosion during combustion of biomass," *Mater. Sci. Forum*, vol. 461–464, pp. 1055–1062, 2004.

[7] Y. Li and M. Spiegel, "Internal Oxidation of Fe – Al Alloys in a KCl-Air Atmosphere at 650 ◦ C," *Oxid. Met.*, vol. 61, no. April, pp. 303–322, 2004.

[8] Y. S. Li, M. Sanchez-Pasten, and M. Spiegel, "High Temperature Interaction of Pure Cr with KCl," *Mater. Sci. Forum*, vol. 461–464, pp. 1047–1054, 2004.

[9] B. Sander, "Properties of Danish biofuels and the requirements for power production," *Biomass and Bioenergy*, vol. 12, no. 3, pp. 177–183, 1997.

[10] H. P. Nielsen, F. J. Frandsen, and K. Dam-Johansen, "Lab-Scale Investigations of High-Temperature Corrosion Phenomena in Straw-Fired Boilers," *Energy & Fuels*, vol. 13, no. 6, pp. 1114–1121, Nov. 1999.

[11] K. Gotthjælp, P. Brøndsted, P. Jansen, M. Montgomery, K. Nielsen, and E. Maahn, "High Temperature Corrosion of Superheater Materials For Power Production Through Biomass, EFP 94 Final Report J. Nr. 1323/94-0006, ISBN 87-550-2205-7," 1994.

[12] J. Andersson, T. Helander, and L. Höglund, "Thermo-Calc & DICTRA, computational tools for materials science," *Calphad*, vol. 26, no. 2, pp. 273–312, 2002.

[13] "HSC Chemistry 7.00, www.hsc-chemistry.com." .

[14] "FactSage 6.2, www.factsage.com." .

[15] H. Nielsen, F. Frandsen, K. Dam-Johansen, and L. Baxter, “The implications of chlorine-associated corrosion on the operation of biomass-fired boilers,” *Prog. Energy Combust. Sci.*, vol. 26, no. 3, pp. 283–298, 2000.

[16] P. Elliott, C. Tyreman, and R. Prescott, “High temperature alloy corrosion by halogens,” *JOM*, no. July, pp. 20–23, 1985.

[17] H. Latreche, S. Doublet, and M. Schütze, “Development of Corrosion Assessment Diagrams for High Temperature Chlorine Corrosion. Part I: State of the Art and Development of the Basis for a New Extended Approach,” *Oxid. Met.*, vol. 72, no. 1–2, pp. 1–30, Mar. 2009.

[18] B. Rammer, T. Weber, and M. Schütze, “Development of Diffusion Coatings on Nickel-base Alloys For The Use In Chlorine-Containg High Temperature Processes,” *Mater. Corros.*, vol. 39, no. 1, pp. 29–32, Jan. 2008.

[19] M. McNallan, “High-temperature corrosion in halogen environments,” *Mater. Perform.*, pp. 54–57, 1994.

[20] Y. Ihara, H. Ohgame, K. Sakiyama, and K. Hashimoto, “The corrosion behaviour of nickel in hydrogen chloride gas and gas mixtures of hydrogen chloride and oxygen at high temperatures,” *Corros. Sci.*, vol. 22, no. 10, pp. 901–912, Jan. 1982.

[21] Y. Ihara, H. Ohgame, K. Sakiyama, and K. Hashimoto, “The corrosion behaviour of chromium in hydrogen chloride gas and gas mixtures of hydrogen chloride and oxygen at high temperatures,” *Corros. Sci.*, vol. 23, no. 2, pp. 167–181, Jan. 1983.

[22] C. S. Tedmon, “The Effect of Oxide Volatilization on the Oxidation Kinetics of Cr and Fe-Cr Alloys,” *J. Electrochem. Soc.*, vol. 113, no. 8, p. 766, 1966.

[23] Y. Ihara, H. Ohgame, K. Sakiyama, and K. Hashimoto, “The corrosion behaviour of iron in hydrogen chloride gas and gas mixtures of hydrogen chloride and oxygen at high temperatures,” *Corros. Sci.*, vol. 21, no. 12, pp. 805–817, 1981.

[24] M. J. McNallan, W. W. Liang, S. H. Kim, and C. T. Kang, “Acceleration of the High Temperature Oxidation of Metals by Chlorine,” in *High Temperature Corrosion, NACE*, 1983, pp. 316–321.

[25] H. Grabke, E. Reese, and M. Spiegel, “The effects of chlorides, hydrogen chloride, and sulfur dioxide in the oxidation of steels below deposits,” *Corros. Sci.*, vol. 37, no. 7, pp. 1023–1043, 1995.

[26] G. Han and W. Cho, “High-Temperature Corrosion of Fe3Al in 1% Cl2/Ar,” *Oxid. Met.*, vol. 58, no. October, pp. 3–10, 2002.

[27] J. Smeggil and N. Bornstein, “The Effect of NaCl (g) on the Oxidation of NiAl,” *J. Electrochem. Soc.*, vol. 125, no. 8, pp. 1283–1290, 1978.

[28] N. Folkeson, L.-G. Johansson, and J.-E. Svensson, “Initial Stages of the HCl-Induced High-Temperature Corrosion of Alloy 310,” *J. Electrochem. Soc.*, vol. 154, no. 9, p. C515, 2007.

[29] J. Oh, M. McNallan, G. Lai, and M. Rothman, “High temperature corrosion of superalloys in an environment containing both oxygen and chlorine,” *Metall. Mater. ...*, vol. 17, no. 600, pp. 1087–1094, 1986.

[30] A. Zahs, M. Spiegel, and H. J. Grabke, “Chloridation and oxidation of iron, chromium, nickel and their alloys in chloridizing and oxidizing atmospheres at 400 - 700C,” *Corros. Sci.*, vol. 42, pp. 1093–1122, 2000.

[31] J. M. Abels and H. H. Strehblow, “A surface analytical approach to the high temperature chlorination behaviour of Inconel 600 at 700 C,” *Corros. Sci.*, vol. 39, no. 1, pp. 115–132, 1997.

[32] T. Jonsson, N. Folkeson, M. Halvarsson, J.-E. Svensson, and L.-G. Johansson, “Microstructural Investigation of the HCl-Induced Corrosion of the Austenitic Alloy 310S (52Fe26Cr19Ni) at 500 °C,” *Oxid. Met.*, vol. 81, no. 5–6, pp. 575–596, Jan. 2014.

[33] M. J. Mcnallan, Y. Y. Lee, Y. W. Chang, N. S. Jacobson, and J. Doychak, “Oxidation-Chlorination of Binary Ni-Cr alloys in Flowing Ar-O2-Cl2 Gas Mixtures at 1200K,” *J. Electrochem. Soc.*, vol. 138, no. 12, pp. 3692–3696, 1991.

[34] K. N. Strafford, P. K. Datta, and G. Forster, “The high temperature chloridation of iron, nickel and some iron-nickel model alloys,” *Corros. Sci.*, vol. 29, no. 6, pp. 703–716, Jan. 1989.

[35] F. Stott, R. Prescott, and P. Elliott, “Corrosion resistance of high temperature alloys in gas containing hydrogen chloride,” *Mater. Sci. ...*, vol. 6, pp. 364–370, 1990.

[36] R. Bender and M. Schutze, “The role of alloying elements in commercial alloys for corrosion resistance in oxidizing-chloridizing atmospheres. Part I: Literature evaluation and thermodynamic calculations,” *Mater. Corros.*, vol. 54, no. 8, pp. 567–586, 2003.

[37] W. D. Cho and G. Han, “High-Temperature Corrosion of Y-Doped Fe3Al in Environments Containing Chlorine and Oxygen,” *J. Mater. Eng. Perform.*, vol. 15, no. 5, pp. 558–563, Oct. 2006.

[38] C. Schwalm and M. Schütze, “The corrosion behavior of several heat resistant materials in air+ 2 vol % Cl2 at 300 to 800° C. Part I–Fe base and Fe containing alloys,” *Mater. Corros.*, vol. 49, pp. 34–49, 2000.

[39] M. McNallan, W. Liang, J. Oh, and C. Kang, “Morphology of corrosion products formed on cobalt and nickel in argon-oxygen-chlorine mixtures at 1000 K,” *Oxid. Met.*, vol. 17, no. 5, pp. 371–389, 1982.

[40] R. Prescott and F. Stott, “The degradation of metals in a hydrogen chloride-containing gas at high temperature,” *Corros. Sci.*, vol. 29, no. 4, pp. 465–469, 1989.

[41] M. Maloney and M. McNallan, “The effect of chlorine on the kinetics of oxidation of cobalt in environments containing 0.5 atmosphere of oxygen between 900 K and 1200 K,” *Metall. Mater. Trans. B*, vol. 16, no. December, pp. 751–761, 1985.

[42] Y. Lee and M. McNallan, “Ignition of nickel in environments containing oxygen and chlorine,” *Metall. Trans. A*, vol. 18, no. June, pp. 1099–1107, 1987.

[43] K. Reinhold, “High Temperature Corrosion of Chromium and Chromium (III) Oxide in Chlorine and Chlorine-Oxygen Mixtures,” *J. Electrochem. Soc.*, vol. 124, no. 6, pp. 875–883, 1977.

[44] M. Hossain and S. Saunders, “A microstructural study of the influence of NaCl vapor on the oxidation of a Ni-Cr-Al alloy at 850° C,” *Oxid. Met.*, vol. 12, no. i, pp. 1–22, 1978.

[45] M. J. McNallan, W. W. Liang, S. H. Kim, and C. T. Kang, “Acceleration of the High Temperature Oxidation of Metals by Chlorine,” in *High Temperature Corrosion, NACE*, 1983, pp. 316–321.

[46] N. Folkeson, T. Jonsson, M. Halvarsson, L.-G. Johansson, and J.-E. Svensson, “The influence of small amounts of KCl(s) on the high temperature corrosion of a Fe-2.25Cr-1Mo steel at 400 and 500°C,” *Mater. Corros.*, vol. 62, no. 7, pp. 606–615, Jul. 2011.

[47] F. Stott, R. Prescott, P. Elliott, and M. Al’Atia, “Assessment of the Degradation of Metals and Alloys in Air-2% Chlorine at High Temperature,” *High Temp. Technol.*, vol. 6, no. 3, pp. 115–129, 1988.

[48] Y. Li and R. Rapp, “Internal chloridation of dilute Ni-Cr alloys,” *Metall. Mater. Trans. B*, vol. 14, no. September, pp. 509–510, 1983.

[49] P. Viklund and R. Pettersson, “HCl-Induced High Temperature Corrosion of Stainless Steels in Thermal Cycling Conditions and the Effect of Preoxidation,” *Oxid. Met.*, vol. 76, no. 1–2, pp. 111–126, Dec. 2010.

[50] F. Stott and C. Shih, “High-Temperature Corrosion of Iron–Chromium Alloys in Oxidizing–Chloridizing Conditions,” *Oxid. Met.*, vol. 54, pp. 425–443, 2000.

[51] A. Kim and M. McNallan, “Mixed Oxidation of Iron-Chromium Alloys in Gases Containing Oxygen and Chlorine at 900 to 1200° K,” *Corrosion*, vol. 46, no. 9, pp. 746–755, 1990.

[52] P. Elliott and A. Ansari, “Behaviour of Selected Commercial Alloys During High Temperature Oxychlorination,” *Corros. Sci.*, vol. 44, no. 8, pp. 544–554, 1988.

[53] M. Rhee, M. McNallan, and M. Forthman, “Long term high temperature corrosion studies of high temperature alloys in chlorine contaminated environments,” *J. Mater. energy*, vol. 7, no. 4, pp. 294–301, 1986.

[54] H. Latreche, S. Doublet, and M. Schütze, “Development of Corrosion Assessment Diagrams for High Temperature Chlorine Corrosion Part II: Development of ‘Dynamic’ Quasi-stability Diagrams,” *Oxid. Met.*, vol. 72, no. 1–2, pp. 31–65, Mar. 2009.

[55] R. Bender and M. Schütze, “The role of alloying elements in commercial alloys for corrosion resistance in oxidizing-chloridizing atmospheres. Part II: Experimental investigations,” *Mater. Corros.*, vol. 54, no. 9, pp. 652–686, 2003.

[56] C. Schwalm and M. Schütze, “The corrosion behavior of several heat resistant materials in air+ 2% Cl2 at 300 to 800° C. Part 3–Alumina formers and intermetallics,” *Mater. Corros.*, vol. 172, pp. 161–172, 2000.

[57] X. Zheng and R. Rapp, “Chloridation-oxidation of nine commercial high-temperature alloys at 800 C,” *Oxid. Met.*, vol. 48, no. 5–6, pp. 553–596, Dec. 1997.

[58] A. Zahs, M. Spiegel, and H. Grabke, “The influence of alloying elements on the chlorine-induced high temperature corrosion of Fe-Cr alloys in oxidizing atmospheres,” *Mater. Corros.*, vol. 50, pp. 561–578, 1999.

[59] C. Schwalm and M. Schütze, “The corrosion behavior of several heat resistant materials in air + 2 % Cl 2 at 300 to 800 8C Part 2 - Nickel base alloys,” *Mater. Corros.*, vol. 51, pp. 73–79, 2000.

[60] H. Latreche, S. Doublet, G. Tegeder, G. Wolf, P. Masset, T. Weber, and M. Schütze, “Behaviour of NiAl APS coatings in chlorine containing atmospheres,” *Mater. Corros.*, vol. 59, no. 7, pp. 573–583, Jul. 2008.

[61] H. Latreche, G. Tegeder, G. Wolf, P. Masset, T. Weber, and M. Schütze, “New Approaches to Improve High Temperature Corrosion Resistance in Chlorine-Based Atmospheres,” *Mater. Sci. Forum*, vol. 595–598, pp. 307–321, 2008.

[62] M. C. Galetz, B. Rammer, and M. Schütze, “The Protection of Aluminides by Alloying with Molybdenum in High Chlorine Containing Atmospheres at 1,000 °C,” *Oxid. Met.*, vol. 81, no. 1–2, pp. 151–165, 2014.

[63] J. Kalivodová, D. Baxter, M. Schütze, and V. Rohr, “Corrosion behaviour of boiler steels, coatings and welds in flue gas environments,” *Mater. Corros.*, vol. 59, no. 5, pp. 367–373, May 2008.

[64] D. Berztiss, A. Zahs, and A. Schneider, “Role of carbides in the high temperature corrosion of steels in HCl-containing atmospheres,” *Zeitschrift für Met.*, vol. 90, pp. 4–12, 1999.

[65] M. Montgomery and A. Karlsson, “In-situ corrosion investigation at Masnedø CHP plant - a straw-fired power plant,” *Mater. Corros.*, vol. 50, pp. 579–584, 1999.

[66] S. van Lith, F. Frandsen, and M. Montgomery, “Lab-scale Investigation of Deposit-induced Chlorine Corrosion of Superheater Materials under Simulated Biomass-firing Conditions . Part 1 : Exposure at 560 ° C,” *Energy & Fuels*, vol. 59, no. 10, pp. 3457–3468, 2009.

[67] Y. Kawahara, “High temperature corrosion mechanisms and effect of alloying elements for materials used in waste incineration environment,” *Corros. Sci.*, vol. 44, pp. 223–246, 2002.

[68] P. D. Miller, H. H. Krause, D. A. Vaughan, and W. K. Boyd, “The Mechanism in High Temperature Corrosion in Municipal Incinerators,” *Corrosion*, vol. 28, no. 7, pp. 274–281, 1972.

[69] J. Pettersson, C. Pettersson, N. Folkeson, L. G. Johansson, E. Skog, and J. E. Svensson, “The Influence of Sulfur Additions on the Corrosive Environments in a Waste-Fired CFB Boiler,” *Mater. Sci. Forum*, vol. 522–523, pp. 563–570, 2006.

[70] N. Folkeson, J. Pettersson, C. Pettersson, L. G. Johansson, E. Skog, B. Å. Andersson, S. Enestam, J. Tuiremo, A. Jonasson, B. Heikne, and J. E. Svensson, “Fireside Corrosion of Stainless and Low Alloyed Steels in a Waste-Fired CFB Boiler; The Effect of Adding Sulphur to the Fuel,” *Mater. Sci. Forum*, vol. 595–598, pp. 289–297, 2008.

[71] S. Karlsson, J. Pettersson, J. E. Svensson, and L. G. Johansson, “KCl-Induced High Temperature Corrosion of the Austenitic Stainless Steel 304L – The Influence of SO_2,” *Mater. Sci. Forum*, vol. 696, pp. 224–229, Sep. 2011.

[72] M. Paneru and G. Stein-Brzozowska, “Corrosion Mechanism of Alloy 310 Austenitic Steel beneath NaCl Deposit under Varying SO2 Concentrations in an Oxy-fuel Combustion Atmosphere,” *Energy & Fuels*, vol. 27, pp. 5699–5705, 2013.

[73] S. Karlsson, T. Jonsson, J. Hall, J. E. Svensson, and J. Liske, “Mitigation of Fireside Corrosion of Stainless Steel in Power Plants : A Laboratory Study of the Influences of SO2 and KCl on Initial Stages of Corrosion,” *Energy & Fuels*, vol. 28, pp. 3102–3109, 2014.

[74] J. Pettersson, H. Asteman, J.-E. Svensson, and L.-G. Johansson, “KCl Induced Corrosion of a 304-type Austenitic Stainless Steel at 600°C; The Role of Potassium,” *Oxid. Met.*, vol. 64, no. 1–2, pp. 23–41, Aug. 2005.

[75] J. Pettersson, J.-E. Svensson, and L.-G. Johansson, “KCl-Induced Corrosion of a 304-type Austenitic Stainless Steel in O2 and in O2 + H2O Environment: The Influence of Temperature,” *Oxid. Met.*, vol. 72, no. 3–4, pp. 159–177, Apr. 2009.

[76] H. Asteman, J. E. Svensson, and L. G. Johansson, “Indication of chromium oxide hydroxide evaporation during oxidation of 304L at 873 K in the presence of 10% water vapor,” *Oxid. Met.*, vol. 52, no. 1, pp. 95–111, 1999.

[77] H. Asteman, J. E. Svensson, M. Norell, and L. G. Johansson, “Influence of water vapor and flow rate on the high-temperature oxidation of 304L; effect of chromium oxide hydroxide evaporation,” *Oxid. Met.*, vol. 54, no. 1, pp. 11–26, 2000.

[78] T. Jonsson, J. Froitzheim, J. Pettersson, J.-E. Svensson, L.-G. Johansson, and M. Halvarsson, “The Influence of KCl on the Corrosion of an Austenitic Stainless Steel (304L) in Oxidizing Humid Conditions at 600 °C: A Microstructural Study,” *Oxid. Met.*, vol. 72, no. 3–4, pp. 213–239, May 2009.

[79] J. Pettersson, N. Folkeson, L.-G. Johansson, and J.-E. Svensson, “The Effects of KCl, K2SO4 and K2CO3 on the High Temperature Corrosion of a 304-Type Austenitic Stainless Steel,” *Oxid. Met.*, vol. 76, no. 1–2, pp. 93–109, Mar. 2011.

[80] J. Pettersson, J. E. Svensson, and L. G. Johansson, “Alkali Induced Corrosion of 304-Type Austenitic Stainless Steel at 600°C; Comparison between KCl, K_2CO_3 and K_2SO_4,” *Mater. Sci. Forum*, vol. 595–598, pp. 367–375, 2008.

[81] J. Lehmusto, B.-J. Skrifvars, P. Yrjas, and M. Hupa, “Comparison of potassium chloride and potassium carbonate with respect to their tendency to cause high temperature corrosion of stainless 304L steel,” *Fuel Process. Technol.*, vol. 105, pp. 98–105, Jan. 2013.

[82] J. Lehmusto, P. Yrjas, B.-J. Skrifvars, and M. Hupa, “High temperature corrosion of superheater steels by KCl and K2CO3 under dry and wet conditions,” *Fuel Process. Technol.*, vol. 104, pp. 253–264, Dec. 2012.

[83] J. Lehmusto, D. Lindberg, P. Yrjas, B.-J. Skrifvars, and M. Hupa, “Thermogravimetric studies of high temperature reactions between potassium salts and chromium,” *Corros. Sci.*, vol. 59, pp. 55–62, Jun. 2012.

[84] R. Pompe, J. E. Svensson, and C. Pettersson, “How to Screen High Temperature Steels for Optimal Use in Biofuel-heated Burners for Residential Boilers: Role of Alkali,” in *CORROSION*, 2011, no. 11194.

[85] K. Segerdahl, J. Pettersson, J. E. Svensson, and L. G. Johansson, “Is KCl(g) Corrosive at Temperatures Above its Dew Point? Influence of KCl(g) on Initial Stages of the High Temperature Corrosion of 11% Cr Steel at 600°C,” *Mater. Sci. Forum*, vol. 461–464, pp. 109–116, 2004.

[86] C. Pettersson, J. E. Svensson, and L. G. Johansson, “Corrosivity of KCl(g) at Temperatures above Its Dew Point - Initial Stages of the High Temperature Corrosion of Alloy Sanicro 28 at 600^{o}C,” *Mater. Sci. Forum*, vol. 522–523, pp. 539–546, 2006.

[87] H. T. Ma, C. H. Zhou, and L. Wang, “High temperature corrosion of pure Fe, Cr and Fe–Cr binary alloys in O2 containing trace KCl vapour at 750°C,” *Corros. Sci.*, vol. 51, no. 8, pp. 1861–1867, Aug. 2009.

[88] Y. S. Li, Y. Niu, and M. Spiegel, “High temperature interaction of Al/Si-modified Fe–Cr alloys with KCl,” *Corros. Sci.*, vol. 49, no. 4, pp. 1799–1815, Apr. 2007.

[89] S. Karlsson and T. Jonsson, “The effect of SO2 (g) on the initial stages of KCl induced high temperature corrosion of 304L at 600° C,” in *HTCPM2012*

[90] C. Pettersson, J. Pettersson, H. Asteman, J.-E. Svensson, and L.-G. Johansson, “KCl-induced high temperature corrosion of the austenitic Fe–Cr–Ni alloys 304L and Sanicro 28 at 600°C,” *Corros. Sci.*, vol. 48, no. 6, pp. 1368–1378, Jun. 2006.

[91] J. Lehmusto, B.-J. Skrifvars, P. Yrjas, and M. Hupa, “High temperature oxidation of metallic chromium exposed to eight different metal chlorides,” *Corros. Sci.*, vol. 53, no. 10, pp. 3315–3323, Oct. 2011.

[92] S. Karlsson, J. Pettersson, L.-G. Johansson, and J.-E. Svensson, “Alkali Induced High Temperature Corrosion of Stainless Steel: The Influence of NaCl, KCl and CaCl2,” *Oxid. Met.*, vol. 78, no. 1–2, pp. 83–102, Apr. 2012.

[93] Y. Shinata and Y. Nishi, “NaCl-induced accelerated oxidation of chromium,” *Oxid. Met.*, vol. 26, pp. 201–212, 1986.

[94] Y. Shinata, “Accelerated oxidation rate of chromium induced by sodium chloride,” *Oxid. Met.*, vol. 27, pp. 315–332, 1987.

[95] Y. Shinata, M. Hara, and T. Nakagawa, “Accelerated oxidation of chromium by trace of sodium chloride vapor,” *Mater. Trans. JIM(Japan)*, vol. 32, no. 10, pp. 969–972, 1991.

[96] Y. Shinata, F. Takahashi, and K. Hashiura, “NaCl-induced hot corrosion of stainless steels,” *Mater. Sci. Eng.*, vol. 87, pp. 399–405, 1987.

[97] Y. S. Li, M. Spiegel, and S. Shimada, “Corrosion behaviour of various model alloys with NaCl–KCl coating,” *Mater. Chem. Phys.*, vol. 93, no. 1, pp. 217–223, Sep. 2005.

[98] T. J. Pan, Y. S. Li, Q. Yang, R. F. Feng, and A. Hirose, “Internal oxidation and phase transformations of multi-phase Fe–Ni–Al and Fe–Ni–Al–Cr alloys induced by KCl corrosion,” *Corros. Sci.*, vol. 53, no. 6, pp. 2115–2121, Jun. 2011.

[99] N. Sato, T. Kaneta, M. Fukumoto, and M. Hara, “High Temperature Corrosion Resistance of Siliconized Stainless Steel under Continuous Deposition of Salt,” *Mater. Sci. Forum*, vol. 696, pp. 266–271, Sep. 2011.

[100] S. Cha and M. Spiegel, “Local reactions between NaCl and KCl particles and metal surfaces,” *Corros. Eng. Sci.*, vol. 40, no. 3, pp. 249–253, 2005.

[101] T. Jonsson, N. Folkeson, J.-E. Svensson, L.-G. Johansson, and M. Halvarsson, “An ESEM in situ investigation of initial stages of the KCl induced high temperature corrosion of a Fe–2.25Cr–1Mo steel at 400°C,” *Corros. Sci.*, vol. 53, no. 6, pp. 2233–2246, Jun. 2011.

[102] M. G. Fontana, *Corrosion Engineering*, 3rd ed. McGaw Hill, 1986.

[103] M. Montgomery and O. Larsen, “Superheater Corrosion in Biomass-Fired Power Plants: Investigation of Welds,” *Corros. 2002*, paper no. 02379, 2002.

[104] J. Pettersson, “Alkali Induced High Temperature Corrosion of Stainless Steels,” Chalmers University of Technology, 2008.

[105] J. Lehmusto, D. Lindberg, P. Yrjas, B.-J. Skrifvars, and M. Hupa, “Studies on the Partial Reactions Between Potassium Chloride and Metallic Chromium Concerning Corrosion at Elevated Temperatures,” *Oxid. Met.*, vol. 77, no. 3–4, pp. 129–148, Nov. 2011.

[106] S. C. Van Lith, F. J. Frandsen, M. Montgomery, T. Vilhelmsen, and S. A. Jensen, “Lab-scale Investigation of Deposit-induced Chlorine Corrosion of Superheater Materials under Simulated Biomass-firing Conditions.,” in *EUROCORR*, 2008, paper no. 1258.

[107] V. Vokál, V. Rohr, M. J. Pomeroy, and M. Schütze, “Corrosion of alloys and their diffusion aluminide coatings by KCl:K2SO4 deposits at 650 °C in air,” *Mater. Corros.*, vol. 59, no. 5, pp. 374–379, May 2008.

[108] T. Yasuda, M. Fukumoto, and Y. Sato, “Formation of Si Diffusion Layer on SUS 430 and SUS 304 Steels and High Temperature Corrosion Resistance,” *J. Japan Inst.*, vol. 71, no. 6, pp. 528–533, 2007.

[109] N. Hiramatsu, Y. Uematsu, T. Tanaka, and M. Kinugasa, “Effects of alloying elements on NaCl-induced hot corrosion of stainless steels,” *Mater. Sci. Eng. A*, vol. 120–121, pp. 319–328, Nov. 1989.

[110] H. Fujikawa and N. Maruyama, “Corrosion behaviour of austenitic stainless steels in the high chloride-containing environment,” *Mater. Sci. Eng. A*, vol. 20, pp. 301–306, 1989.

[111] Y. S. Li, M. Spiegel, and S. Shimada, “Effect of Al/Si addition on KCl induced corrosion of 9% Cr steel,” *Mater. Lett.*, vol. 58, no. 29, pp. 3787–3791, Nov. 2004.

[112] Y. Chang and F. Wei, “High-temperature chlorine corrosion of metals and alloys,” *J. Mater. Sci.*, vol. 26, 1991.

[113] C. Proff, T. Jonsson, and C. Pettersson, “Microstructural investigation of the KCl-induced corrosion of the austenitic alloy Sanicro 28 (35Fe27Cr31Ni) at 600C,” *Mater. High Temp.*, vol. 26, no. 2, pp. 113–125, 2009.

[114] C. Pettersson, L.-G. Johansson, and J.-E. Svensson, “The Influence of Small Amounts of KCl(s) on the Initial Stages of the Corrosion of Alloy Sanicro 28 at 600 °C,” *Oxid. Met.*, vol. 70, no. 5–6, pp. 241–256, Aug. 2008.

[115] K. Gotthjælp, P. Brøndsted, P. Jansen, J. Markussen, M. Montgomery, and E. Maahn, “High Temperature Corrosion in Biomass Incineration Plants, Final Report for EFP 95, J. Nr. 1323/95-0008, ISBN 87-550-2305-3,” 1995.

[116] M. Montgomery, A. Karlsson, and O. Larsen, “Field test corrosion experiments in Denmark with biomass fuels. Part 1: Straw-firing,” *Mater. Corros.*, vol. 53, no. 2, pp. 121–131, 2002.

[117] B. Pujilaksono, T. Jonsson, M. Halvarsson, I. Panas, J.-E. Svensson, and L.-G. Johansson, “Paralinear Oxidation of Chromium in O2 + H2O Environment at 600–700 °C,” *Oxid. Met.*, vol. 70, no. 3–4, pp. 163–188, Jul. 2008.

[118] C. Pettersson, T. Jonsson, C. Proff, M. Halvarsson, J.-E. Svensson, and L.-G. Johansson, "High Temperature Oxidation of the Austenitic (35Fe27Cr31Ni) Alloy Sanicro 28 in O2 + H2O Environment," *Oxid. Met.*, vol. 74, no. 1–2, pp. 93–111, Apr. 2010.

[119] S. Enestam, D. Bankiewicz, J. Tuiremo, K. Mäkelä, and M. Hupa, "Are NaCl and KCl equally corrosive on superheater materials of steam boilers?," *Fuel*, vol. 104, pp. 294–306, Feb. 2013.

[120] S. Chevalier, S. Ched'Homme, a. Bekaddour, K. Amilain-Basset, and L. Buisson, "High temperature alloy chloridation at 850°C. Part I: Comparison of Ni-based and Fe-based alloy behaviour," *Mater. Corros.*, vol. 58, no. 4, pp. 254–264, Apr. 2007.

[121] J. O. Andersson, "Thermo-Calc and DICTRA, Computational tools for materials science.," *Calphad*, vol. 26, pp. 273–312.

[122] G. Lai, *High Temperature Corrosion of Engineering Alloys*, 3rd ed. ASM International, 1997.

[123] R. C. Weast, *Handbook of Chemistry and Physics*, 67th ed. CRC Press, 1987.

[124] M. Hossain, "The influence of HCl gas in enhancing corrosion rates in NiCr-base alloys and the implications for coal-fired gas turbines," *Corros. Sci.*, vol. 21, no. 12, pp. 843–861, 1981.

[125] E. Yazhenskikh, K. Hack, and M. Müller, "Critical thermodynamic evaluation of oxide systems relevant to fuel ashes and slags Part 2: Alkali oxide–alumina systems," *Calphad*, vol. 30, no. 4, pp. 397–404, Dec. 2006.

[126] E. Yazhenskikh, K. Hack, and M. Müller, "Critical thermodynamic evaluation of oxide systems relevant to fuel ashes and slags. Part 1: Alkali oxide–silica systems," *Calphad*, vol. 30, no. 3, pp. 270–276, Sep. 2006.

[127] E. M. Levin, H. F. McMurdie, and F. . Hall, *Phase Diagrams for Ceramists: Volume 1*. Columbus, Ohio: The American Ceramic Society, 1956.

[128] G. Eriksson and A. Pelton, "Critical evaluation and optimization of the thermodynamic properties and phase diagrams of the MnO-TiO2, MgO-TiO2, FeO-TiO2, Ti2O3-TiO2, Na2O-TiO2, and K2O-," *Metall. Trans. B*, vol. 2, no. October, 1993.

[129] P. Goodhew, J. Humphreys, and R. Beanland, *Electron Microscopy and -Analysis*, 3rd ed. London and New York: Taylor & Francis, 2001.

[130] L. Reimer, *Scanning Electron Microscopy: Physics of Image Formation and Microanalysis*, 2nd ed. Springer, 1998.

[131] N. A. University, "Effects of Electron Bombardment." [Online]. Available: http://www4.nau.edu/microanalysis/Microprobe/Interact-Effects.html. [Accessed: 26-Jun-2012].

[132] C. Hammond, *The Basics of Crystallography and Diffraction*, 3rd ed. Oxford University Press, 2009.

[133] KU Leuven, "X-ray diffraction – Bruker D8 Discover." [Online]. Available: https://fys.kuleuven.be/iks/nvsf/images/xrd_figure_1.jpg. [Accessed: 15-Oct-2014].

[134] UCDavis, "Powder X-ray Diffraction." [Online]. Available: http://chemwiki.ucdavis.edu/@api/deki/files/232/xrd.png?size=bestfit&width=323&height=237&revision=1. [Accessed: 15-Oct-2014].

[135] E. Larsson, "The Corrosive Effects of Chloride Salts on Water Walls and Superheater Materials in Waste and Biomass-Fired Power Plants," Chalmers University of Technology, 2014.

[136] V. Rohr, M. Schütze, E. Fortuna, D. N. Tsipas, a. Milewska, and F. J. Pérez, "Development of novel diffusion coatings for 9-12 % Cr ferritic-martensitic steels," *Mater. Corros.*, vol. 56, no. 12, pp. 874–881, Dec. 2005.

9. Papers

9.1 Paper I

Saeed Kiamehr, Kristian V. Dahl, Trine N. Lomholt, Thomas L. Christiansen, Marcel A.J. Somers

High Temperature Corrosion due to Biomass Firing: A Study on the Reactivity between Potassium Chloride and Oxides

ISHOC2014. International Symposium on High-temperature Oxidation and Corrosion 2014. Abstracts, pages: 144-147, 2014, The Iron and Steel Institute of Japan

High Temperature Corrosion due to Biomass Firing: A Study on the Reactivity between Potassium Chloride and Oxides

Saeed Kiamehr *, Kristian V. Dahl, Trine N. Lomholt, Thomas L. Christiansen, Marcel A.J. Somers

Technical University of Denmark (DTU), Department of Mechanical Engineering,
Produktionstorvet, Building 425, 2800 Kgs. Lyngby, Denmark

sabag@mek.dtu.dk

1. INTRODUCTION

During the past decades biomass has become a point of focus as a substitute source of energy to replace the fossil fuels. This is mainly because it has the potential to be a CO_2-neutral fuel. However, efficient utilization of biomass has shown to be a challenging task. In this regard the most important difficulty is the high temperature corrosion of heat exchangers due to the formation of deposits rich in potassium chloride (KCl). This, in turn, limits the output steam temperature of the current power plants to a maximum of 540^{o}C [1]. There is still no general agreement in the literature about the exact mechanism of high temperature corrosion by KCl. Classic theory of corrosion under biomass firing environment considers $O_2(g)$ and $Cl_2(g)$ to be the prime species responsible for accelerated attack and considers $SO_2(g)$ as an intermediate species [2]. According to this mechanism $Cl_2(g)$ mainly evolves due to the sulfation of KCl (eq. 1) and then $O_2(g)$ and $Cl_2(g)$ compose the aggressive mixture that subsequently degrades the alloy according to the "active oxidation" model. Details of this mechanism can be found elsewhere [3–5].

$$2KCl + SO_2(g) + O_2(g) = K_2SO_4 + Cl_2(g) \qquad (1)$$

A second theory suggests potassium as the major degrading species, at least in the early stage of corrosion [6]. This is based on a reaction between KCl and Cr_2O_3 in the protective oxide layer (eq. 2).

$$4KCl + Cr_2O_3 + (5/2)O_2(g) = 2K_2CrO_4 + 2Cl_2(g) \qquad (2)$$

When Cr_2O_3 reacts with KCl the oxide layer loses its protective property and instead of a slow-growing Cr_2O_3-rich oxide a fast-growing double layer oxide is formed. In case of austenitic stainless steels such oxide is composed of an outward growing Fe_2O_3 and an inward growing $(Fe,Cr,Ni)_3O_4$ layer [6]. Corrosion beneath a porous KCl-containing deposit under a gaseous atmosphere containing multiple corrosive species is a complex phenomenon and there is still no general agreement in the literature on whether potassium or chlorine is more detrimental for the overall lifetime. Therefore a safe alloy design strategy requires simultaneous consideration of the reactivity of oxides with KCl as well as relative affinities of the alloying elements to both oxygen and chlorine.

2. THERMODYNAMIC CONSIDERATIONS

In the current study, as the first step, predominance diagrams for a large number of metallic elements of the periodic Table were calculated applying Thermocalc (database SSUB3) [7] and HSC Chemistry [8]. These diagrams show the stable phases at a constant temperature under different oxygen and chlorine partial pressures. Calculations show that Al, Si, Cr, Ti, Y, Ce, Ta, Hf and Zr possess large oxide stability areas making them candidates for an oxide forming element under a $O_2(g)+Cl_2(g)$ containing gas. Choice of employing pure elements is limited in many engineering applications due to insufficient mechanical properties and therefore alloys need to be utilized. For an alloy a suitable matrix element under oxidizing-chlorinating conditions is an element with low affinity to chlorine under low $P_{O2(g)}$ conditions i.e. beneath an oxide layer [9]. Referring to the predominance diagrams Mo, Ni and Co were found to have this characteristic. However, in this study Mo was not considered further as Mo(VI) oxide is volatile at 650°C [7]. At the end Fe and Mn were also included in the experimental plan. Choice of these was due to their abundance as well as the fact that although these elements (in pure form) do not offer protection in oxidizing-chlorinating atmospheres, they might be a good choice of the matrix element if an oxide layer is able to establish quickly.

As mentioned earlier, in addition to oxygen and chlorine, potassium also plays a significant role in the degradation of materials during biomass combustion. This imposes an additional requirement for the alloying elements: low reactivity of the corresponding oxide with KCl. In this study, as a first step, affinities of the oxides were evaluated by calculating the standard Gibbs energy change for the corresponding reactions. Unfortunately, for some of the considered oxides the thermochemical data for possible reaction products are not available. Results of the calculations are given in Table 1. Based on these values it is expected that the reactivity increases in the order of $Fe_2O_3<Al_2O_3<SiO_2<Ta_2O_5<Cr_2O_3<TiO_2$. It has to be mentioned that the choice of reaction products is based on the available species in the databases of the employed softwares. In reality the reaction product and therefore the stoichiometry might be different from what has been considered here.

Table 1: Affinity of a number of oxides to KCl at 600°C. ΔG^o values are calculated by Thermocalc (database SSUB3) unless cited otherwise. Choice of temperature is based on a target temperature of 600°C for new generation of superheater materials. Due to the endothermicty of the reactions a similar trend (higher reactivity) is expected at higher temperatures. $P_{O2(g)}$=0.05 and $P_{H2O(g)}$=0.15 atm were used to calculate the equilibrium partial pressure of HCl(g). These values approximately correspond to the oxidizing potential of the off-gas due to the biomass combustion.

oxide	Reaction equation	ΔG^o (KJ)	P_{HCl}^{eq} $*10^6$
Al_2O_3	$(1/2)Al_2O_3 + KCl + (1/2)H_2O(g) = (1/2)K_2O.Al_2O_3 + HCl(g)$	+112.3	0.07
Cr_2O_3	$(1/2)Cr_2O_3 + KCl + (1/2)H_2O(g) = (1/2)K_2O.Cr_2O_3 + HCl(g)$	+95.4	0.76
	$(1/4)Cr_2O_3 + KCl + (1/2)H_2O(g) + (3/8)O_2(g) = (1/2)K_2O.CrO_3 + HCl(g)$	+37.8	690
	$(1/2)Cr_2O_3 + KCl + (1/2)H_2O(g) + (3/4)O_2(g) = (1/2)K_2O.2CrO_3(l) + HCl(g)$	+29.9 [8]	666
Fe_2O_3	$(1/2)Fe_2O_3 + KCl + (1/2)H_2O(g) = (1/2)K_2O.Fe_2O_3 + HCl(g)$	+131.0	0.005
SiO_2	$(1/2)SiO_2 + KCl + (1/2)H_2O(g) = (1/2)K_2O.SiO_2 + HCl(g)$	+96.2	0.68
	$SiO_2 + KCl + (1/2)H_2O(g) = (1/2)K_2O.2SiO_2 + HCl(g)$	+68.7	30
	$2SiO_2 + KCl + (1/2)H_2O(g) = (1/2)K_2O.4SiO_2 + HCl(g)$	+73.3	16
TiO_2	$(1/2)TiO_2 + KCl + (1/2)H_2O(g) = (1/2)K_2O.TiO_2 + HCl(g)$	-56.2 [8]	$891*10^6$
Ta_2O_5	$(1/2)Ta_2O_5 + KCl + (1/2)H_2O(g) = (1/2)K_2O.Ta_2O_5 + HCl(g)$	+58.5 [8]	122

3. EXPERIMENTAL PROCEDURE

Oxides considered in this study consist of ZrO_2, TiO_2 (both rutile and anatase), Y_2O_3, SiO_2, Ta_2O_5, Fe_2O_3, Cr_2O_3, HfO_2, CeO_2, Al_2O_3, NiO, Co_3O_4 and Mn_3O_4. Except Ta_2O_5, Mn_3O_4 and TiO_2(rutile), which had unspecified particle size, the rest of the oxides had particle sizes ranging from 20 to 200nm. In addition, KCl had a particle size of 63-90μm. Assuming that the condensed reaction product consists of 1 mole of K_2O and 1 mole of oxide (i.e. with the general formula $K_2O.M_2O_x$) the reaction equations were balanced and subsequently each oxide was mixed with KCl according to this anticipated stoichiometry. Mixing was done using an agate mortar. Thereafter, part of the mixture was transferred to a mold and pressed manually to produce cylindrical tablets of 17mm diameter. The thermal cycle consisted of heating to 650^{o}C at a rate of ~5^{o}C/min, holding at this temperature for 15 hours and then cooling to room temperature under furnace cooling. The Atmosphere was N_2(g)+5%O_2(g)+15%H_2O(g) flowing at a rate of 0.5 cm/s at the inlet temperature. Heating and cooling was performed under the mentioned atmosphere when the temperature was above 500^{o}C. Below this temperature the water bath was switched off to avoid condensation of water vapor on cold parts of the furnace tube. Flow rates of O_2(g) and N_2(g) were controlled by means of thermal mass flow controllers (GF40/80 series, Brooks Instrument). $P_{H2O(g)}$ was fixed at 0.15atm by keeping the temperature of the water bath at 54^{o}C. To avoid cross contamination, exposures were performed separately for each sample. Before heating, samples were placed on a gold coated alumina plate and then loaded into the furnace lying close to the thermocouple tip. Prior to and after the exposures samples were studied by X-Ray Diffraction (XRD) using a Bruker D8 Discover diffractometer. Measurements were done in parallel beam condition using CrK_α (λ=2.2897 Å) radiation. In addition, morphology of the exposed samples were examined by a JEOL JSM-5900 Scanning Electron Microscope (SEM) equipped with an Energy Dispersive X-Ray Spectroscopy (EDS) detector.

4. RESULTS AND DISCUSION

For Fe_2O_3, TiO_2 (both anatase and rutile), NiO, Co_3O_4, CeO_2, Ta_2O_5, HfO_2, ZrO_2 and Y_2O_3 no new peaks emerged on the diffractograms after the exposure. No compound which is composed of K, M and O (where M is the corresponding metal) or hydrated form of that was found in the diffractograms. This suggests lack of reactivity between these oxides and KCl under the experimental conditions of this study. It is noted that XRD is not able to detect a phase if its amount is below ~3wt%. Therefore, these results only show that there is no *major* reactivity between the abovementioned oxides and KCl. Lack of reaction between TiO_2 and KCl is opposite to the thermodynamic calculations (Table 1). This indicates that the activation energy for this reaction is large in a way that higher temperatures are needed for the reaction to start. For Al_2O_3 there is an infinitesimal single peak appearing at 105.48^o. However, this peak does not correspond to any compound containing K, Al and O (or hydrated form of that). This indicates lack of a major reaction between KCl and Al_2O_3. In case of Cr_2O_3 presence of K_2CrO_4 is clearly visible (figure 1a). This means that Cr_2O_3 is reactive and this oxide may not offer protection against KCl. In addition, this result shows that the reaction follows the stoichiometry of the second equation (among the reactions for Cr_2O_3) in Table 1. For Mn_3O_4 it was found that the compound $K_{2-x}Mn_8O_{16}$, where x

denotes the non-stoichiometry, has major peaks that overlap with those of $Mn_{0.98}O_2$ and Mn_3O_4. Therefore, the result based on XRD is not conclusive for the reactivity of Mn_3O_4 and KCl. In case of SiO_2 new peaks emerge on the diffractogram after the exposure (figure 1b). These peaks correspond to either trydimite or cristobalite. As the SiO_2 was originally amorphous this means that crystallization has taken place to some extent. Calculation by Thermocalc shows that at 650°C quartz is the stable crystalline form of SiO_2. Tridymite should not form up to 870°C and cristobalite up to 1471°C. Therefore an explanation for the formation of these two phases can be due to KCl affecting the crystallography of phase transformation. This is supported by the observation that a pure SiO_2 sample (without KCl) exposed under similar conditions did not show a major crystallization. Co-existence of trydimite and cristobalite is likely due to small molar Gibbs energy difference between quartz, tridymite and cristobalite over a wide temperature range.

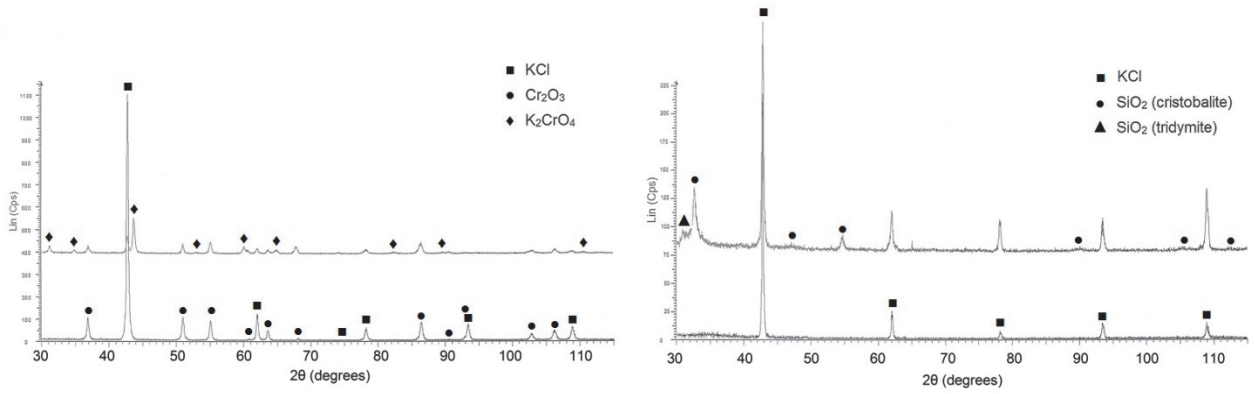

(a) (b)

Figure 1: X-Ray diffractograms corresponding to (a) Cr_2O_3+KCl and (b) SiO_2+KCl samples. The diffractogram at the bottom of each figure corresponds to the sample before the exposure and the one at the top to the sample after the exposure.

As the original SiO_2 was amorphous, due to concerns about the formation of amorphous reaction products, the SiO_2+KCl pellet was examined by SEM/EDS. The microstructure consisted of cubic KCl crystals partially covered by a Si-rich compound. This compound had a solidified appearance and at some points it only consisted of K, Si and O without any Cl. This indicates that SiO_2 has reacted and potassium silicate(s) has formed. Combining this information with XRD analysis of this compound shows that this is composed of amorphous potassium silicate(s) along with pure silica that has (at least partly) crystalline structures of tridymite and cristobalite. Comparing the obtained result with the data in Table 1, it is expected that when SiO_2 turns out to be reactive, then Ta_2O_5 should be reactive too. Lack of any reactivity for Ta_2O_5 indicates that, similar to TiO_2, the activation energy for the reaction is too high. Apart from the SiO_2 all the other oxides were crystalline in the as-received state. Therefore it is expected that the reaction product after KCl exposure is crystalline too. On this basis it seems that only Cr_2O_3 is reactive among the rest of the oxides. To support this, all the samples were studied by SEM. The result showed a clear difference between Cr_2O_3/SiO_2 and the rest of the oxides. Only on these two samples a convoluted morphology had formed. Rounded edges of the reaction product in case of Cr_2O_3 and SiO_2 suggest formation of a molten phase. For the former oxide this can be attributed to the KCl-K_2CrO_4 system with a eutectic temperature of 650°C [10] and for the latter to the K_2O-SiO_2 system with a eutectic

temperature of 649°C [11]. For the rest of the oxides, a granular structure of the oxide and a clear distinction between the oxide and KCl particles could be seen. These observations along with the results of XRD suggest that except for Cr_2O_3 and SiO_2 the oxides studied do not significantly react with KCl.

5. CONCLUSIONS

Reactivity of a number of oxides with KCl was studied at 650°C under flowing $N_2(g)+5\%O_2(g)+15\%H_2O(g)$ gas atmosphere. It was observed that Cr_2O_3 and SiO_2 are reactive with KCl. This implies that care must be taken employing Cr and Si as alloying elements in KCl-containing high temperature environments. For Cr_2O_3 the reaction product is K_2CrO_4. For SiO_2 the exact stoichiometry of the product cannot be determined with XRD due to the amorphous nature of the silicate formed. For Mn_3O_4, XRD cannot give an indication whether this oxide is reactive with KCl due to peak overlap. However observation of the sample under SEM suggests lack of a major reactivity. For ZrO_2, TiO_2, Y_2O_3, Ta_2O_5, Fe_2O_3, HfO_2, CeO_2, Al_2O_3, NiO and Co_3O_4 results from XRD as well as observation under SEM suggest lack of a major reaction between theses oxides and the salt. Lack of reactivity between TiO_2 and KCl as well as Ta_2O_5 and KCl indicates that the activation energies for these reactions are too high.

Acknowledgement

This work is part of the project GREEN financed by the center DSF GREEN. Help and support from John C. Troelsen, Peter J.S. Westermann and Chamathkara Palangasinghe is greatly acknowledged.

References

[1] M. Montgomery, S. A. Jensen, U. Borg, O. Biede, and T. Vilhelmsen: *Mater. Corros.*, 2011, vol. 62, pp. 593–605.

[2] Hanne Philbert Nielsen, Flemming J. Frandsen, and Kim Dam-Johansen: *Energy & Fuels*, 1999, vol. 13, pp. 1114–1121.

[3] M.J. McNallan, W.W. Liang, S.H. Kim, and C.T. Kang: in *High Temp. Corros. NACE*, NACE, 1983, pp. 316–321.

[4] YY Lee and MJ McNallan: *Metall. Trans. A*, 1987, vol. 18, pp. 1099–1107.

[5] HJ Grabke, E Reese, and M. Spiegel: *Corros. Sci.*, 1995, vol. 37, pp. 1023–1043.

[6] J. Pettersson, H. Asteman, J. -E. Svensson, and L. -G. Johansson: *Oxid. Met.*, 2005, vol. 64,pp. 23–41.

[7] JO Andersson, T Helander, and L Höglund: *Calphad*, 2002, vol. 26, pp. 273–312.

[8] HSC Chemistry 7.00, www.hsc-chemistry.com

[9] R. Bender and M Schutze: *Mater. Corros.*, 2003, vol. 54, pp. 567–586.

[10] J. Lehmusto, D. Lindberg, P. Yrjas, B.-J. Skrifvars, and M. Hupa: *Oxid. Met.*, 2011.

[11] Mark D Allendorf and Karl E Spear: *J. Electrochem. Soc.*, 2001, vol. 148, pp. 59–67.

9.2 Paper II

Saeed Kiamehr, Kristian V. Dahl, Melanie Montgomery, Marcel A.J. Somers

KCl-Induced High Temperature Corrosion of Selected Commercial Alloys Part I: Chromia-formers

The manuscript is ready for submission

KCl-Induced High Temperature Corrosion of Selected Commercial Alloys

Part I: Chromia-formers

Saeed Kiamehr[*1], *Kristian V. Dahl*[1], *Melanie Montgomery*[1,2], *Marcel A.J. Somers*[1]

1) Technical University of Denmark (DTU), Department of Mechanical Engineering, Produktionstorvet, Building 425, 2800 Kgs. Lyngby, Denmark
2) COWI A/S Parallelvej 2, 2800 Kgs. Lyngby, Denmark

Abstract

Laboratory testing of selected chromia-forming alloys was performed to rank the materials and gain further knowledge on the mechanism of KCl-induced high temperature corrosion. This is related to the performance of heat exchanger materials in biofuel-based power plants. The investigated alloys were stainless steels EN1.4021, EN1.4057, EN1.4521, TP347H (coarse-grained), TP347HFG (fine-grained), Sanicro 28 and the nickel-based alloys 625, 263 and C276. Exposure was performed at 600°C for 168h in flowing N_2(g)-5%O_2(g)-15% H_2O(g) (vol.%). Samples were covered with KCl powder prior to exposure. A salt-free exposure was also performed for comparison. Corrosion morphology and products were studied with Scanning Electron Microscopy (SEM), Energy Dispersive X-Ray Spectroscopy (EDS) and X-Ray Diffractometry (XRD). It was observed that in the salt-free exposure, stainless steels TP347H (coarse-grained) and EN1.4521 failed to form a thin protective oxide layer compared to the oxide formed on the other alloys. In the presence of solid KCl, all the alloys showed significant corrosion. Measurement of corrosion extent indicated that alloys EN1.4057, Sanicro 28 and 625 show a better performance compared to the industrial state of the art material TP347HFG. An additional test was performed with KCl vapor in static lab air for the same duration and at the same temperature. This was undertaken to investigate the role of the vapor phase and revealed that KCl vapor at 600°C can initiate attack.

Keywords: biomass combustion, deposit, potassium chloride, high temperature corrosion, chromia-former.

1. Introduction

During the past decades, increasing concern about the global warming effects has been a large driving force for utilization of CO_2-neutral fuels. Combustion of biomass instead of fossil fuels is an attractive option, especially in countries with large forest and agricultural resources. However, employing biomass is not free from challenges. Compared to the fossil fuels, such as coal and oil, biomass contains large amounts of alkali and chlorine. Consequently combustion of biomass leads to deposits rich in alkali chlorides, especially potassium chloride KCl, on the heat exchangers. Such

deposits are so corrosive that avoiding materials failures in biomass fired power plants necessitates a reduction of the outlet steam temperature to a value below that for fossil fuel fired power plants. Currently, the maximum outlet steam temperature for biomass firing is 540^{o}C for state of the art power plants using stainless steels such as TP347HFG as superheater tube material [1]. The relatively low steam temperature makes the biomass based power plants less efficient compared to plants firing fossil fuels. Therefore reducing the extent of KCl induced corrosion will directly affect the feasibility of substituting fossil fuels with biomass.

High temperature alloys often rely on the formation of a chromium-rich oxide layer for protection against corrosion. Therefore any interaction with the environment that damages this oxide layer accelerates corrosion of the underlying alloy. It has been shown [2] that in alkali-containing environments, a reaction between the alkali elements and chromia in the oxide layer can lead to the formation of alkali chromate. The reaction for the case of potassium chloride is:

$$4KCl(s,g)+Cr_2O_3+(5/2)O_2(g) =2K_2CrO_4+2Cl_2(g) \quad (1)$$

Chromate formation depletes the original oxide of chromium and hence the oxide is no longer protective [2], [3]. Consequently it is anticipated that with an increase in the alloy's chromium content, the overall damage could be mitigated as a protective oxide can form at later stages. However, when the alkali is bound to chlorine (i.e. alkali-chlorides) the effect of chromium and especially chromium-rich phases in the alloy is a matter of controversy. In fact, pure chromium has been shown to be extremely reactive with alkali chlorides above a certain temperature [4]–[10]. In line with this, field exposure tests by Montgomery et al.[11], [12] demonstrated that for the plant conditions, an increase in chromium content above 15-18wt% deteriorated the performance of the studied alloys under the KCl-rich deposits. The first part of this study, which is reported in the present paper (Part 1), was aimed at investigating a wide range of chromia-forming alloys for ranking as well as obtaining deeper understanding of the mechanism of corrosion. Several authors [13]–[17] have reported that aluminum and/or silicon additions to the stainless steels lead to better protection against high temperature corrosion induced by alkali chloride and alkali chloride-alkali sulfate mixtures. Therefore employing substitute oxide-forming elements or modification of chromia-formers by such elements seems to be a possible remedy. This is studied in the second part of this work in a companion paper (Part 2).

2. Experimental Procedure

The chemical composition of the studied alloys is given in Table 1. Samples were coupons (7-8 mm x 17-20 mm) cut with a precision cutter to a thickness of 250-340 μm. Alloys 625, 263 and C276 were delivered in cold-rolled condition. An annealing treatment on these alloys was performed at 1150^{o}C for 45 minutes in Ar(g)(99.999% purity)+25vol.%H_2(g) followed by furnace-cooling. Annealing was preceded by grinding with 1000-grit SiC paper to remove the solid surface contaminants due to the rolling. Prior to exposure, all samples were ground with 4000-grit SiC paper. Initial sample thickness prior to exposure was measured with a micrometer. A ~1 mm thick layer of KCl powder (particle size of 63-90 μm) was applied to about 2/3 of the sample length.

Samples were placed on flat alumina coupons and loaded into a multi-channel alumina sample holder with the KCl-free part of the samples towards the gas stream. The sample holder itself was placed in the even temperature zone of a horizontal furnace equipped with a silica tube. Figure 1 shows a schematic representation of the experimental set-up.

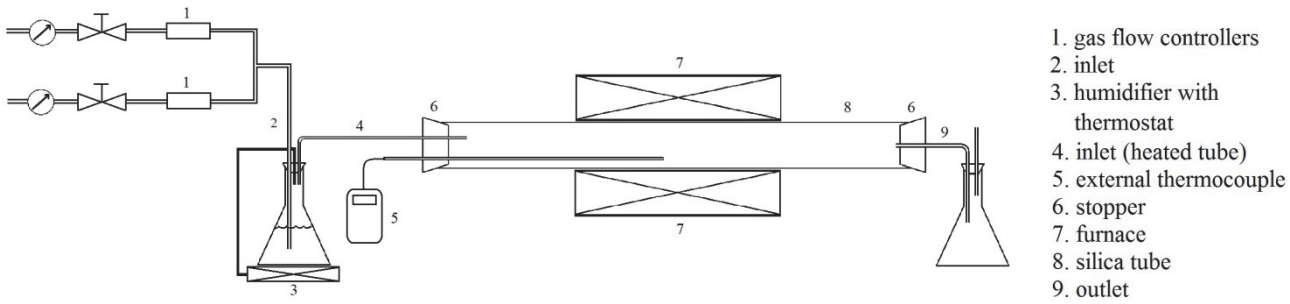

Figure 1: Schematic of the experimental set-up

The samples were exposed for 168h at 600°C to flowing N_2(g)+5%O_2(g)+15%H_2O(g) with a velocity of 0.25cm/s at the inlet temperature. As a reference, a salt-free exposure was carried out for all the alloys. The salt-containing exposure was repeated for alloys 263, 625 and C276. However, this time samples were ground with 1000 grit paper prior to grinding with 4000 grit paper. This was performed to ensure that any oxides formed during annealing were removed. To distinguish between the two batches, samples ground with only 4000 grit paper are referred to as series 1 and the samples ground with both 1000 and 4000 grit papers are referred to as series 2. In addition to the above-mentioned exposures, one additional test was performed to investigate the corrosiveness of potassium chloride vapor. In this test, coupons of alloys 263 and 625 (series 2 samples for both alloys) as well as Sanicro 28 were placed on top of an alumina boat containing KCl powder. The surface of the salt in the boat was flattened to give a uniform distance of ~2 mm between the salt and the samples. Exposure was performed at 600°C for 168h in static lab air.

After the exposures, salt-affected samples were mounted in epoxy resin in an upright position without removing the KCl layer. Half the original width was removed by grinding and then the sample was ground and polished down to 1μm diamond suspension step. Grinding and polishing was performed using 96% ethanol up to 1000 grit SiC paper and 99.9% ethanol on finer papers. The epoxy used for mounting the series 1 samples (specifix-20) proved to contain chlorine. Therefore, a chlorine-free epoxy (Eli-Cast clear epoxy) was used for the series 2 samples and samples exposed to salt vapor.

Samples subjected to salt-free exposure were studied with X-Ray Diffraction (XRD) using a Bruker D8 Discover diffractometer in grazing incidence (GI) mode. CrK_α (λ=2.2897 Å) radiation was used at an incidence angle of 5°. After XRD, the samples were embedded in epoxy and ground and polished in a similar way as the salt-exposed samples, with the only difference that water was used as a lubricant. For salt-affected samples it was not possible to perform XRD. This was due to

the sintering of KCl and incorporation of the corrosion products into the deposit. Consequently mechanical removal of KCl without removing some of the corrosion products proved challenging.

The decrease in metal thickness for the salt-covered samples was measured in a Reflective Light Microscope (RLM) equipped with a travelling stage. Twenty measurements were undertaken at intervals of 0.5 mm and average and standard deviation were calculated for each sample. Thereafter the surface was re-scanned to find the location with the deepest penetrating damage. Average and worst case values less than 5µm were considered insignificant with respect to the accuracy achieved with pre-exposure micrometer measurements of the sample thickness.

Finally, the morphology of the corrosion products was studied with an FEI Inspect S Scanning Electron Microscope (SEM) equipped with an Energy Dispersive X-Ray Spectroscopy (EDS) detector. Imaging was always performed in Back-Scattered Electron (BSE) mode unless otherwise mentioned. The chemical compositions of the alloys as listed in Table 1 were measured with EDS. Carbon and nitrogen contents were measured with Fusion Thermal Conductivity Detection units LECO CS230 and LECO TN500 respectively. The commercial software package Thermo-Calc [18] was used for thermodynamic calculations using data from Thermo-Calc databases SSUB3, TCFE6 and TCNI5.

Table 1: Chemical composition of the investigated alloys. Carbon and nitrogen contents were measured with Fusion Thermal Conductivity Detection units LECO CS230 and LECO TN500 respectively. Other elements determined with EDS. All values are in wt% (values in parentheses are in at%). Elements without a value in the last column were present in trace amounts.

alloy	Fe	Cr	Ni	Al	Si	Mo	Co	Mn	Ti	C	N	other
TP347HFG[a]	bal.	19.1 (20.1)	10.0 (9.3)		1.0 (1.9)			1.7 (1.7)		0.057	0.019	Nb
TP347H	bal.	19.1 (20.2)	10.0 (9.4)		0.6 (1.1)			1.9 (1.9)		0.047	0.019	Nb
Sanicro 28	35.1 (35.3)	28.2 (30.5)	29.6 (28.2)		0.5 (1.1)	3.8 (2.2)		1.8 (1.8)		0.021	0.058	Cu 1.0 (0.9), Al
EN1.4021	bal.	13.9 (14.7)			0.5 (0.9)					0.192	0.022	Mn
EN1.4057	bal.	18.4 (19.4)	1.9 (1.8)		0.3 (0.6)			0.7 (0.7)		0.179	0.039	Al
EN1.4521	bal.	19.4 (20.5)			0.6 (1.2)	1.9 (1.1)		0.4 (0.4)	0.2 (0.3)	0.024	0.024	Cu,Nb
Alloy 263	0.4 (0.4)	21.8 (24.2)	bal.	0.6 (1.2)	0.2 (0.4)	6.3 (3.8)	19.7 (19.3)		2.1 (2.6)	0.059	0.004	
Alloy 625	4.1 (4.4)	23.4 (26.8)	bal.	0.2 (0.4)	0.3 (0.6)	9.5 (5.9)				0.033	0.044	Nb3.5 (2.2), Ti
Alloy C276	6.3 (7.1)	16.6 (20.0)	bal.	0.3 (0.6)		16.4 (10.8)	1.2 (1.3)	0.6 (0.7)		0.007	0.022	W4.1 (1.4), V

[a] Fine-grain TP347H

3. Results

3.1 Reference exposure in N_2(g)+5%O_2(g)+15%H_2O(g)

Only alloys TP347H and EN1.4521, showed formation of fast-growing oxides. A dull-red colored oxide could be clearly observed on these alloys and SEM on cross sections showed a double layer oxide (Figures 2a-b). This is in agreement with XRD results (Figure 3). The presence of $(Fe,Cr)_3O_4$ peaks as well as the relative intensity of $(Fe,Cr)_2O_3$ revealed that non-protective oxides have formed on these alloys. On EN1.4521 a molybdenum-rich phase was detected with EDS in the bulk alloy. This phase was present along all grain boundaries and also within grains of the microstructure (bright contrast in Figure 2c). Investigation of the as-received microstructure showed that this phase had not been present before exposure.

For EN1.4021 and EN1.4057 peaks corresponding to $(Fe,Cr)_3O_4$ could be detected, however no indication of a corrosion product was visually observed on the samples and the metallic luster was preserved. This observation along with the relative intensity of the $(Fe,Cr)_2O_3$ and SEM micrographs of the cross section (not shown here) suggest that these alloys have not developed fast-growing oxides, however they are on the verge of such behavior. A protective behavior was observed for the remaining steels and nickel-based alloys (see diffractograms in Figures 3 and 4).

XRD also revealed the presence of carbides in the steels; $Cr_{23}C_6$ in TP347H, Sanicro28, EN1.4021 and EN1.4057 and NbC in TP347H and TP347HFG. The finding of BCC in the TP347 steels is either due to the deformation-induced martensite (sample was ground with 4000 paper prior to the exposure) or due to the formation of ferrite at the exposure temperature. In alloy 625, both Ni_3Nb intermetallic phase and NbC carbide could be identified. In alloy C276, precipitates most probably correspond to a molybdenum and tungsten-enriched intermetallic phase. This phase was also detected in the unexposed sample.

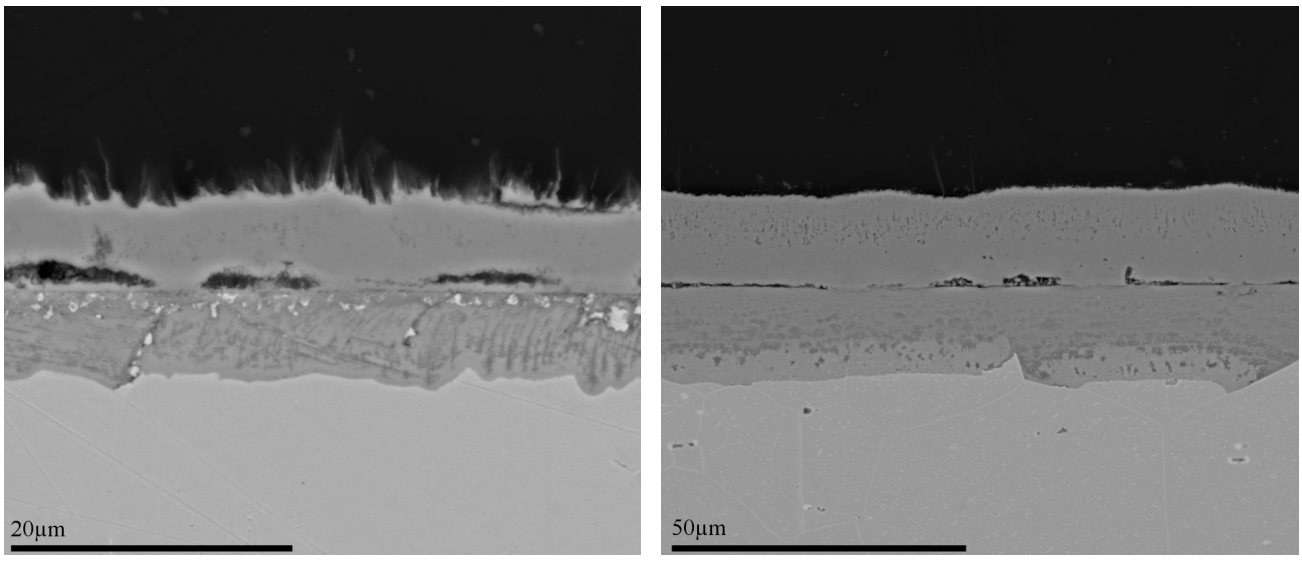

(a) (b)

Figure 2: The oxide microstructure observed on (a) TP347H (b) EN1.4521. Figure (c) shows the molybdenum-rich phase on EN1.4521 which has formed along the grain boundaries and within the grains.

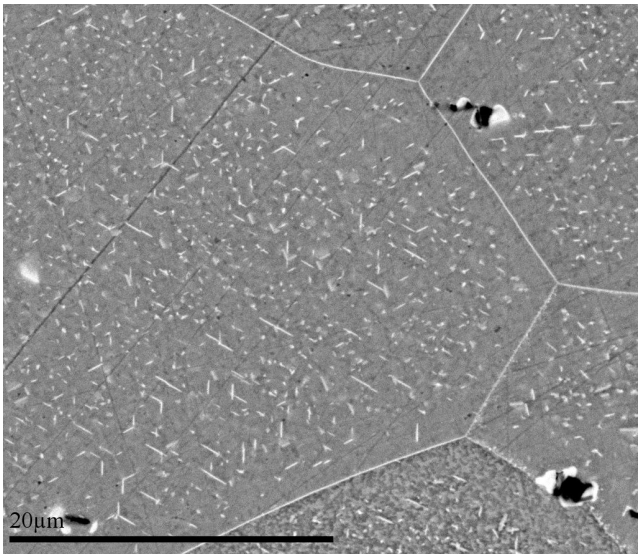

(c)

Figure 2 (cont.)

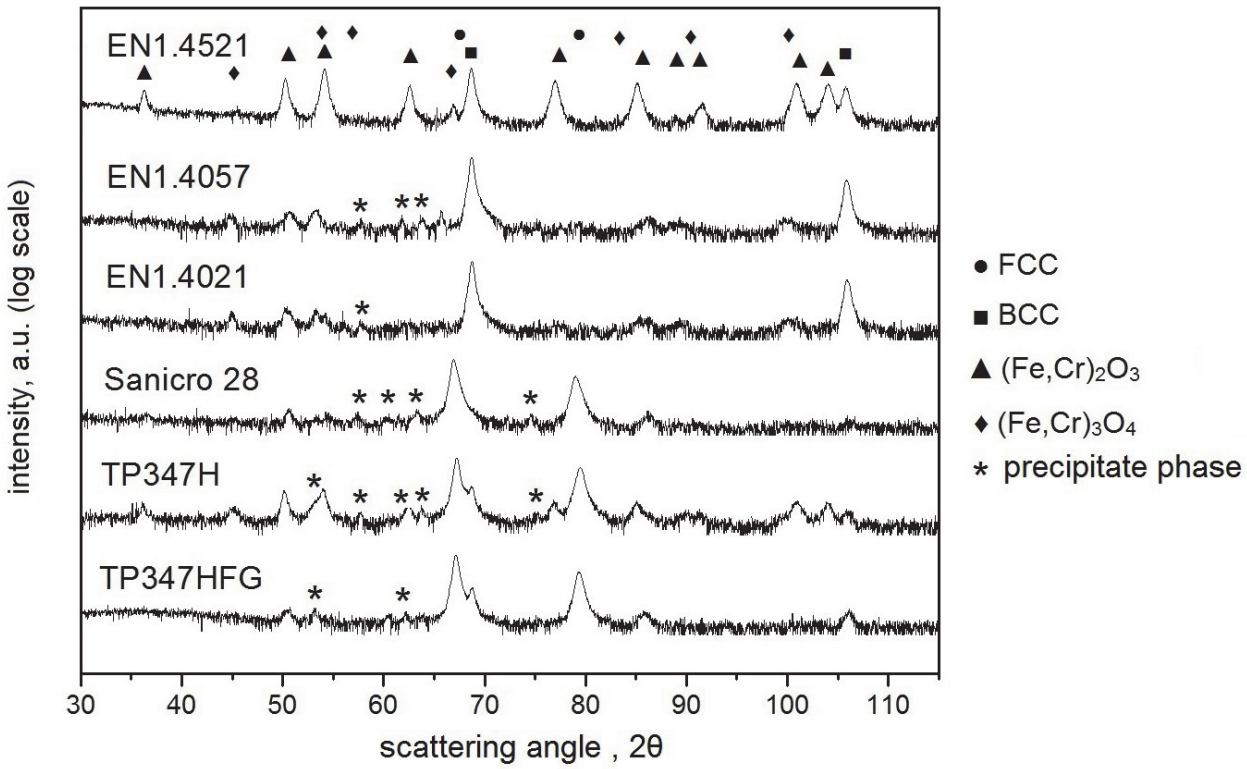

Figure 3: CrK_{α} X-ray diffractograms for the investigated steels after salt-free exposure. Precipitates which could be identified are: (a) $Cr_{23}C_6$ in TP347H, Sanicro28, EN1.4021 and EN1.4057 and (b) NbC in TP347H and TP347HFG.

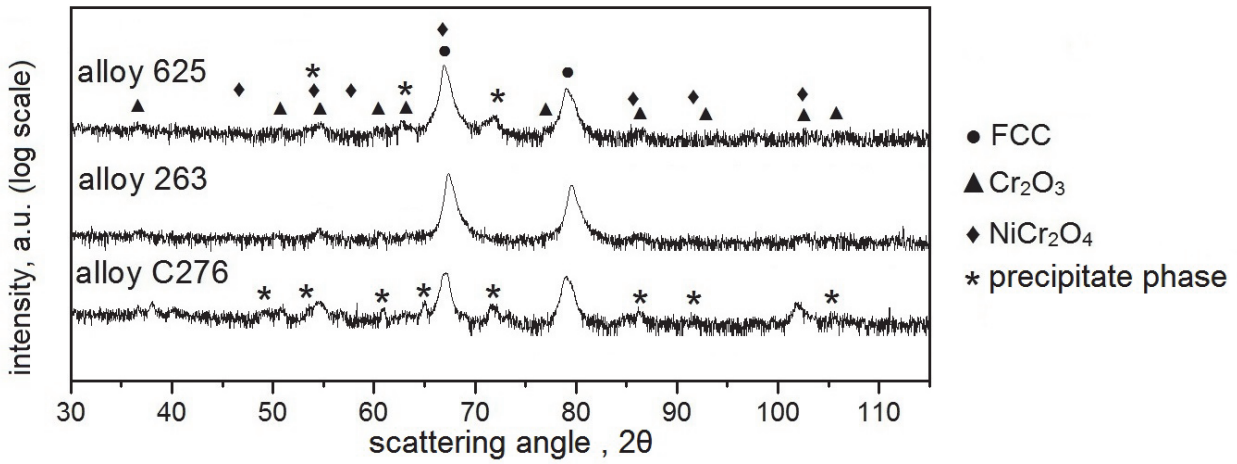

Figure 4: CrK_α X-Ray diffractograms for the investigated nickel-based alloys after the salt-free exposure (series 1 samples).

3.2 Exposure in $N_2(g)+5\%O_2(g)+15\%H_2O(g)$ under KCl(s)

The presence of KCl led to severe attack on all alloys even those that showed a protective behavior in the absence of salt. Cross sections were studied with SEM-EDS primarily in the mapping mode. Figure 5 compares the measured extent of damage for the investigated alloys in terms of loss in metal thickness. Internal oxidation, grain boundary attack and void formation also contribute to the decrease in metal thickness. Due to the error bar overlap, one has to be cautious when drawing definitive conclusions. Apparently, alloys EN1.4057, 625 and Sanicro 28 perform slightly better than the currently widely used TP347HFG. The series 2 samples are shown for the nickel-based alloys in the diagram. This is because the series 1 samples showed small (<5μm) values for the average attack, presumably because an oxide had already formed during the annealing process. However, the extent of worst case damage was similar for both series 1 and 2 on all the alloys. The morphology of the corrosion products and the distribution of the alloying elements throughout the corrosion products (investigated with EDS mapping) are described in the following sections.

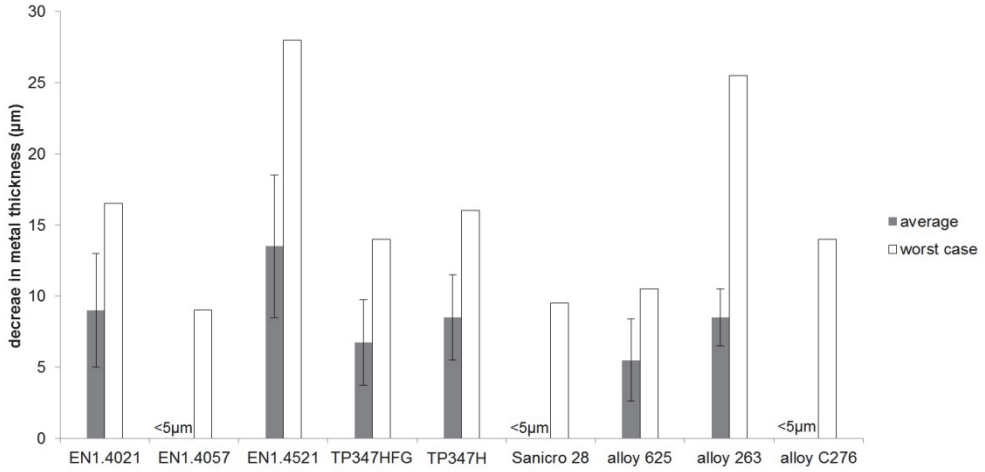

Figure 5: Average and worst case decrease in metal thickness observed after 168h exposure at 600°C in flowing N_2(g)+5%O_2(g)+15%H_2O(g) under KCl(s).

3.2.1 Austenitic stainless steels TP347HFG, TP347H and Sanicro 28

The morphologies of corrosion products on TP347HFG and TP347H were similar (Figures 6a-b). Two types of oxides were present on the alloys: an outer spongy part (marked as type A) and an inner more dense oxide (marked as type B). Type B consisted of outer and inner parts and included the underlying grain boundary attack. The difference in grain size for the two steels was clearly visible through the extent of grain boundary attack. EDS mapping of the alloying elements (Figure 7) showed that type A oxide was rich in iron. Type B oxide was rich in iron on the outer side and chromium on the inner side. Nickel could be identified as small metallic islands embedded in type B oxide. For TP347HFG a faint enrichment of potassium could be seen in type A oxide, but chlorine could not be clearly located in the mapped area. For TP347H, potassium was detected in the outer parts of the oxide, in the middle part and in one case at a grain boundary tip. Chlorine could be detected together with potassium at the tip of the grain boundary attack. Despite the difference in grain size for the two alloys (ASTM grain size 12 for TP347HFG and ASTM grain size 7 for TP347H) the extent of attack in terms of thickness loss is comparable for the two.

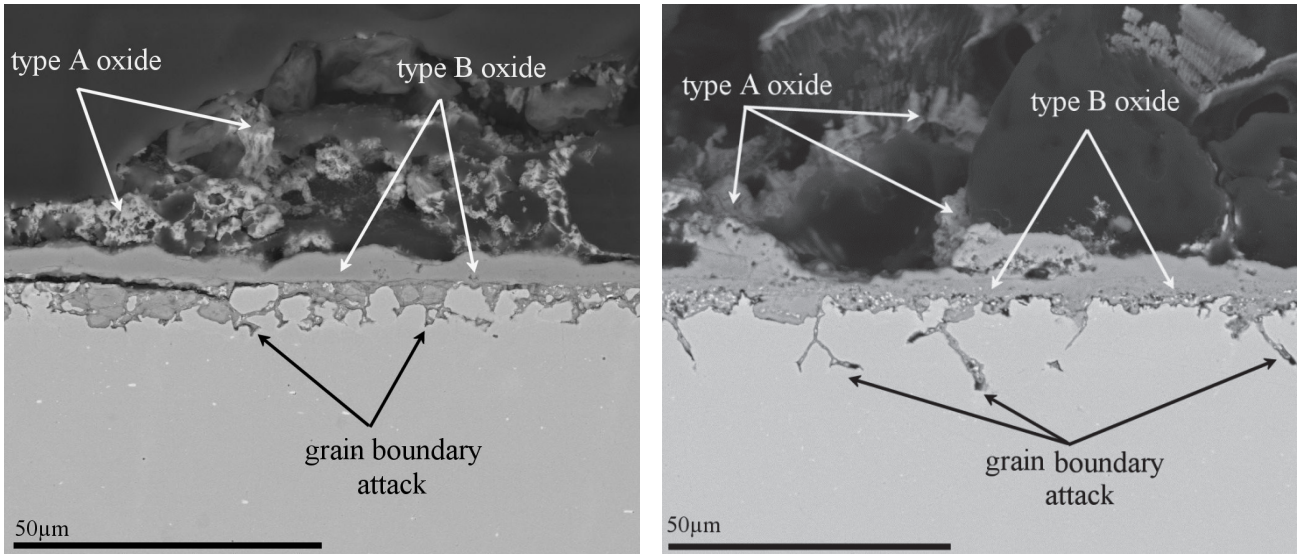

(a) (b)

Figure 6: General morphology of corrosion products on (a) TP347HFG (b) TP347H. Voids in the epoxy (upper half of the images) are the location of salt particles which have been grazed-out during grinding.

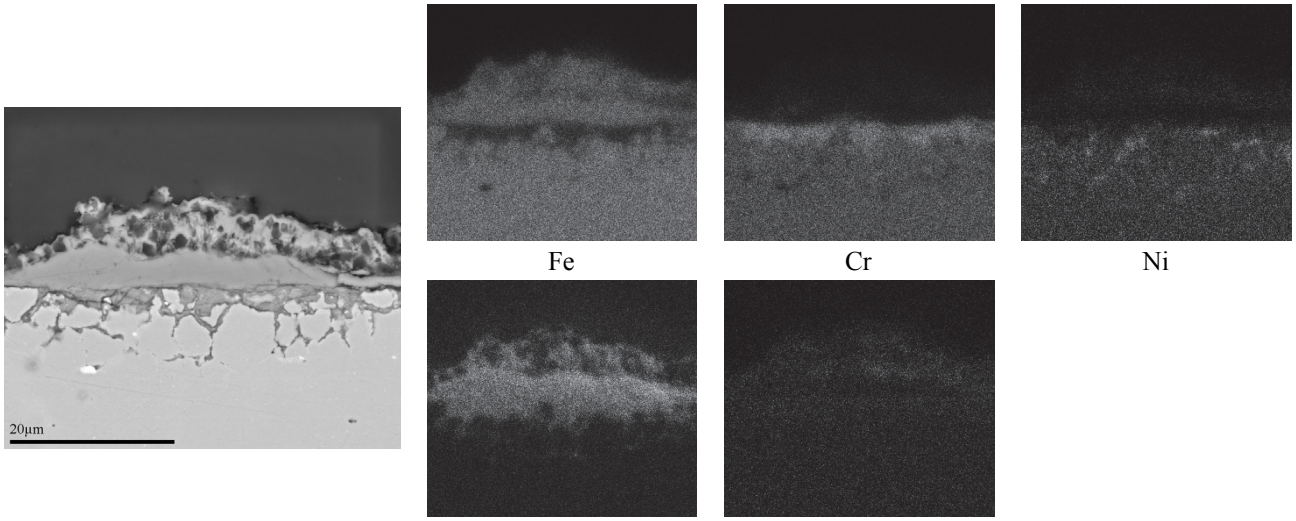

Figure 7: Distribution of the alloying elements, potassium and oxygen for TP347HFG.

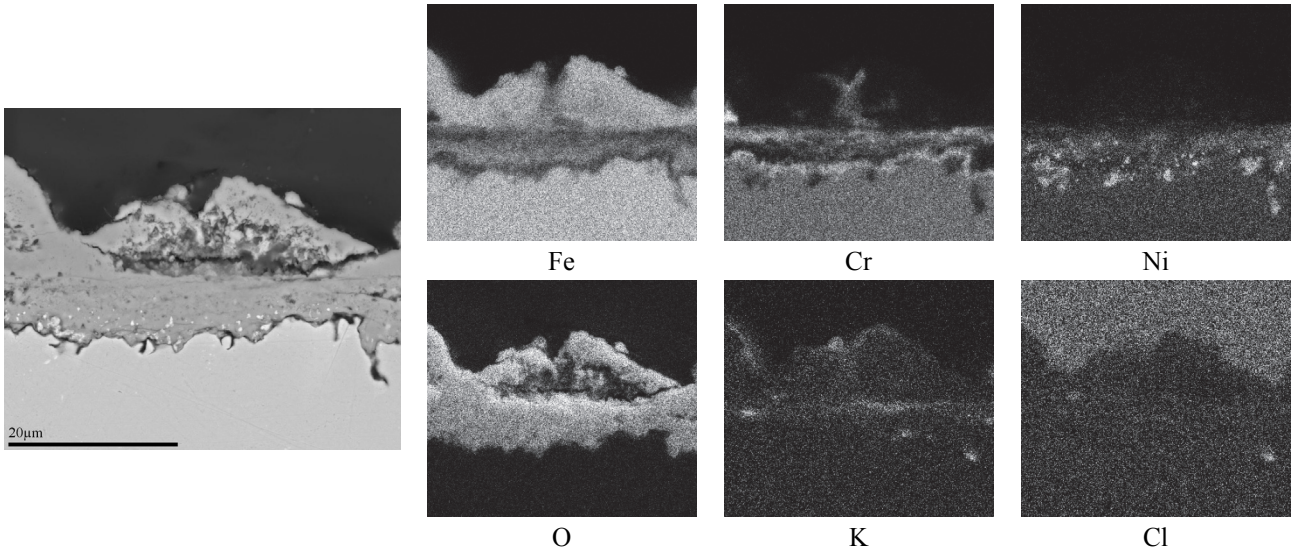

Figure 8: Distribution of alloying elements, potassium, chlorine and oxygen for TP347H. The chlorine response in the top of the chlorine map originates from the epoxy mount.

Sanicro 28 shows similar features to both TP347H and TP347HFG although it had much larger grains (ASTM grain size 4). In addition, a compound highly rich in potassium, chromium and oxygen could be detected. This compound was always located within the type A oxide (see Figure 9). Two layers of nickel enrichment, one in the middle part of the type B oxide and one in the underlying alloy were evident. Molybdenum enrichment was observed throughout the lower part of the type B oxide. No clear indication of chlorine could be detected in the mapped area.

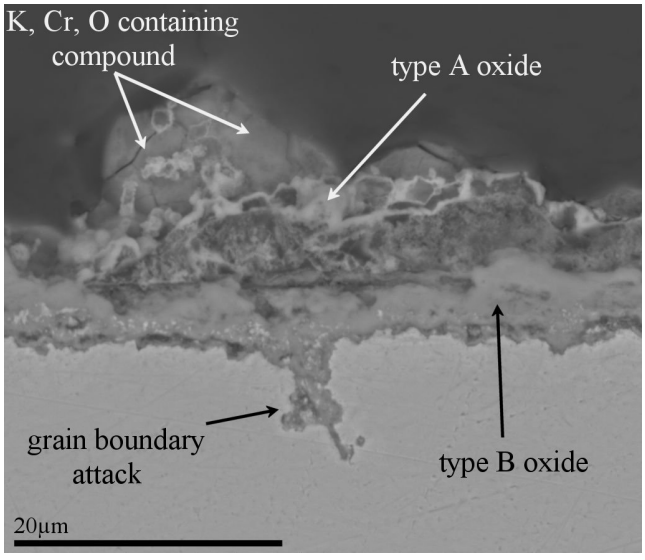

Figure 9: General morphology of corrosion on Sanicro28.

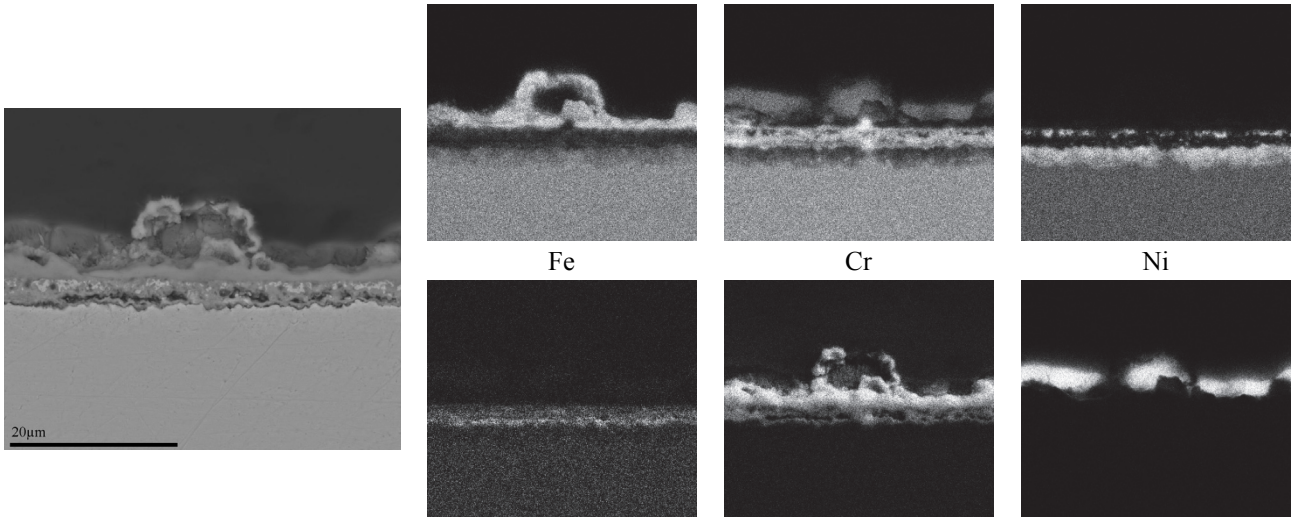

Figure 10: Distribution of alloying elements, potassium and oxygen on Sanicro 28.

3.2.2 Ferritic-Martensitic stainless steels EN1.4021, EN1.4057 and EN1.4521

Analogous to the austenitic grades, type A and type B oxides could be observed on the ferritic-martensitic stainless steels (Figure 11a-c); however, no grain boundary attack was identified. EDS mapping of the corrosion products are shown in Figures 12-13. Similar to that observed for the austenitic steels, the type A oxide is rich in iron as is the outer part of the type B oxide whereas the inner part of the type B oxide is rich in chromium. For EN 1.4021 and EN1.4057, potassium could be found localized within the type A oxide together with chromium. No clear enrichment of chlorine could be observed for these two alloys. For EN1.4521 potassium could be clearly seen in parts of the type A oxide and shows a clear correlation to chromium and molybdenum, see Figure 14. In addition, a slight indication of the presence of chlorine is observed along the middle part of the type B oxide. Molybdenum enrichment can be seen in the lower part of the type B oxide (in addition to the molybdenum in the type A oxide).

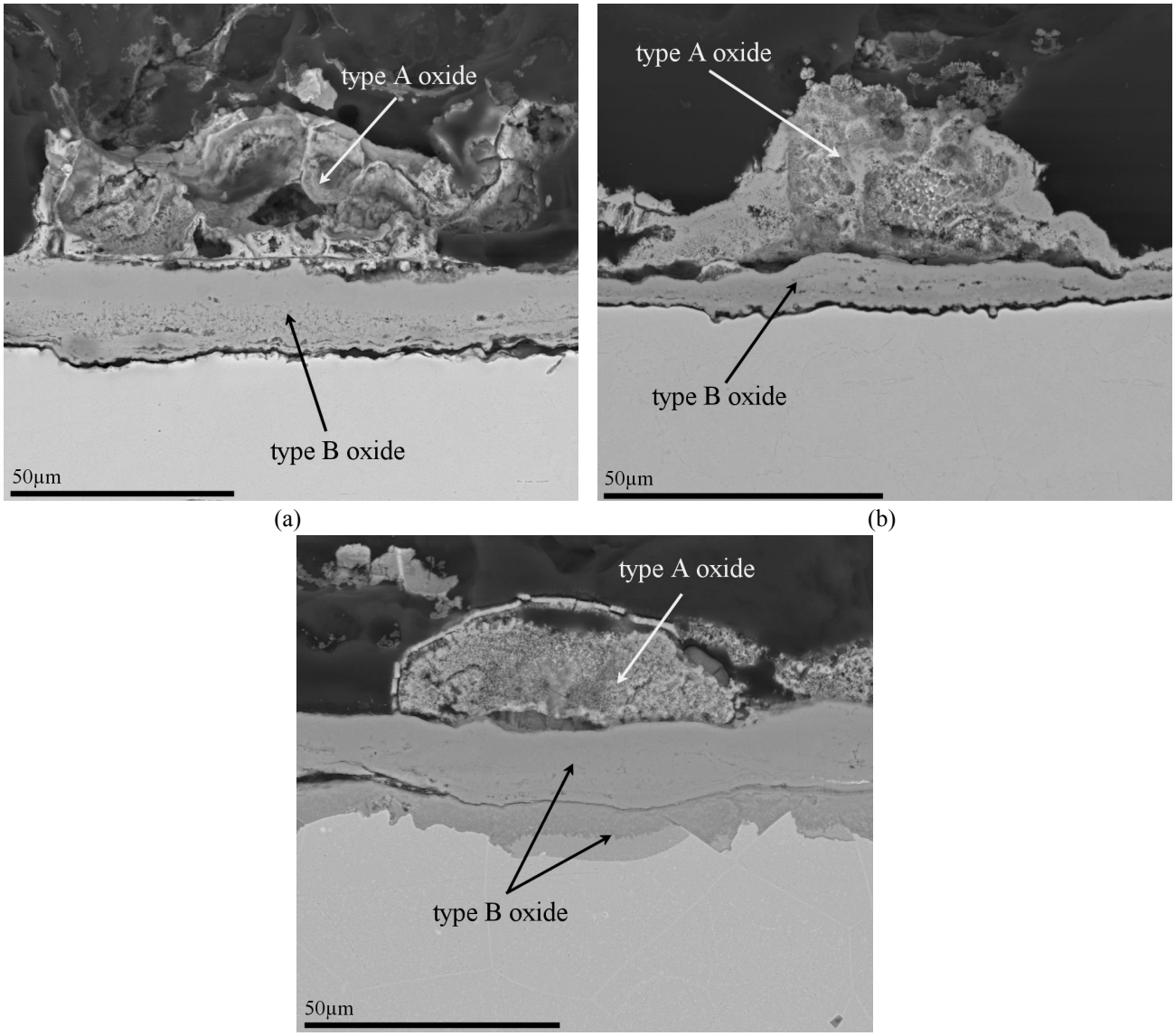

Figure 11: Microstructure of the ferritic-martensitic steels after the exposure (a) EN 1.4021 (b) 1.4057 (c) EN1.4521.

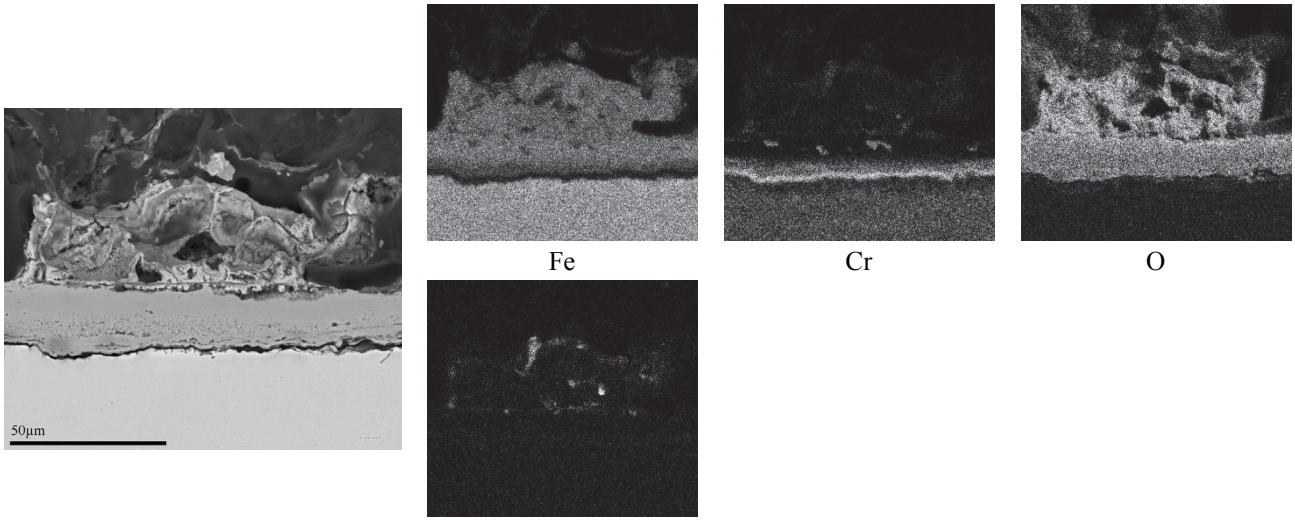

Figure 12: Distribution of the alloying elements, potassium and oxygen on EN1.4021.

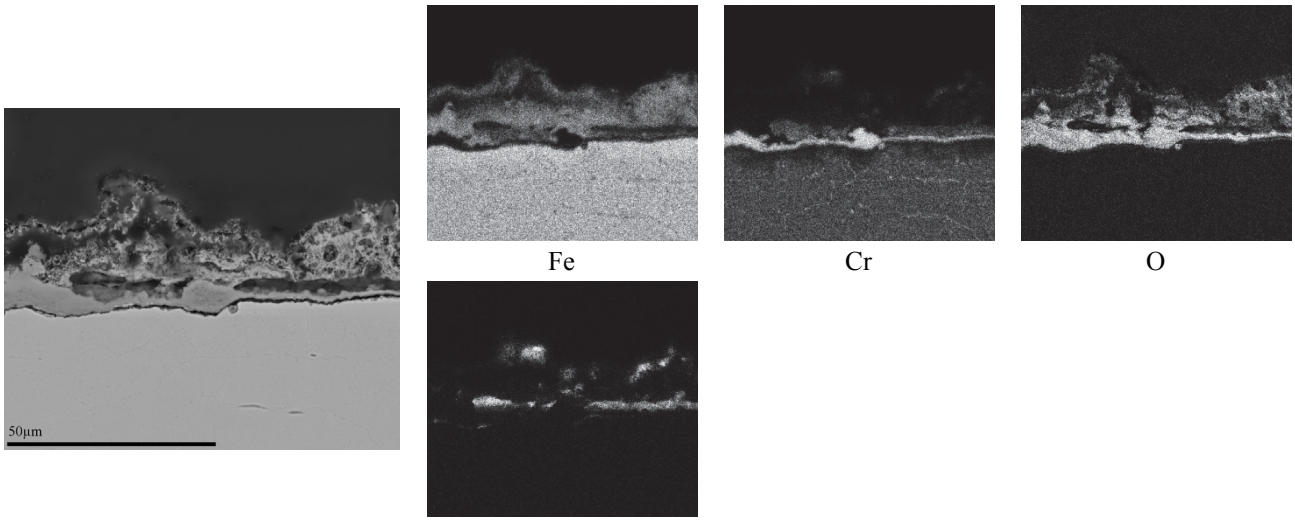

Figure 13: Distribution of the alloying elements, potassium and oxygen on EN1.4057.

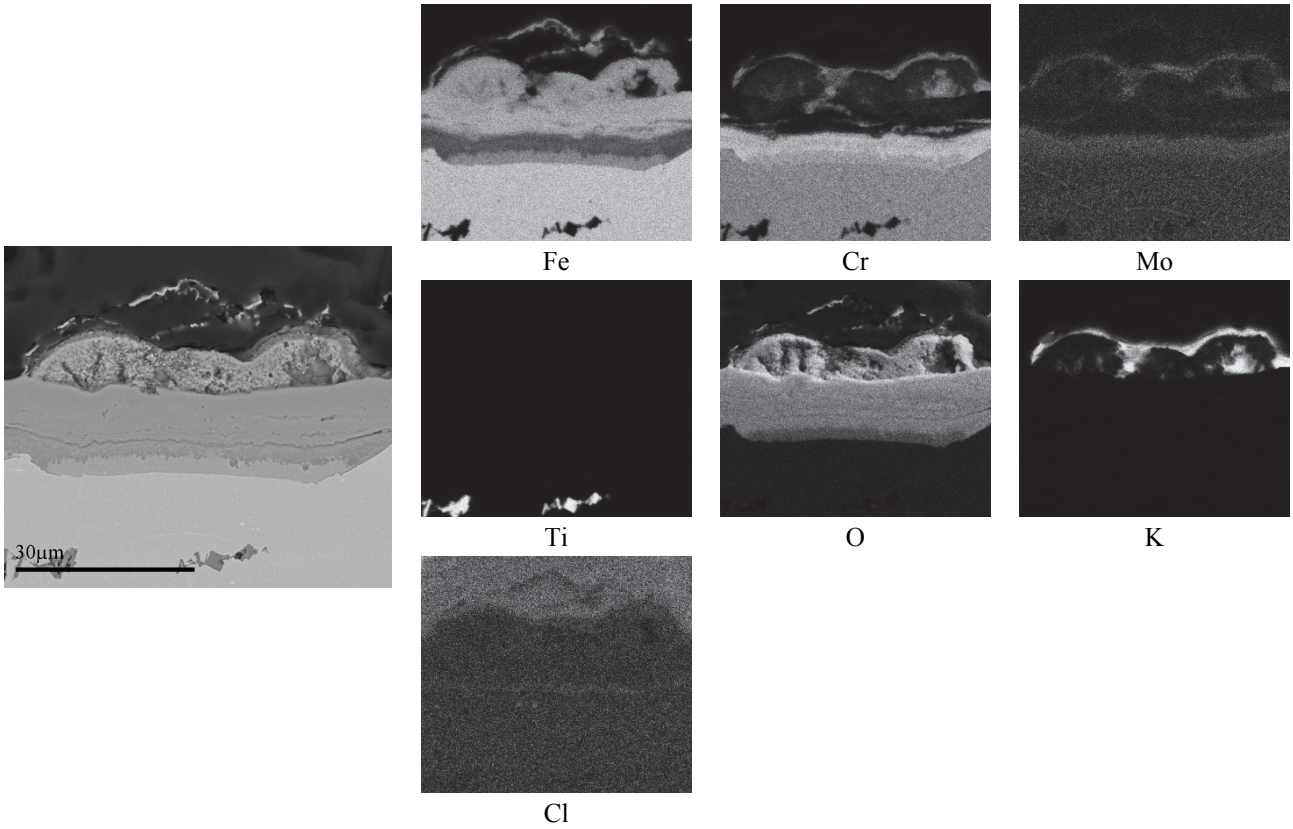

Figure 14: Distribution of the alloying elements, potassium, chlorine and oxygen on EN1.4521. The chlorine response in the top of the chlorine map originates from the epoxy. Ti-rich particle is part of the bulk alloy and is not related to the surface attack.

3.2.3 Nickel-based alloys

Alloy 263

The series 1 sample of this alloy showed no significant attack on the majority of the surface. However, in a few cases deep voids could be found along the grain boundaries (Figures 15a-b). At a few locations, large cavities in the form of shallow pits were observed. Often, immediately above the cavities, a spongy oxide was present on top of a thin continuous layer (Figure 15c). The distribution of the alloying elements revealed that all elements are removed from the alloy at the location of the cavity and are present in the type A oxide (Figure 16). This spongy oxide is porous and also contains potassium. Therefore it resembles the type A oxide observed on the steels, but with the important difference that iron is replaced with nickel. Similar to what was observed for the stainless steel EN1.4521 potassium, chromium and molybdenum were found at the same locations in the type A oxide. The cavities were filled with epoxy and could therefore not have formed due to the preparation. The thin continuous layer that separates the spongy oxide from the cavity appears from the EDS mapping to be an oxide layer highly enriched in titanium and aluminum. Only some molybdenum is left behind within the cavity where there seems to be a metallic phase. It is not possible to make a definitive statement about the distribution of chlorine due to the presence of chlorine within the epoxy.

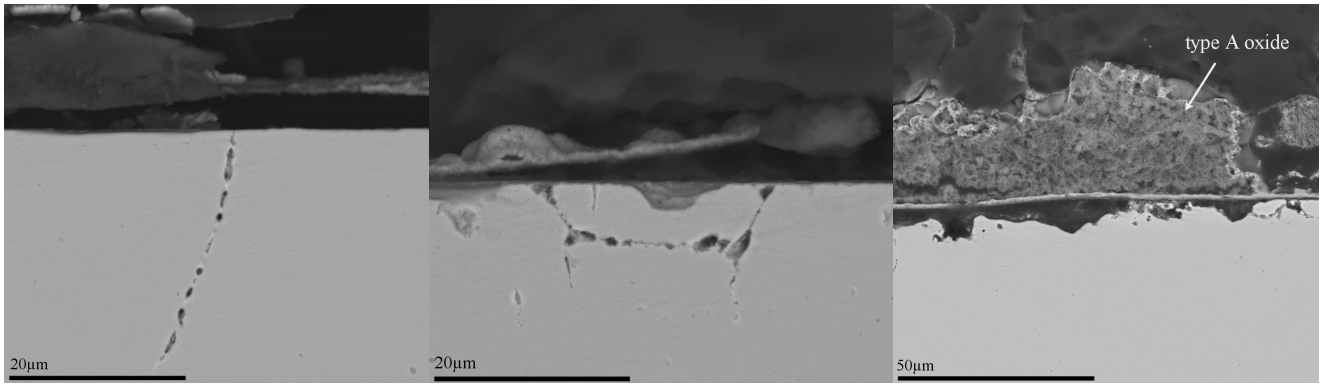

(a) (b) (c)

Figure 15: Two distinct corrosion morphologies could be observed on alloy 263 (series 1 sample) (a-b) local void formation (c) formation of shallow pit.

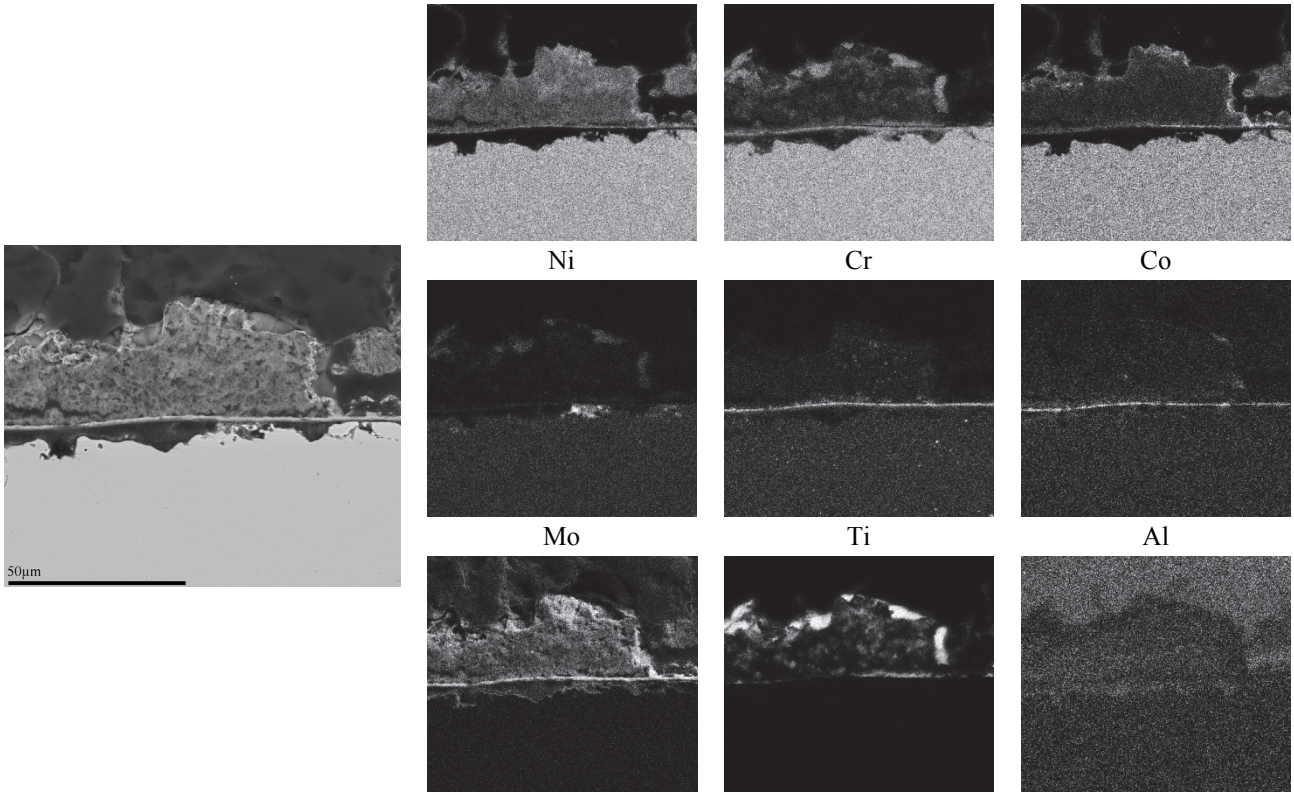

Figure 16: Distribution of the alloying elements, potassium, chlorine and oxygen on alloy 263 (series 1 sample). The chlorine response in the top and in the middle part of the chlorine map originates from the epoxy.

In contrast to the series 1 sample, the series 2 sample showed significant damage all over the surface. Similar to the iron-based alloys, type A and type B oxides could be found. However, unlike for the iron-based alloys, deep cavities (pits) and large nickel-rich islands were observed in the inner part of the type B oxide (Figure 17a). EDS mapping of the alloying elements is given in Figure 18. Evidently the type A oxide is rich in nickel, cobalt, potassium and contains some chromium, with chromium enrichment observed immediately above the cavity. The base of the

periphery of the cavity is enriched in nickel. The type B oxide shows nickel and cobalt enrichment in the outer dense parts and chromium enrichment in the inner parts. Large nickel-rich islands are observed in the inner part of the type B oxide. The contrast of the nickel-rich islands in the BSE micrographs indicates that they are metallic. No clear indication of chlorine could be seen in the mapped area. In a few cases, EDS spot analysis showed locations with potassium, titanium and oxygen (or potassium, molybdenum, chromium and oxygen) in the lower part of the type B oxide. An example of such morphology is shown in Figure 17b. The titanium/aluminum-rich oxide, observed on the series 1 sample, could not be found on this series 2 sample.

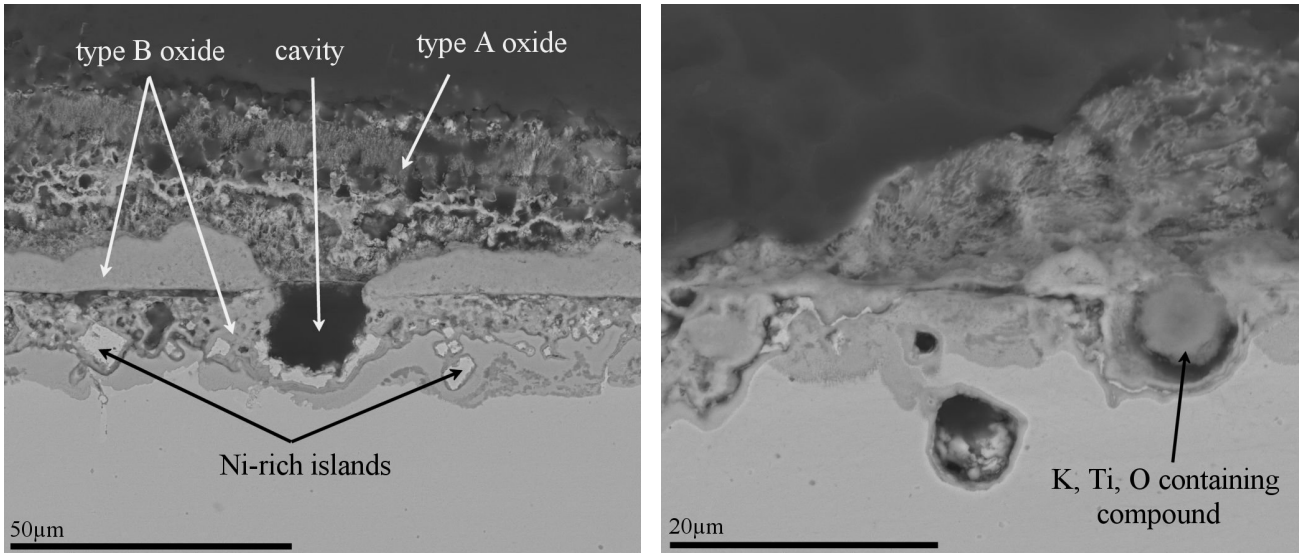

(a) (b)

Figure 17: (a) General morphology of corrosion on alloy 263 (series 2 sample) (b) Titanium, potassium, oxygen containing compound.

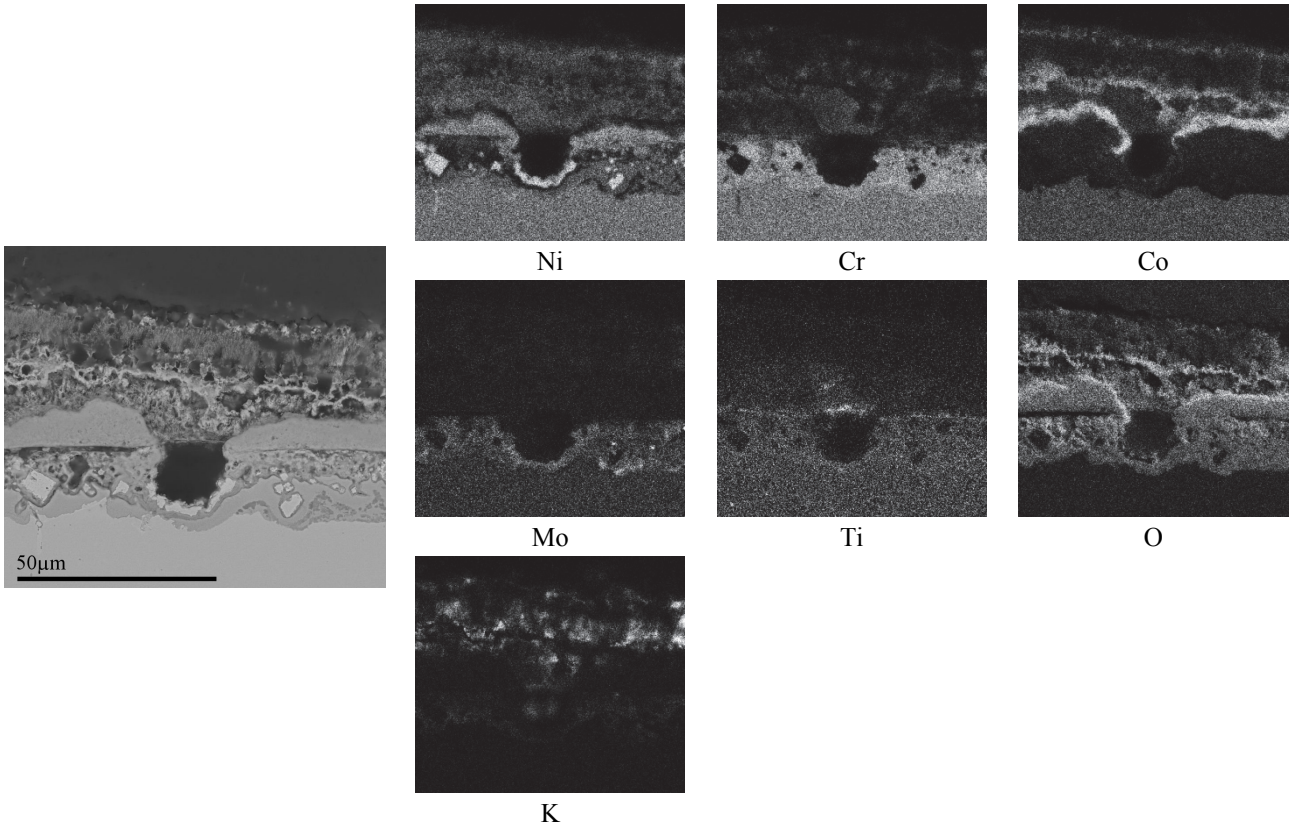

Figure 18: Distribution of the alloying elements, potassium and oxygen on alloy 263 (series 2 sample).

Alloy 625

Similar to alloy 263, the series 1 sample showed only local attack. The degradation was most often in the form of void formation relatively deep in the metal (Figure 19a-b). This was associated with selective removal of chromium, iron and niobium. In one case a shallow pit was found (Figure 19c).

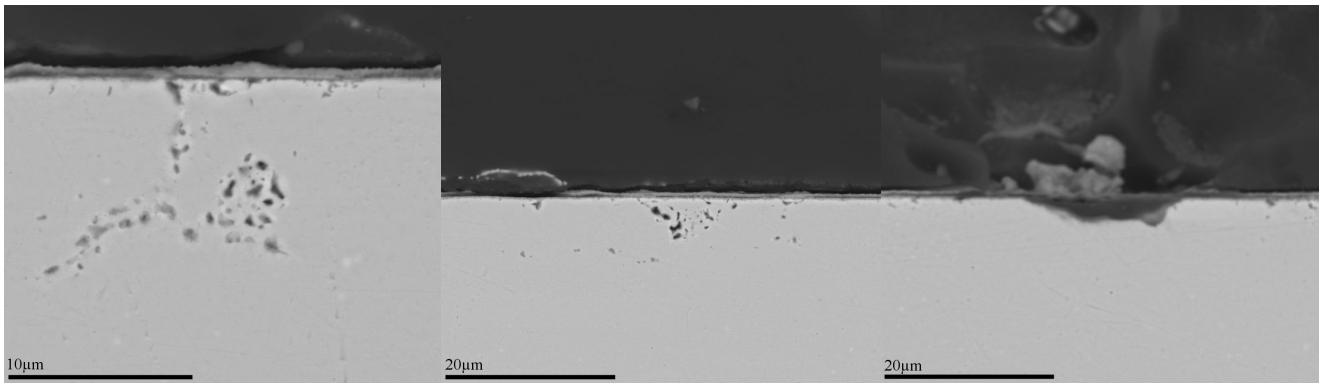

(a) (b) (c)

Figure 19: The morphology of corrosion on alloy 625 (series 1 sample) (a-b) local void formation (c) formation of a shallow pit.

The series 2 sample also showed local attack. However, compared to the series 1 sample the locations with attack were significantly more frequent in the series 2 sample. The dominant morphology consisted of shallow pits where most of the alloying elements had been removed to form a spongy oxide above the presumed original alloy surface, i.e. a type A oxide (Figure 20). Potassium was present in this oxide. Chlorine could also be detected among the corrosion products. However, due to partial loss of the corrosion product during preparation it is difficult to say which other elements are accompanying chlorine. Formation of local voids was frequently observed.

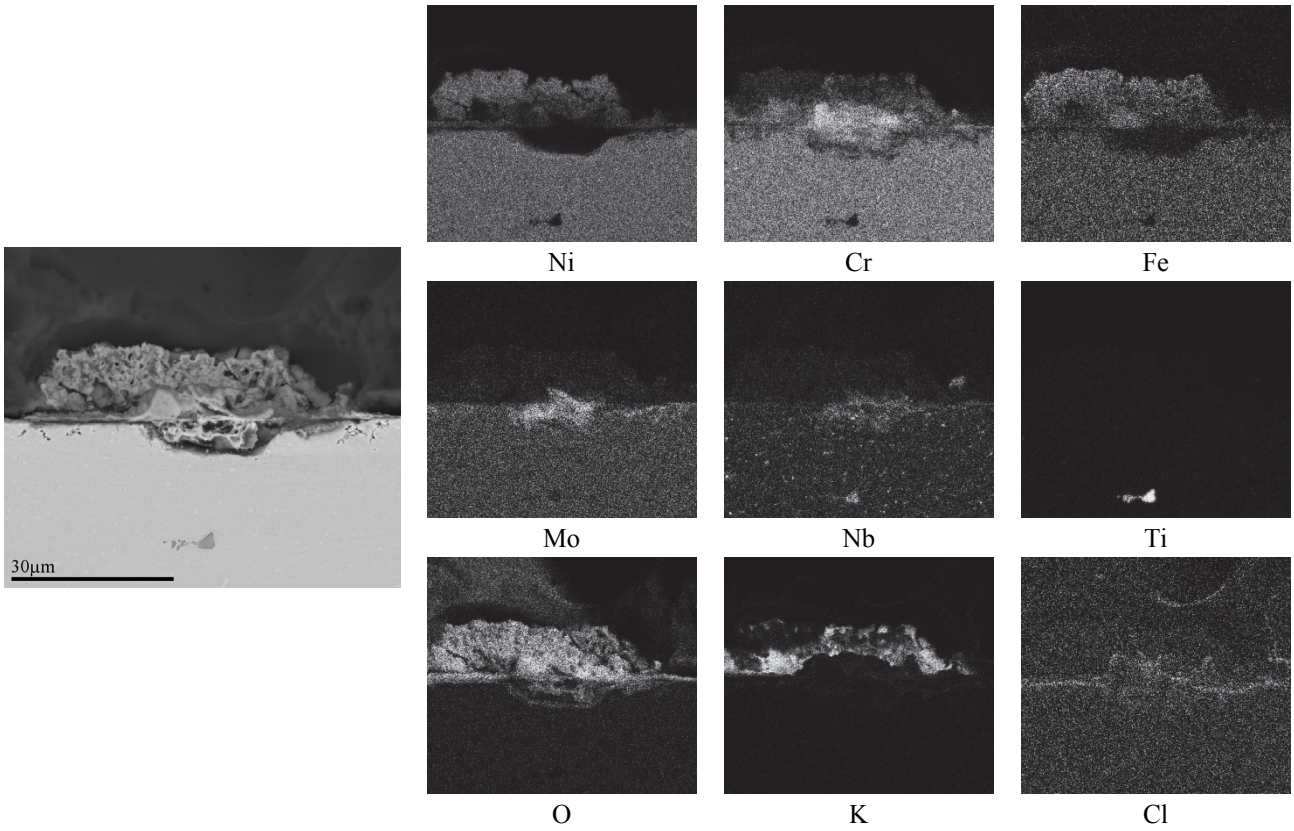

Figure 20: Distribution of the alloying elements, potassium, chlorine and oxygen on alloy 625 (series 2 sample). Note that the spongy oxide was partially lost during the preparation. Ti-rich particle is part of the bulk alloy and is not related to the surface attack A chlorine-free epoxy has been used for this sample.

Alloy C276

On alloy C276 void formation was very scarce and similar behavior could be seen for both surface qualities (series 1 and 2). Two types of morphologies could be observed. The first morphology consisted of shallow epoxy-filled pits with a spongy type A oxide on top (Figure 21a). The second morphology also consists of a spongy type A oxide but with what appears to be type B oxide at the lower part (see Figure 21b and EDS mapping in Figure 22). Chromium, molybdenum and tungsten are enriched in this oxide. In addition, a faint enrichment of potassium is also detected within the type B oxide. Type A oxide contains all the alloying elements present in alloy C276 as

well as potassium. However, the amount of molybdenum in type A oxide appears to be relatively low compared to the Mo content in the alloy. Chlorine could be found in the outer part of the type A oxide together with potassium. Similar to the sample in the salt-free exposure, a molybdenum and tungsten-enriched phase was found in the unaffected alloy close to the surface; this phase appears as white particles in the matrix in Figures 21-22.

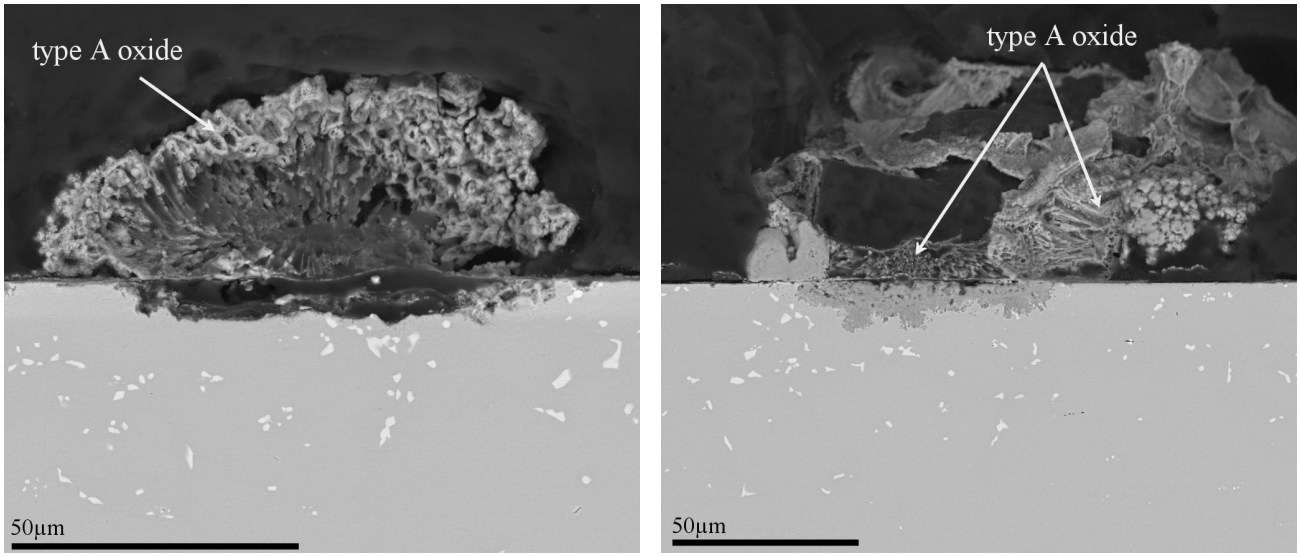

(a) (b)

Figure 21: General corrosion morphologies on alloy C276 (series 2 sample).

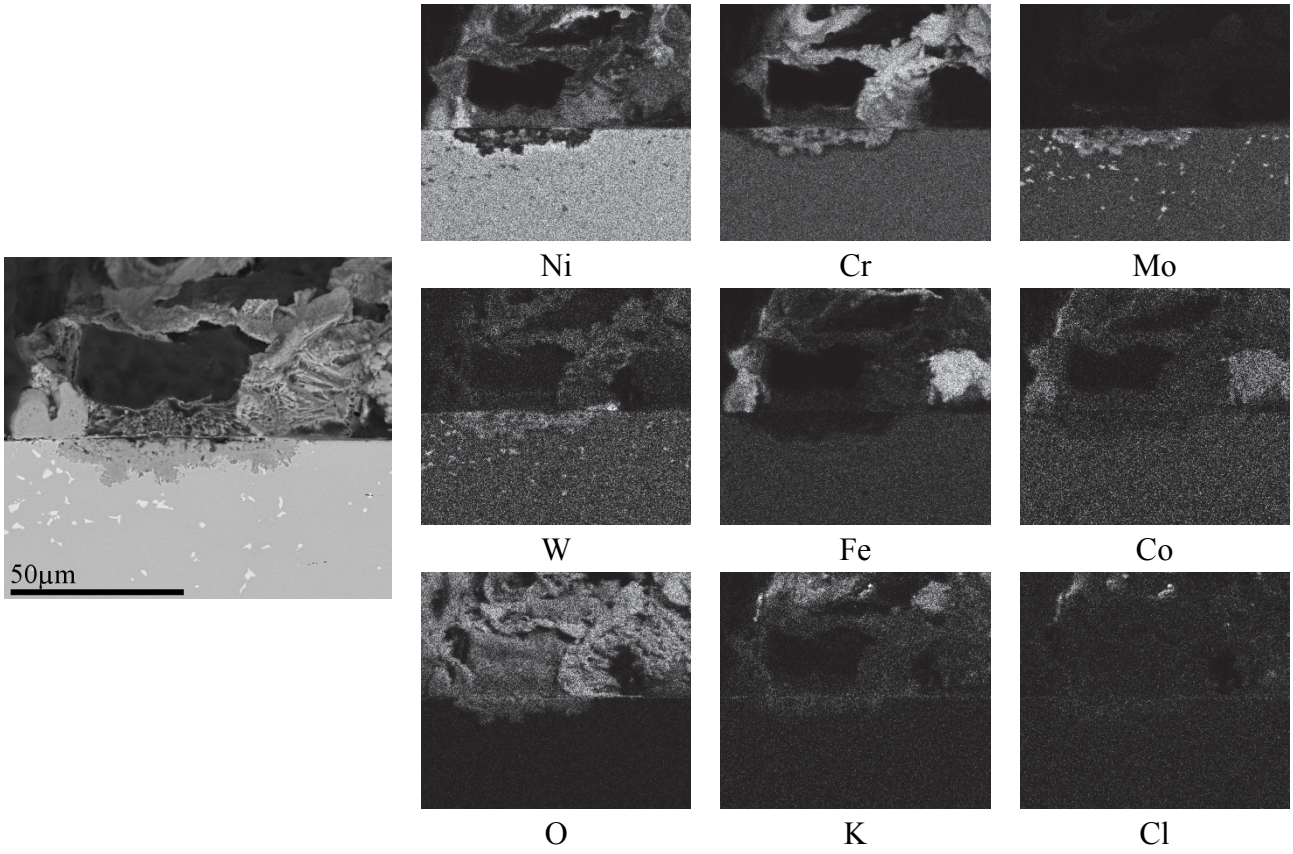

Figure 22: Distribution of the alloying elements, potassium, chlorine and oxygen on alloy C276 (series 2 sample). A chlorine-free epoxy was used for this sample.

3.3 Exposure in static lab air+KCl(g)

None of the exposed alloys (Sanicro 28, alloy 263 and alloy 625) formed a protective oxide during exposure in static lab air+KCl (g). On alloys 263 and 625, a double layered oxide was formed with a flat line in the middle, presumably the original alloy surface (Figure 23a-b). According to EDS spot analysis (not shown here), the outer oxide on alloy 263 was rich in nickel and cobalt. The inner oxide showed chromium enrichment compared to the outer oxide. Underneath these two oxide layers, voids were observed at several locations. Such voids were always associated with significant chromium and titanium depletion. The morphology of corrosion products on alloy 625 is similar to that on alloy 263, however instead of cobalt in the outer oxide layer, now iron is detected. Sanicro 28 showed general void formation on large parts of the surface (Figure 23c). Although the general attack was shallow (~5-10µm), at the grain boundaries void formation extended substantially deeper (Figure 23d). EDS mapping of the alloying elements in such a region clearly shows selective removal of chromium and iron, coupled to enrichment of nickel and molybdenum (Figure 24). Potassium without chlorine could be found in the oxide while a clear chlorine response was found at the grain boundary penetrating deep into the metal.

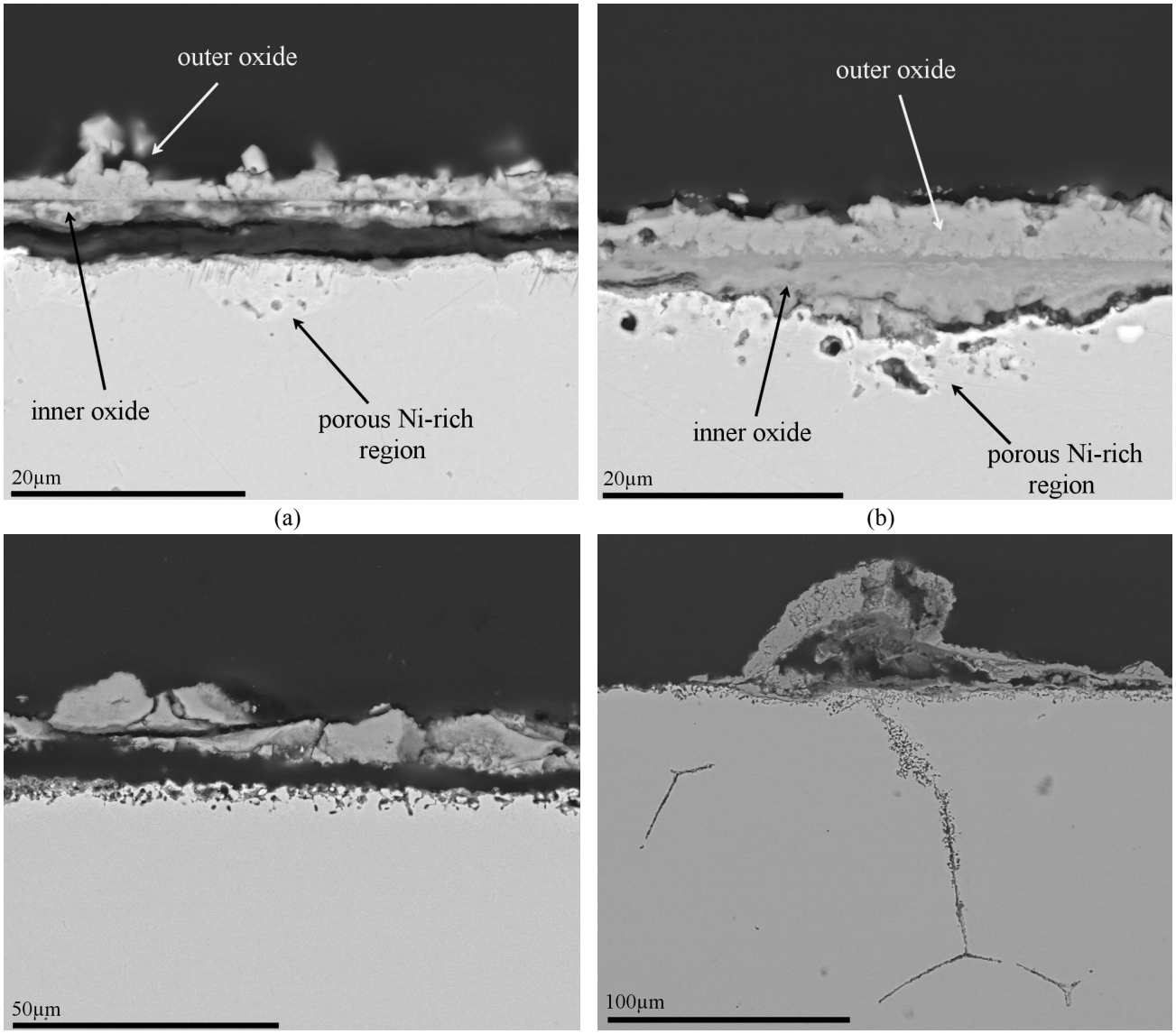

Figure 23: General morphology of corrosion on (a) alloy 263 (b) alloy 625 and (c) Sanicro28 exposed under static lab air+KCl(g). (d) Grain boundary attack on Sanicro 28.

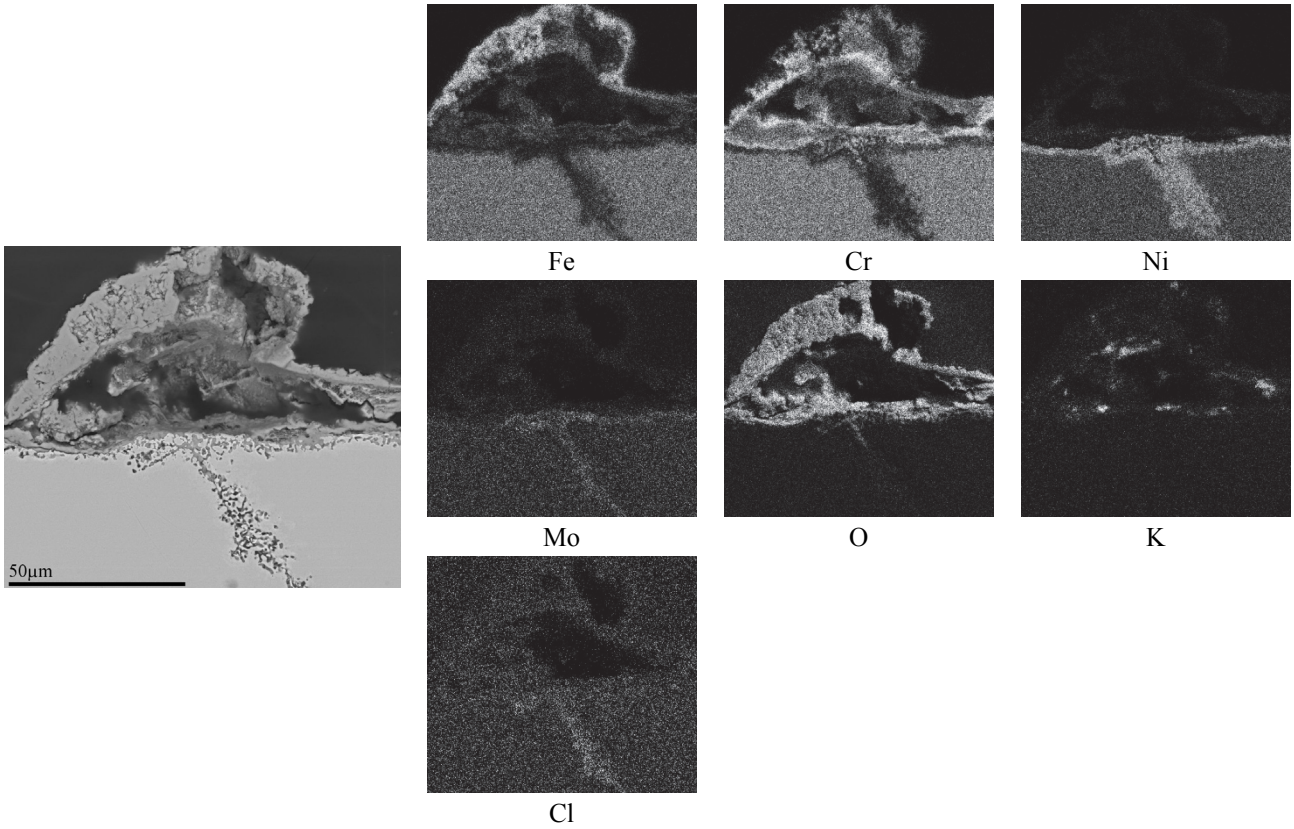

Figure 24: Distribution of the alloying elements, potassium, chlorine and oxygen on Sanicro 28 exposed in static lab air+KCl(g). A chlorine-free epoxy was used for this sample.

4. Discussion

4.1 Reference Exposure in N_2(g)+5%O_2(g)+15%H_2O(g)

In a flowing O_2(g)+H_2O(g) atmosphere chromium can evaporate in the form of chromic acid, $CrO_2(OH)_2$, thereby depleting the original protective oxide layer of chromium. If chromium diffusion to the surface is not sufficient to replenish the chromium level in the oxide, a duplex oxide layer is formed with an outer iron-rich oxide and an inner chromium rich oxide [19][20]. The more excessive oxidation observed for TP347H compared to the passive behavior observed on TP347HFG and Sanicro 28 is in agreement with the existing literature concerning laboratory investigations into steam oxidation of stainless steels [21], [22]. This oxidation behavior for TP347H can be attributed to the lower chromium content as compared to Sanicro 28 (20.2 at% vs 30.5 at%). In addition, the poor performance of this steel compared to its fine-grain variant TP347HFG is consistent with the known effect of grain size on oxidation resistance; a higher grain boundary density enables a larger outward flux of chromium atoms to maintain a uniform chromium-rich oxide layer. Moreover, the better performance of the ferritic-martensitic grades EN1.4021 and EN1.4057 (containing 14.7 at% and 19.4 at% chromium respectively) compared to TP347H can be explained by faster diffusion of chromium in a ferritic matrix compared to chromium diffusion in an austenitic matrix [23].

The failure of EN1.4521 (containing 20.5 at% chromium) cannot be related to the chromium content as EN1.4021 and EN1.4057 did not develop fast-growing oxides. The microstructure of EN1.4521 shows that a molybdenum-enriched phase has formed along grain boundaries and as discrete particles inside the grains (Figure 2c). Equilibrium calculations with Thermo-Calc [18] indicate that several molybdenum-enriched phases (σ, χ, μ and Laves phase) can form at 600°C in this steel. As an example, the formation of Fe_2Mo Laves phase in molybdenum-containing ferritic-martensitic and austenitic stainless steels around 600°C has been reported in the literature [24], [25]. The molybdenum-enriched phase at the grain boundaries will probably affect the diffusive flux both along and across grain boundaries. This could have led to the observed corrosion behavior as lowering the chromium-flux toward the surface will reduce the amount of chromium available to sustain a chromium-rich oxide layer.

For the nickel-based alloys, low intensity peaks in the diffractogram (Figure 4) makes unambiguous phase analysis difficult. However, the slight background elevation near 36.7° and 86.4° suggests the presence of Cr_2O_3 on alloys 263 and 625. On alloy C276 small peaks near 36.7° and 55° indicate Cr_2O_3 formation. In addition, analysis of an unexposed sample with XRD revealed that the majority of the observed peaks belongs to a precipitate phase in the matrix which, according to EDS, is enriched in molybdenum and tungsten (see the white particles in Figure 21). This phase is believed to have formed during the annealing procedure and was only observed relatively close to the surface. Therefore formation of this phase could be a consequence of favorable nucleation sites and faster diffusion kinetics introduced by non-uniform deformation during rolling. Thus, subsequent annealing at a high temperature (e.g. at 1150°C) leads to nucleation of this phase.

4.2 Exposure in N_2(g)+5%O_2(g)+15%H_2O(g) under KCl(s)

Despite the resistant behavior of the majority of the alloys under the salt-free exposure, they all failed to form a protective oxide when KCl was present. This can be explained using reaction 1 showing that the original chromium-rich oxide reacts with potassium to form chromate [2]. Consequently all alloys relying on chromia for protection suffer from (at least an initial) corrosive attack by this mechanism. Therefore, the series of events taking place after the initial breakdown, especially involvement of other species, determines how much damage will eventually be incurred. In fact, many of the results strongly suggest a contribution from chlorine to propagate the attack. Further discussion regarding such effects as well as the resulting corrosion product morphologies is given in the following sections.

4.2.1 Stainless steels

As mentioned before two distinct oxide morphologies, referred to as type A and type B, could be seen on all the exposed stainless steels. Such differentiation has also been reported by Enestam et al. [26]. The difference in corrosion product morphology is related to the mechanism of its formation. Since type A oxide was not observed after salt-free exposure (see Figures 2a and b), its formation is directly related to the presence of KCl. Jonsson et al. [27] and Folkeson et al. [28] studied KCl-induced high temperature corrosion of Fe-2.25Cr-1Mo (wt%) steel and attributed the morphology of the outermost iron oxide to the oxidation of metastable $FeCl_2$ in a KCl-$FeCl_2$ eutectic mixture. In

other words, chlorine is somehow extracted from KCl and plays a role in the oxide formation. The exact mode of chlorine extraction is not clear. However, it is noted that for both Fe-base and Ni-base alloys, potassium without chlorine can often be found in the corrosion product morphology (see Figures 10, 12, 13, 14, 16, 18 and 20). This shows that chlorine evolution during the exposure of alloys to KCl(s) has taken place and is a strong indication that the evolved chlorine can also play a role in the course of corrosion. One possible reaction that evolves chlorine is reaction 1. However, contribution from other chlorine-evolving mechanisms cannot be excluded.

Unlike the type A oxide, the dense morphology of type B oxide and its similarity to the oxide formed during the salt-free exposure (e.g. compare Figures 11c and 2b) suggests that the mechanism of its formation is similar to the oxidation under $O_2(g)+H_2O(g)$.

The extent of corrosion damage (Figure 5) indicates that for the stainless steels, a general improvement in corrosion resistance is observed with an increase in chromium content and/or diffusivity. This means that under the experimental conditions of this study, regardless of what might have happened during the early stages of attack, eventually a chromium-rich oxide can form and slow down the corrosion rate. Similar extents of damage observed for TP347H and TP347HFG do not comply with the above-mentioned argumentation. However, it needs to be considered that the accuracy of the measurement method (5μm) makes it difficult to make a conclusive comparison between these two alloys.

Similar to the salt-free exposure, the poor performance of EN1.4521 (containing 20.5 at%Cr) compared to EN1.4057 (containing 19.4 at%Cr) can be attributed to the presence of the molybdenum-rich phase along the grain boundaries leading to a reduction of the outward chromium flux.

4.2.2 Nickel-based Alloys

The nickel-based alloys considered in this study showed three different corrosion product morphologies: void formation, pitting and double layer oxide. Montgomery et al. [11] studied the corrosion behavior of selected iron-base and nickel-base chromia-forming alloys in a Danish biomass-firing power plant and ascribed void formation to the selective removal of chromium by chlorine according to a chlorination-evaporation-oxidation sequence [29], [30]. The features shown in Figures 15a-b could be related to the volatilization of chromium (and other alloying elements) as chlorides.

To the author's knowledge, when the temperature is below the melting point of the salt, pitting has not been addressed in the literature for high temperature corrosion solely due to alkali chlorides. In salt-induced high temperature corrosion the formation of local pits is usually attributed to molten salt-corrosion (type II hot corrosion) [23]. The presence of potassium-containing porous corrosion products on top of pits (e.g. Figure 15c) supports the hypothesis that a similar molten-salt corrosion mechanism applies for the present case. Fontana [31] states that *"A porous, non-protective oxide in the salt is a trademark of hot corrosion"*. However, unlike that observed for the hot corrosion by sulfate melts, where corrosion products in pits consist of oxides and sulfides, the absence of

corrosion products in the pits suggests the involvement of volatile species, such as metal chlorides. Transition metal chlorides are generally volatile at high temperatures and tend to form low melting point eutectic mixtures with KCl (see data in [33]). The lack of depletion/enrichment phenomena in the underlying alloy indicates that the attack has been very fast. However, whether the mass transport takes place through a gas phase or a liquid phase (or in both) is unclear. The observation that void formation in alloy C276 was scarce can perhaps be attributed to its small carbon content. It is believed that presence of chromium carbides aggravates the selective attack for chlorine-induced high temperature corrosion [34], [35].

The non-uniformity in corrosion product morphology especially observed on the Ni-base alloys (e.g. compare Figure 15b and c) is attributed to the heterogeneity of the salt/surface interface. At some locations the alloy surface is in direct contact with the salt particles, while other locations are only in contact with gaseous KCl. In addition, although a narrow particle size distribution was chosen for the salt (63-90μm), a variation in particle size will translate into a difference in the abundance of potassium and chlorine at different locations. Non-uniformity may be further introduced by some small salt particles sintering together and locally creating large aggregates.

The observation that large parts of the surface on the series 1 samples of alloys 625 and 263 were not attacked, indicates that a protective oxide has been present from the beginning. This is strongly supported by the presence of a thin aluminum and titanium-enriched oxide layer present on alloy 263 series 1 (see Figure 16) and the absence of such an oxide on the corresponding series 2 sample. This would also explain the observation that on the series 2 samples, the attack was distributed more evenly across the surface; probably due to removal of the original oxide by the coarser grinding paper (1000 grit-SiC paper for series 2 as compared to 4000 grit SiC paper for series 1). The oxide was formed during heat treatment in $Ar(g)+H_2(g)$ performed on the nickel-based alloys, where a small amount of oxygen or nitrogen impurity will be sufficient to react with chromium, niobium and in particular with aluminum and titanium. Apparently grinding with only 4000 grit SiC paper did not effectively remove this oxide layer. Absence of any effect from a preformed oxide in alloy C276 can be attributed to the lack of considerable amounts of aluminum, titanium and niobium in this alloy and that a thin preformed chromia layer will react with KCl according to reaction 1. As the nickel-based alloys tested in the salt-free exposure were all series 1, the presence of a preformed oxide casts doubt on the reliability of the results obtained in that test for these alloys. However, comparison between the series 1 samples and the salt-free exposures showed that even the preformed oxide could not protect the alloy. In fact, the depth of worst case damage on the nickel-based alloys was similar for both series 1 and 2 samples.

4.2.3 Exposure in static air+KCl(g)

The corrosion morphology observed on the samples exposed to KCl vapor provides additional information with respect to corrosion mechanisms. Most importantly KCl(g) is able to break the original chromia layer present on these alloys. An equilibrium calculation with Thermo-Calc [18] (using TAB module) yields a value of only 4 ppm for the total vapor pressure of KCl species i.e. $KCl(g)+K_2Cl_2(g)$ at 600^oC. As the initial chromia scale is very thin at this relatively low

temperature, even this small amount of KCl is able to damage it by formation of potassium chromate. It must also be considered that the calculation does not take into account kinetic effects and it is likely that a continuous release of KCl species into the gas phase and onto the samples occurs in the furnace. A similar effect from KCl(g) has been reported by Pettersson et al. [36] and Segerdahl et al. [37] as well. This explains the attack all over the surface of the salt-covered samples even at the locations where there is no direct contact between the salt and the alloy. Furthermore this vapor-induced corrosion implies that KCl(g) can play a role in continuation of the attack for the salt-covered samples. This can be the case when solid KCl in direct contact with the alloy is completely consumed and/or when the distance between the unreacted solid KCl and the unaffected alloy is large as a result of the formation of voluminous corrosion products.

On alloys 263 and 625 the double layer morphology of the oxide illustrates the inward-growing and outward-growing oxides. In addition, voids are observed at the metal/oxide interface indicating the chlorine-attack (see the previous section). Another interesting observation is the absence of type A oxide in the experiment with the salt vapor. This can be an indication that a liquid state, e.g. KCl-$FeCl_2$, is involved in the formation of the outermost oxide.

The KCl(g) attack on Sanicro 28 illustrates the importance of grain boundaries. Although there is a general selective corrosion on the alloy (Figure 23c), the local selective corrosion at the grain boundary is at least one order of magnitude more severe (5-10µm compared to ~130µm, see Figure 23d). The distribution of the alloying elements in Figure 24 clearly shows the selective nature of the attack. The large depth of chromium and iron removal further supports the hypothesis of removal in the form of subliming chlorides rather than solid state diffusion. Finally, a comparison of the performance of Sanicro 28 exposed in flowing N_2(g)+5%O_2(g)+15%H_2O(g) under KCl(s) with that exposed to KCl(g) shows the importance of the experimental conditions. Although in the former condition, a large amount of salt is supplied the contribution from chlorine in the attack appears to be less compared to that for the exposure to KCl(g). That a high chromium-containing stainless steel like Sanicro 28 is showing a significant difference between the two conditions has implications for material selection in KCl-containing environments. In other words, depending on the gas phase composition and dynamics, employing a highly alloyed material may or may not be a remedy towards the high temperature corrosion.

5. Conclusions

Under the experimental conditions of the present study the following conclusions can be drawn:

- Stainless steels TP347H and EN1.4521 develop fast-growing oxides even without the KCl. The original chromium-rich oxide on these alloys breaks down within 168h in N_2(g)+5%O_2(g)+15%H_2O(g) at 600^{o}C. In addition, it is indicated that the presence of a molybdenum-rich phase along the grain boundaries is detrimental for the oxidation resistance.

- All the alloys investigated in this study suffered from an accelerated attack when a KCl(s) layer was present on the surface.

- Compared to the currently used austenitic stainless steel TP347HFG, the following materials indicated slightly less corrosion damage in the laboratory exposure in N_2(g)+5%O_2(g)+15%H_2O(g) under KCl(s): EN1.4057, Sanicro 28 and alloy 625.

- On iron-based alloys, generally an improved corrosion performance was observed for a higher chromium content when the exposure was performed under N_2(g)+5%O_2(g)+15%H_2O(g)+KCl(s). This improved performance was for the range of 14-19 at% chromium for ferritic stainless steels and 19-28 at% for the austenitic grades, for the nickel-based alloys no clear trend was observed.

- At a temperature of 600^{o}C in static laboratory air, the generated vapor pressure of KCl(g) is enough to breakdown the initial chromium-rich oxide on the alloys that rely on chromia for protection. In addition, even with the small concentration of chlorine-bearing species a remarkable effect from chlorine could be observed. The observed role of KCl(g) has implications for corrosion continuation when the solid KCl in direct contact with the metal is consumed.

- Sanicro 28 exposed to KCl(g) in static lab air had much deeper attack than when it was exposed under solid KCl in flowing N_2(g)+5%O_2(g)+15%H_2O(g). This shows that gas phase composition and dynamics play a significant role in the extent of damage due to KCl-induced high temperature corrosion.

Acknowledgements

This work was performed within the framework of the project GREEN financed by the Danish Council for Strategic Research. John C. Troelsen and Peter J.S. Westermann are acknowledged for their help and technical support during this work. Haynes® International is greatly appreciated for provision of alloys 625, 263 and C276.

References

[1] M. Montgomery, S. A. Jensen, U. Borg, O. Biede, and T. Vilhelmsen, “Experiences with high temperature corrosion at straw-firing power plants in Denmark,” *Mater. Corros.*, vol. 62, no. 7, pp. 593–605, Jul. 2011.

[2] J. Pettersson, H. Asteman, J.-E. Svensson, and L.-G. Johansson, “KCl Induced Corrosion of a 304-type Austenitic Stainless Steel at 600°C; The Role of Potassium,” *Oxid. Met.*, vol. 64, no. 1–2, pp. 23–41, Aug. 2005.

[3] J. Pettersson, N. Folkeson, L.-G. Johansson, and J.-E. Svensson, “The Effects of KCl, K2SO4 and K2CO3 on the High Temperature Corrosion of a 304-Type Austenitic Stainless Steel,” *Oxid. Met.*, vol. 76, no. 1–2, pp. 93–109, Mar. 2011.

[4] Y. Shinata and Y. Nishi, “NaCl-induced accelerated oxidation of chromium,” *Oxid. Met.*, vol. 26, pp. 201–212, 1986.

[5] Y. Shinata, “Accelerated oxidation rate of chromium induced by sodium chloride,” *Oxid. Met.*, vol. 27, pp. 315–332, 1987.

[6] Y. S. Li, M. Sanchez-Pasten, and M. Spiegel, “High Temperature Interaction of Pure Cr with KCl,” *Mater. Sci. Forum*, vol. 461–464, pp. 1047–1054, 2004.

[7] J. Lehmusto, D. Lindberg, P. Yrjas, B.-J. Skrifvars, and M. Hupa, “Studies on the Partial Reactions Between Potassium Chloride and Metallic Chromium Concerning Corrosion at Elevated Temperatures,” *Oxid. Met.*, Nov. 2011.

[8] J. Lehmusto, B.-J. Skrifvars, P. Yrjas, and M. Hupa, “High temperature oxidation of metallic chromium exposed to eight different metal chlorides,” *Corros. Sci.*, vol. 53, no. 10, pp. 3315–3323, Oct. 2011.

[9] J. Lehmusto, D. Lindberg, P. Yrjas, B.-J. Skrifvars, and M. Hupa, “Thermogravimetric studies of high temperature reactions between potassium salts and chromium,” *Corros. Sci.*, Mar. 2012.

[10] J. Lehmusto, P. Yrjas, B. J. Skrifvars, and M. Hupa, “Detailed Studies on the High Temperature Corrosion Reactions between Potassium Chloride and Metallic Chromium,” *Mater. Sci. Forum*, vol. 696, pp. 218–223, Sep. 2011.

[11] M. Montgomery and A. Karlsson, “In-situ corrosion investigation at Masnedø CHP plant - a straw-fired power plant,” *Mater. Corros.*, vol. 50, pp. 579–584, 1999.

[12] M. Montgomery, A. Karlsson, and O. Larsen, “Field test corrosion experiments in Denmark with biomass fuels. Part 1: Straw-firing,” *Mater. Corros.*, vol. 53, no. 2, pp. 121–131, 2002.

[13] H. Fujikawa and N. Maruyama, “Corrosion behaviour of austenitic stainless steels in the high chloride-containing environment,” *Mater. Sci. Eng. A*, vol. 20, pp. 301–306, 1989.

[14] N. Hiramatsu, Y. Uematsu, T. Tanaka, and M. Kinugasa, “Effects of alloying elements on NaCl-induced hot corrosion of stainless steels,” *Mater. Sci. Eng. A*, vol. 120–121, pp. 319–328, Nov. 1989.

[15] T. Ishitsuka, “Stability of protective oxide films in waste incineration environment - solubility measurement of oxides in molten chlorides,” *Corros. Sci.*, vol. 44, 2002.

[16] Y. S. Li, M. Spiegel, and S. Shimada, “Effect of Al/Si addition on KCl induced corrosion of 9% Cr steel,” *Mater. Lett.*, vol. 58, no. 29, pp. 3787–3791, Nov. 2004.

[17] Y. S. Li, Y. Niu, and M. Spiegel, “High temperature interaction of Al/Si-modified Fe–Cr alloys with KCl,” *Corros. Sci.*, vol. 49, no. 4, pp. 1799–1815, Apr. 2007.

[18] J. Andersson, T. Helander, and L. Höglund, “Thermo-Calc & DICTRA, computational tools for materials science,” *Calphad*, vol. 26, no. 2, pp. 273–312, 2002.

[19] H. Asteman, J. E. Svensson, and L. G. Johansson, “Indication of chromium oxide hydroxide evaporation during oxidation of 304L at 873 K in the presence of 10% water vapor,” *Oxid. Met.*, vol. 52, no. 1, pp. 95–111, 1999.

[20] H. Asteman, J. E. Svensson, M. Norell, and L. G. Johansson, “Influence of water vapor and flow rate on the high-temperature oxidation of 304L; effect of chromium oxide hydroxide evaporation,” *Oxid. Met.*, vol. 54, no. 1, pp. 11–26, 2000.

[21] A. N. Hansson, K. Pantleon, F. B. Grumsen, and M. A. J. Somers, “Microstructure Evolution During Steam Oxidation of a Nb Stabilized Austenitic Stainless Steel,” *Oxid. Met.*, vol. 73, no. 1–2, pp. 289–309, Oct. 2009.

[22] B. Pujilaksono, T. Jonsson, H. Heidari, M. Halvarsson, J.-E. Svensson, and L.-G. Johansson, “Oxidation of Binary FeCr Alloys (Fe–2.25Cr, Fe–10Cr, Fe–18Cr and Fe–25Cr) in O2 and in O2 + H2O Environment at 600 °C,” *Oxid. Met.*, vol. 75, no. 3–4, pp. 183–207, Jan. 2011.

[23] D. J. Young, *High Temperature Oxidation and Corrosion of Metals*, 1st ed. Elsevier, 2008.

[24] Y. Hosoi, N. Wade, S. Kunimitsu, and T. Urita, “Precipitation behavior of laves phase and its effect on toughness of 9Cr-2Mo Ferritic-martensitic steel,” *J. Nucl. Mater.*, vol. 143, pp. 461–467, 1986.

[25] T. Sourmail and H. K. D. . Bhadeshia, “Modelling simultaneous precipitation reactions in austenitic stainless steels,” *Calphad*, vol. 27, no. 2, pp. 169–175, Jun. 2003.

[26] S. Enestam, D. Bankiewicz, J. Tuiremo, K. Mäkelä, and M. Hupa, “Are NaCl and KCl equally corrosive on superheater materials of steam boilers?,” *Fuel*, vol. 104, pp. 294–306, Feb. 2013.

[27] T. Jonsson, N. Folkeson, J.-E. Svensson, L.-G. Johansson, and M. Halvarsson, “An ESEM in situ investigation of initial stages of the KCl induced high temperature corrosion of a Fe–2.25Cr–1Mo steel at 400°C,” *Corros. Sci.*, vol. 53, no. 6, pp. 2233–2246, Jun. 2011.

[28] N. Folkeson, T. Jonsson, M. Halvarsson, L.-G. Johansson, and J.-E. Svensson, “The influence of small amounts of KCl(s) on the high temperature corrosion of a Fe-2.25Cr-1Mo steel at 400 and 500°C,” *Mater. Corros.*, vol. 62, no. 7, pp. 606–615, Jul. 2011.

[29] H. Grabke, E. Reese, and M. Spiegel, “The effects of chlorides, hydrogen chloride, and sulfur dioxide in the oxidation of steels below deposits,” *Corros. Sci.*, vol. 37, no. 7, pp. 1023–1043, 1995.

[30] M. J. McNallan, W. W. Liang, S. H. Kim, and C. T. Kang, “Acceleration of the High Temperature Oxidation of Metals by Chlorine,” in *High Temperature Corrosion, NACE*, 1983, pp. 316–321.

[31] M. G. Fontana, *Corrosion Engineering*, 3rd ed. McGaw Hill, 1986.

[32] R. Bender and M. Schutze, “The role of alloying elements in commercial alloys for corrosion resistance in oxidizing-chloridizing atmospheres. Part I: Literature evaluation and thermodynamic calculations,” *Mater. Corros.*, vol. 54, no. 8, pp. 567–586, 2003.

[33] S. C. Cha and M. Spiegel, “Local reactions of KCl particles with iron, nickel and chromium surfaces,” *Mater. Corros.*, vol. 57, no. 2, pp. 159–164, Feb. 2006.

[34] D. Berztiss, A. Zahs, and A. Schneider, “Role of carbides in the high temperature corrosion of steels in HCl-containing atmospheres,” *Zeitschrift für Met.*, 1999.

[35] M. McNallan, “High-temperature corrosion in halogen environments,” *Mater. Perform.*, pp. 54–57, 1994.

[36] C. Pettersson, J. E. Svensson, and L. G. Johansson, “Corrosivity of KCl(g) at Temperatures above Its Dew Point - Initial Stages of the High Temperature Corrosion of Alloy Sanicro 28 at 600^{o}C,” *Mater. Sci. Forum*, vol. 522–523, pp. 539–546, 2006.

[37] K. Segerdahl, J. Pettersson, J. E. Svensson, and L. G. Johansson, “Is KCl(g) Corrosive at Temperatures Above its Dew Point? Influence of KCl(g) on Initial Stages of the High Temperature Corrosion of 11% Cr Steel at 600°C,” *Mater. Sci. Forum*, vol. 461–464, pp. 109–116, 2004.

9.3 Paper III

Saeed Kiamehr, Kristian V. Dahl, Melanie Montgomery, Marcel A.J. Somers

KCl-Induced High Temperature Corrosion of Selected Commercial Alloys Part II: Alumina and Silica-formers

Manuscript is ready for submission

KCl-Induced High Temperature Corrosion of Selected Commercial Alloys

Part II: Alumina and Silica-formers

Saeed Kiamehr[*1], *Kristian V. Dahl*[1], *Melanie Montgomery*[1,2], *Marcel A.J. Somers*[1]

1) Technical University of Denmark (DTU), Department of Mechanical Engineering, Produktionstorvet, Building 425, 2800 Kgs. Lyngby, Denmark
2) COWI A/S Parallelvej 2, 2800 Kgs. Lyngby, Denmark

Abstract

Laboratory testing on selected alumina and silica-forming alloys was performed to evaluate their performance against high temperature corrosion induced by potassium chloride (KCl). The alloys studied were FeCrAlY, Kanthal APM, Nimonic 80A, 214, 153MA and HR160. Exposure was conducted at 600^{o}C for 168h in flowing N_2(g)+5%O_2(g)+15%H_2O(g) (vol.%) with samples covered under KCl powder. A KCl-free exposure was also performed for comparison. Corrosion morphology and products were studied with Scanning Electron Microscopy (SEM), Energy Dispersive X-Ray Spectroscopy (EDS) and X-Ray Diffractometry (XRD). It was observed that alloying with aluminum did not lead to the formation of protective alumina for the studied alloys. The silicon containing stainless steel 153MA showed an analogous performance to low-silicon austenitic stainless steels of similar chromium and nickel contents. For alloy HR160, a potassium-chromium-silicon-oxygen containing layer forms as the innermost corrosion product. The layer was uniformly distributed over the surface and appears to render some protection as this alloy exhibited the best performance among the investigated alloys.

To reveal further aspects of the corrosion mechanism, Nimonic 80A was exposed in static laboratory air for the same duration and temperature with either KCl or K_2CO_3 deposits. Comparison of results obtained with these experiments showed that both potassium and chlorine can play a role in material degradation by KCl.

Keywords: biomass combustion, deposit, potassium chloride, potassium carbonate, high temperature corrosion, chromia-former, alumina-former, silica-former.

1. Introduction

High temperature corrosion of heat exchangers due to potassium chloride (KCl) is a crucial factor in limiting the efficiency of power plants firing biomass. To keep the corrosion rates at an acceptable level, it is recommended that the outlet steam temperature does not exceed 540^{o}C [1], which reduces the efficiency of the plant. Therefore development of corrosion resistant materials

has attracted much attention. The majority of high temperature alloys contain significant amounts of chromium to be able to form a chromium-rich oxide which protects against corrosion. However if the environment contains alkali elements, the initial oxide can be damaged due to alkali chromate formation [2]. To counteract such a problem, one solution could be to employ alloys with higher chromium content. However, several studies [3]–[5] show that increase in chromium content is not always a remedy against alkali chloride-induced high temperature corrosion. In fact, it has been demonstrated that if the temperature is high enough (above 500^{o}C) pure chromium is extremely reactive when exposed to alkali chlorides under oxidizing conditions [6]–[11]. Therefore the logical direction in materials selection is to employ other oxide-forming elements or improve the performance of chromia-forming alloys by addition of suitable alloying elements. There have been a number of investigations indicating that the presence of aluminum and/or silicon in Fe-Cr-(Ni) alloys is beneficial for corrosion resistance. For NaCl-induced attack in air under cyclic temperature conditions, Hiramatsu et al.[12] reported a better corrosion resistance with addition of aluminum in ferritic alloys and silicon in austenitic stainless steels. Fujikawa and Maruyama [13] investigated the effect of silicon content and aging on the high temperature corrosion of austenitic stainless steels exposed to NaCl in air. They reported a positive effect of silicon and a negative effect of aging due to the formation of chromium carbides. Li et al.[14] studied the effect of aluminum and/or silicon addition to 9wt% chromium steel P91 on its resistance against KCl vapor-induced corrosion at 650^{o}C in static air. Both elements were found to have a positive effect in reducing corrosion; silicon showing a superior beneficial effect compared to aluminum. In a similar study within the same research group, iron, chromium and a range of iron-chromium alloys along with their aluminum/silicon modifications were evaluated at 650^{o}C under air+KCl deposit. A positive effect on the corrosion resistance was observed with aluminum or silicon additions[4].

The mechanism of alkali chloride-induced high temperature corrosion is still a subject of discussion. Pettersson et al.[2] showed that the presence of potassium is enough to cause breakdown of the initial chromium-rich protective oxide on chromia-forming alloys due to the formation of potassium chromate (K_2CrO_4). Lehmusto et al.[15], [16] investigated the corrosion behavior of selected chromia-forming alloys under either KCl or K_2CO_3 and found both salts corrosive. In another study within the same research group it was found that when pure chromium is exposed to either KCl or K_2CO_3, the presence of potassium alone could initiate the attack, while chloride was necessary for the reaction to continue [11].

The present paper is the second part of a larger study evaluating the performance of a wide range of commercial alloys. In the first part [17] selected chromia-forming alloys were shown to fail to form a protective oxide layer when KCl was present, either as a salt or as a gas. The formed oxide on stainless steels consisted of an outer part with a highly porous morphology (referred to as type A oxide) and an inner part which was apparently dense (referred to as type B oxide). For nickel-based alloys, type A oxide was always present. However, instead of an inner oxide as for the stainless steels, the nickel-based alloys could show deep-penetrating voids (indicative of selective corrosion) and/or pitting. This paper addresses the performance of selected chromia-forming alloys that contain aluminum or silicon. However, unlike the exposures in the aforementioned literature, the gas composition was adjusted with respect to oxygen and water vapor content in order to simulate

power plant conditions. Finally, a complementary test was performed with either KCl or K_2CO_3 to obtain further understanding on the corrosion mechanism(s).

2. Experimental Procedure

The chemical composition of the investigated alloys is given in Table 1. Samples were in the form of coupons (7-8 mm x 17-20 mm) with a thickness in the range of 250-340 µm. The samples were cut with a precision cutter. Alloy HR160 was delivered in rolled condition. For recrystallization the sample was annealed at 1150°C for 45min in Ar(g)(99.999% purity)+25vol.%H_2(g) followed by cooling in the furnace. Before annealing the sample was ground with 1000-grit SiC paper to remove solid surface contaminants.

Prior to exposure in a corrosive environment, all samples were ground with 4000 grit SiC paper and covered with a ~1 mm thick layer of KCl powder (particle size 63-90 µm) for ~2/3 of their length. Samples were placed on flat alumina coupons and then loaded into a multi-channel alumina sample holder with the KCl-free part towards the entrance of the gas flow. The sample holder itself was then placed in the zone of uniform temperature in a silica tube in the horizontal furnace. A schematic representation of the experimental set-up is shown in Figure 1.

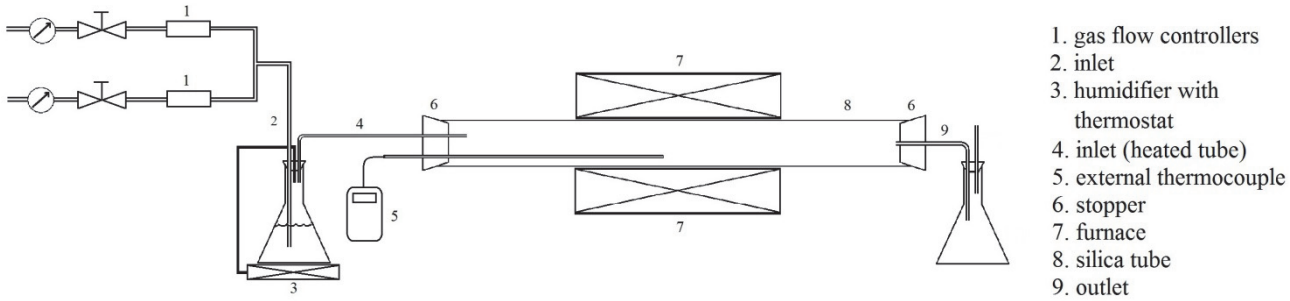

Figure 1: Schematic of the experimental set-up

Exposures were conducted at 600°C for 168h. The gaseous atmosphere consisted of flowing N_2(g)+5%O_2(g)+15%H_2O(g) with a calculated velocity of 0.25cm/s at the inlet temperature. An exposure without salt was performed for all of the alloys as a reference test. For alloy HR160 the exposure with salt was repeated. In this second run, the sample was ground with 1000 paper prior to grinding with 4000 paper. This was undertaken to remove any possible oxide formed during annealing. To distinguish between the two samples, the one ground with only 4000 paper is referred to as series 1 and the sample ground with, 1000 and then 4000 paper is referred to as series 2. In addition to the above-mentioned exposures, one extra test was performed with Nimonic 80A where one sample was covered with KCl and the other with K_2CO_3 of the same particle size. Samples were separately exposed at 600°C for 168h. As the K_2CO_3 is deliquescent, this test was performed in static lab air to avoid formation of a liquid phase during the purging period of the furnace.

After the exposures, KCl-exposed samples were clamped in an upright position and embedded in epoxy resin without removing the salt layer. For the K_2CO_3-exposed sample, the salt layer spalled off after the test, therefore only the sample was embedded. Half the width of the embedded samples

was removed by grinding with 180-grit SiC paper and then grinding/polishing was continued on finer paper/cloth grades down to 1µm diamond suspension. As lubricant, 96% ethanol was used for grinding up to the 1000-grit paper and 99.9% ethanol on finer papers. Since chlorine was detected in the original epoxy (specifix-20), a chlorine-free epoxy (Eli-Cast clear epoxy) was used for the series 2 sample of alloy HR160. In addition, one exposed (series 2) sample of this alloy was thoroughly washed with de-ionized water after the test to remove the water soluble corrosion products. Phase analysis of the samples of the reference exposure (i.e. the KCl-free exposure) were performed with an X-Ray Diffractometer (Bruker D8 Discover). CrK_{α} (λ=2.2897 Å) radiation was applied in grazing incidence mode to limit the information depth of the applied radiation and, thus investigate the surface adjacent region of the samples. Due to the incorporation of corrosion products into the residual salt layer, removal of the salt without unintentional removal of the corrosion products proved to be challenging. Therefore KCl exposed samples were not investigated with XRD. Reflective Light Microscopy (RLM) was used to measure the decrease in metal thickness for the salt-affected samples. Twenty measurements were done at intervals of 0.5mm. The average and standard deviation were calculated for each sample based on these measurements. Subsequently, the entire surface was thoroughly inspected to find the worst case damage. Average and worst case values less than 5µm were considered insignificant, considering the accuracy of the micrometer employed for pre-exposed sample thickness measurements. The morphology of corrosion and elemental distribution in the corrosion products were investigated by means of an FEI Inspect S Scanning Electron Microscope (SEM) equipped with an Energy Dispersive X-Ray Spectroscopy (EDS) detector. Image acquisition was always performed in Back-Scattered Electron (BSE) mode unless otherwise mentioned. The chemical compositions of the alloys as listed in Table 1 were measured with EDS. Carbon and nitrogen contents were measured with Fusion Thermal Conductivity Detection units LECO CS230 and LECO TN500 respectively.

Table 1: Chemical composition of the alloys. Carbon and nitrogen contents were measured with Fusion Thermal Conductivity Detection units LECO CS230 and LECO TN500, respectively. All values are in wt% (values in the parentheses are in at%). Elements without a value in the last column were present in trace amounts.

alloy	Fe	Cr	Ni	Al	Si	Mo	Co	Ti	C	N	other
FeCrAlY	bal.	23.2 (23.2)		5.1 (9.8)					0.040	0.018	Si,Ti, Zr
Kanthal APM	bal.	23.1 (22.9)		5.7 (10.9)	0.6 (1.1)				0.032	0.017	Ti,Zr
Nimonic 80A	0.8 (0.8)	20.7 (22.2)	bal.	1.4 (2.9)	0.4 (0.8)			2.3 (2.7)	0.070	0.014	
Alloy 214	3.6 (3.5)	17.2 (18.0)	bal.	4.8 (9.7)					0.038	0.002	Zr
HR160	0.3 (0.3)	29.3 (30.8)	bal.		3.3 (6.5)	0.2 (0.1)	29.2 (27.1)	0.4 (0.5)	0.052	0.007	Al
153MA	bal.	20.4 (21.3)	10.0 (9.2)		1.6 (3.1)				0.048	0.15	Ce,La,Ti, Mn

3. Results

3.1 Reference exposure in N_2(g)+5%O_2(g)+15%H_2O(g)

After the salt-free exposure in N_2(g)+5%O_2(g)+15%H_2O(g), only the austenitic stainless steel 153MA developed a fast growing oxide. A dull-red colored oxide had developed on the surface and the cross section revealed a double layer oxide (Figure 2). For the other alloys, no oxide was observed on visual inspection and the metallic luster was preserved. Corresponding diffractograms are given in Figure 3. For alloy HR160 the diffractogram corresponds to a series 1 sample. The precipitate phases were identified as Ni_3Al for alloy 214 and $Cr_{23}C_6$ for 153MA. For 153MA, peaks belonging to $(Fe,Cr)_2O_3$ and $(Fe,Cr)_3O_4$ can be clearly distinguished. For the other alloys, no indication of a fast-growing oxide was observed.

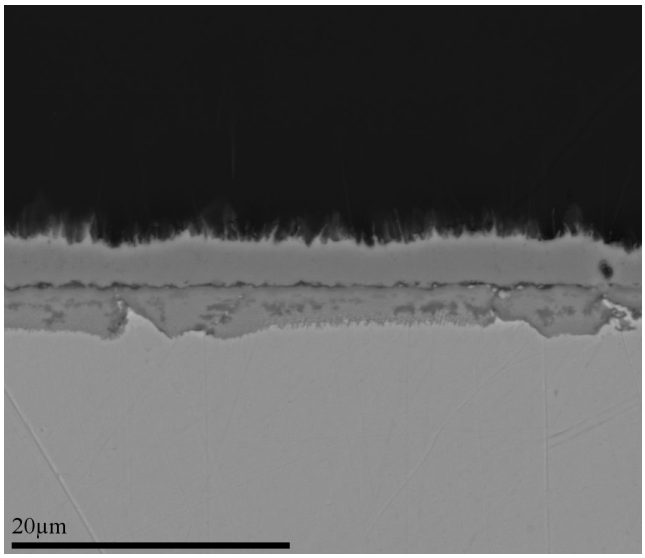

Figure 2: Oxide morphology observed on 153MA due to the exposure in N_2(g)+5%O_2(g)+15%H_2O(g) at 600°C.

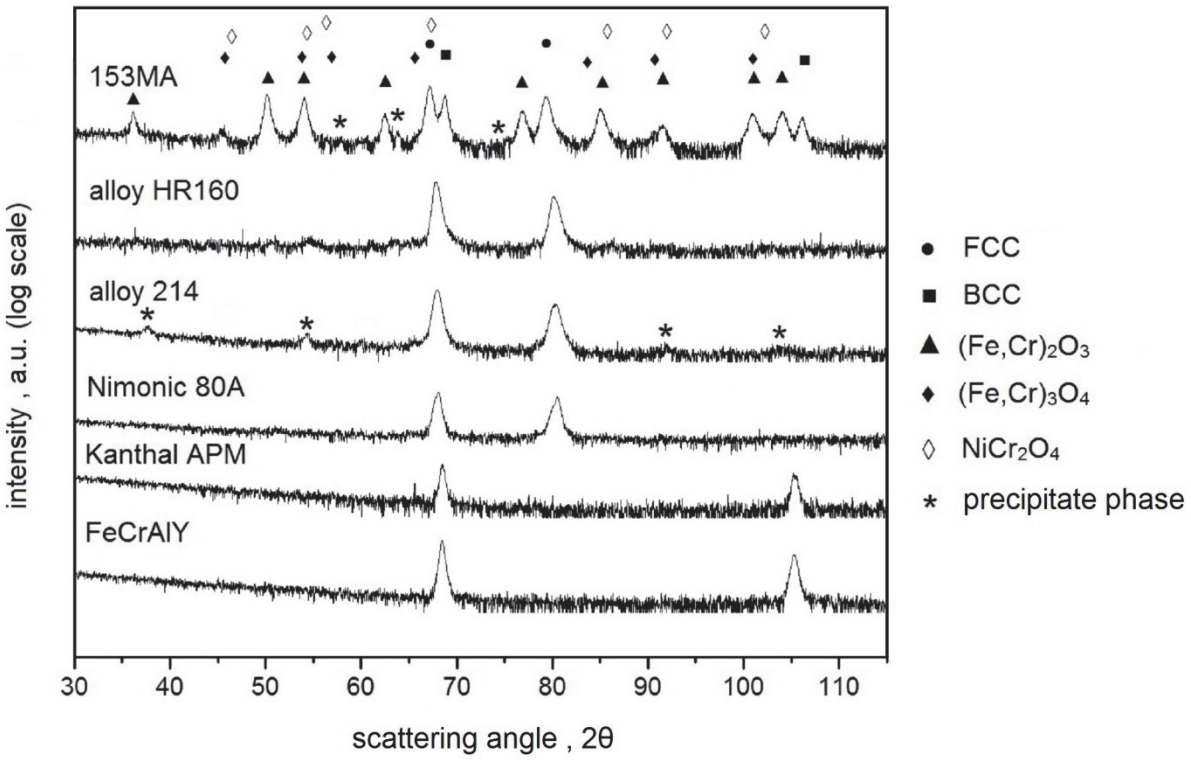

Figure 3: CrK_{α} X-ray diffractograms for the investigated alloys after the salt-free exposure. The angle of incidence has been between 1-5 degrees.

3.2 Exposure in $N_2(g)+5\%O_2(g)+15\%H_2O(g)$ under KCl(s)

Although the majority of the alloys formed protective oxides in the salt-free exposure, they all suffered from significant corrosion under a KCl deposit. Figure 4 shows the reduction in metal thickness for the investigated alloys. As TP347HFG is the alloy currently utilized for superheater materials in many biomass fired plants, the result for this alloy (taken from the first part of this study [17]) is included for comparison. In addition to the general thickness loss, internal oxidation, grain boundary attack and void formation are also included as part of the reported decrease in metal thickness. Considering both average and worst case measurements, none of the alumina-forming alloys performed better than TP347HFG. For Alloy 214, the average thickness loss is lower than for TP347HFG, however localized thickness loss is higher. For the two silica-forming alloys, 153MA does not show any improvement compared to TP347HFG while it is indicated that the nickel-based alloy HR160 shows a slightly better performance. The value reported for HR160 in Figure 4 is for a series 2 sample, but no significant difference between series 1 and 2 samples of the alloy could be found. Corrosion morphologies and EDS mapping of the corrosion products for different alloys are reported in the following sections.

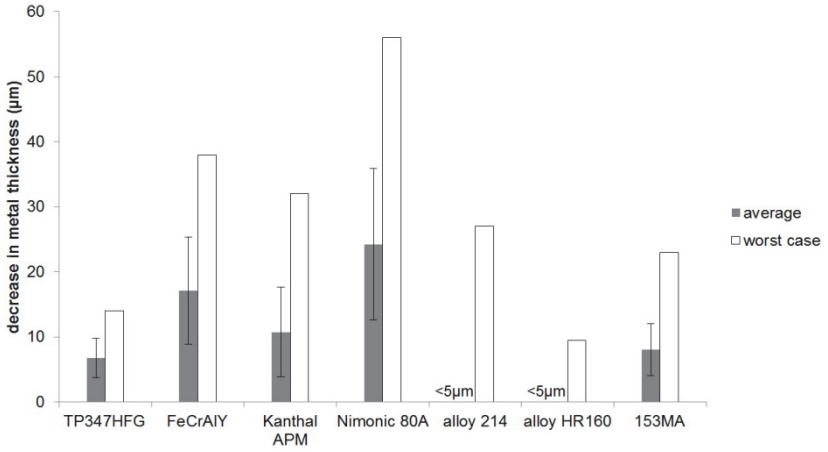

Figure 4: Average and highest thickness loss observed on the studied alloys after 168h exposure at 600°C in N_2(g)+5%O_2(g)+15%H_2O(g) under KCl(s). The result for TP347HFG is adopted from [17] and included for comparison.

3.2.1 Alumina-formers

FeCrAlY and Kanthal APM

The microstructure of the corrosion products on FeCrAlY and Kanthal APM showed many similarities (Figures 5a-b). For both FeCrAlY and Kanthal APM, two distinct oxide morphologies (referred to as type A and type B) were observed, similar to the stainless steels mentioned in the first part of this study [17]. The cavities in the epoxy are the locations where salt particles were grazed-out during grinding for sample preparation. The outermost oxide (type A) was voluminous showing considerable porosity. This oxide was rich in iron and also contained aluminum and chromium (Figures 6 and 7). Minor amounts of potassium could be detected in this oxide too. The type B oxide, located underneath the type A oxide, was relatively dense and was rich in chromium and aluminum, showing aluminum enrichment with depth. The type B oxide was often locally extended deep into the alloy, presumably along alloy grain boundaries. Underneath the type B oxide, a region was observed with darker contrast compared to the matrix and brighter contrast compared to the oxide. Spot analysis revealed the presence of oxygen throughout this region indicating an internal oxidation zone (IOZ). This zone was thicker for FeCrAlY than for Kanthal APM. Chromium depletion was observed for both alloys in the IOZ. The high chromium content found at the tip of the grain boundary in Figure 7 is suggested to be a chromium carbide particle lying at this location. Similar high chromium locations were also observed in the unexposed microstructure of Kanthal APM. Spot analysis revealed that the thin dark line separating the IOZ from the unaffected alloy is slightly enriched in nitrogen and aluminum. Below this dark line, aluminum depletion is observed. In a number of cases, potassium and/or chlorine could be found in the type B oxide, in the IOZ and even at the metal/IOZ interface. It is not clear whether this is a real effect or an artefact of the polishing process, for example by smearing these species over the surface.

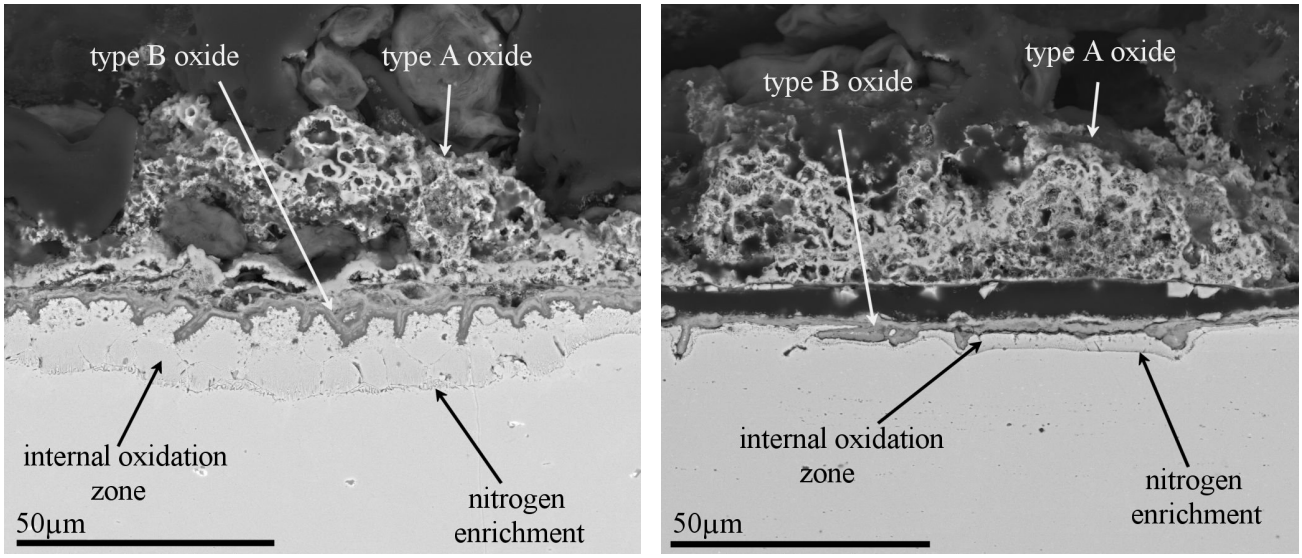

(a) (b)

Figure 5: General corrosion morphology on (a) FeCrAlY and (b) Kanthal APM showing grain boundary attack and internal oxidation.

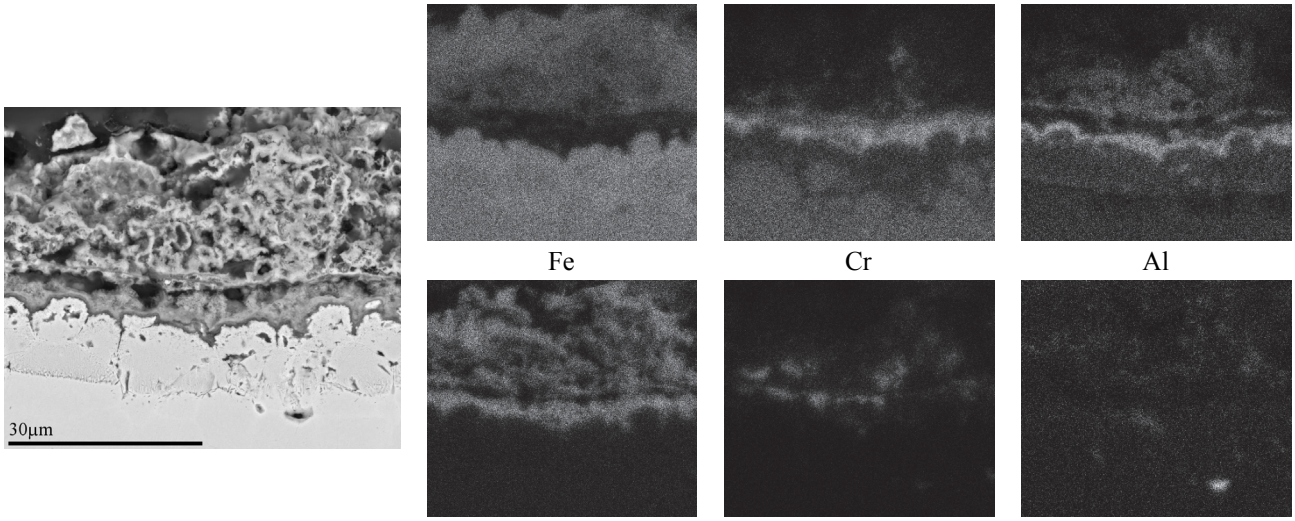

Figure 6: Distribution of the alloying elements, potassium, chlorine and oxygen in the corrosion product developed on FeCrAlY.

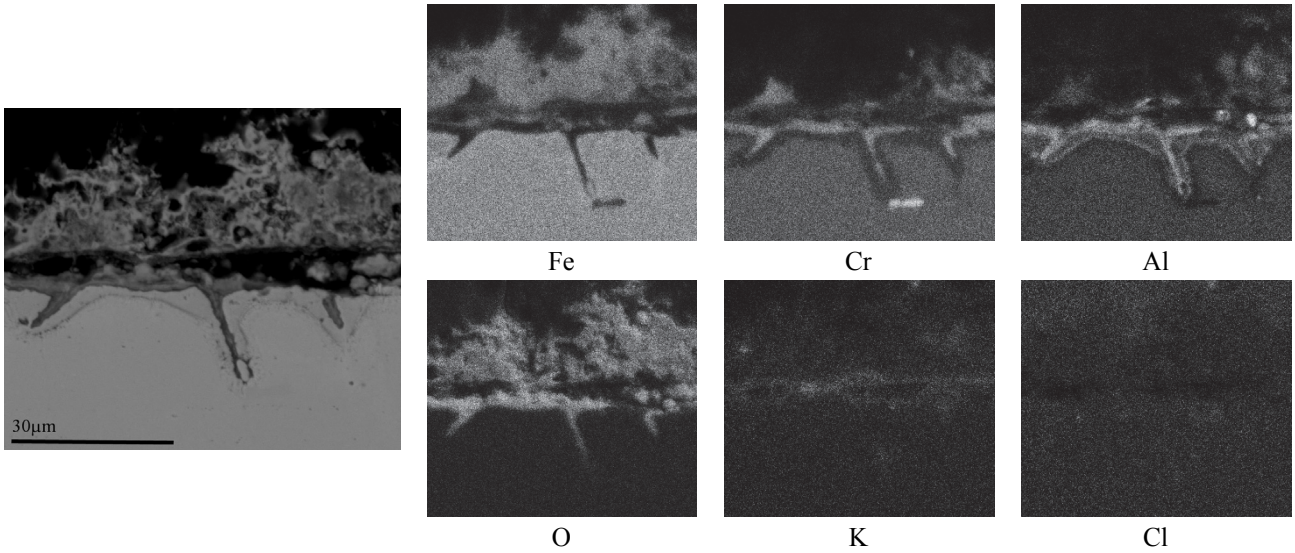

Figure 7: Distribution of the alloying elements, potassium, chlorine and oxygen in the corrosion product on Kanthal APM.

Nimonic 80A and Alloy 214

For Nimonic 80A, the corrosion products consisted of a spongy oxide containing chromium, aluminum, titanium and potassium with minor amounts of nickel (Figure 8a-c). This oxide was highly porous and voluminous and thus had the same characteristics as the type A oxide observed on the investigated stainless steels reported in [17] and FeCrAlY/Kanthal APM (see Figure 8a). No clear sign of chlorine enrichment could be seen in the corrosion morphology. The outer parts of the spongy oxide showed a eutectic-looking structure (Figure 8b) with strips embedded in a potassium-chromium-oxygen compound suggesting a solidification product. Alloying elements were found at distances more than 100µm away from the original metal surface, see Figures 8b-c. Beneath the spongy type A oxide, a porous metallic zone was observed. This zone was enriched in nickel and depleted in chromium, aluminum and titanium. In some cases the nickel skeleton was absent, indicating that even nickel had been attacked (see the cavity marked in Figure 8c). A ~1-2 µm thin layer separates the porous nickel-rich alloy from the spongy corrosion product (see aluminum, titanium and chromium map in Figure 9). A titanium-rich phase could be found in the bulk alloy microstructure (marked with dashed arrows in Figure 8a). EDS spot analysis indicated the presence of nitrogen in this phase, therefore it is assumed to be titanium nitride. Interestingly, the particle with dark contrast in the porous nickel-rich zone (Figure 8a) seems to be intact, which suggests that this phase has not been significantly attacked. In addition to the titanium-rich phase, a chromium-rich phase, likely to be carbides, was found at many locations in the microstructure (marked with solid short arrows in Figure 8a).

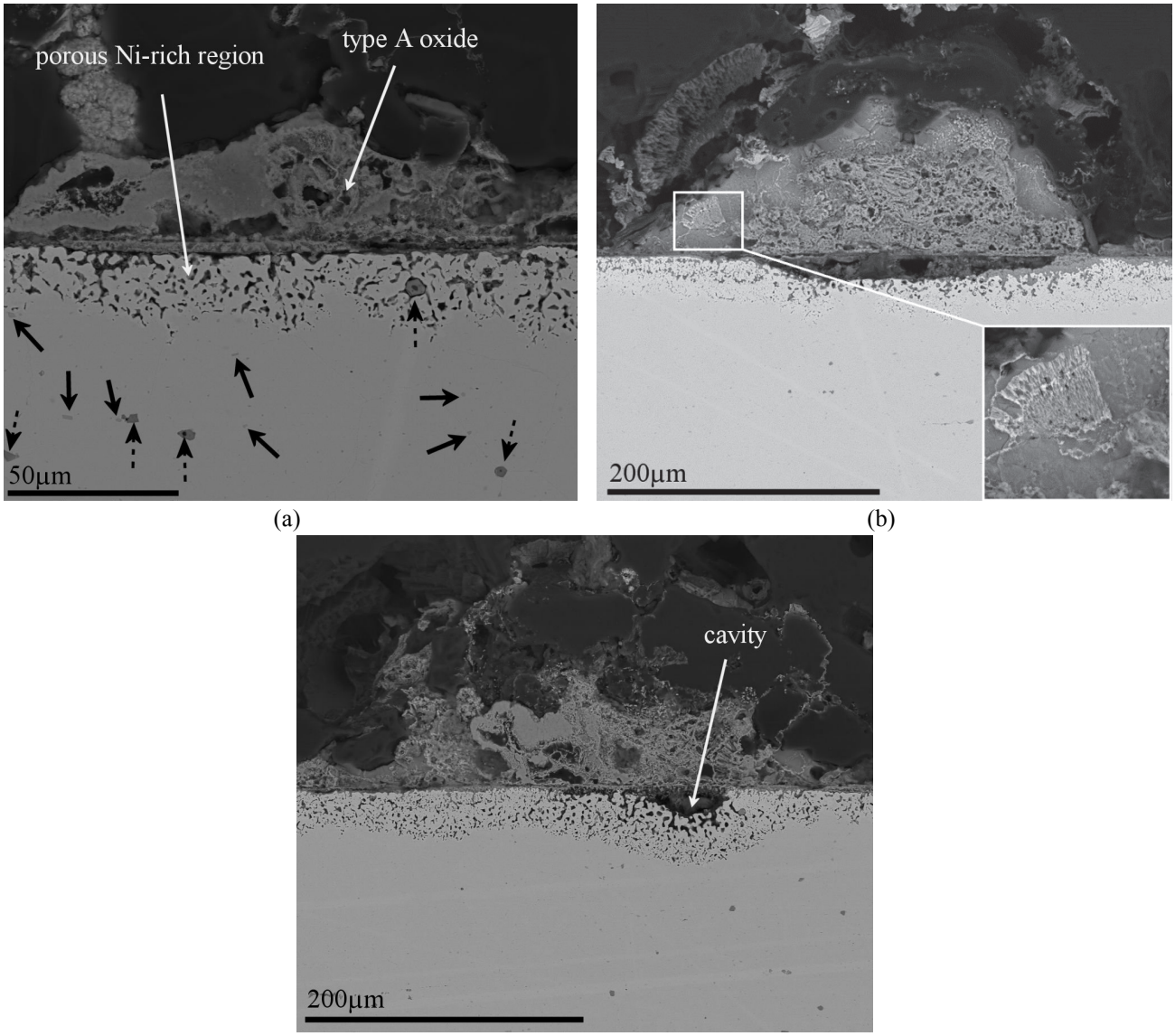

Figure 8: General morphology of corrosion products on Nimonic 80A. (a) Dashed short markers denote the titanium nitride and the solid short markers denote the chromium-rich phase in the bulk. (b) Eutectic structure of the outer corrosion products (higher magnification in inset). (c) Depressions in the alloy indicate that even nickel has been attacked locally.

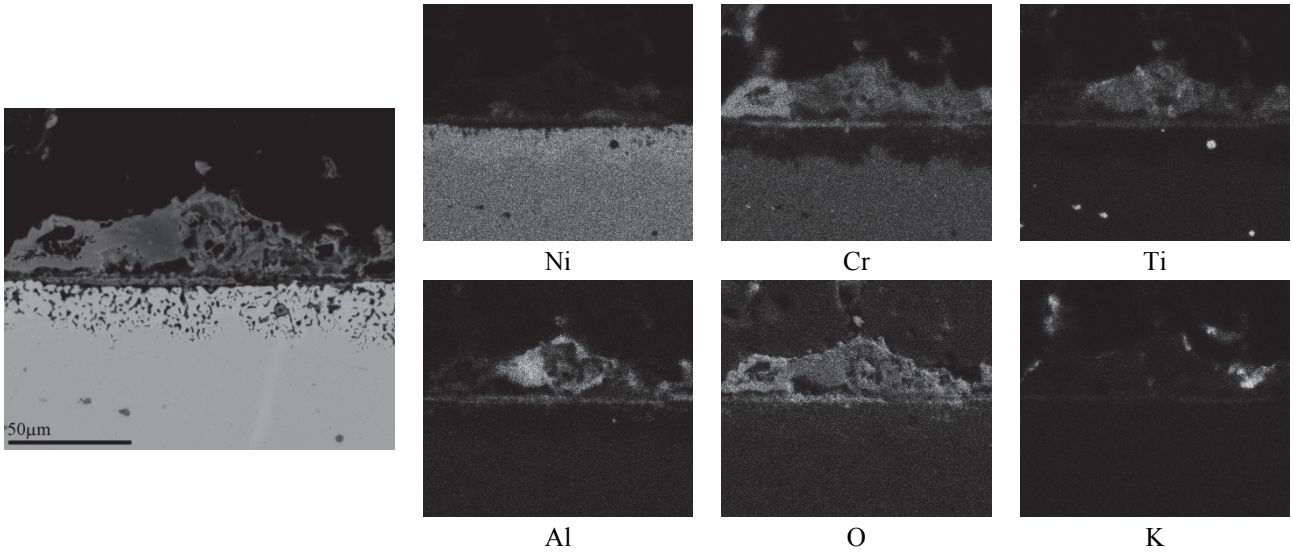

Figure 9: Distribution of the alloying elements, potassium, chlorine and oxygen in the corrosion product on Nimonic 80A.

Alloy 214 showed a unique behavior. On most of the surface, no significant thickness loss (5µm<) was observed and a dense uniform nickel-rich band of 4-5µm was present (see the bright contrast close to the surface in Figure 10a). What appears to be a thin aluminum and chromium-rich oxide could be observed over the entire surface (see aluminum map in Figure 11). There were only two areas along the 12 mm long specimen where localized attack and porous nickel rich areas could be found (Figure 10b). EDS mapping and spot analysis of these porous areas showed strong nickel-enrichment and aluminum/chromium depletion similar to the general behavior observed on Nimonic 80A. In addition, detection of nickel in the oxide as well as a cavity underneath the oxide suggests that even nickel was removed. EDS mapping of the spongy oxide above the two deep nickel-rich areas showed a mixture of aluminum, chromium and iron oxides with a small amount of nickel (Fig 11). A chromium-rich phase could be seen in the microstructure (marked with short arrows in Figures 10a and b). In addition to the unreacted KCl, a faint enrichment of both potassium and chlorine can be seen in the spongy nickel-rich area. However, it is not clear if this is a real effect or an artefact of polishing. Bubble-like oxides extending more than 100 µm away from the corrosion front were often observed (Figure 10c). The selective nature of corrosion as well as the presence of a voluminous and highly porous oxide was similar to Nimonic 80A.

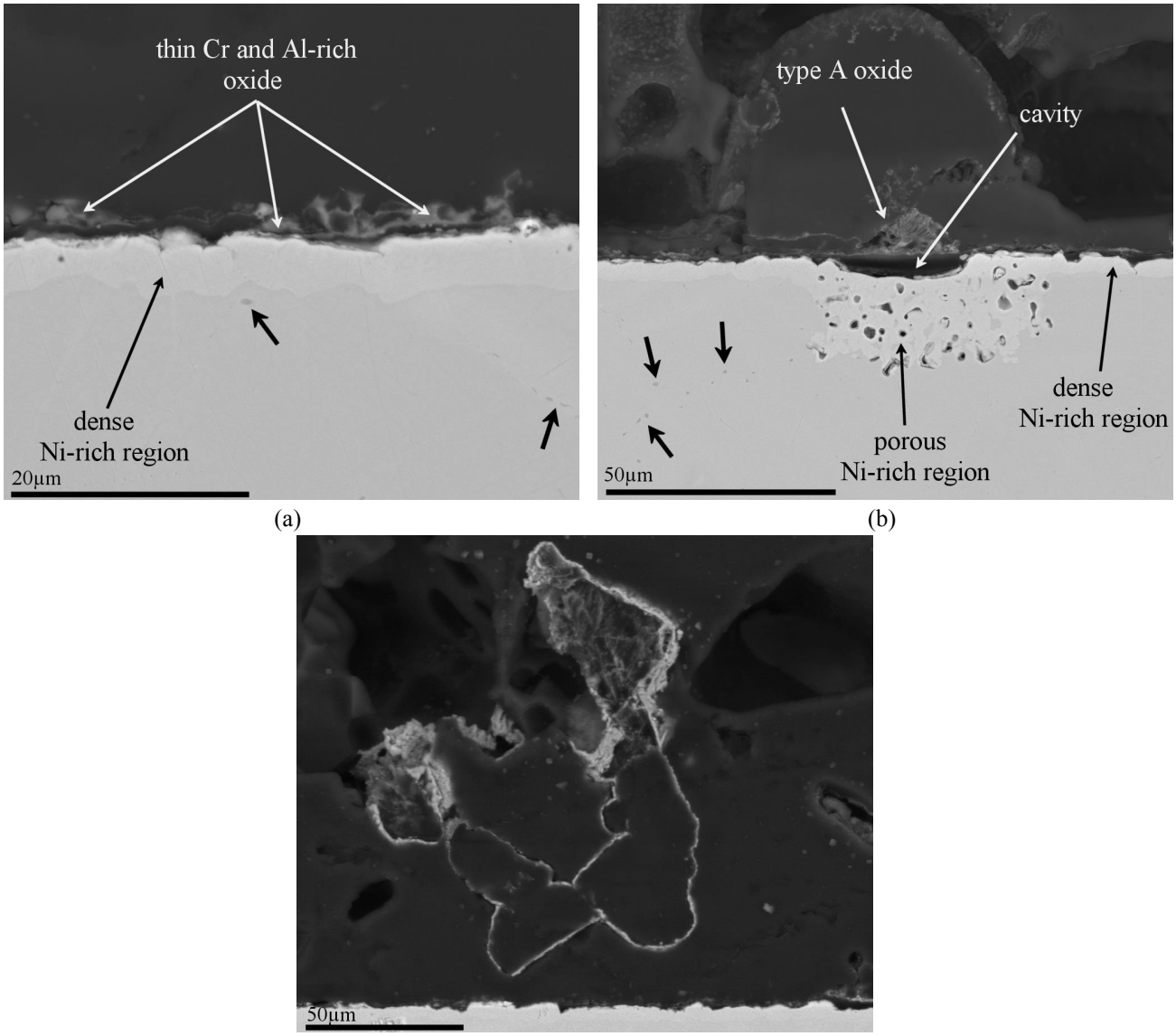

Figure 10: Corrosion morphologies on alloy 214. (a) large parts of the surface show a dense nickel-rich band. Short arrows denote the chromium-rich phase (b) local attack of the alloy in the form of selective corrosion. (c) bubble-like oxides reach far into the KCl deposit.

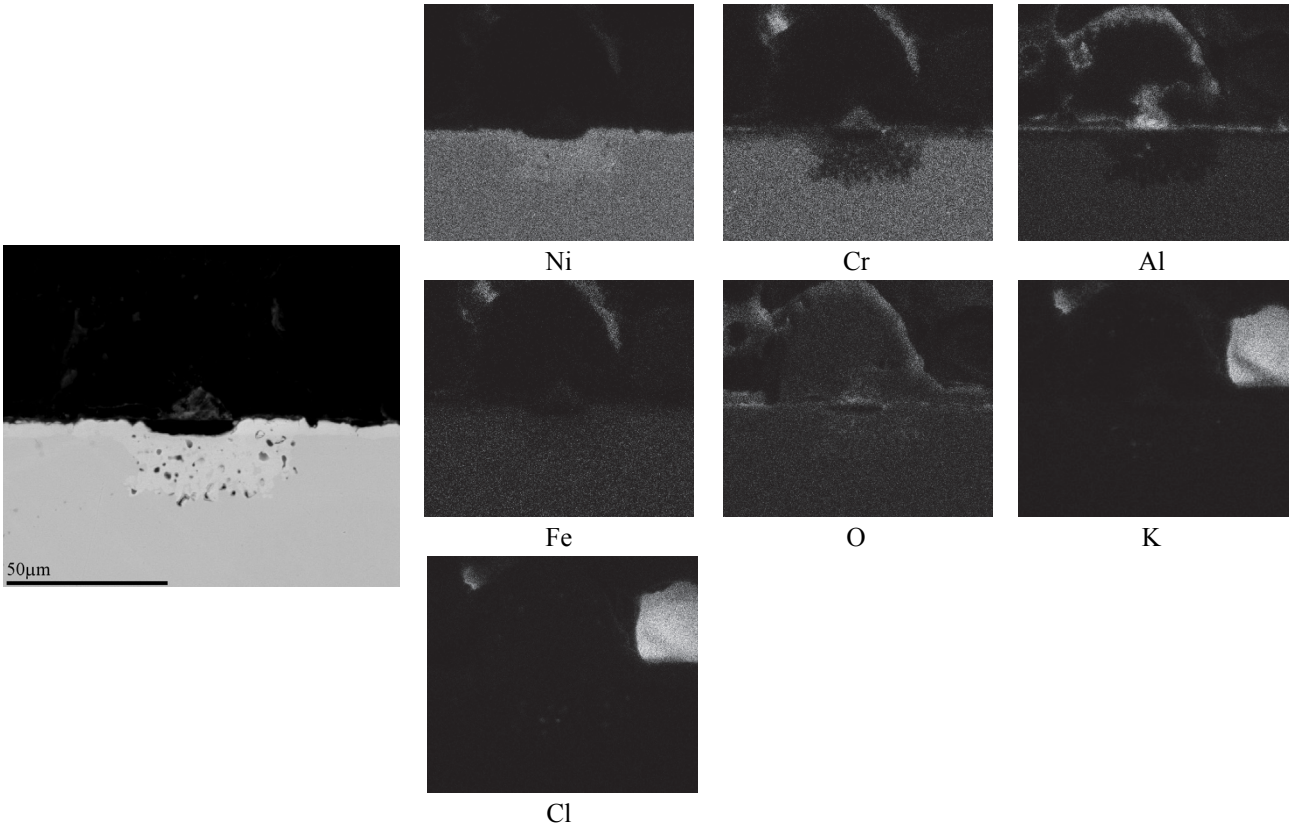

Figure 11: Distribution of the alloying elements, potassium, chlorine and oxygen in the corrosion product on alloy 214.

3.2.2 Silica formers

153MA

Similar to the stainless steels considered in the first part of this study, the morphology of corrosion products on 153MA consisted of type A and type B oxides (Figure 12). The higher Si content of 153MA (1.6 wt%) compared to the other investigated stainless steels, did not appear to have a significant effect on the behavior of this alloy. The distribution of the alloying elements throughout the corrosion product is shown in Figure 13. The type A oxide was rich in iron and contained a small area where potassium and chromium were both present. The outer type B oxide was iron rich above the assumed original metal surface and chromium rich below this interface; there were also indications of silicon enrichment at the presumed original surface and within the inner part of type B oxide together with chromium. Metallic islands enriched in iron and nickel were also identified. No clear chlorine enrichment was detected.

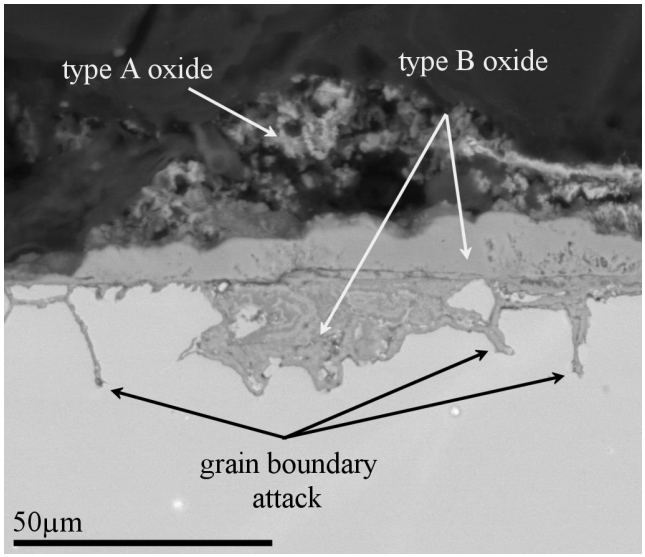

Figure 12: General corrosion morphology observed on 153MA.

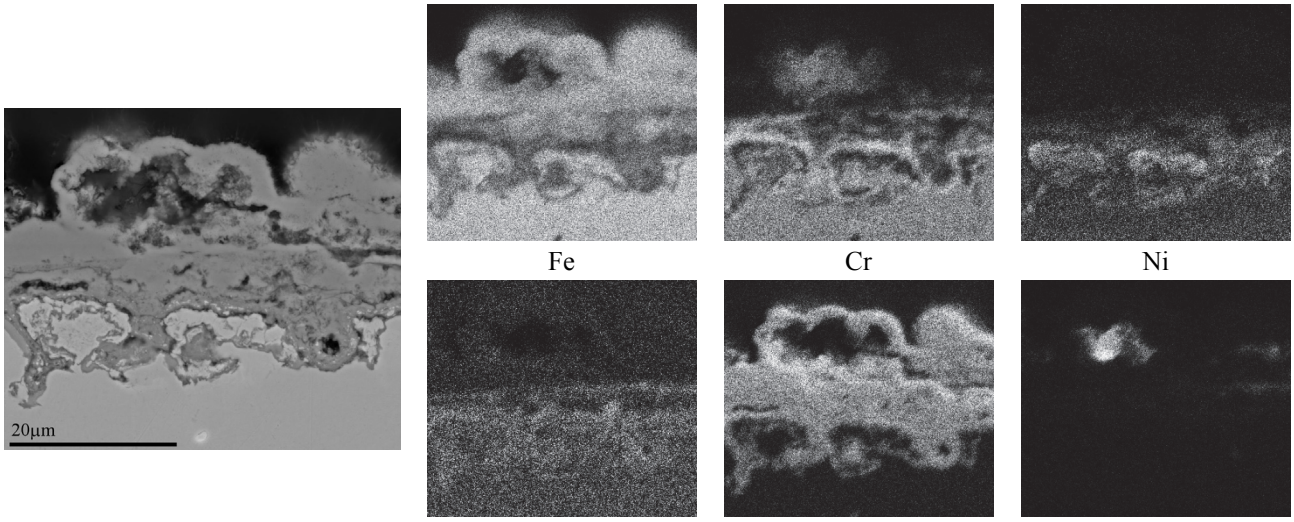

Figure 13: Distribution of the alloying elements, potassium and oxygen on 153MA.

Alloy HR160

Alloy HR160 shows similar corrosion morphology as type A and type B oxides for both surface qualities (series 1 and 2). Type A oxide was composed of spongy cobalt and nickel-rich oxides mixed with large amounts of a potassium-chromium-oxygen containing compound. Type B oxide is rich in nickel and cobalt on the top (at the presumed original metal surface) and consists of a potassium-silicon-chromium-oxygen type compound (or mixture of compounds) below this (Figures 14 and 15). No clear enrichment of chlorine was observed. In a few cases the corrosion product showed a shallow penetration into the alloy, presumably along grain boundaries (Figure 14). Examination of the sample that was rinsed with de-ionized water showed that potassium was not removed from the type B oxide by washing, indicating that potassium is not present as a water

soluble compound. A nickel and cobalt-rich band could be observed below the corrosion front together with depletion of chromium and silicon, but void formation in this band was very rare. Titanium was present as needle-like precipitates within the alloy close to the surface (marked with short arrows in Figure 14). However, these precipitates were present in the microstructure of the unexposed alloy as well and are therefore not a result of the exposure. EDS spot analysis showed that nitrogen was present in these precipitates i.e. titanium nitride was found in the microstructure close to the surface.

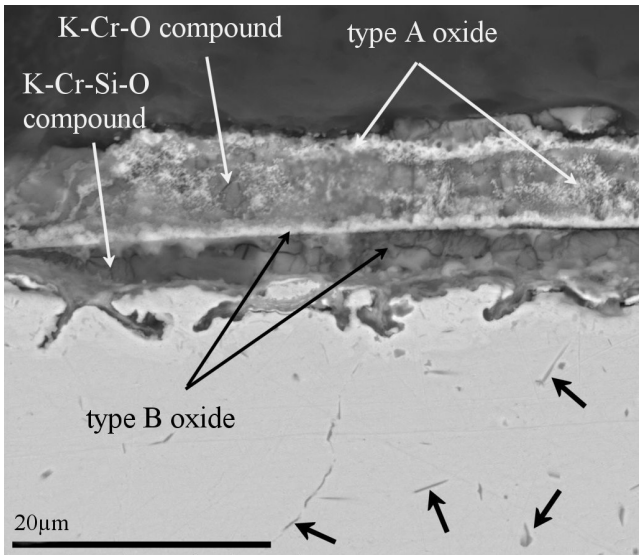

Figure 14: General corrosion morphology observed on alloy HR160. Short arrows indicate a titanium-rich phase

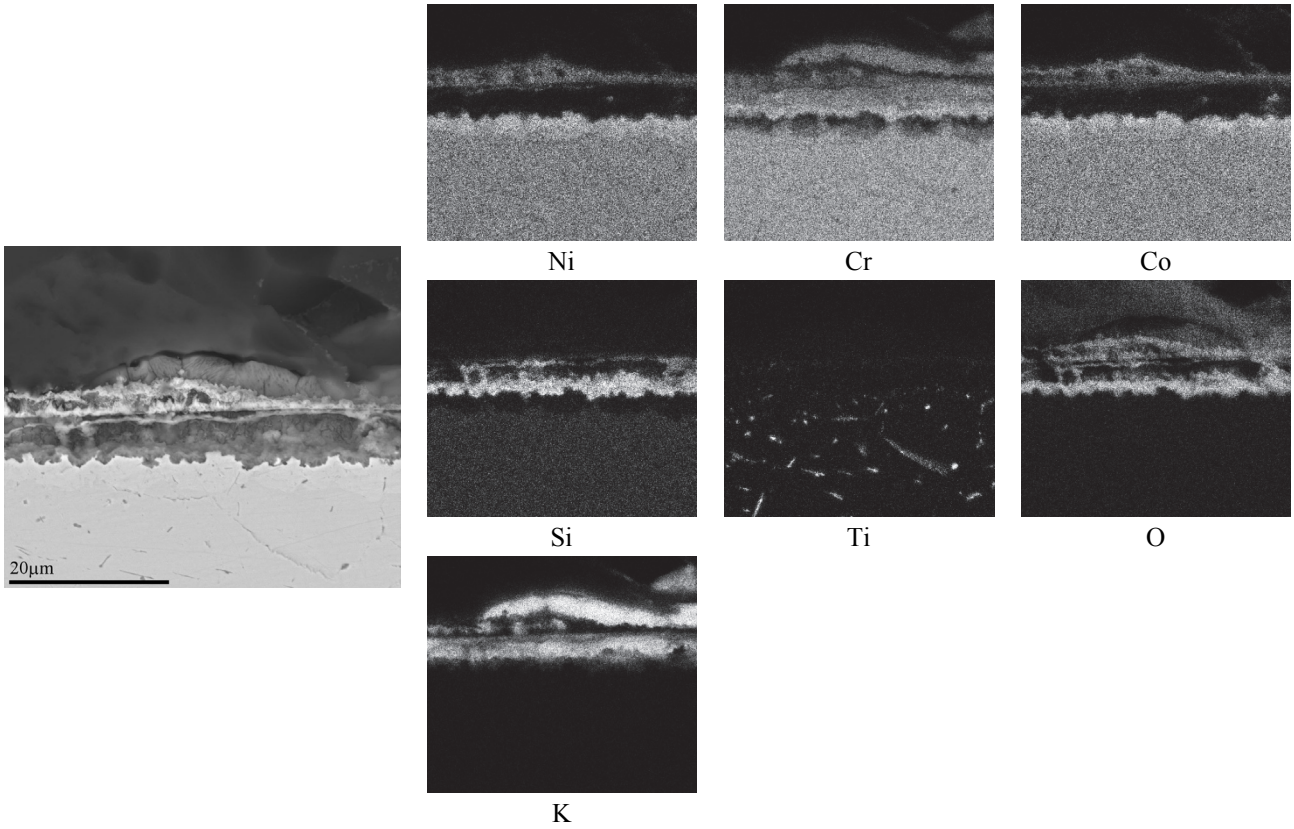

Figure 15: Distribution of the alloying elements, potassium and oxygen in the corrosion product on alloy HR160.

3.3 Comparison between KCl and K_2CO_3 on Nimonic 80A

The morphology of corrosion products on Nimonic 80A exposed in static lab air under KCl(s) was quite similar to the exposure in flowing N_2(g)+5%O_2(g)+15%H_2O(g) under KCl(s). However, replacing KCl by K_2CO_3 resulted in a significant change in the corrosion product morphology. No highly porous outermost oxide (type A oxide) was found, neither was a eutectic-looking mixture identified after exposure with K_2CO_3. Moreover, no voids were detected in the metal above the corrosion front. The distribution of the alloying elements showed inner and outer corrosion products for the K_2CO_3 exposure (Figure 16a). The outer corrosion product was rich in nickel, while nickel was depleted in the underlying alloy. Moreover, the EDS spot analysis and the very bright contrast of the outer corrosion product in Figure 16a indicated the presence of metallic nickel in the outer layer. The nickel denuded region has higher chromium and higher oxygen content; these observations combined with the dark contrast in the BSE image in Figure 16a is ascribed to internal oxidation of chromium. In contrast, the KCl-affected sample displays a morphology where chromium is removed and nickel is enriched in the alloy (Figure 16b). The nickel-rich area showed development of porosity deep into the alloy.

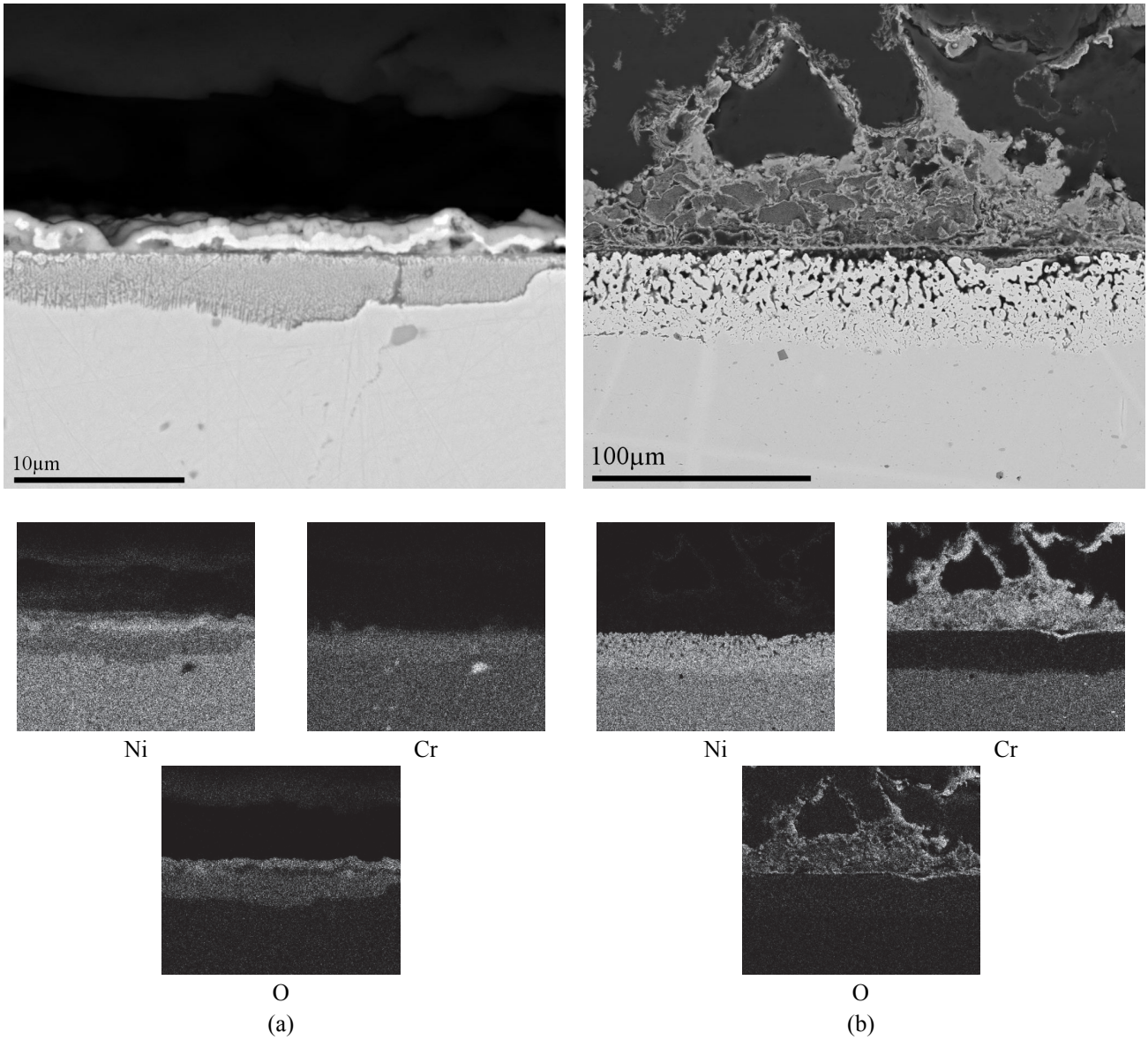

Figure 16: Comparison between corrosion morphologies on Nimonic 80A after exposure to (a) K_2CO_3 and (b) KCl. The distribution of nickel, chromium and oxygen is shown below the corresponding micrograph.

4. Discussion

4.1 Reference exposure $N_2(g)+5\%O_2(g)+15\%H_2O(g)$

It has been indicated that for alloys relying on chromia for protection, evaporation of chromium from the oxide in the form of chromic acid, $CrO_2(OH)_2$, induces breakdown of chromium oxide in humid-oxidizing conditions [18][19]. Accordingly, the protective capacity of the oxide layer depends on a balance of the rates of chromium depletion by evaporation and chromium replenishing by supply from the substrate. Alumina and silica are less volatile than chromia in humid oxidizing environments and therefore aluminum and silicon form protective oxides [20]. However, due to the limited solubility of aluminum and silicon in iron and nickel, formation of a protective alumina or silica layer on a binary solid solution of iron or nickel with silicon or aluminum under humid-

oxidizing conditions is not expected; rather internal oxidation of these elements would be anticipated. Therefore an initial chromia layer is necessary to retard the oxygen ingress so that diffusion of aluminum or silicon to the oxidation reaction front can proceed faster than diffusion of oxygen into the alloy; the so called "third element" effect [21]. Hence, alumina or silica can develop underneath a chromia layer and, consequently, the resistance of alumina and silica-forming alloys is, at least partly, dependent on the chromium content and/or the supply of chromium to the surface. Under the experimental conditions of this study, only the stainless steel 153MA (containing 21.3at% Cr) does not satisfy this condition. Apparently, for this alloy the flux of chromium to the surface is insufficient to maintain the chromia layer. Consequently no protective silica layer forms on this alloy. A chromia layer is formed for the other alloys where the Cr content was evidently of an adequate level at 22.2-30.8 at.%.. However, alloy 214 has only 18 at.% Cr so in that case, the 9.7 at.% Al must have contributed to the formation of the initial oxide layer. This hypothesis is supported by the fact that alumina has some solubility in chromia therefore it can contribute to the formation of a protective oxide at a very early stage of oxidation.

4.2 Exposure in N_2(g)+5%O_2(g)+15%H_2O(g) under KCl(s)

In contrast with the salt-free exposure, where the majority of the investigated alloys showed passive behavior, all alloys suffered from significant attack when KCl was present. This shows that none of the studied alloys is able to form a protective oxide during the early stages of the attack. This effect is attributed to the presence of potassium reacting with chromia to form potassium chromate and thus acting as a chromium sink [2]. In this respect, water vapor and oxygen have a synergy with potassium in removing chromium from the oxide layer. However, Jonsson et al. [22] showed that even under dry conditions at 600^{o}C the presence of a small amount of KCl suffices to locally break down the protective chromium-rich oxide on stainless steel 304L (Fe18Cr10Ni wt%). Further discussion for the different alloys is given in the following sections.

4.2.1 Alumina formers

FeCrAlY and Kanthal APM

FeCrAlY and Kanthal APM exhibited both the outer porous type A oxide and the more dense type B inner oxide. In addition an internal oxidation zone was present for both alloys at the corrosion front. The difference in the morphology of type A and type B oxides strongly suggests that the mechanisms contributing to the formation of these oxides are different. The highly porous structure of type A oxide and the presence of potassium in it suggests the presence of a molten phase at some stage during the exposure. In high temperature corrosion the formation of a molten phase due to alkali chlorides has often been reported [23]–[27]. For pure iron and low alloy steel, a molten phase is believed to form from $FeCl_2$ and unreacted KCl with a eutectic temperature of 355^{o}C [24]. If $FeCl_2$ does not evaporate, it will subsequently oxidize as it is metastable at the oxide/gas interface. The presence of aluminum in type A oxide shows that it is incorporated into the

oxide in a similar way as iron and, hence, does not always contribute to a protective layer. The dense appearance of the type B oxide, on the other hand, suggests that it has formed due to solid state diffusion of ions in a dense crystalline lattice. However, the formation of an internal oxidation zone (IOZ) underneath type B oxide shows that it is not an effective diffusion barrier. These findings indicate that oxygen is supplied faster to aluminum in solid solution than aluminum to the oxidation front leading to the formation of an IOZ. In addition, the aluminum enrichment in the lower part of the type B oxide does not offer sufficient protection against the inward diffusion of oxygen (and nitrogen). This is in agreement with the study by Zahs et al. [28] where it was found that on Fe-15Cr-5Al (wt%) exposed to N_2(g)-5%O_2(g) at 600^{o}C only γ-alumina forms within 168h. The γ polymorph of alumina is not desired as it is often believed that only the α-alumina, which forms at higher temperatures, is slow-growing i.e. protective [21]. The superior performance of TP347HFG as compared to FeCrAlY/Kanthal APM shows that the presence of aluminum in Fe-Cr solid solutions under the present low temperature humid oxidizing conditions leads to a larger reduction in metal thickness due to internal oxidation than an aluminum-free alloy. In this case the presence of aluminum does not promote the formation of a protective oxide layer. This has also another outcome: nitrogen enrichment underneath the IOZ can lead to the formation of aluminum nitride. The nitrogen involved in the formation of nitrides most likely originates from (reactions with) the carrier gas N_2(g); alternatively it can be the result of the dissolved nitrogen in the alloy that is pushed ahead of the internal oxidation front.

Observation of similar features for FeCrAlY and Kanthal APM can be attributed to a general similarity in composition. The result in Figure 4 indicates a slight difference between the two, which originates from a thicker IOZ for FeCrAlY compared to Kanthal APM. This can be due to a smaller grain size for FeCrAlY (ASTM no 10) compared to Kanthal APM (ASTM no 7). If a protective oxide fails to form, grain boundaries may act as preferential oxygen "inlet" and therefore a thicker IOZ will form.

Nimonic 80A and Alloy 214

The morphologies of the corrosion products on Nimonic 80A and alloy 214 are similar to type A oxide observed on the stainless steels. This suggests that these oxides are formed from oxidation of metal chlorides. Even though the oxide on both nickel-based alloys is chromium and aluminum-rich, it is highly porous and not protective. Apparently the presence of aluminum (and even chromium) in the alloy has not been beneficial as preferential removal of the alloying elements leads to a porous alloy consisting of Ni. The observation that only highly electropositive elements as chromium, aluminum and titanium have been removed from the alloy shows that a selective corrosion mechanism causes the attack, This is most likely due to a chlorination-evaporation-oxidation sequence. Selective removal of chromium, aluminum and titanium and rather passive behavior of nickel can be described in terms of relative thermodynamic stability of the alloying elements' chlorides [29].

Comparing Figures 8a and 10b, it is obvious that Nimonic 80A is attacked more severely by chlorination than alloy 214, since a porous nickel enriched band is observed uniformly along the

surface of Nimonic 80A, while it occurs only locally for alloy 214. A straightforward explanation for this difference cannot be given on the basis of the results obtained and further investigation is necessary.

4.2.2 Silica formers

153MA

The content of 1.6 wt% (3.1 at%) silicon in this alloy did not result in a significant difference compared to low-silicon stainless steels of comparable chromium and nickel contents (TP347HFG and TP347H). As no regions with a contrast darker than the metal and brighter than the oxide in the BSE images (similar to what was observed on FeCrAlY/Kanthal APM) were found, it is indicated that no internal oxidation/nitridation of silicon has occurred.

Alloy HR160

The corrosion product on alloy HR160 is largely composed of potassium, chromium, silicon and oxygen (Figure 15). This is consistent with previous observations that chromia and silica react with KCl in an oxygen containing environment [30]. Limited thickness loss on this alloy (Figure 4) indicates that the corrosion product retards the progress of corrosion. Whether it is the higher chromium content, formation of a silica layer at the metal/oxide interface or the potassium-chromium-silicon-oxygen containing compound(s) itself that provides this protection requires further investigation. Since rinsing in water did not remove potassium, it is suggested that amorphous potassium silicate (or a mixture of silicates) has formed; amorphous potassium silicate(s) is (are) only slightly soluble in water at the ambient temperature [31]. The reason that the silicate does not form on 153MA may be due to the lower silicon content in 153 MA compared to HR160, viz. 3.1 vs 6.5at.%.

In the first part of this study [17] it was shown that even infinitesimal amounts of oxygen and nitrogen impurities in the $Ar(g)+H_2(g)$ gas mixture used for annealing can cause oxidation and/or nitridation of alloys containing reactive oxide/nitride-forming elements such as aluminum or titanium. The presence of needle shaped titanium nitride particles close to the surface of alloy HR160 is attributed to such an effect. The fact that the annealing gas atmosphere had reacted with the sample surface may introduce inaccuracies to the result of the salt-free exposure. This is because a pre-formed oxide (silica or chromia+silica in case of alloy HR160) might have contributed to the passivation. However, since the series 1 sample was also attacked by KCl it shows that the effect of a preformed thin oxide has been small (series 2 is ground with 1000 and 4000 papers, series 1 only 4000). In addition, the similar damage extent observed on both series 1 and 2 also discounts the presence of a thin oxide formed from annealing affecting the results. The lack of a significant protective effect from a preformed chromia and/or silica layer can be due to the reactivity of KCl with both silica and chromia [30].

4.3 Comparison between KCl and K_2CO_3 on Nimonic 80A

In the experiment with K_2CO_3, the formation of outer and inner corrosion products instead of a thin slow-growing oxide shows that the original protective oxide (chromia) on the alloy has been damaged. This can be explained by the reaction between K_2CO_3 and chromia leading to formation of potassium chromate (K_2CrO_4) [2], [11], [15], [16], [32]. Hence, the original diffusion barrier is lost and inward diffusion of anions coupled to outward diffusion of cations can take place leading to the formation of outer and inner corrosion products. However, a different morphology was observed after exposure of Nimonic 80A to KCl. Instead of oxygen ingress, the alloying element chromium, rather than the matrix element, is transported out of the alloy, leaving behind a porous nickel-rich skeleton. This demonstrates that chlorine is also playing a role during high temperature corrosion where KCl is involved. The role of chlorine in accelerating the high temperature corrosion of metals and alloys is often ascribed to the volatilization of the alloying elements as their chlorides and oxychlorides [33]–[37]. Removal in form of subliming/evaporating chlorides is plausible for the current case as it explains void formation deep into the alloy. However, the exact mode of inward transport of chlorine and outward transport of species through the oxide layer requires further investigation.

5. Conclusions

From this study, the following conclusions can be drawn:

- Among the alloys Kanthal APM, FeCrAlY, Nimonic 80A, 214, HR160 and 153MA, only the 153MA formed a fast growing duplex oxide within 168h at 600°C in $N_2(g)+5\%O_2(g)+15\%H_2O(g)$. The presence of KCl led to extensive corrosion of all alloys.
- The presence of aluminum did not lead to the formation of a protective alumina layer on any of the investigated alloys exposed to $N_2(g)+5\%O_2(g)+15\%H_2O(g)+KCl(s)$ at 600°C. Based on a worst case criterion, under the experimental conditions of this study, none of the alumina-forming alloys showed less damage than the currently widely used material TP347HFG.
- The failure of aluminum to form a protective oxide on the iron-chromium and nickel-chromium alloys under the investigated conditions is due to a) aluminum chlorination and subsequent formation of alumina from oxidation of its chloride (alumina in type A oxide) and b) internal oxidation of aluminum (alumina under the type B oxide).
- The presence of 3.1 at% silicon in the austenitic stainless steel 153MA did not lead to a significant difference in performance compared to the low-silicon austenitic stainless steels of similar chromium and nickel contents.
- On alloy HR160, a potassium-chromium-silicon-oxygen containing corrosion product was formed which seems to have a barrier effect against the continuation of corrosion. This alloy was the only alloy (among the ones addressed in this paper) that showed a better performance compared to TP347HFG.

- Both potassium and chlorine can play a role in the KCl-induced high temperature corrosion of chromia-forming alloys.

Acknowledgment

This work was performed within the framework of the project GREEN financed by the Danish Council for Strategic Research under grant number 10-093956. Anette N. Hansson, John C. Troelsen, Flemming B. Grumsen and Peter J.S. Westermann are acknowledged for their help and technical support during this work. Haynes® International is appreciated for supplying alloys 214 and HR160. Outokumpu is acknowledged for supplying stainless steel 153MA.

References

[1] M. Montgomery, S. A. Jensen, U. Borg, O. Biede, and T. Vilhelmsen, "Experiences with high temperature corrosion at straw-firing power plants in Denmark," *Mater. Corros.*, vol. 62, no. 7, pp. 593–605, Jul. 2011.

[2] J. Pettersson, H. Asteman, J.-E. Svensson, and L.-G. Johansson, "KCl Induced Corrosion of a 304-type Austenitic Stainless Steel at 600°C; The Role of Potassium," *Oxid. Met.*, vol. 64, no. 1–2, pp. 23–41, Aug. 2005.

[3] Y. Shinata, F. Takahashi, and K. Hashiura, "NaCl-induced hot corrosion of stainless steels," *Mater. Sci. Eng.*, vol. 87, pp. 399–405, 1987.

[4] Y. S. Li, Y. Niu, and M. Spiegel, "High temperature interaction of Al/Si-modified Fe–Cr alloys with KCl," *Corros. Sci.*, vol. 49, no. 4, pp. 1799–1815, Apr. 2007.

[5] M. Montgomery and A. Karlsson, "In-situ corrosion investigation at Masnedø CHP plant - a straw-fired power plant," *Mater. Corros.*, vol. 50, pp. 579–584, 1999.

[6] Y. Shinata and Y. Nishi, "NaCl-induced accelerated oxidation of chromium," *Oxid. Met.*, vol. 26, pp. 201–212, 1986.

[7] Y. Shinata, "Accelerated oxidation rate of chromium induced by sodium chloride," *Oxid. Met.*, vol. 27, pp. 315–332, 1987.

[8] Y. S. Li, M. Sanchez-Pasten, and M. Spiegel, "High Temperature Interaction of Pure Cr with KCl," *Mater. Sci. Forum*, vol. 461–464, pp. 1047–1054, 2004.

[9] J. Lehmusto, D. Lindberg, P. Yrjas, B.-J. Skrifvars, and M. Hupa, "Studies on the Partial Reactions Between Potassium Chloride and Metallic Chromium Concerning Corrosion at Elevated Temperatures," *Oxid. Met.*, Nov. 2011.

[10] J. Lehmusto, B.-J. Skrifvars, P. Yrjas, and M. Hupa, “High temperature oxidation of metallic chromium exposed to eight different metal chlorides,” *Corros. Sci.*, vol. 53, no. 10, pp. 3315–3323, Oct. 2011.

[11] J. Lehmusto, D. Lindberg, P. Yrjas, B.-J. Skrifvars, and M. Hupa, “Thermogravimetric studies of high temperature reactions between potassium salts and chromium,” *Corros. Sci.*, Mar. 2012.

[12] N. Hiramatsu, Y. Uematsu, T. Tanaka, and M. Kinugasa, “Effects of alloying elements on NaCl-induced hot corrosion of stainless steels,” *Mater. Sci. Eng. A*, vol. 120–121, pp. 319–328, Nov. 1989.

[13] H. Fujikawa and N. Maruyama, “Corrosion behaviour of austenitic stainless steels in the high chloride-containing environment,” *Mater. Sci. Eng. A*, vol. 20, pp. 301–306, 1989.

[14] Y. S. Li, M. Spiegel, and S. Shimada, “Effect of Al/Si addition on KCl induced corrosion of 9% Cr steel,” *Mater. Lett.*, vol. 58, no. 29, pp. 3787–3791, Nov. 2004.

[15] J. Lehmusto, B.-J. Skrifvars, P. Yrjas, and M. Hupa, “Comparison of potassium chloride and potassium carbonate with respect to their tendency to cause high temperature corrosion of stainless 304L steel,” *Fuel Process. Technol.*, Jan. 2012.

[16] J. Lehmusto, P. Yrjas, B.-J. Skrifvars, and M. Hupa, “High temperature corrosion of superheater steels by KCl and K2CO3 under dry and wet conditions,” *Fuel Process. Technol.*, vol. 104, pp. 253–264, Dec. 2012.

[17] S. Kiamehr, K. V. Dahl, M. Montgomery, and M. A. J. Somers, “KCl-induced high temperature corrosion of selected commercial alloys part I: chromia-formers.”

[18] H. Asteman, J. E. Svensson, and L. G. Johansson, “Indication of chromium oxide hydroxide evaporation during oxidation of 304L at 873 K in the presence of 10% water vapor,” *Oxid. Met.*, vol. 52, no. 1, pp. 95–111, 1999.

[19] H. Asteman, J. E. Svensson, M. Norell, and L. G. Johansson, “Influence of water vapor and flow rate on the high-temperature oxidation of 304L; effect of chromium oxide hydroxide evaporation,” *Oxid. Met.*, vol. 54, no. 1, pp. 11–26, 2000.

[20] E. J. Opila, “Volatility of Common Protective Oxides in High-Temperature Water Vapor: Current Understanding and Unanswered Questions,” *Mater. Sci. Forum*, vol. 461–464, pp. 765–774, 2004.

[21] D. J. Young, *High Temperature Oxidation and Corrosion of Metals*, 1st ed. Elsevier, 2008.

[22] T. Jonsson, J. Froitzheim, J. Pettersson, J. E. Svensson, L. G. Johansson, and M. Halvarsson, “Microstructural investigation of the influence of KCl on the corrosion of 304L exposed to 5% O2+ N2,” in *16th International Corrosion Congress, 2005, Beijing, China*, no. 15x15x2 mm.

[23] N. Folkeson, T. Jonsson, M. Halvarsson, L.-G. Johansson, and J.-E. Svensson, "The influence of small amounts of KCl(s) on the high temperature corrosion of a Fe-2.25Cr-1Mo steel at 400 and 500°C," *Mater. Corros.*, vol. 62, no. 7, pp. 606–615, Jul. 2011.

[24] T. Jonsson, N. Folkeson, J.-E. Svensson, L.-G. Johansson, and M. Halvarsson, "An ESEM in situ investigation of initial stages of the KCl induced high temperature corrosion of a Fe–2.25Cr–1Mo steel at 400°C," *Corros. Sci.*, vol. 53, no. 6, pp. 2233–2246, Jun. 2011.

[25] S. Cha and M. Spiegel, "Local reactions between NaCl and KCl particles and metal surfaces," *Corros. Eng. Sci.*, vol. 40, no. 3, pp. 249–253, 2005.

[26] S. C. Cha and M. Spiegel, "Local reactions of KCl particles with iron, nickel and chromium surfaces," *Mater. Corros.*, vol. 57, no. 2, pp. 159–164, Feb. 2006.

[27] S. Cha and M. Spiegel, "Fundamental studies on alkali chloride induced corrosion during combustion of biomass," *Mater. Sci. Forum*, vol. 461–464, pp. 1055–1062, 2004.

[28] A. Zahs, M. Spiegel, and H. Grabke, "The influence of alloying elements on the chlorine-induced high temperature corrosion of Fe-Cr alloys in oxidizing atmospheres," *Mater. Corros.*, 1999.

[29] R. Bender and M. Schutze, "The role of alloying elements in commercial alloys for corrosion resistance in oxidizing-chloridizing atmospheres. Part I: Literature evaluation and thermodynamic calculations," *Mater. Corros.*, vol. 54, no. 8, pp. 567–586, 2003.

[30] S. Kiamehr, K. V Dahl, T. N. Lomholt, T. L. Christiansen, and M. A. J. Somers, "High Temperature Corrosion due to Biomass Firing : A Study on the Reactivity between Potassium Chloride and Oxides," in *International Symposium on High Temperature Oxidation and Corrosion (ISHOC), Hakodate, Japan*, 2014, vol. 2, no. Vi.

[31] "soluble silicates." [Online]. Available: http://www.solublesilicates.eu/docs/solsil_broch_1302.pdf. [Accessed: 05-Sep-2014].

[32] J. Pettersson, N. Folkeson, L.-G. Johansson, and J.-E. Svensson, "The Effects of KCl, K2SO4 and K2CO3 on the High Temperature Corrosion of a 304-Type Austenitic Stainless Steel," *Oxid. Met.*, vol. 76, no. 1–2, pp. 93–109, Mar. 2011.

[33] A. Kim and M. McNallan, "Mixed Oxidation of Iron-Chromium Alloys in Gases Containing Oxygen and Chlorine at 900 to 1200° K," *Corrosion*, vol. 46, no. 9, pp. 746–755, 1990.

[34] J. Oh, M. McNallan, G. Lai, and M. Rothman, "High temperature corrosion of superalloys in an environment containing both oxygen and chlorine," *Metall. Mater. ...*, vol. 17, no. 600, pp. 1087–1094, 1986.

[35] M. Rhee, M. McNallan, and M. Forthman, "Long term high temperature corrosion studies of high temperature alloys in chlorine contaminated environments," *J. Mater. energy*, vol. 7, no. 4, pp. 294–301, 1986.

[36] M. McNallan, “High-temperature corrosion in halogen environments,” *Mater. Perform.*, pp. 54–57, 1994.

[37] H. Grabke, E. Reese, and M. Spiegel, “The effects of chlorides, hydrogen chloride, and sulfur dioxide in the oxidation of steels below deposits,” *Corros. Sci.*, vol. 37, no. 7, pp. 1023–1043, 1995.

9.4 Paper IV

Saeed Kiamehr, Sunday C. Okoro, Kristian V. Dahl, Melanie Montgomery, Marcel A.J. Somers

KCl-Induced High Temperature Corrosion Part III: Performance of Model Alloys and Argumentations on the Involved Mechanisms

The manuscript is under modification

KCl-Induced High Temperature Corrosion

Part III: Performance of Model Alloys and Argumentations on the Involved Mechanisms

Saeed Kiamehr[*1], *Sunday C. Okoro*[1], *Kristian V. Dahl*[1], *Melanie Montgomery*[1,2], *Marcel A.J. Somers*[1]

1) Technical University of Denmark (DTU), Department of Mechanical Engineering, Produktionstorvet, Building 425, 2800 Kgs. Lyngby, Denmark
2) COWI A/S Parallelvej 2, 2800 Kgs. Lyngby, Denmark

Abstract

KCl-induced high temperature corrosion of three model alloys and pure nickel was studied aiming at evaluating performance and obtaining further insight into the corrosion mechanism(s). The alloys consisted of Fe-14Cr-3Si, Fe-19Cr-3Si-2. Ni and Ni-45Cr-4Nb (all in wt.%). Exposures were performed at 600^{o}C for 168h in flowing N_2(g)-5%O_2(g)-15%H_2O(g) (vol.%) with samples covered under KCl(s). After the exposures, cross sections of the samples were studied with Scanning Electron Microscopy (SEM) and Energy Dispersive X-Ray Spectroscopy (EDS). The three model alloys all showed poor performance. The silicon containing iron-chromium alloys suffered from internal oxidation/nitridation and grain boundary attack. The nickel-based model alloy suffered from extensive selective chromium removal. Pure nickel was not significantly affected by KCl and, interestingly, showed least damage among the investigated alloys. The results are discussed in the light of an extensive literature survey and thermodynamic calculations. Finally, a tentative mechanism is proposed to account for the KCl-induced selective corrosion.

Keywords: biomass combustion, deposit, potassium chloride, high temperature corrosion, model alloys, silica-former, chromium-rich phase.

1. Introduction

It is well-documented that the combustion of biomass results in the deposition of potassium chloride (KCl) on the heat exchangers in power plants [1]–[4]. KCl-rich deposits are so corrosive towards the conventional stainless materials that in order to avoid unacceptable material losses, it is necessary to maintain the outlet steam temperature below a certain limit [5]. Consequently biomass-based power plants have a lower efficiency compared to power plants firing coal, oil and natural gas. This has been the incentive for extensive studies on alkali chloride-induced high temperature corrosion of metals and alloys.

The mechanism of the KCl-induced high temperature corrosion is not yet fully understood. The classic description attributes the corrosive nature of chloride deposits to chlorine [6][7]. In this mechanism sulfation of the condensed chloride is proposed to extract the chlorine from the chloride deposit. Since combustion atmospheres often contain moisture the liberated chlorine will be in form of hydrogen chloride HCl(g) (eq. 1). However, HCl(g) can be converted to chlorine according to eq. 2.

$$2KCl + SO_2(g) + 0.5O_2(g) + H_2O(g) = K_2SO_4 + 2HCl(g) \quad (1)$$

$$2HCl(g) + 0.5O_2(g) = H_2O(g) + Cl_2(g) \quad (2)$$

The role of chlorine to accelerate corrosion of metals and alloys is often described by the "active oxidation" model [8], [9]. In this model $Cl_2(g)$ penetrates the oxide layer through cracks and pores and forms chlorides of the alloying elements at the metal/oxide interface where the oxygen partial pressure, $P_{O2(g)}$, is low. Since chlorides are generally volatile at high temperatures they sublime through the cracks and pores of the oxide layer. Upon outward migration the subliming chlorides meet regions of higher $P_{O2(g)}$ and convert to the corresponding oxides. This leads to the regeneration of $Cl_2(g)$ which returns to the metal/oxide interface to repeat the the chlorination-oxidation cycle. Although this mechanism accounts well for the morphology of corrosion products often observed in chlorine-induced corrosion, it still leaves behind a number of unanswered questions. An important ambiguity is explaining how the oxide can be permeable to $Cl_2(g)$ and metal chlorides while it is impermeable to $O_2(g)$, which is the smaller molecule [10][11]. To describe the penetration of chlorine through the oxide layer Folkeson et al. [12]–[14] proposed an electrochemical route for the extraction of chlorine (from chlorides) and its subsequent ionic transport through the grain boundaries of the oxide layer (equations 3-5).

cathode

$$2HCl(g)+(1/2)O_2(g)+2e^- = H_2O(g)+2Cl^- \quad (3)$$

and/or

$$2KCl(s,g)+(1/2)O_2(g)+H_2O(g)+2e^- = 2KOH(g)+2Cl^- \quad (4)$$

anode

$$M = M^{n+} + ne^- \quad (5)$$

In this model it is assumed that since the Cl^- ion has less charge than O^{2-} it is more mobile and therefore travels easily along the oxide grain boundaries. Although this mechanism can explain the transport of chlorine through preformed oxides it does not address the extensive preferential removal (selective corrosion) of alloying elements, as is usually observed when chlorine-bearing species are involved in the atmosphere. Selective corrosion has been reported for many nickel-based alloys and austenitic stainless steels upon exposure to a chlorine-containing atmosphere at high temperature [15]–[18]. This type of attack is promoted significantly if the alloy contains chromium carbides [19], [20]. In addition to the above-mentioned mechanisms chlorine has also been reported to damage metals and alloys by the following mechanisms:

- deteriorating the adhesion of oxide to the alloy: several researchers [21]–[25] reported that when chlorine is present in the environment, the formed oxide poorly adheres and spalls-off easily during exposure or subsequent cooling.
- Volatizing the oxide layer by conversion into volatile chlorides and/or oxychlorides [26].
- Changing the transport properties of the oxide by modification of the defect chemistry (increase in cation vacancy) [27]–[29] or increasing the ionic conductivity of the oxide due to presence of alloying element chlorides at oxide grain boundaries [12].
- Interfacial catalysis: acceleration of oxidation kinetics at the metal/oxide interface if chloride ions are present [30].
- Internal chlorination (analogous to internal oxidation) [31].
- Formation of liquid chloride melts underneath the oxide scale [32].
- Fissuring and cracking of the oxide due to the presence of chloride ions [33].

While numerous reports in the literature regarding alkali chloride-induced high temperature corrosion focus on the detrimental effects of chlorine, Pettersson et al. [11] showed that a significant role is also played by the alkali component of the salt. High temperature alloys often rely on the formation and maintenance of a Cr_2O_3 (chromia) layer for protection. In alkali chloride-containing environments, a reaction between the alkali metal and chromia can take place leading to the formation of chromate (e.g. eq.6).

$$4KCl(s,g)+Cr_2O_3+(3/2)O_2(g)+2H_2O(g) =2K_2CrO_4+4HCl(g) \quad (6)$$

Similar to chromic acid formation in water vapor [34], [35], chromate formation acts as a sink for chromium from the oxide layer whereby it loses its protective properties [11]. In fact, it has been demonstrated that solid alkali carbonates are corrosive as well [36][37]. In addition, Karlsson et al. [38] showed that the presence of $SO_2(g)$ in the gas decreases KCl attack on austenitic stainless steel 304L (Fe-18.5Cr-10.2Ni wt.%). This result was explained by much lower reactivity between the potassium sulfate (K_2SO_4) and the chromia in the oxide layer. Such observations further underline the importance of potassium in KCl on the corrosion mechanism. Accordingly it is expected that all chromia-forming alloys suffer from (at least) an initial attack by potassium chromate formation. Hence for alloys relying on chromia, passivation is not possible and other corrosion mitigation strategies should be adopted.

If the initial breakdown of the protective oxide by alkali chromate formation was the only problem, an increase in chromium content of the alloy could potentially lower the extent of damage by supplying enough chromium to facilitate the re-formation of a chromium-rich oxide. However, due to the presence of chlorine the situation becomes more complicated. In fact, for chlorine and alkali chloride-induced high temperature corrosion widely different effects of an increase in chromium content are reported in the literature. Whether an improvement will be achieved or not appears to depend on the temperature, microstructure, $P_{O2(g)}/P_{Cl2(g)}$ ratio and $P_{H2O(g)}$. Consequently, slightly different exposure conditions can result in entirely different results and conclusions. Viklund et al.[39] reported that an increase in chromium content from 15 to 25 wt% in Fe-Cr-Ni

alloys significantly improved the performance of these alloys on exposure at 700°C in N_2(g)+10%O_2(g)+5%H_2O(g) +0.05%HCl(g) (vol.%). However Stott and Shih [23] reported that an Fe-28wt.%Cr alloy showed a mass gain comparable to pure iron after exposure to Ar(g)+20%O_2(g)+1%HCl(g) (vol.%) at 700 °C. Similar observations were reported for exposures to alkali chlorides. Pettersson et al.[40] reported that Sanicro 28 (Fe-27%Cr-31%Ni) shows less damage compared to 304L (Fe-18.5%Cr-10.2 Ni wt.%) when exposed to N_2(g)+5%O_2(g)+40%H_2O(g)+0.1 mg/cm^2 KCl(s) at 600°C. On the other hand, Li et al.[41] observed that Fe-35Cr wt.% showed higher mass gains compared to Fe-15wt.%Cr when exposed under a KCl deposit at 650°C in static lab air. Interpretation of field test results is even more difficult as the exposure environment is more complex. However, for exposure of steels and nickel based alloys in Danish power plants Montgomery et al.[42] reported the general trend that an increase in chromium content above 15-18wt.% deteriorated the corrosion resistance; an observation that encourages employing other oxide-forming elements than chromium. In the literature, it has been reported that aluminum and/or silicon additions to chromia-forming alloys mitigates alkali chloride-induced high temperature corrosion [41], [43]–[45].

The present article is the third part of a larger study evaluating the performance of a wide range of commercial and model alloys under KCl-induced high temperature corrosion. In the first part of this study it was found that none of the chromia-forming alloys shows passive behavior, most likely as a consequence of a breakdown of the initial chromium-rich oxide caused by chromate formation. In addition, a beneficial effect from an increase in chromium content of the solid solution in iron-chromium-(nickel) alloys was indicated, while no clear trend could be seen for nickel-base alloys.

In the second part of this study, the effect of presence of aluminum or silicon in selected chromia-forming alloys was investigated. No beneficial effect from aluminum could be observed in the investigated alloys. However, for silicon the effect could not be clarified. Among the two investigated silicon-modified alloys the content of silicon in 153MA turned out to be too low to reveal a significant difference in the corrosion extent. For HR160, which showed a relatively good performance, it is not clear whether the effect originated from silicon or whether it was just the high chromium content in solid solution that provided improved performance. In the current study two model alloys with silicon content higher than in 153MA were chosen to obtain further insight into the effect of silicon. The compositions of these alloys were based on the compositions of EN1.4021 and EN1.4057 as investigated in the first part of this study [46]. Another important observation in the second part of this study was the detrimental effect from chromium-rich precipitate phases in the nickel-base alloys. Therefore to further elucidate this effect a high chromium nickel-based alloy, with a chromium content far above the solubility limit, was adopted for further investigation. Pure nickel was included in the experimental studies for comparison. Finally, based on the findings in the current study and in the two previous papers, the mechanism of KCl-induced high temperature corrosion is attempted to be clarified.

2. Experimental Procedure

The chemical compositions of the studied model alloys are given in Table 1. Samples were coupons of 7-8mm x 17-20mm cut with a precision cutter to a thickness between 250-340μm. Prior to exposure, all the samples were polished with 4000-grit SiC paper and then partly (~2/3 of length) covered with KCl powder. The thickness of the KCl layer was ~1mm and the powder had a particle size of 63-90μm. Samples were placed on flat alumina coupons and then loaded to a multi-channel alumina sample holder with the KCl-free part towards the gas stream. The sample holder itself was then placed in the even temperature zone of a horizontal furnace equipped with a silica tube. Figure 1 shows a schematic representation of the experimental set-up.

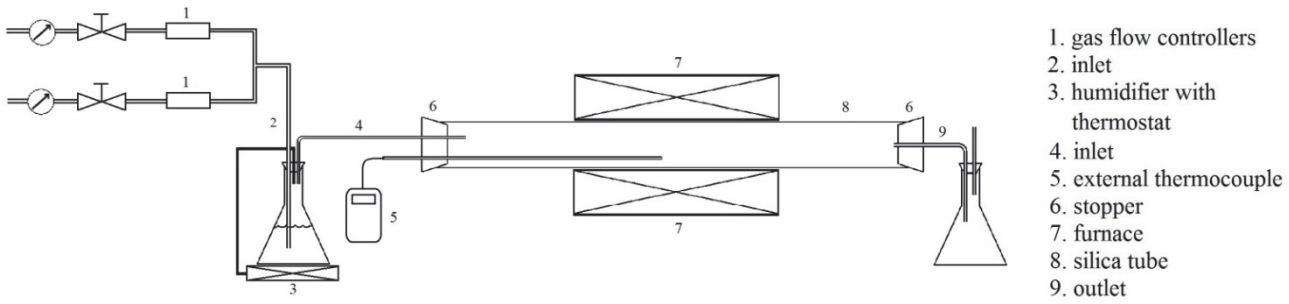

Figure 1: Schematic of the experimental set-up

Exposures were performed at 600°C for 168h in flowing N_2(g)+5%O_2(g)+15%H_2O(g) with a velocity of 0.25cm/s at the inlet temperature. After the exposures, samples were clamped in an upright position and mounted in epoxy resin without removing the KCl layer. Subsequently they were ground up to the middle (half the original width was removed) and polished down to 1μm diamond suspension step. Grinding and polishing were performed using 96% ethanol up to 1000 grit SiC paper and 99.9% ethanol on finer papers and during diamond polishing. The exposures were done twice for model alloys Fe14Cr3Si and Fe19Cr3Si2Ni with one set of samples that were investigated directly and one set that was thoroughly washed by de-ionized water after the exposure to remove water soluble corrosion products. The washed samples were also embedded in epoxy resin but their cross sections were prepared using water as lubricant during grinding. For the model alloys, the decrease in metal thickness after exposure was measured by means of a light optical microscope (LOM) equipped with a travelling stage. Measurements were done for twenty points, spaced 0.5mm, and average/standard deviation was calculated for each sample. Thereafter the location along the surface with the deepest penetrating damage was found and defined as worst case attack. Finally, the morphology of the corrosion products was studied using an FEI Inspect S Scanning Electron Microscope (SEM) equipped with an Energy Dispersive X-Ray Spectroscopy (EDS) detector. Imaging was always performed in Back-Scattered Electron (BSE) mode, unless otherwise mentioned. On the pure nickel sample, the corrosion extent (thickness reduction) was measured using SEM images, because the boundaries of the oxide were well defined.

Table 1: Chemical composition of the materials according to the supplier. All values are in wt% (values in the parenthesis are in at.%)

alloy	Fe	Cr	Ni	Si	Ti	C	N	other
Fe14Cr3Si*	bal.	14.10 (14.53)	0.04 (0.036)	3.14 (5.99)		0.008 (0.036)	0.007 (0.027)	
Fe19Cr3Si2Ni*	bal.	19.00 (19.55)	2.02 (1.84)	3.06 (5.83)		0.007 (0.031)	0.009 (0.034)	
Ni45Cr4Nb**		44.80 (48.39)	bal.	0.05 (0.1)	0.53 (0.62)	0.013 (0.061)	0.001 (0.004)	Nb4.06 (2.45)
pure nickel			99.99					

* Cast alloys (exposed in as-cast condition)
** Powder metallurgical alloy

3. Results

3.1 Fe14Cr3Si

The morphology of corrosion product consisted of a highly porous outer oxide layer (referred to as type A oxide) and a relatively dense inner part (referred to as type B oxide, see Figure 2a). Grain boundary attack was often observed (Figure 2b) and precipitates were frequently detected below the metal/oxide interface (Figure 2c). A chromium-rich phase was observed along the alloy grain boundaries before and after the exposure (Figure 2b).

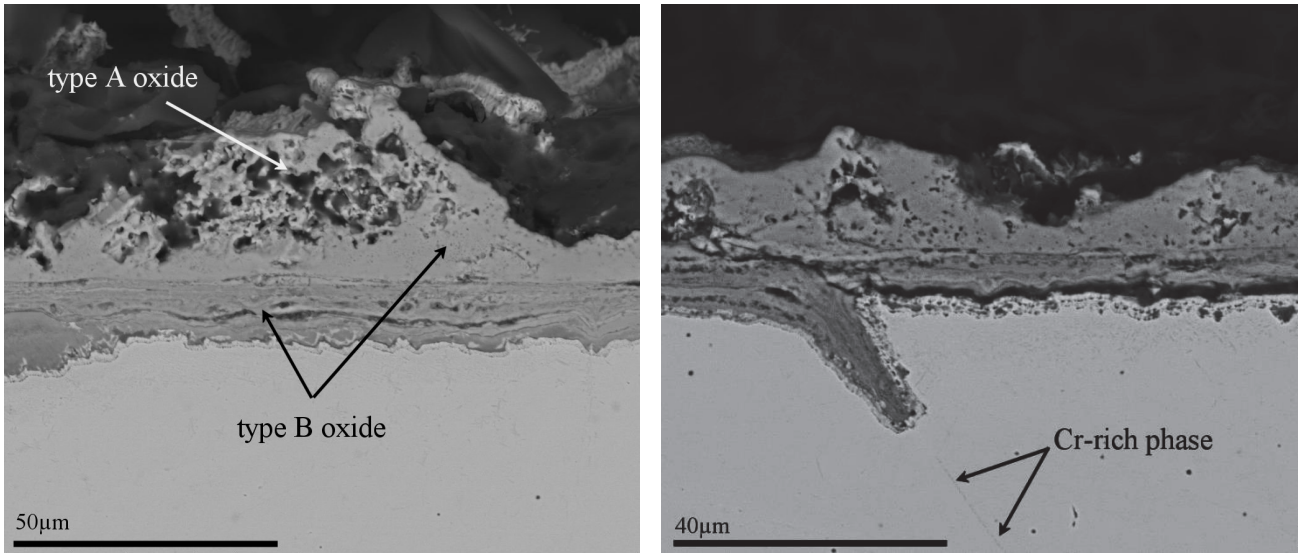

(a) (b)

Figure 2: Features observed on Fe14Cr3Si (a) general corrosion morphology (b) grain boundary attack (c) precipitates underneath the metal/oxide interface.

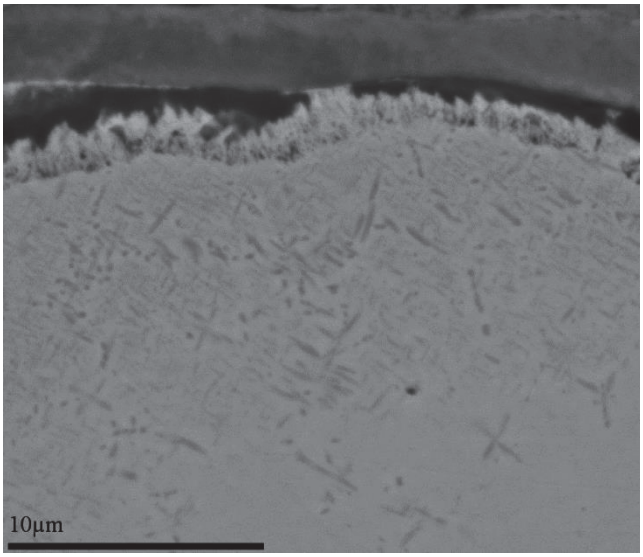

(c)

Figure 2 (cont.)

The distribution of alloying elements over the corrosion product morphology is shown in Figure 3. The outer oxide is enriched in iron and contains some chromium. The inner part is iron-rich in the upper part and chromium/silicon-rich in the lower part. In addition potassium is identified in the lower part of the type B oxide. A layered structure containing local enrichments of iron (corresponding to lower chromium content) is apparent. Chlorine was detected in the lower part of the type B oxide, but was more concentrated at the metal/oxide interface. EDS spot analysis revealed the presence of oxygen and nitrogen in the precipitation zone. In addition, mapping of the corrosion morphology shown in Figure 2b showed the presence of chlorine and minor amounts of potassium along the grain boundary (Figure 4).

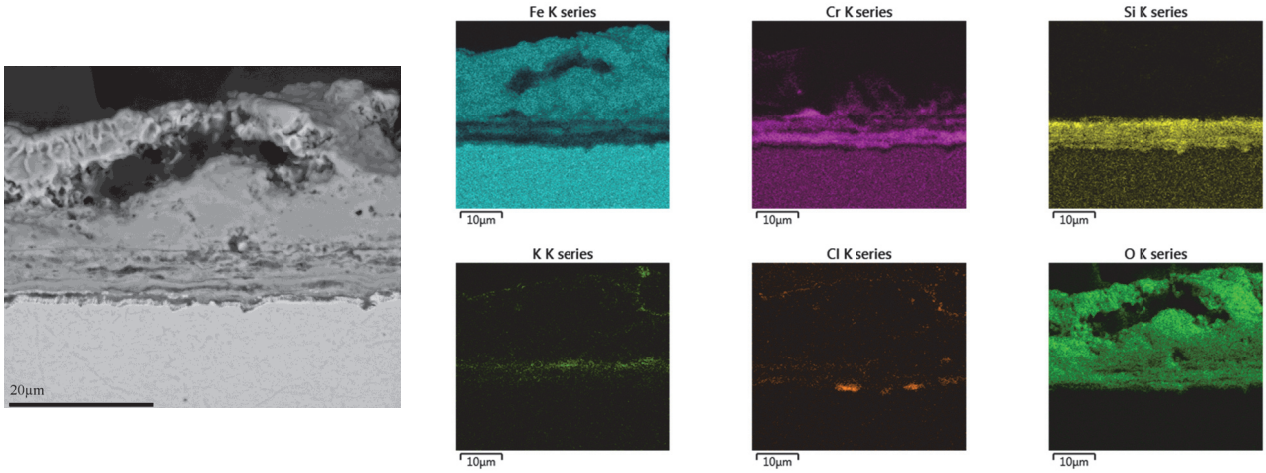

Figure 3: Distribution of the alloying elements, potassium and chlorine throughout the corrosion product on Fe14Cr3Si.

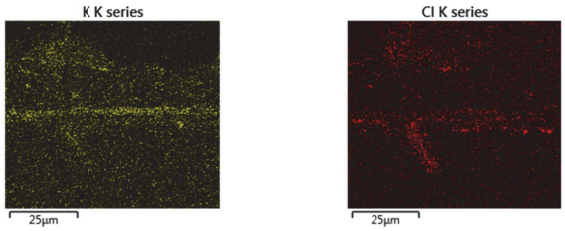

Figure 4: Presence of potassium and chlorine in the corrosion product along the grain boundary shown in Figure 2b.

3.2 Fe19Cr3Si2Ni

In general, the corrosion morphology and distribution of alloying elements was similar to those in Fe14Cr3Si (see Figures 5a-c and 6). However, potassium was detected together with chromium in type A oxide as well. In both model alloy samples, which were washed with de-ionized water prior to the embedding, potassium was found in lower part of type B oxide.

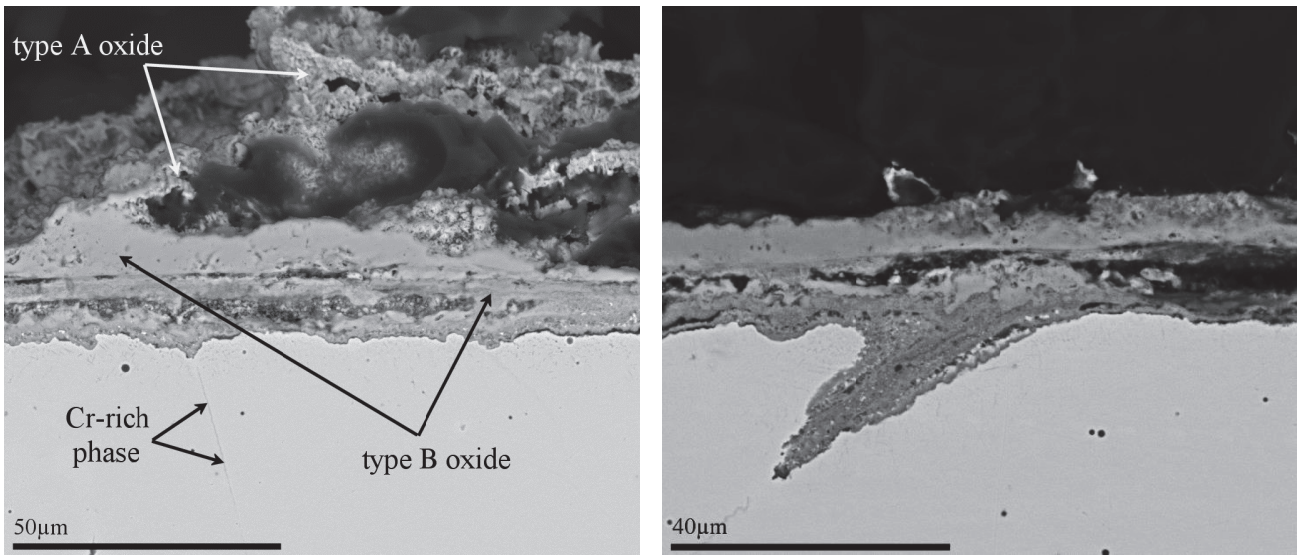

(a) (b)

Figure 5: Features observed on Fe19Cr3Si2Ni (a) general corrosion morphology (b) grain boundary attack (c) precipitates underneath the metal/oxide interface.

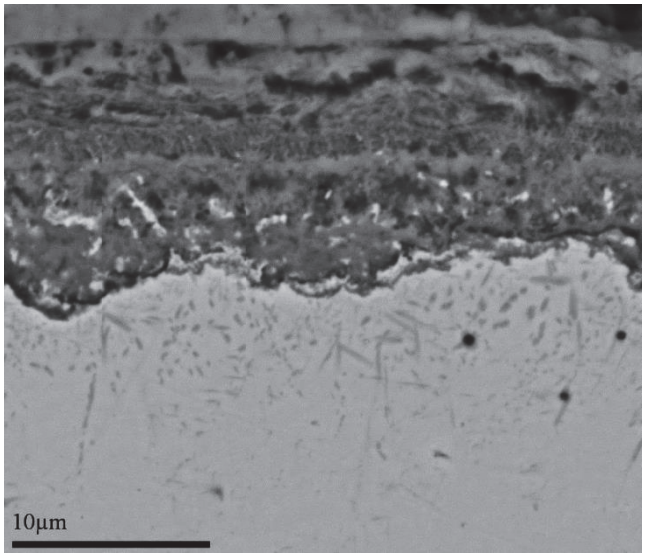

(c)

Figure 5 (cont.)

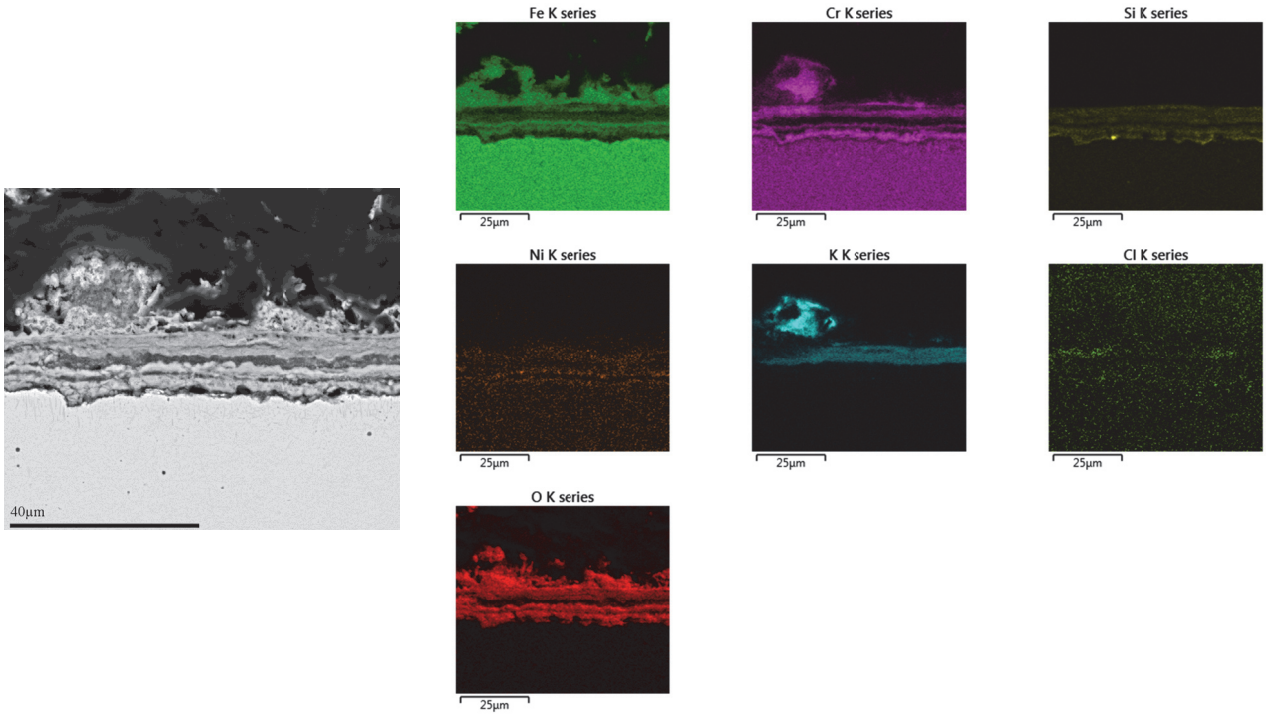

Figure 6: Distribution of the alloying elements, potassium and chlorine throughout the corrosion product on Fe19Cr3Si2Ni.

3.3 Ni45Cr4Nb

Detailed microstructural analysis of this alloy by Bihlet et al.[47] revealed that the microstructure consists of α-Cr and $Ni_3(Nb,Ti)$ phases embedded in a Ni matrix. The attack was characterized by void formation deep in the alloy to the most pronounced extent observed for the alloys investigated in this study (including parts 1 and 2 [46], [48]) (Figure 7a). In some areas void formation was

found as deep as 200µm from the original alloy surface. The outer corrosion product consists of an outermost eutectic-looking mixture with dark and bright phases in a BSE image (Figure 7b). The mixture is rich in potassium, chromium and oxygen with trace contents of chlorine (less than 0.5 at% from EDS spot analysis). The dark phases were rich in potassium and the bright phases were rich in chromium. Below the mixture a denser corrosion product is found on top of the original alloy surface. The dense region is rich in chromium and oxygen. Below this region, i.e. underneath the original alloy surface, deep void formation is observed. The distribution of alloying elements is shown in Figure 8. Titanium and niobium are present along a line that marks the position of the original alloy surface. Chromium was selectively removed from the alloy, leaving an enrichment of nickel in the porous part.

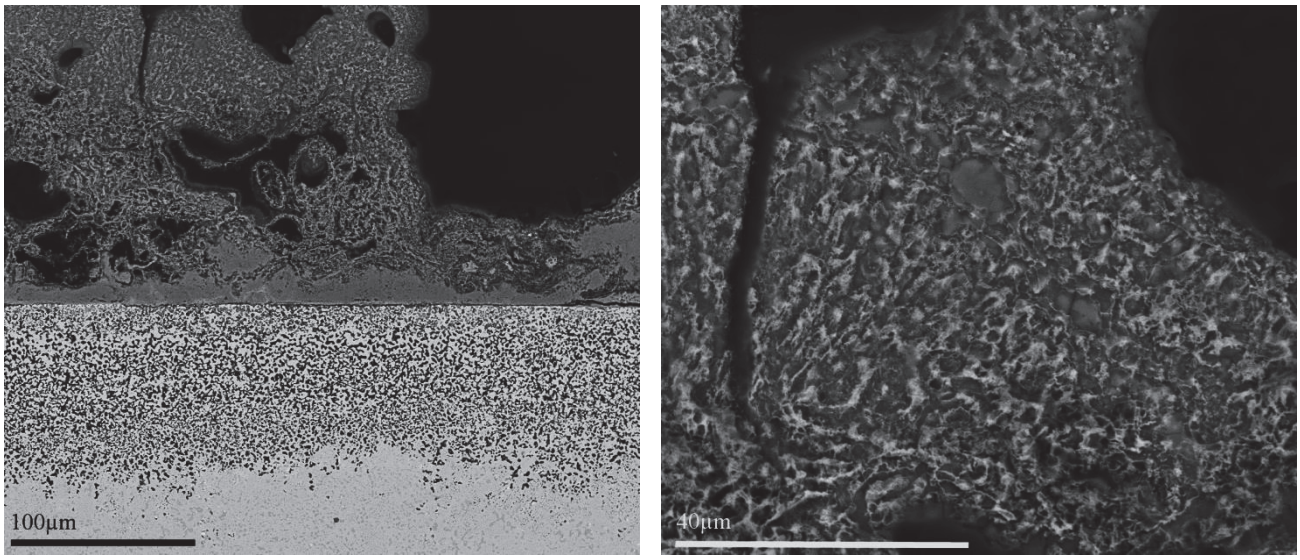

(a) (b)

Figure 7: (a) morphology of corrosion observed on Ni45Cr4Nb (b) appearance of the outermost corrosion product suggesting the presence of a solidified eutectic.

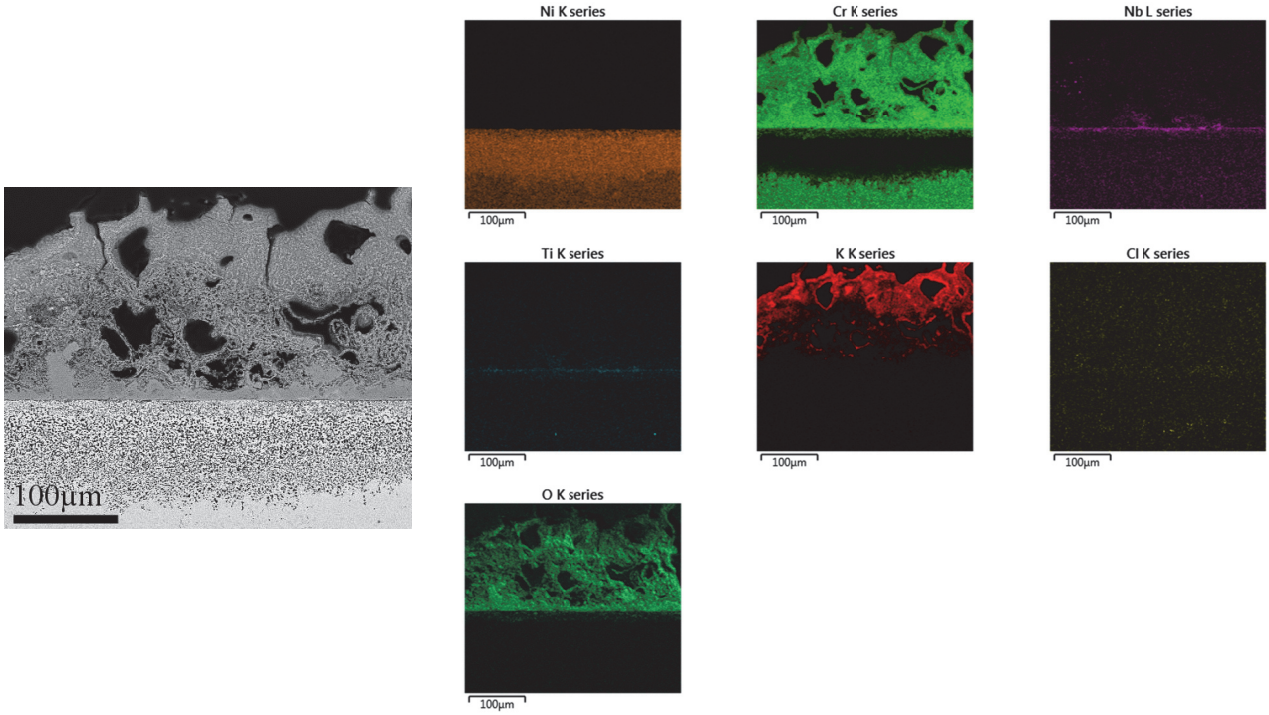

Figure 8: Distribution of the alloying elements, potassium, chlorine and oxygen on Ni45Cr4Nb.

3.4 Pure Nickel

Pure Ni showed a uniform oxide over the entire surface. The thicknesses of the oxide layer are comparable for the part covered with KCl and the part without deposit (Figures 9a-b). The only difference was that the KCl covered area showed more porosity. No spongy oxide (type A oxide) was observed and the boundaries of the oxide layer were well-defined. The position of the original metal surface could not be clearly distinguished. Therefore a subsequent gold-marker experiment was performed (Figure 9c) that gave an average value of 3.5µm for the thickness of the inward growing oxide. This value is approximately half of the total oxide layer thickness. EDS spot analysis on the cross section of the oxide layer did not indicate the presence of other elements than nickel and oxygen.

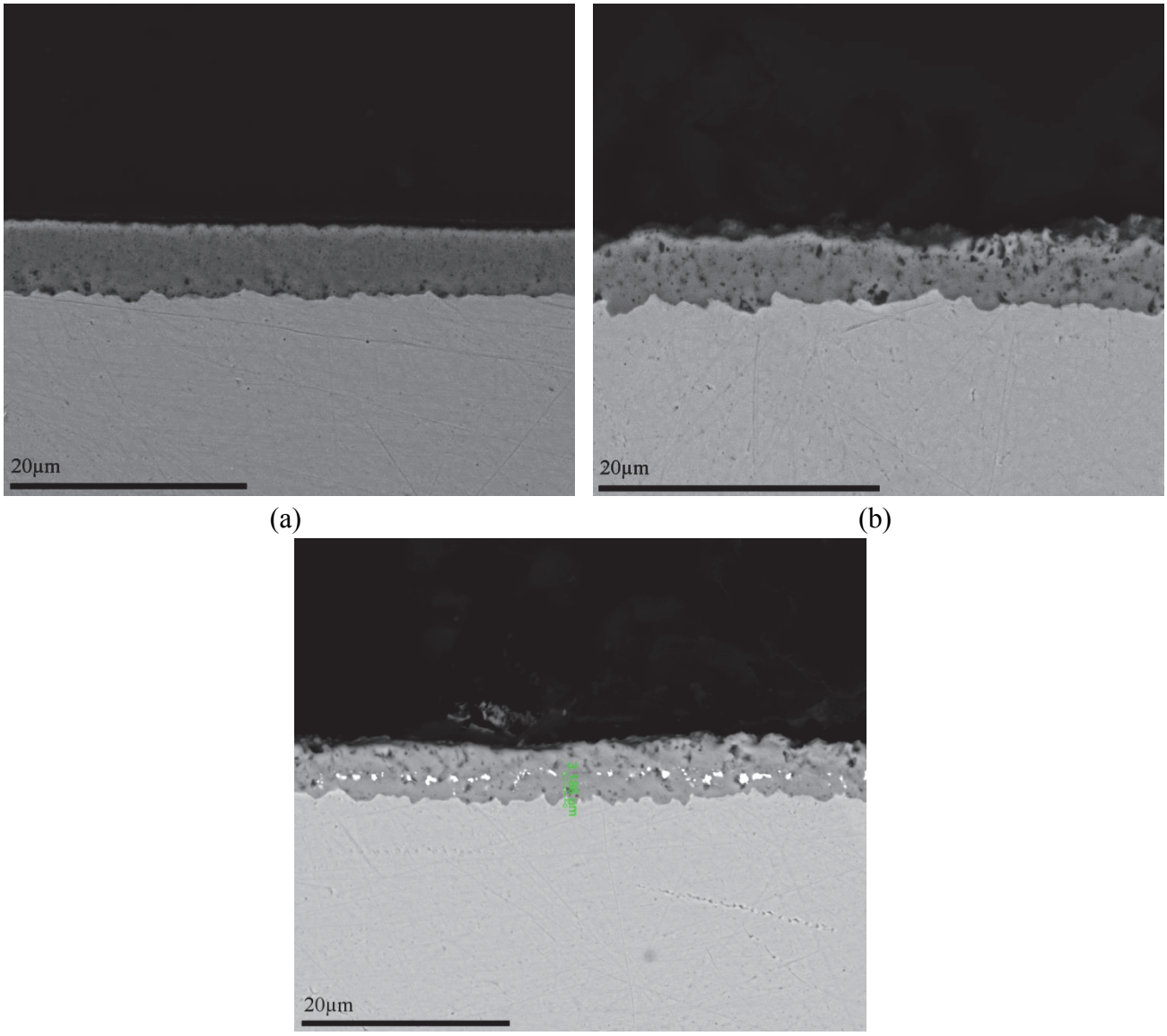

Figure 9: Morphology of the oxide on the pure nickel sample (a) KCl-free part (b) KCl-covered part. (c) The same as b with the original metal surface marked with gold (bright particles in the middle of the oxide layer).

The extents of damage on the model alloys and pure nickel are compared with data from the previous parts of this study in Figure 10. Evidently, the presence of silicon in Fe14Cr3Si and Fe19Cr3Si2Ni did not lead to an improvement in performance compared to the two ferritic-martensitic steels with similar chromium content (EN1.4021 and EN1.4057). Pure nickel showed a better performance compared to all of its chromium-containing alloys and Ni45Cr4Nb had by far the highest metal thickness loss.

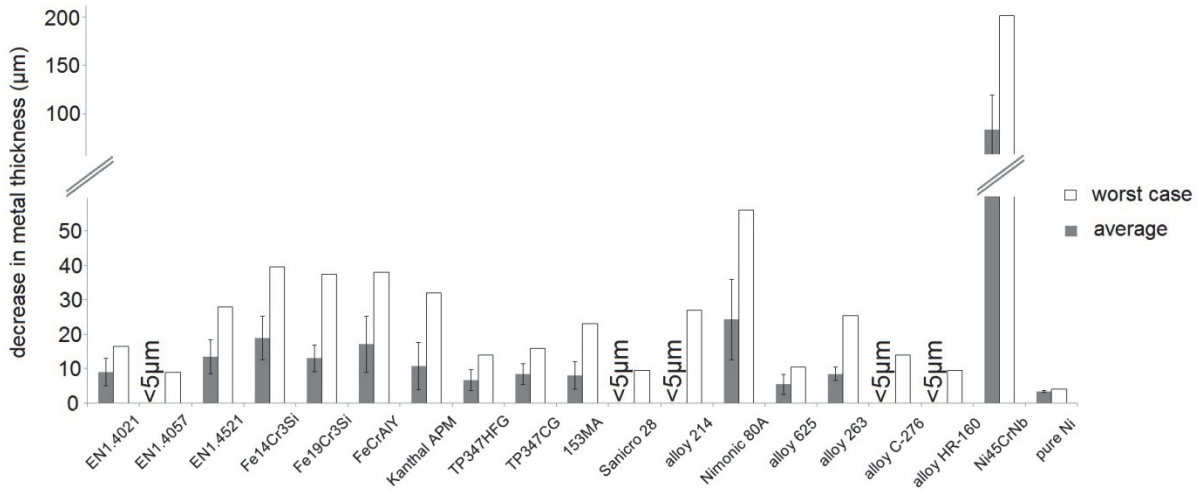

Figure 10: Average and largest thickness loss observed on the studied alloys after 168 exposure at 600°C under N_2(g)+5%O_2(g)+15%H_2O(g)+KCl(s). Values less than 5µm are beyond the accuracy of the employed micrometer. For pure nickel SEM images were used to measure the lost thickness.

4. Discussion

4.1 Fe14Cr3Si and Fe19Cr3Si2Ni

The presence of type A and type B oxides on both model alloys was typical for all the iron-chromium-(nickel) alloys previously investigated [46], [48]. Formation of an outermost highly porous oxide appears to be due to its formation from oxidation of chlorides rather than combination of metal cations and oxide anions diffusing in the solid crystalline lattice. Several authors [13], [14], [49], [50] reported the formation of low eutectic temperature melts (such as KCl-$FeCl_2$) when metals are exposed to alkali chlorides in an oxidizing atmosphere. Subsequent oxidation of metal chlorides from such a mixture can account for the formation of type A oxide. On the other hand, the dense appearance of type B oxide indicates that it has formed due to a direct combination of metal cations and oxide/hydroxide anions rather than oxidation of metal chlorides.

The inner oxide for Fe14Cr3Si and Fe19Cr3Si2Ni showed the presence of potassium, which was otherwise only observed for alloy HR160 (containing 6.5at.% silicon) among all the alloys investigated in previous work [48]. Equilibrium calculations with Thermo-Calc [51] show that potassium-containing compounds can be stable even at regions where the oxygen potential is low i.e. inner oxides (see Figure 11). The presence of a potassium-silicon-oxygen containing compound in Fe14Cr3Si and Fe19Cr3Si2Ni is further supported by the observation that rinsing in water did not entirely remove the potassium from the microstructure. It is reported that amorphous potassium silicates have limited solubility in water at room temperature [52]. Whether the presence of potassium silicate is beneficial or detrimental for corrosion resistance cannot be deduced from what is observed here and requires longer exposures. However, formation of internal oxides and nitrides shows that silicon, in the investigated model alloys, does not have enough diffusivity at 600°C to form a protective silica layer underneath the inner oxide. Nitrogen most probably originates from

the carrier gas. However possibility of dissolved nitrogen in the alloy being pushed back due to internal oxidation cannot be excluded.

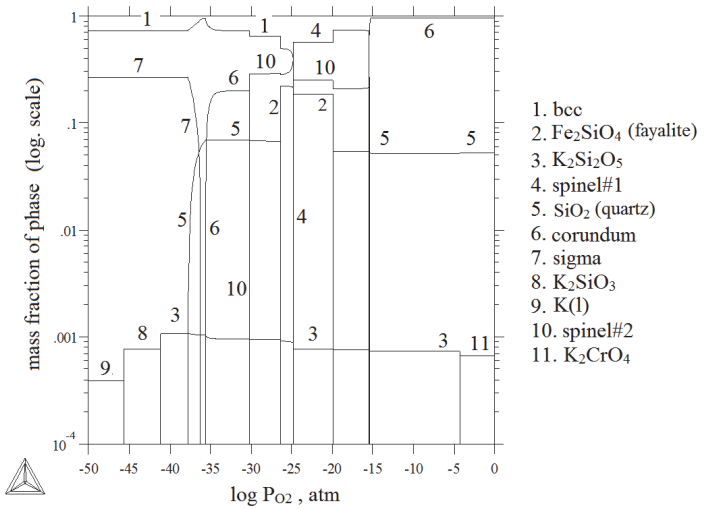

Figure 11: Stable phases vs oxygen potential in a system corresponding to the composition of Fe14CrSi3 and 0.01 mole potassium. Calculations were performed with Thermo-Calc [51]. Thermochemical data for bcc, sigma, spinel-oxide and corundum-oxide phases are from database TCFE6 and for the rest of the phases from database SSUB3.

Regarding grain boundary attack, two extra factors need to be considered. Firstly, the presence of a chromium-rich phase at the grain boundaries of these alloys. It is well-known that formation of chromium-rich phases, especially $Cr_{23}C_6$, can lead to chromium depletion of the neighboring region, enhancing the susceptibility for grain boundary attack; so called sensitization [53]. Therefore it is possible that presence of this phase in the as-received microstructure influences the observed damage already in an early stage. However, it appears that grain boundary attack has come to a halt as indicated by chromium depletion close to the attack tip (see Figures 2b and 5b). Such depletion indicates that a chromium-rich oxide may have formed at the tip of the corrosion front, which would limit continued oxygen ingress. The second factor related to the grain boundary attack is detection of chlorine within the grain boundary oxide. If evaporation by volatile chlorides had taken place then voids would have been observed close to the grain boundary. Absence of such voids shows that chlorine is promoting the attack by another mechanism. Therefore the observed effect can likely be attributed to mechanical damage to the oxide and/or increase in the ionic conductivity of the oxide due to chlorine incorporation; both effects leading to an increase in the inward flux of oxygen.

4.2 Ni45Cr4Nb

In the second part of this study [48] a comparison of the corrosion of Nimonic 80A by KCl and K_2CO_3 showed that chlorine can play an important role in KCl-induced high temperature corrosion. Calculation of phase equilibria in the chromium-potassium-oxygen-chlorine system (Figure 12) shows that at 600°C for an oxygen partial pressure of 0.05atm, the equilibrium chlorine partial

pressure will be $7*10^{-7}$atm. Although this value is small it is high enough to chlorinate chromium, iron and even nickel and molybdenum (see Figure 12 and table to the right of the diagram, which gives the equilibrium $P_{Cl2(g)}$ for the listed chloride formation). In addition, the chlorine developed by electrochemical interaction (e.g. eq. 4) between the salt and the metallic elements promotes the contribution of chlorine to corrosion.

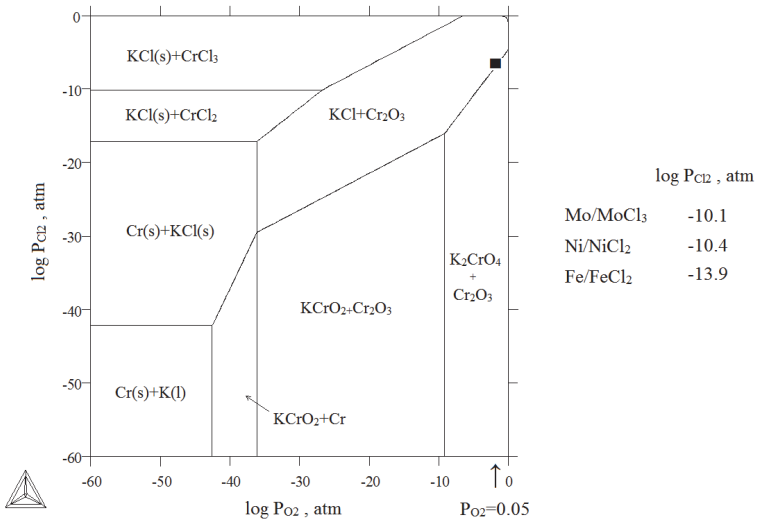

Figure 12: Phase equilibria in Cr-K-O-Cl system at 600°C calculated with ThermoCalc [51]. Thermochemical data for different phases is taken from database SSUB3. $P_{O2(g)}$ of the experimental condition and the established $P_{Cl2(g)}$ are shown with a square. Chlorine partial pressure in equilibrium with metal-metal chloride for iron, nickel and molybdenum is given in the table to the right side of the diagram. The phase diagram is calculated for 1 mole of Cr and 0.01 mole of K.

The mechanism by which chlorine attacks this alloy is discussed in detail in section 4.4. However, it can already be concluded that presence of chromium-rich phases is detrimental in case of alkali-chloride-induced high temperature corrosion. Such a negative role has been reported for chromium carbides in austenitic and ferritic stainless steels exposed to gaseous chlorine attack [19], [20]. In addition, Uusitalo et al.[54] showed that Cr_3C_2 was significantly damaged when exposed to air+KCl(s). The results in this work show that metallic chromium-rich phases are also susceptible to the attack when alkali chlorides are present in the environment. This is in agreement with the previous literature reports showing an extreme reactivity between pure chromium and alkali chlorides at temperatures above 500°C [55]–[60]. However, the reason for the lack of such an effect for $Cr_{23}C_6$-containing ferritic and austenitic stainless steels in this study [46], [48] is still unclear. An important difference between the experimental conditions of this study and the abovementioned reports is the presence of 15 vol.% water vapor in the atmosphere. This will be further addressed in section 4.4.

4.3 Pure Nickel

The observed change in the porosity of the oxide (see Figure 9) is indicative of a change in transport properties. This means that due to the presence of KCl, ionic conductivity in nickel oxide

(grain boundary and/or lattice) has been affected. However, from a practical point of view this change is irrelevant because the oxide thickness is not affected by the presence of KCl. Similar behavior for nickel was observed by Jonsson et al.[61]. Compared to iron and chromium; nickel has a much lower affinity to oxygen and chlorine. In addition, although NiO is not a slow-growing oxide (compared to Al_2O_3, Cr_2O_3 etc) the rate of its growth is relatively low (see parabolic rate constants in [62]). It has also been shown that no significant reaction takes place between NiO and KCl at least up to 650^{o}C [63]. Also for an electrochemical reaction path (see Eqs. 2-4) the driving force for the reaction of nickel is small (Table 2). All these factors appear to contribute to the rather noble nature of pure nickel under the investigated conditions.

Table 2: Overall reactions of iron, nickel and chromium assuming an electrochemical reaction path. Reactions are balanced for 1 mole of KCl. Calculations with Thermo-Calc [51] using TAB module and data from SSUB3 database.

reaction	$\Delta G^o(600^oC)$, KJ
$Ni+(1/2)O_2(g)+(1/2)H_2O(g)+KCl=(1/2)NiCl_2+(1/2)NiO+KOH(g)$	+55.8 KJ
$Fe+(5/8)O_2(g)+(1/2)H_2O(g)+KCl=(1/2)FeCl_2+(1/4)Fe_2O_3+KOH(g)$	-41.0 KJ
$Cr+(5/8)O_2(g)+(1/2)H_2O(g)+KCl=(1/2)CrCl_2+(1/4)Cr_2O_3+KOH(g)$	-147.5 KJ

4.4 An Overall Discussion of the Corrosion Mechanisms

The presence of several corrosive species in the environment (O_2, H_2O, KCl and even N_2) and the diversity of the compositions of the investigated alloys in this study (including parts 1 and 2) makes it difficult to deduce a universal mechanism for the KCl-induced high temperature corrosion. In fact, time-resolved exposures are required to clarify the actual sequence of events. However, combining observations reported in the literature, the current experimental results and thermodynamic calculations (using TAB module in Thermo-Calc [51]) tentative mechanisms can be suggested.

As mentioned earlier potassium and water vapor both play a significant role in high temperature corrosion of chromia-forming alloys by retracting chromium from the oxide layer [11], [34], [35]. In addition, comparison between KCl and K_2CO_3 in [48] showed that also chlorine plays a crucial role in the course of corrosion. Although potassium and water vapor both break down Cr_2O_3, water vapor is reported to have a moderating effect on the chlorine and alkali chloride-induced corrosion [37], [64]–[66]. This moderating effect can be attributed to a shift of the equilibria expressed by equations. 2 and 3 to the left by water vapor (also consider that Cl^- produced according to eq. 4 will be converted by $H_2O(g)$ to HCl(g) according to eq. 3). In addition, water vapor has a tendency to promote the formation of inward-growing oxides. The articles by Bamba et al.[67] and Hansson et al.[68] indicate that OH^- ions, formed by the reduction of $H_2O(g)$ at the oxide/gas interface, diffuse faster than O^{2-} ions and hence enhance the oxygen flux toward the metal/oxide interface. This means that under the presence of water vapor, Cl^- has to travel through a thicker diffusion barrier to reach the metal/oxide interface. Hence with water vapor present, the chlorine effect is less

pronounced. Another important issue is the amount of chlorine in the system. In KCl-induced high temperature corrosion, the source of chlorine is KCl provided that no chlorine is included in the inlet gas. Therefore the reactions that extract chlorine from KCl will determine how much this element will contribute to corrosion. The (calculated) partial pressure of $Cl_2(g)$ due to dissociation of KCl at 600°C is 10^{-42} atm. Therefore it is insignificant and cannot cause chlorination of iron, chromium and nickel (see Figure 12). Consequently the possibilities for chlorine evolution are reactions 3 and 6. Considering that after the initial stage of reaction, KCl in contact with the metal is consumed and a spongy oxide (type A oxide) is left behind, then the only chlorine source left is KCl vapor. Any ionic diffusion of chlorine (produced according to reaction 3) through the lattice of type A oxide will be much slower than molecular diffusion of KCl(g), $O_2(g)$ and $H_2O(g)$ through the pores (to reach the type B oxide/gas interface). Considering the (calculated) total vapor pressure of $KCl(g)+K_2Cl_2(g)$ which is only $4*10^{-6}$ atm at 600°C and comparing it with 0.15atm partial pressure of $H_2O(g)$ one finds that chlorine will become less abundant over time. Therefore the effects of $H_2O(g)$ can be expected to become dominant with time. This means that if the alloy has enough chromium, the corrosion slows down after an initial period. Accordingly the better performance of Sanicro28 compared to TP347HFG (reported in [46]) can be described in this way.

For the nickel based alloys as the nickel itself is rather noble and its oxidation rate is relatively low, assessment of the effect of chromium content (in solid solution) is not straight-forward. However, it could be clearly observed that the presence of chromium-rich phases was extremely detrimental as observed for alloys 214, Nimonic 80A and Ni45Cr4Nb, where selective corrosion was the dominant mechanism. For these alloys the depth of removal of chromium (and aluminum, titanium etc) strongly suggests that outward transport of depleted elements has taken place by chlorine-induced volatilization through the sublimation/evaporation of metal chloride(s) rather than solid state diffusion. However, as mentioned in the introduction part, if the oxide layer is permeable to metal chloride molecules it will be permeable to oxygen molecules as well [10], [11]. To account for the observed effect another description is necessary.

Formation of subsurface voids due to the vacancy injection during contaminant-free oxidation of highly alloyed austenitic stainless steels has been reported by Pettersson et. al[69] and Jonsson et al.[70]. Due to the high chromium and nickel content of Ni45Cr4Nb alloy a similar situation is expected to take place for this alloy in chlorine-free exposure as well. In other words, chromium leaves the alloy (to form an outward growing thin oxide) and nickel stays in the alloy leading to the vacancy formation at the metal/oxide interface. Considering the possibility for formation of sub-surface voids and inspired by the electrochemical model [12], [13] the following hypotheses can be put forward to account for the selective corrosion.

Hypothesis A: As the Cl^- penetrates the oxide layer (e.g. through the grain boundaries of oxide[12], [13]) $NiCl_2(s)$ can form at the metal/oxide/void interface where Ni enrichment has taken place due to a preferential oxidation of Cr. This would lead to the presence of $Cl_2(g)$ within the void as the $NiCl_2(s)=Ni+Cl_2(g)$ equilibrium is reached. According to calculations $P_{Cl2(g)}$ for this reaction at 600°C is 10^{-10} atm. This partial pressure is significantly higher than the similarly calculated equilibrium $P_{Cl2(g)}$ for $CrCl_2(s)=Cr+Cl_2(g)$ at 600°C (10^{-17} atm). Subsequently chlorination of

chromium will take place wherever $Cl_2(g)$ comes into contact with a chromium atom on the pore walls. As the calculated vapor pressure of $CrCl_2(s)$ at 600°C is not negligible (10^{-7} atm) volatilization of chromium as $CrCl_2(g)$ takes place (this can be $CrCl_3(g)$ if the atmosphere has a high enough $P_{Cl2(g)}$). However, upon reaching the void/oxide interface $CrCl_2(g)$ can dissociate according to $CrCl_2(g)=Cr^{3+}+Cl_2(g)+e^-$ and $Cl_2(g)$ is released to repeat the cycle. Oxidation of $CrCl_2(g)$ at the oxide/void interface is coupled to the reduction of $O_2(g)$ at the gas/oxide interface. Subsequently Cr_2O_3 will form wherever Cr^{3+} and O^{2-} meet (see the schematic representation in Figure 13a).

Hypothesis B: As the calculated vapor pressure of $NiCl_2(s)$ at 600°C is significant ($1.28*10^{-4}$ atm) it will sublime if $NiCl_2(s)$ forms at the metal/oxide/void interface. When $NiCl_2(g)$ comes into contact with a Cr atom on the pore walls the displacement reaction $NiCl_2(g)+Cr=Ni+CrCl_2(g)$ will take place. Subsequently when the sublimed $CrCl_2(g)$ comes into contact with a Ni atom at the metal/oxide/void interface the reaction $CrCl_2(g)+Ni=Cr^{3+}+2NiCl_2(g)+e^-$ will take place restoring the $NiCl_2(g)$ to repeat the cycle (see the schematic representation in Figure 13b).

It is also possible that the reactions according to hypothesis A and hypothesis B could occur simultaneously. In that case, due to the higher vapor pressure of $NiCl_2(g)$ compared to $P_{Cl2(g)}$ in equilibrium with Ni-$NiCl_2(s)$ it would seem that the contribution from hypothesis B would be larger. In addition, if the oxide layer contains any Ni^{2+}, the displacement reactions $CrCl_2(g)+Ni^{2+}=Cr^{3+}+NiCl_2(g)+e^-$ (void/oxide interface) and $NiCl_2(g)+Cr=Ni+CrCl_2(g)$ (void/metal interface) could return Ni into the metal lattice. It is also possible that after $CrCl_2(g)$ is formed due to $NiCl_2(g)+Cr=Ni+CrCl_2(g)$ it will continue the reaction path according to hypothesis A. In this case the $NiCl_2(g)$ acts only as an initiator. The result in both hypotheses is that the voids become larger as chromium removal introduces more and more vacancies to the lattice. Eventually an interconnected network of porosity forms which will further facilitate $Cl_2(g)$ and $CrCl_2(g)$ transport.

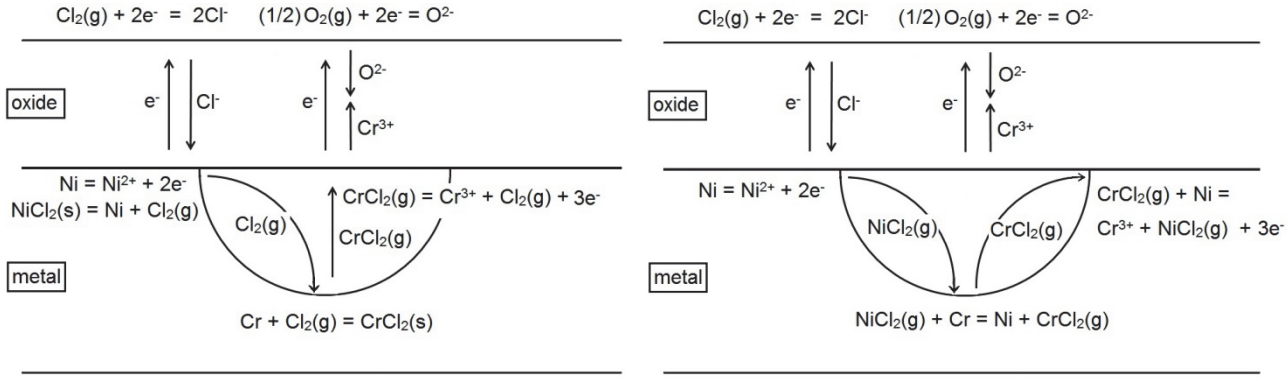

(a) (b)

Figure 13: Schematic of the hypothetical models to explain the selective corrosion in a Ni-Cr alloy when (a) $Cl_2(g)$ and (b) $NiCl_2(g)$ accelerate Cr transport across an oxidation-induced void at the metal/oxide interface (half-circles represent the voids). For simplicity the oxide and metal grain boundaries are not shown in the figures. According to [12], [13] transport of Cl^- is suggested to take place through the oxide grain boundaries.

The above-mentioned hypotheses can explain the formation of porous nickel-rich regions as chromium leaves the alloy and nickel is left behind. In addition, they do not require that $CrCl_2(g)$ travels through the oxide layer to reach regions of higher $P_{O2(g)}$.

The major difference of volatilization compared with other mechanisms is that, as the material transport is much faster in gas phase compared to the solid phase, this mechanism leads to a rapid thickness loss in a very short period of time. In fact, the attack on Ni45Cr4Nb is two orders of magnitude larger than that observed on pure nickel. That the selective corrosion was rare for the rest of the alloys (including the ones investigated in [46], [48]) is thought to be related to the presence of water vapor promoting the formation of internal oxides and therefore disfavoring formation of subsurface voids. In addition water vapor stabilizes HCl(g) which, in turn, decreases the available Cl^- (see eq. 3). The values in table 2 show that, in absence of a protective oxide, chromium is highly prone to interact with KCl and therefore the presence of chromium-rich phases promotes chlorine contribution in the course of corrosion. Accordingly, the alloys with chromium-rich phases show the selective corrosion behavior even in an atmosphere containing 15% water vapor.

Conclusions

Under the experimental conditions of this study the following conclusions can be drawn:

1- The presence of up to 3wt% silicon in ferritic stainless steels did not lead to the formation of a protective silica layer for the investigated alloys. Potassium could be found together with silicon in the inner oxide and internal oxidation/nitridation took place.
2- Ni-45Cr-4Nb wt.% showed the worst performance among all the investigated alloys. This is explained by the presence of a large fraction of chromium-rich phase (α-Cr) in the microstructure. Extensive selective removal of chromium took place which was attributed to the volatilization of chromium in form of chromium chloride(s).
3- On pure nickel the presence of KCl only led to a slight increase in the oxide porosity. However, the change in the extent of oxidation was insignificant. In fact, pure nickel showed a better performance compared to all of the investigated alloys. This was attributed to the lack of reactivity between nickel oxide and KCl as well as small thermodynamic driving force for any electrochemical interaction between the salt and pure nickel.
4- A hypothetical model was proposed to account for the selective corrosion induced by chlorine and alkali chlorides. This model attributes the selective corrosion to the formation of oxidation-induced subsurface voids. It was suggested that formation of volatile metal chlorides at the metal/oxide interface leads to the gas phase transport across such voids. Hence accelerating the selective removal of more reactive elements from the alloy.

Acknowledgement

This work was performed within the framework of the project GREEN financed by the Danish Council for Strategic Research under grant no. 10-093956. John C. Troelsen, Flemming B. Grumsen and Peter J.S. Westermann are acknowledged for their help and technical support during this work.

References

[1] H. P. Michelsen, F. Frandsen, K. Dam-Johansen, and O. H. Larsen, "Deposition and high temperature corrosion in a 10 MW straw fired boiler," *Fuel Process. Technol.*, vol. 54, no. 1–3, pp. 95–108, Mar. 1998.

[2] H. Nielsen, L. Baxter, G. Sclippab, C. Morey, F. Frandsen, and K. Dam-Johansen, "Deposition of potassium salts on heat transfer surfaces in straw-fired boilers: a pilot-scale study," *Fuel*, vol. 79, no. 2, pp. 131–139, 2000.

[3] F. J. Frandsen, H. P. Nielsen, P. A. Jensen, A. Lone, H. Livbjerg, K. Dam-johansen, P. F. B. Hansen, K. H. Andersen, H. S. Sørensen, O. H. Larsen, N. Henriksen, and P. Simonsen, "Deposition and Corrosion in Straw and Coal-Straw Co-fired Utility Boilers Danish Experiences," *Biomass*, no. 1, pp. 271–283, 1999.

[4] L. Hansen, H. Nielsen, and F. Frandsen, "Influence of deposit formation on corrosion at a straw-fired boiler," *Fuel Process.*, vol. 64, pp. 189–209, 2000.

[5] M. Montgomery, S. A. Jensen, U. Borg, O. Biede, and T. Vilhelmsen, "Experiences with high temperature corrosion at straw-firing power plants in Denmark," *Mater. Corros.*, vol. 62, no. 7, pp. 593–605, Jul. 2011.

[6] P. D. Miller, H. H. Krause, D. A. Vaughan, and W. K. Boyd, "The Mechanism in High Temperature Corrosion in Municipal Incinerators," *Corrosion*, vol. 28, no. 7, pp. 274–281, 1972.

[7] H. P. Nielsen, F. J. Frandsen, and K. Dam-Johansen, "Lab-Scale Investigations of High-Temperature Corrosion Phenomena in Straw-Fired Boilers," *Energy & Fuels*, vol. 13, no. 6, pp. 1114–1121, Nov. 1999.

[8] H. Grabke, E. Reese, and M. Spiegel, "The effects of chlorides, hydrogen chloride, and sulfur dioxide in the oxidation of steels below deposits," *Corros. Sci.*, vol. 37, no. 7, pp. 1023–1043, 1995.

[9] M. J. McNallan, W. W. Liang, S. H. Kim, and C. T. Kang, "Acceleration of the High Temperature Oxidation of Metals by Chlorine," in *High Temperature Corrosion, NACE*, 1983, pp. 316–321.

[10] J. Smeggil and N. Bornstein, “The Effect of NaCl (g) on the Oxidation of NiAl,” *J. Electrochem. Soc.*, vol. 125, no. 8, pp. 1283–1290, 1978.

[11] J. Pettersson, H. Asteman, J.-E. Svensson, and L.-G. Johansson, “KCl Induced Corrosion of a 304-type Austenitic Stainless Steel at 600°C; The Role of Potassium,” *Oxid. Met.*, vol. 64, no. 1–2, pp. 23–41, Aug. 2005.

[12] N. Folkeson, L.-G. Johansson, and J.-E. Svensson, “Initial Stages of the HCl-Induced High-Temperature Corrosion of Alloy 310,” *J. Electrochem. Soc.*, vol. 154, no. 9, p. C515, 2007.

[13] N. Folkeson, T. Jonsson, M. Halvarsson, L.-G. Johansson, and J.-E. Svensson, “The influence of small amounts of KCl(s) on the high temperature corrosion of a Fe-2.25Cr-1Mo steel at 400 and 500°C,” *Mater. Corros.*, vol. 62, no. 7, pp. 606–615, Jul. 2011.

[14] T. Jonsson, N. Folkeson, J.-E. Svensson, L.-G. Johansson, and M. Halvarsson, “An ESEM in situ investigation of initial stages of the KCl induced high temperature corrosion of a Fe–2.25Cr–1Mo steel at 400°C,” *Corros. Sci.*, vol. 53, no. 6, pp. 2233–2246, Jun. 2011.

[15] R. Bender and M. Schütze, “The role of alloying elements in commercial alloys for corrosion resistance in oxidizing-chloridizing atmospheres. Part II: Experimental investigations,” *Mater. Corros.*, vol. 54, no. 9, pp. 652–686, 2003.

[16] F. Stott, R. Prescott, P. Elliott, and M. Al’Atia, “Assessment of the Degradation of Metals and Alloys in Air--2% Chlorine at High Temperature,” *High Temp. Technol.*, 1988.

[17] M. Rhee, M. McNallan, and M. Forthman, “Long term high temperature corrosion studies of high temperature alloys in chlorine contaminated environments,” *J. Mater. energy*, vol. 7, no. 4, pp. 294–301, 1986.

[18] J. Oh, M. McNallan, G. Lai, and M. Rothman, “High temperature corrosion of superalloys in an environment containing both oxygen and chlorine,” *Metall. Mater. ...*, vol. 17, no. 600, pp. 1087–1094, 1986.

[19] D. Berztiss, A. Zahs, and A. Schneider, “Role of carbides in the high temperature corrosion of steels in HCl-containing atmospheres,” *Zeitschrift für Met.*, 1999.

[20] M. McNallan, “High-temperature corrosion in halogen environments,” *Mater. Perform.*, pp. 54–57, 1994.

[21] J. Johnson, J. Nicholls, R. Hurst, and P. Hancock, “The mechanical properties of surface scales on nickel-base superalloys—II. Contaminant corrosion,” *Corros. Sci.*, vol. 18, no. January 1977, 1978.

[22] A. Zahs, M. Spiegel, and H. J. Grabke, “Chloridation and oxidation of iron, chromium, nickel and their alloys in chloridizing and oxidizing atmospheres at 400 - 700C,” *Corros. Sci.*, vol. 42, pp. 1093–1122, 2000.

[23] F. Stott and C. Shih, “High-Temperature Corrosion of Iron–Chromium Alloys in Oxidizing–Chloridizing Conditions,” *Oxid. Met.*, vol. 54, pp. 425–443, 2000.

[24] T. Jonsson, J. Froitzheim, J. Pettersson, J. E. Svensson, L. G. Johansson, and M. Halvarsson, “Microstructural investigation of the influence of KCl on the corrosion of 304L exposed to 5% O2+ N2,” in *16th International Corrosion Congress, 2005, Beijing, China*, no. 15x15x2 mm.

[25] H. T. Ma, C. H. Zhou, and L. Wang, “High temperature corrosion of pure Fe, Cr and Fe–Cr binary alloys in O2 containing trace KCl vapour at 750°C,” *Corros. Sci.*, vol. 51, no. 8, pp. 1861–1867, Aug. 2009.

[26] M. J. Mcnallan, Y. Y. Lee, Y. W. Chang, N. S. Jacobson, and J. Doychak, “Oxidation-Chlorination of Binary Ni-Cr alloys in Flowing Ar-O2-Cl2 Gas Mixtures at 1200K,” *J. Electrochem. Soc.*, vol. 138, no. 12, pp. 3692–3696, 1991.

[27] M. Hossain and S. Saunders, “A microstructural study of the influence of NaCl vapor on the oxidation of a Ni-Cr-Al alloy at 850° C,” *Oxid. Met.*, vol. 12, no. i, pp. 1–22, 1978.

[28] M. Maloney and M. McNallan, “The effect of chlorine on the kinetics of oxidation of cobalt in environments containing 0.5 atmosphere of oxygen between 900 K and 1200 K,” *Metall. Mater. Trans. B*, vol. 16, no. December, pp. 751–761, 1985.

[29] M. J. McNallan, W. W. Liang, S. H. Kim, and C. T. Kang, “Acceleration of the High Temperature Oxidation of Metals by Chlorine,” in *High Temperature Corrosion, NACE*, 1983, pp. 316–321.

[30] P. Szakálos, P. Henderson, and R. Pettersson, “Mechanisms of chlorine induced corrosion and effect of sulphur additions in superheater corrosion in biomass- and waste fired boilers,” in *16th Internal Corrosion Conference*, 2005.

[31] Y. Li and R. Rapp, “Internal chloridation of dilute Ni-Cr alloys,” *Metall. Mater. Trans. B*, vol. 14, no. September, pp. 509–510, 1983.

[32] R. Prescott and F. Stott, “The degradation of metals in a hydrogen chloride-containing gas at high temperature,” *Corros. Sci.*, vol. 29, no. 4, pp. 465–469, 1989.

[33] J. Robertson and J. E. Forrest, “Corrosion of carbon steels in high temperature acid chloride solutions,” *Corros. Sci.*, vol. 32, no. 5, pp. 521–540, 1991.

[34] H. Asteman, J. E. Svensson, and L. G. Johansson, “Indication of chromium oxide hydroxide evaporation during oxidation of 304L at 873 K in the presence of 10% water vapor,” *Oxid. Met.*, vol. 52, no. 1, pp. 95–111, 1999.

[35] H. Asteman, J. E. Svensson, M. Norell, and L. G. Johansson, “Influence of water vapor and flow rate on the high-temperature oxidation of 304L; effect of chromium oxide hydroxide evaporation,” *Oxid. Met.*, vol. 54, no. 1, pp. 11–26, 2000.

[36] J. Pettersson, N. Folkeson, L.-G. Johansson, and J.-E. Svensson, “The Effects of KCl, K2SO4 and K2CO3 on the High Temperature Corrosion of a 304-Type Austenitic Stainless Steel,” *Oxid. Met.*, vol. 76, no. 1–2, pp. 93–109, Mar. 2011.

[37] J. Lehmusto, B.-J. Skrifvars, P. Yrjas, and M. Hupa, “Comparison of potassium chloride and potassium carbonate with respect to their tendency to cause high temperature corrosion of stainless 304L steel,” *Fuel Process. Technol.*, Jan. 2012.

[38] S. Karlsson, J. Pettersson, J. E. Svensson, and L. G. Johansson, “KCl-Induced High Temperature Corrosion of the Austenitic Stainless Steel 304L – The Influence of SO_2,” *Mater. Sci. Forum*, vol. 696, pp. 224–229, Sep. 2011.

[39] P. Viklund and R. Pettersson, “HCl-Induced High Temperature Corrosion of Stainless Steels in Thermal Cycling Conditions and the Effect of Preoxidation,” *Oxid. Met.*, vol. 76, no. 1–2, pp. 111–126, Dec. 2010.

[40] C. Pettersson, J. Pettersson, H. Asteman, J.-E. Svensson, and L.-G. Johansson, “KCl-induced high temperature corrosion of the austenitic Fe–Cr–Ni alloys 304L and Sanicro 28 at 600°C,” *Corros. Sci.*, vol. 48, no. 6, pp. 1368–1378, Jun. 2006.

[41] Y. S. Li, Y. Niu, and M. Spiegel, “High temperature interaction of Al/Si-modified Fe–Cr alloys with KCl,” *Corros. Sci.*, vol. 49, no. 4, pp. 1799–1815, Apr. 2007.

[42] M. Montgomery and A. Karlsson, “In-situ corrosion investigation at Masnedø CHP plant - a straw-fired power plant,” *Mater. Corros.*, vol. 50, pp. 579–584, 1999.

[43] H. Fujikawa and N. Maruyama, “Corrosion behaviour of austenitic stainless steels in the high chloride-containing environment,” *Mater. Sci. Eng. A*, vol. 20, pp. 301–306, 1989.

[44] N. Hiramatsu, Y. Uematsu, T. Tanaka, and M. Kinugasa, “Effects of alloying elements on NaCl-induced hot corrosion of stainless steels,” *Mater. Sci. Eng. A*, vol. 120–121, pp. 319–328, Nov. 1989.

[45] Y. S. Li, M. Spiegel, and S. Shimada, “Effect of Al/Si addition on KCl induced corrosion of 9% Cr steel,” *Mater. Lett.*, vol. 58, no. 29, pp. 3787–3791, Nov. 2004.

[46] S. Kiamehr, K. V. Dahl, M. Montgomery, and M. A. J. Somers, “KCl-induced high temperature corrosion of selected commercial alloys part I: chromia-formers,” *Manuscr.*

[47] U. D. Bihlet, “High Temperature Resistant Exhaust Valve Spindle,” Technical University of Denmark, 2013.

[48] S. Kiamehr, K. V. Dahl, M. Montgomery, and M. A. J. Somers, “KCl-induced high temperature corrosion of selected commercial alloys part II: alumina and silica formers,” *Manuscr.*

[49] S. C. Cha and M. Spiegel, “Local reactions of KCl particles with iron, nickel and chromium surfaces,” *Mater. Corros.*, vol. 57, no. 2, pp. 159–164, Feb. 2006.

[50] S. Cha and M. Spiegel, “Local reactions between NaCl and KCl particles and metal surfaces,” *Corros. Eng. Sci.*, vol. 40, no. 3, pp. 249–253, 2005.

[51] J. Andersson, T. Helander, and L. Höglund, “Thermo-Calc & DICTRA, computational tools for materials science,” *Calphad*, vol. 26, no. 2, pp. 273–312, 2002.

[52] “soluble silicates.” [Online]. Available: http://www.solublesilicates.eu/docs/solsil_broch_1302.pdf. [Accessed: 05-Sep-2014].

[53] M. G. Fontana, *Corrosion Engineering*, 3rd ed. McGaw Hill, 1986.

[54] M. A. Uusitalo, R. Backman, L.-M. Berger, P. M. J. Vuoristo, and T. A. Mäntylä, “Stability of Carbides in Chlorine-Containing High-Temperature Environments,” *Key Eng. Mater.*, vol. 264–268, pp. 497–500, 2004.

[55] Y. Shinata and Y. Nishi, “NaCl-induced accelerated oxidation of chromium,” *Oxid. Met.*, vol. 26, pp. 201–212, 1986.

[56] Y. Shinata, “Accelerated oxidation rate of chromium induced by sodium chloride,” *Oxid. Met.*, vol. 27, pp. 315–332, 1987.

[57] Y. S. Li, M. Sanchez-Pasten, and M. Spiegel, “High Temperature Interaction of Pure Cr with KCl,” *Mater. Sci. Forum*, vol. 461–464, pp. 1047–1054, 2004.

[58] J. Lehmusto, D. Lindberg, P. Yrjas, B.-J. Skrifvars, and M. Hupa, “Studies on the Partial Reactions Between Potassium Chloride and Metallic Chromium Concerning Corrosion at Elevated Temperatures,” *Oxid. Met.*, Nov. 2011.

[59] J. Lehmusto, D. Lindberg, P. Yrjas, B.-J. Skrifvars, and M. Hupa, “Thermogravimetric studies of high temperature reactions between potassium salts and chromium,” *Corros. Sci.*, Mar. 2012.

[60] J. Lehmusto, B.-J. Skrifvars, P. Yrjas, and M. Hupa, “High temperature oxidation of metallic chromium exposed to eight different metal chlorides,” *Corros. Sci.*, vol. 53, no. 10, pp. 3315–3323, Oct. 2011.

[61] T. Jonsson, A. Slomian, T. N. Lomholt, S. Kiamehr, and K. V. Dahl, “Microstructural Investigations of Pure Ni Exposed to KCl Induced High Temperature Corrosion,” in *Microscopy of Oxidation 9*, 2014.

[62] D. J. Young, *High Temperature Oxidation and Corrosion of Metals*, 1st ed. Elsevier, 2008.

[63] S. Kiamehr, K. V Dahl, T. N. Lomholt, T. L. Christiansen, and M. A. J. Somers, “High Temperature Corrosion due to Biomass Firing : A Study on the Reactivity between Potassium Chloride and Oxides,” in *International Symposium on High Temperature Oxidation and Corrosion (ISHOC), Hakodate, Japan*, 2014, vol. 2, no. Vi.

[64] Y. Chang and F. Wei, “High-temperature chlorine corrosion of metals and alloys,” *J. Mater. Sci.*, vol. 26, 1991.

[65] J. Lehmusto, P. Yrjas, B.-J. Skrifvars, and M. Hupa, “High temperature corrosion of superheater steels by KCl and K2CO3 under dry and wet conditions,” *Fuel Process. Technol.*, vol. 104, pp. 253–264, Dec. 2012.

[66] C. Pettersson, L.-G. Johansson, and J.-E. Svensson, “The Influence of Small Amounts of KCl(s) on the Initial Stages of the Corrosion of Alloy Sanicro 28 at 600 °C,” *Oxid. Met.*, vol. 70, no. 5–6, pp. 241–256, Aug. 2008.

[67] G. Bamba, Y. Wouters, a. Galerie, G. Borchardt, S. Shimada, O. Heintz, and S. Chevalier, “Inverse growth transport in thermal chromia scales on Fe–15Cr steels in oxygen and in water vapour and its effect on scale adhesion,” *Scr. Mater.*, vol. 57, no. 8, pp. 671–674, Oct. 2007.

[68] A. N. Hansson, K. Pantleon, F. B. Grumsen, and M. A. J. Somers, “Microstructure Evolution During Steam Oxidation of a Nb Stabilized Austenitic Stainless Steel,” *Oxid. Met.*, vol. 73, no. 1–2, pp. 289–309, Oct. 2009.

[69] C. Pettersson, T. Jonsson, C. Proff, M. Halvarsson, J.-E. Svensson, and L.-G. Johansson, “High Temperature Oxidation of the Austenitic (35Fe27Cr31Ni) Alloy Sanicro 28 in O2 + H2O Environment,” *Oxid. Met.*, vol. 74, no. 1–2, pp. 93–111, Apr. 2010.

[70] T. Jonsson, N. Folkeson, M. Halvarsson, J.-E. Svensson, and L.-G. Johansson, “Microstructural Investigation of the HCl-Induced Corrosion of the Austenitic Alloy 310S (52Fe26Cr19Ni) at 500 °C,” *Oxid. Met.*, vol. 81, no. 5–6, pp. 575–596, Jan. 2014.

9.5 Paper V

Saeed Kiamehr, Trine N. Lomholt, Kristian V. Dahl, Marcel A. J. Somers

Application of Aluminum Diffusion Coatings to Mitigate the KCl-induced High Temperature Corrosion

Manuscript is under modification

Application of Aluminum Diffusion Coatings to Mitigate the KCl-induced High Temperature Corrosion

Saeed Kiamehr [1], Trine N. Lomholt [2], Kristian V. Dahl [1], Marcel A. J. Somers [1]*

1) Technical University of Denmark (DTU), Department of Mechanical Engineering, Produktionstorvet, Building 425, 2800 Kgs. Lyngby, Denmark

2) FORCE A/S, Park Alle 345, 2605 Brøndby , Denmark

Abstract

Pack cementation was used to produce $Fe_{1-x}Al$ and Fe_2Al_5 coatings on ferritic-martensitic stainless steel P91 and a Ni_2Al_3 coating on pure nickel. The performance of the coatings against high temperature corrosion induced by potassium chloride (KCl) was evaluated by exposing the samples at 600°C for 168h in static lab air under KCl deposit. A salt-free experiment was also performed for comparison. Microstructure, chemical and phase composition of the samples were analyzed with Scanning Electron Microscopy (SEM), Energy Dispersive X-Ray Spectroscopy (EDS) and X-Ray Diffractometry (XRD) before and after the exposures. It was found that all the coatings formed protective oxides under the salt-free exposure in air. Under the salt deposit, $Fe_{1-x}Al$ showed local failure while on large parts of the sample a protective oxide had formed. Fe_2Al_5 was attacked over the entire surface and the dominant mode of attack was selective aluminum removal. Ni_2Al_3 showed excellent performance and no sign of attack was observed anywhere on the sample.

Key words: biomass firing, potassium chloride, high temperature corrosion, iron aluminide, nickel aluminide, pack cementation.

1. Introduction

Currently there is a strong interest to substitute fossil fuels, such as coal and oil, by fuels that have the potential to be CO_2-neutral. Biomass is an attractive fuel option for electricity and heat generating power plants, especially in countries with large forest and agricultural resources. However, deposits formed during biomass combustion have shown to be so corrosive that the effective utilization of biomass has been remarkably hampered. During biomass firing deposits rich in potassium chloride (KCl) develop on the heat exchangers and cause remarkable damage to the hot sections of the power plant, especially the superheater tubes. In order to keep the material loss below an acceptable rate under these corrosive conditions, the temperature of the outlet steam is currently kept below 540°C [1], thereby achieving a lower efficiency than with fossil fuels. Accordingly selection or development of corrosion-resistant materials with lower corrosion rates

would allow a higher steam temperature, so that effective utilization of biomass is realized in the future.

Unfortunately field tests involving a wide range of commercial chromia-forming high temperature alloys have not shown any promising results [2]–[6]. Therefore application of coatings relying on alumina (and/or silica) for protection has attracted attention. Among the different possibilities for alumina-forming materials, iron and nickel aluminides are interesting options due to both a high aluminum content and a high diffusivity of aluminum in the intermetallic compounds. As the phase diagrams in Figure 1 show, most of the phases in the iron-aluminum and nickel-aluminum systems are non-stoichiometric. This can facilitate diffusion of aluminum and increase the potential for developing protective oxide.

The literature reports both satisfactory and poor achievements for aluminides depending on their exact composition and exposure environment. Li et al. [7] evaluated the performance of $Fe_{1-x}Al$ and NiAl in static lab air under KCl deposit at 650°C. They reported excellent performance for NiAl while $Fe_{1-x}Al$ suffered from local attack in the form of selective aluminum removal. A similar trend was observed when the abovementioned alloys were tested at 670°C in static lab air under a

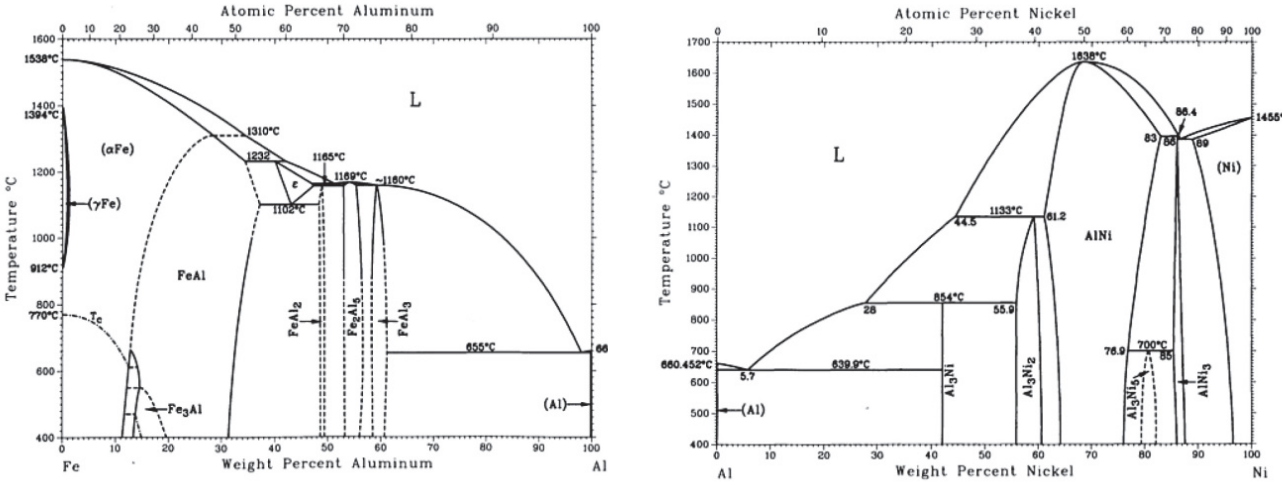

Figure 1: Ni-Al and Fe-Al phase diagrams [8].

molten KCl-NaCl mixture [9]. Vokal et al. [10] aluminized several alloys and studied their performance in static lab air under a KCl-50mol%K_2SO_4 deposit at 650°C. The studied alloys were ferritic-martensitic stainless steel P91, austenitic stainless steels 17Cr-13Ni and 800 as well as nickel-base alloy Inconel 617. It was reported that the Fe_2Al_5 coating formed on P91 suffered from the least damage and the other coatings were significantly corroded. Pan et al. [11] investigated the behavior of Fe-21Ni-10Al and Fe-21.5Ni-10Al-12.5Cr (wt%) alloys against solid and vapor KCl at 650°C in static lab air. They reported that none of these multiphase alloys, containing FeAl and NiAl phases, showed a passive behavior.

Due to the similarity between the corrosion induced by KCl and NaCl [12], [13] it is worthwhile to mention a number of literature reports with regard to the performance of iron and nickel

aluminides against NaCl as well. McKee et al. [14] exposed NiAl at 750°C under a Na_2SO_4-10wt.%NaCl deposit with $N_2(g)+76\%O_2(g)+0.1\%SO_2(g)$ as the gas atmosphere. They observed catastrophic attack, which was attributed to chlorine evolved due to the sulfation of NaCl. Smeggil et al. [15] exposed NiAl to air contaminated with NaCl vapor at 900°C and observed isothermal spallation of the oxide layer as well as growth of alumina whiskers. They attributed the whisker formation to a gas phase transport process induced by the presence of NaCl(g). Magdziarz et al. [16] investigated the corrosion of Ni_3Al under air and NaCl-Na_2SO_4 mixtures with different chloride to sulphate ratios. They reported an excellent performance for Ni_3Al up to 1000°C when the salt is purely NaCl. There are also a number of articles reporting on the performance of nickel and iron aluminides in oxygen and chlorine gas mixtures [17]–[25]. In general, it is observed that the performance of aluminide coatings is superior to that of the corresponding chromia-forming substrate alloy.

The current investigation aims at evaluating the performance of $Fe_{1-x}Al$, Fe_2Al_5 and Ni_2Al_3 phases against KCl-induced high temperature corrosion. Pack cementation was used to produce the coatings. In this process the substrate alloy is embedded in a powder pack consisting of the metal source (e.g. aluminum), an inactive filler material (e.g. alumina) and a halide activator (e.g. ammonium chloride or aluminum chloride). Heating the mixture up to a sufficiently high temperature in an inert atmosphere (e.g. argon) activates the surface and initiates deposition. The halogen forms volatile metal chlorides that decompose at the sample surface leaving behind a metallic deposit. Reactive diffusion of the deposited metal atoms and compounds in the alloy leads to the formation of the intermetallic phases [26], [27].

2. Experimental Procedure

Pure nickel (99.99 wt%) and ferritic-martensitic stainless steel P91 (Fe-9Cr-1Mo-0.5Si-0.2V wt%) were chosen as the substrate materials to be aluminized. Samples were coupons of ~ 20x8x0.3 mm cut by means of a precision cutter. Prior to coating, the samples were ground with 500grit SiC paper and subsequently cleaned with ethanol. Pack cementation was done in a tube furnace with an argon protective atmosphere. The pack powder consisted of aluminum, anhydrous $AlCl_3$ as the activator and alumina powder as inert filler in the amounts shown in table 1. For coating with $Fe_{1-x}Al$, the pack aluminum activity was lowered by including iron powder in the pack mixture. Powders for the pack were weighed and mixed thoroughly. Pack powder and samples were then packed into alumina containers that were inserted into the tube furnace. The pack was heated to 650ºC using a heating rate of approximately 10ºC/min, held for the process time listed in table 1 and then after the treatment cooled to room temperature inside the furnace in an argon flow.

After the coating, samples were separated from the residues and cleaned in an ultrasonic bath of ethanol. Subsequently one sample of each aluminide phase was partly (2/3 of length) covered with a ~1mm thick layer of KCl powder (particle size 63-90μm) and was exposed for 168h at 600°C in static lab air. A salt-free exposure was also performed for comparison. The as-coated and exposed

Table 1: Parameters of the pack cementation process

pack component (wt%)	specification	phase to be formed		
		$Fe_{1-x}Al$	Fe_2Al_5	Ni_2Al_3
Al	99.9%purity, max 60µm	10	10	10
Fe		10	0	0
$AlCl_3$	anhydrous	6	6	6
Al_2O_3		74	84	84
Duration (h)		20	6	8

samples were investigated with XRD to determine their phase composition. For this purpose a Bruker D8 Discover X-Ray diffractometer was used and the analysis for each sample was performed under both grazing-incidence and Bragg-Brentano configurations. CrK_α (λ=2.2897Å) radiation was used as the incident beam. Thereafter cross sections of the samples were prepared by embedding them in epoxy resin and grinding/polishing using ethanol as lubricant. The microstructure of the samples was studied using an Inspect S SEM equipped with an EDS detector. Imaging was performed in Back-Scattered Electron (BSE) mode unless mentioned otherwise.

3. Results

3.1 Performance of $Fe_{1-x}Al$ on P91

The microstructures of the as-coated and the salt-free exposures are given in Figures 2a and 2b respectively. Clearly, exposure in static lab air without salt did not lead to significant surface degradation. Concentration profiles of aluminum and chromium, acquired with EDS line analysis, are given in Figure 2c and demonstrate that interdiffusion of components from the coating and from the substrate alloy has occurred. The effect of interdiffusion on the aluminum concentration profile is most pronounced; for the chromium concentration profile a slight increase in chromium content in the coating is observed.

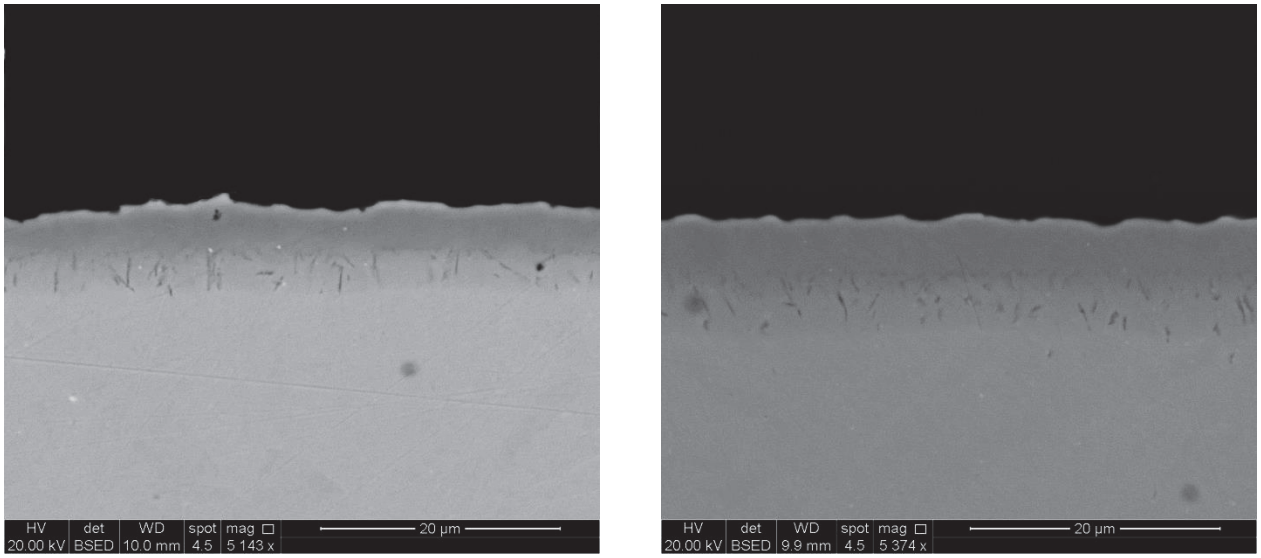

(a) (b)

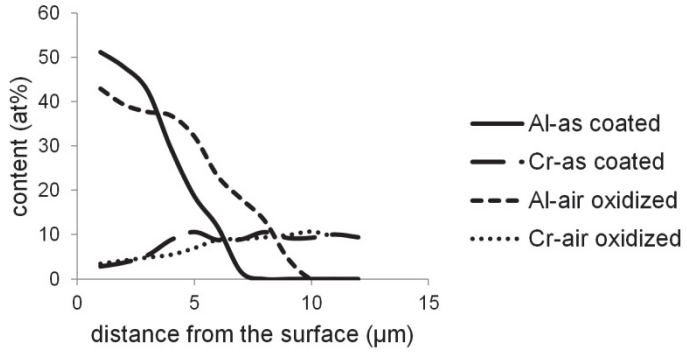

(c)

Figure 2: Microstructure of the $Fe_{1-x}Al$ coating on P91 (a) as-coated (b) air-oxidized for 168h at 600°C without KCl (c) concentration profiles of aluminum and chromium in the as-coated and air-oxidized samples.

The KCl affected sample was almost unaffected on large areas of the surface (Figure 3a). However, both on the salt-free part of the sample (Figure 3b) and the salt-covered part (Figure3c) local attack was noticed. At few locations the coating was penetrated.

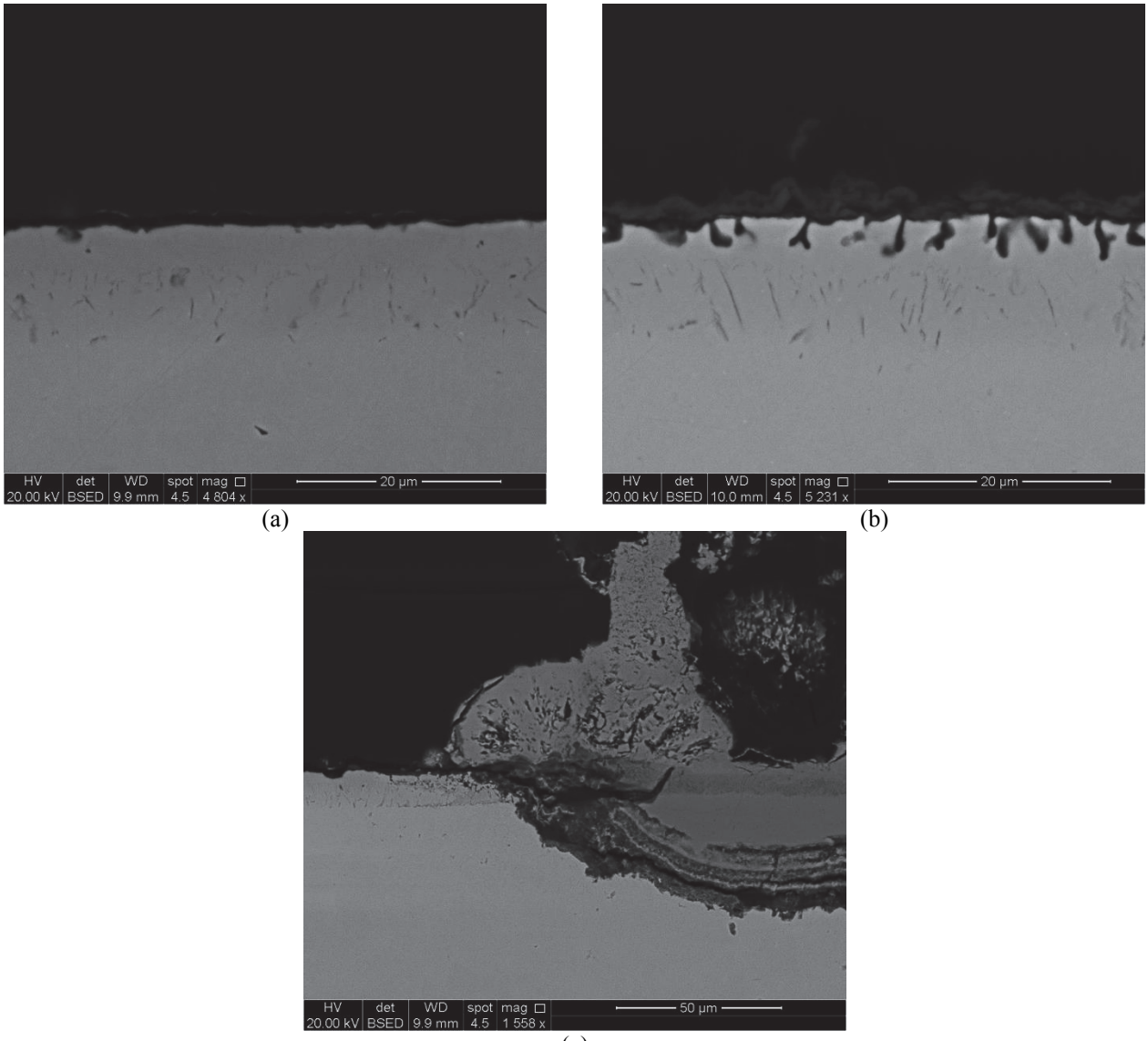

Figure 3: Different corrosion product morphologies observed on the KCl-affected sample (a) An area without significant degradation (b) local attack on salt-free part of the sample (c) local attack on the KCl-covered part.

Figure 4 shows the distribution of the alloying elements throughout the corrosion morphology shown in figure 3a. Generally a thin corrosion product can be observed on the coating and potassium without chlorine is detected all over the surface. EDS spot analysis on the alloy close to surface in Figure 3a shows an average aluminum content of 32at.% while that in the Figure 3b is only 21at.% (average over three points). In addition, further spot analysis revealed that at locations where no attack was observed the aluminum content close to the surface was at least 29 at.%.

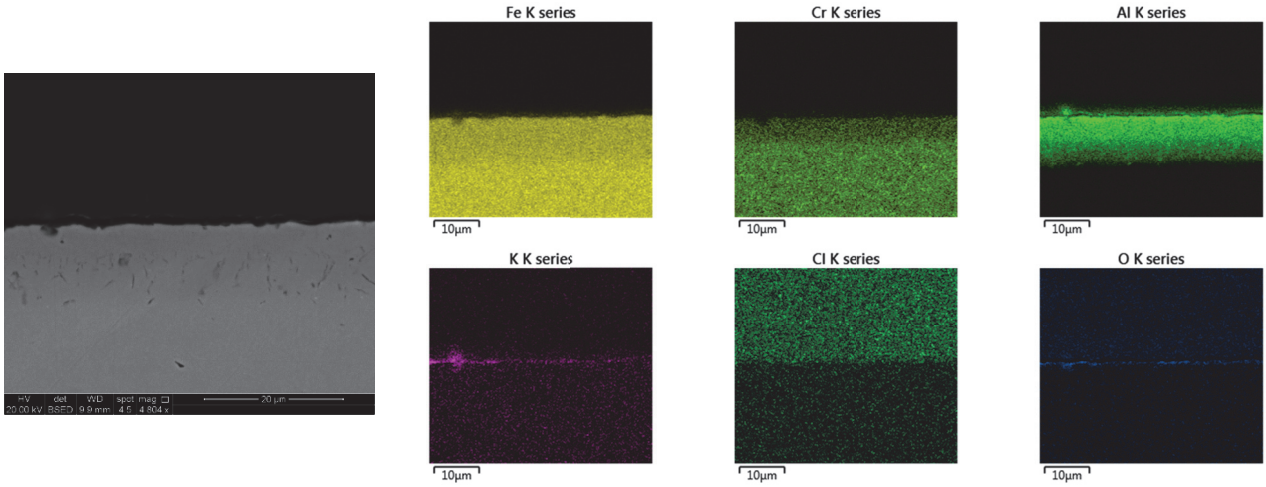

Figure 4: Mapping of the corrosion product morphology on $Fe_{1-x}Al$-coated P91 exposed under air+KCl(s). Chlorine on the upper half of its map comes from the epoxy used for embedding the sample.

Figure 5 shows the distribution of the alloying elements throughout the corrosion product morphology at a location where the local attack is well developed. The outer oxide was rich in iron and contained smaller amounts of aluminum and potassium. The inner oxide was rich in chromium and contained remnants of the aluminum close to the original alloy surface. Nitrogen enrichment was observed close to the region where local attack had occurred. EDS spot analysis also revealed the presence of small amounts of potassium (up to 4 at.%) and chlorine (up to 3at.%) in the corrosion products. However, the values for chlorine must be interpreted with care as the chlorine might have come from the epoxy used for embedding the samples.

Figure 6 shows the X-Ray diffractograms for the samples before and after exposure. The diffractograms suggest that the as-coated layer consists of $Fe_{1-x}Al$ in the bulk with a minor amount of (possibly) Fe_2Al_5 in the surface. The diffractogram for the sample subjected to the salt-free exposure does not give an indication of any oxide. However, after exposure to KCl two peaks around 50 and $54^{o}2\theta$ can be detected which can be attributed to Fe_2O_3. In addition, the peak around $40^{o}2\theta$ as well as a faint background elevation around 82^{o} indicates the presence of Fe_3Al. No potassium containing compound could be identified unambiguously. Compared to the as-coated microstructure, peaks were slightly shifted to the right after both exposures.

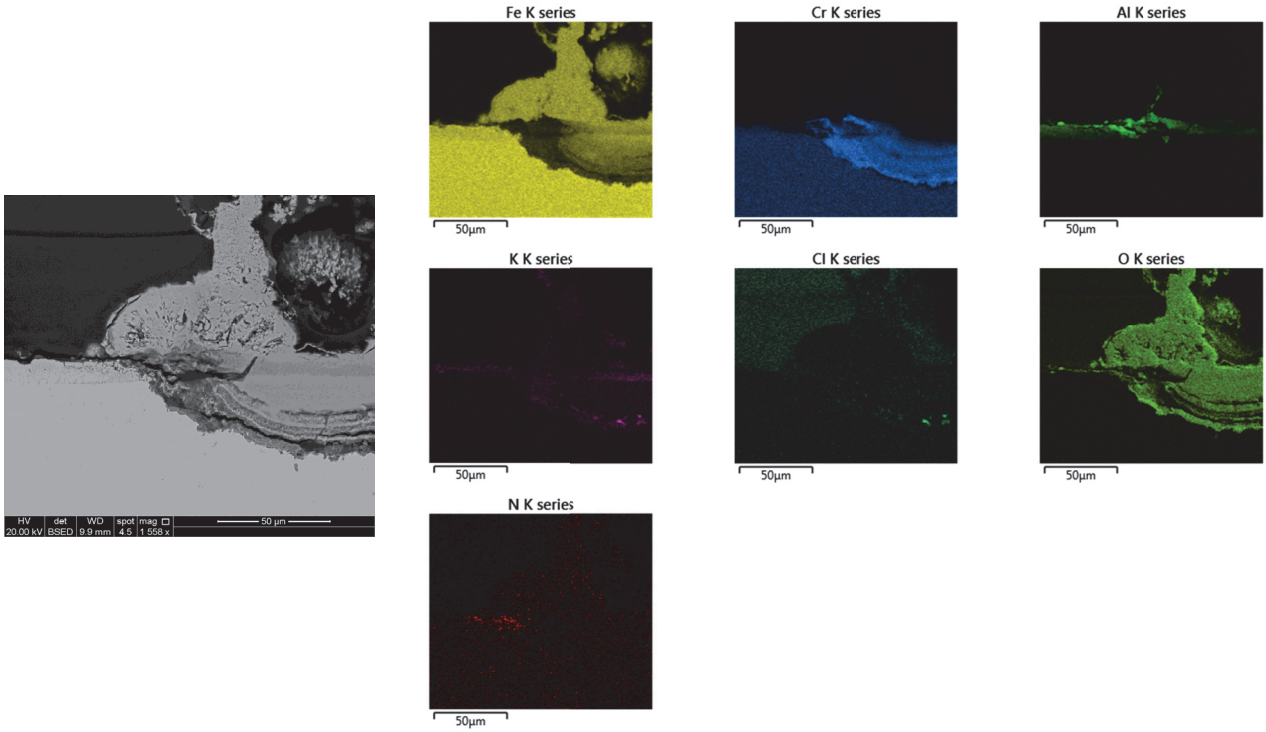

Figure 5: Mapping of the corrosion product morphology on $Fe_{1-x}Al$-coated P91 exposed under air+KCl(s). Note that the chlorine on the upper half of its map comes from the epoxy used for embedding the sample.

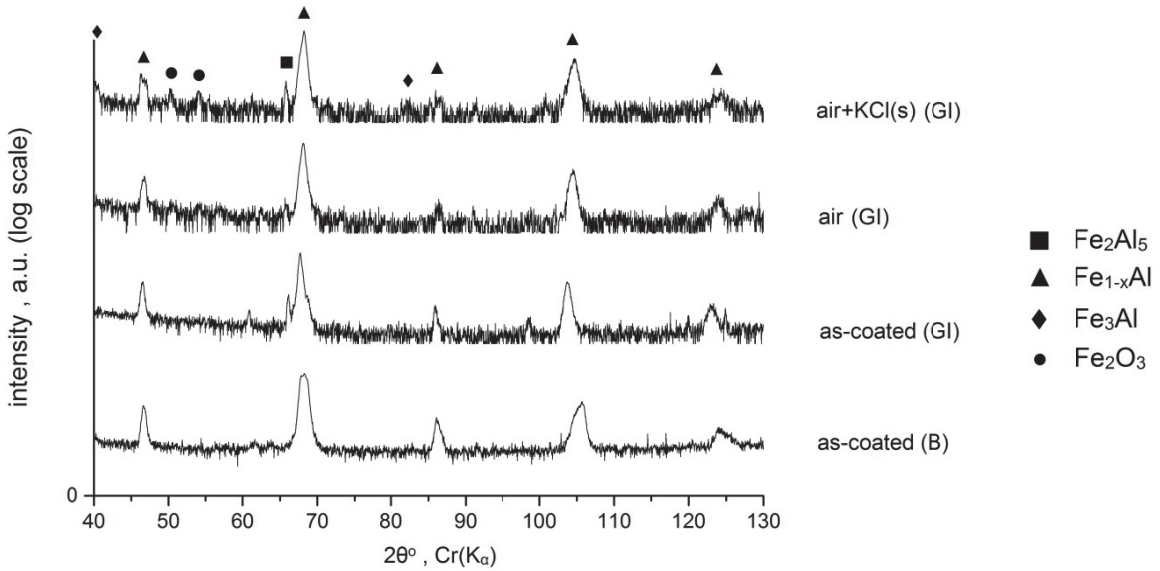

Figure 6: Phase composition of the $Fe_{1-x}Al$-coated P91 before and after the exposures. B denotes measurement in Bragg-Brentano configuration. The rest of the measurements have been performed in grazing-incidence (GI) configuration at an angle of 2^{o}.

3.2 Performance of Fe_2Al_5 on P91

The microstructure of the as-produced coating is given in Figure 7a. The deposited Fe_2Al_5 showed cracks in the growth direction, indicating tensile stress in the coating, and also non-uniformity in thickness. In addition the coating showed a multiphase structure. Mapping showed

that a chromium-rich phase, in the form of narrow strips, was present in the microstructure extending from the alloy-coating interface towards the surface. In addition, chromium and silicon-rich particles were detected in the outer part of the coating (Figure 7b). Salt-free exposure did not lead to significant surface degradation. The only apparent microstructural change was the formation of an interdiffusion zone between the Fe_2Al_5 and the substrate alloy (Figure 8a). An EDS line scan across the coating is given in Figure 8b. The aluminum profile (after the salt-free exposure) showed a small step around 50 at.% aluminum.

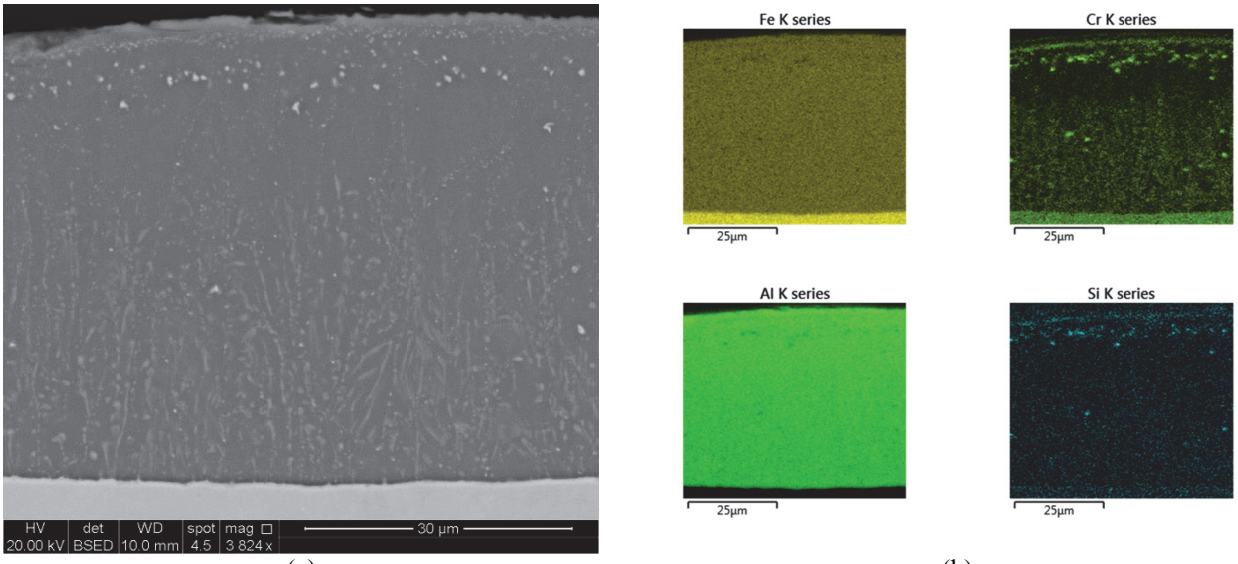

(a) (b)

Figure 7: (a) As-coated Fe_2Al_5 on P91 (b) distribution of iron, aluminum, chromium and silicon throughout the coating suggesting the formation of a chromium-rich phase as well as a chromium-silicon-rich phase in the coating.

Unlike the passive behavior observed for the salt-free exposure, the presence of KCl caused severe attack all over the surface, even on the salt-free part. The generally observed corrosion morphology was selective removal of aluminum and formation of a voluminous and porous aluminum-rich oxide on top of the coating. EDS spot analysis on the aluminum-depleted areas close to the surface gave an average value of 51at.% aluminum. Depletion of aluminum was coupled to an enrichment of iron and chromium in the underlying layer. Figure 9a shows an example of this mode of attack. In a few cases Fe_2Al_5 was completely consumed and a thick double layer oxide, in addition to the outermost highly porous oxide, had formed (see figure 9b). In both cases potassium was found all over the oxide layer. EDS spot analysis on the aluminum-rich outermost oxide gave values between 0-0.8at.% for chlorine and 0-9.85at.% for potassium. However, values for chlorine must be regarded with care as the epoxy used for embedding the samples also contained some chlorine. Distribution of the alloying elements over the above-mentioned corrosion product morphologies are given in Figures 10 and 11, respectively.

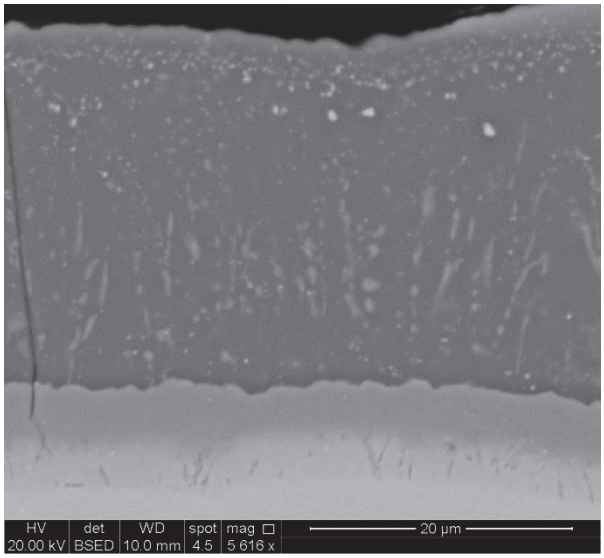

(a)

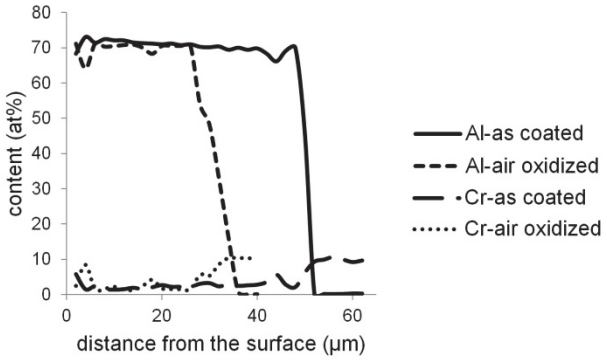

(b)

Figure 8: (a) Microstructure of the alloy and the coating after the salt-free exposure. (b) Aluminum and chromium concentration profiles before and after the salt-free exposure. Serrations in the aluminum profile are due to the presence of chromium and chromium-silicon rich phases.

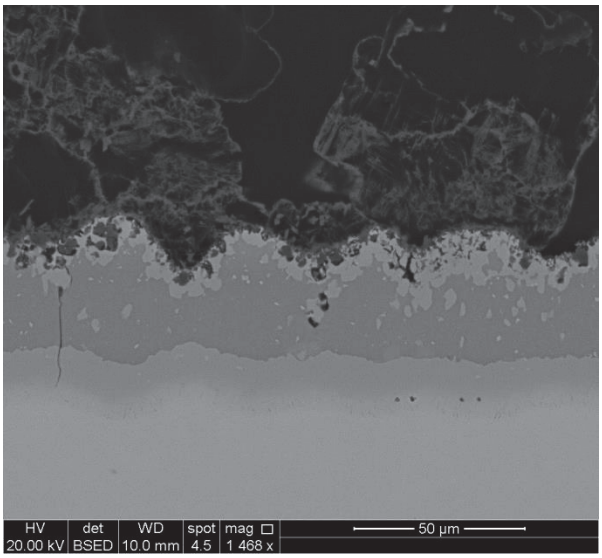

(a)

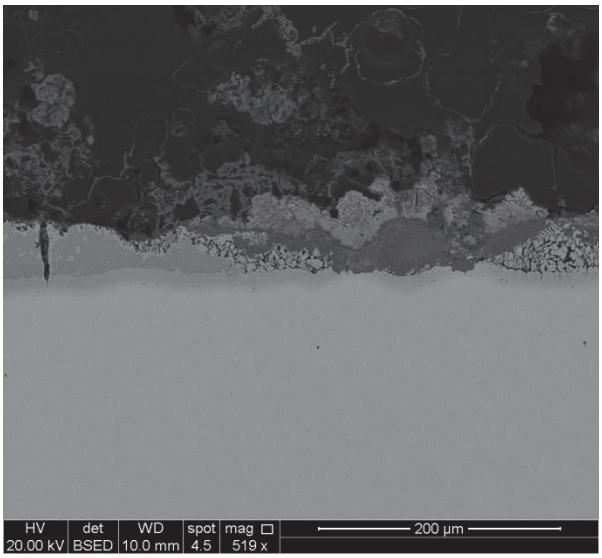

(b)

Figure 9

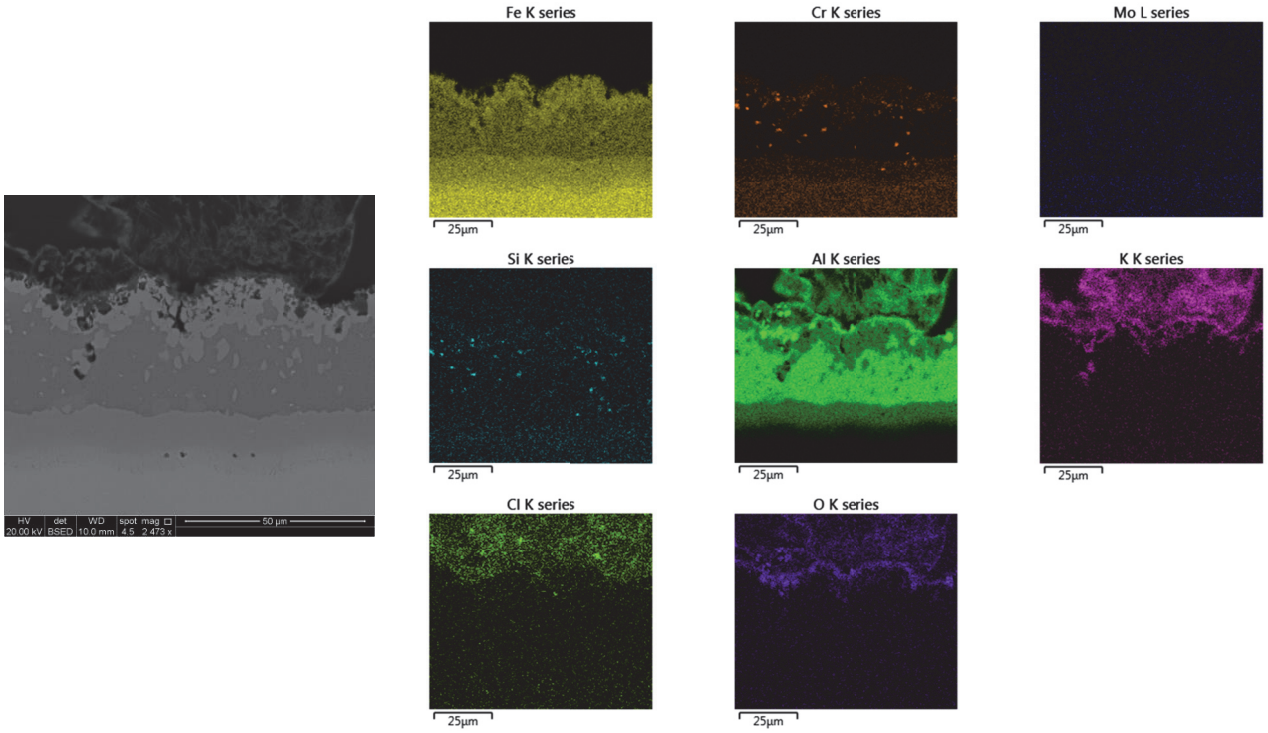

Figure 10: Distribution of the alloying elements throughout the corrosion morphology on Fe_2Al_5-coated P91. Note that the chlorine on the upper half of its map comes from the epoxy used for embedding the sample.

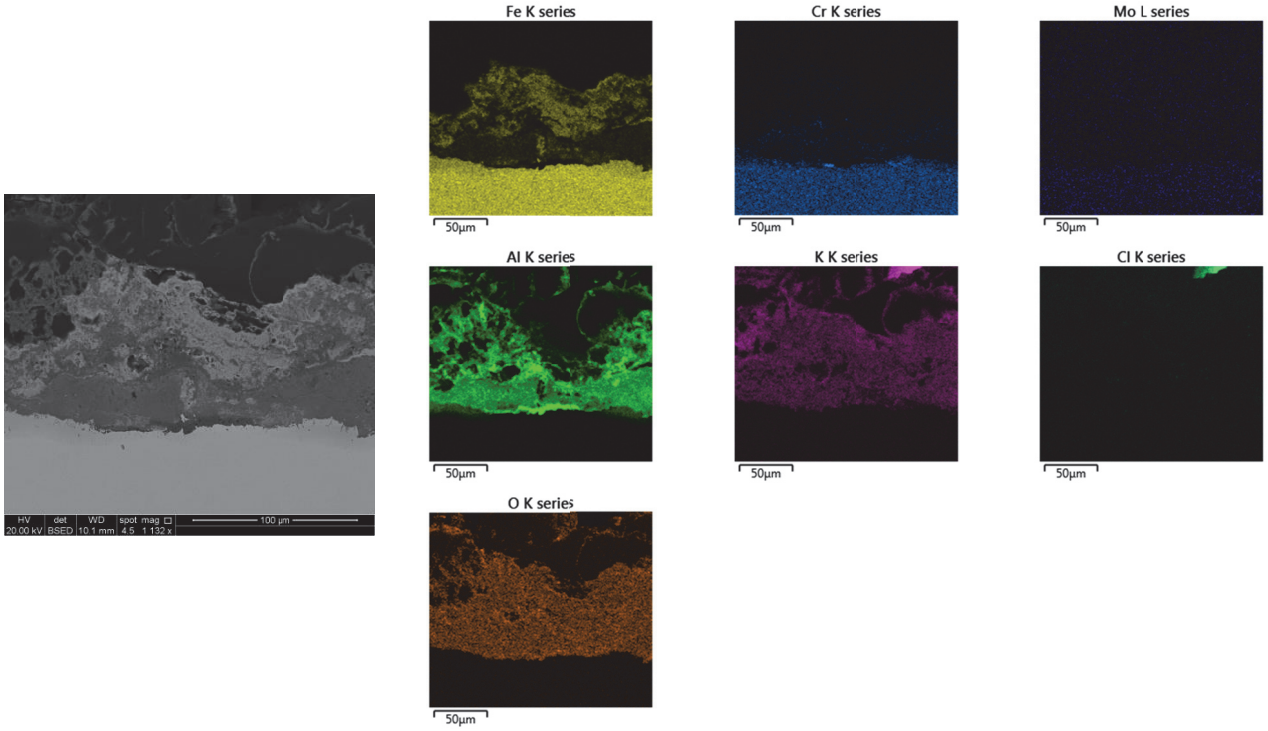

Figure 11: Distribution of the alloying elements throughout the corrosion product morphology on Fe_2Al_5-coated P91.

Figure 12 shows the results of phase analysis with XRD. The as-coated layer consists of Fe_2Al_5 with a small amount of Cr_3Si consistent with the mapping in Figure 7b and aluminum concentration

profile in Figure 8b. The salt-free exposure does not lead to a significant change compared to the as-deposited coating. Only a slight background elevation can be detected around $52^{o}2\theta$. The diffractogram after the exposure to KCl clearly shows the presence of Al_2O_3 (corundum). However, no other oxide and/or potassium containing compound could be unambiguously detected. In addition, increasing the incidence angle to 5^{o} (not shown in Figure 12) revealed that a small amount of $Fe_{1-x}Al$ had formed as well.

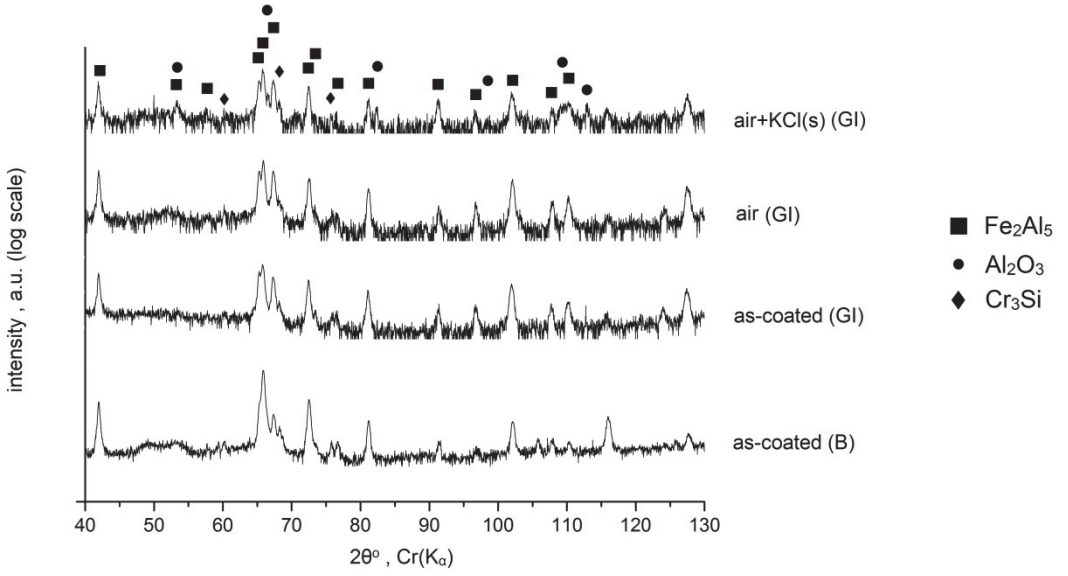

Figure 12: Phase composition of the Fe_2Al_5-coated P91 before and after the exposures. B denotes measurement in Bragg-Brentano configuration. The rest of the measurements have been performed in grazing-incidence (GI) configuration at an angle of 2^{o}.

3.3 Performance of Ni_2Al_3 on Ni

Figures 13a and 13b show the microstructure of the coating before and after the salt-free exposure. The as-coated layer showed non-uniformities in the thickness but no deep penetrating vertical cracks, as was observed for Fe_2Al_5. No significant degradation could be detected after the salt-free exposure and interdiffusion between the coating and the nickel substrate was the only apparent effect. Results of EDS line scans across the coating and the substrate are given in Figure 13d. For the as-coated sample, the drop in aluminum concentration is abrupt while the aluminum concentration profile on the exposed sample is more diffuse. In addition, a step on the concentration profile can be clearly seen at around 25 at.% aluminum. The microstructure of the sample after exposure to KCl (Figure 13c) was quite similar to the one without salt indicating that the coating is not attacked by the salt. No local attack could be observed anywhere on the sample. Mapping of the cross section gave a faint indication of a thin oxide formed on the surface (Figure 14).

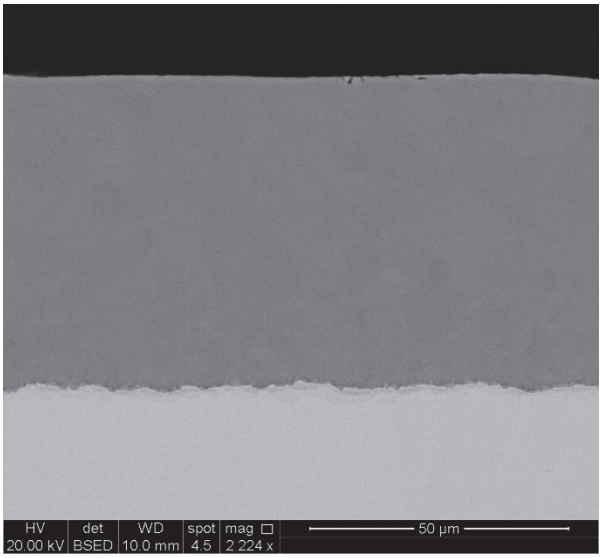

(a)

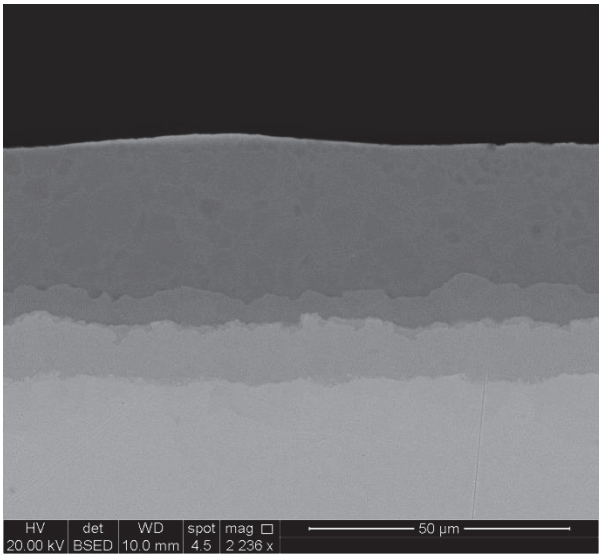

(b)

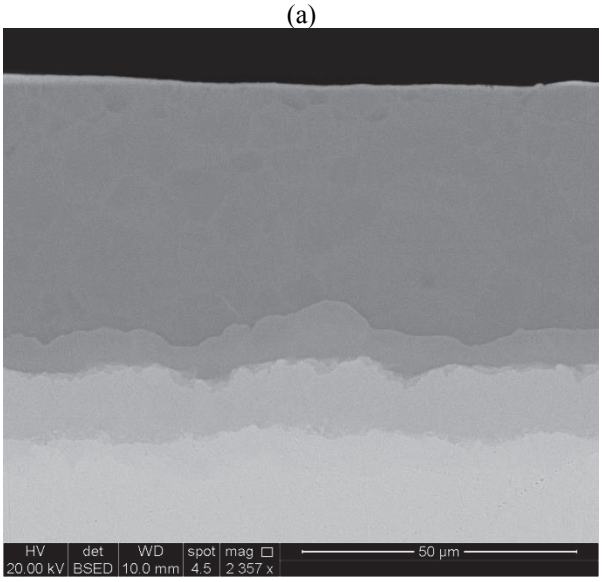

(c)

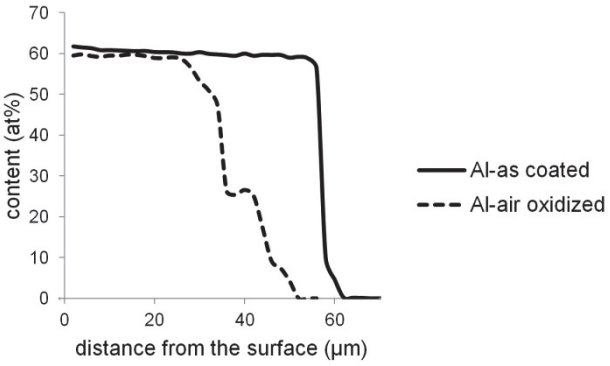

(d)

Figure 13: Microstructure of (a) As-coated Ni_2Al_3 and (b) oxidized sample in the absence of KCl. (c) oxidized sample in the presence of KCl (d) Aluminum concentration profile before and after the salt-free exposure.

Figure 15 shows the diffractograms corresponding to the samples before and after exposures. After the salt-free exposure, in addition to the Ni_2Al_3 peaks, only minor peaks corresponding to $Ni_{1-x}Al$ could be detected. However, repeating the XRD in Bragg condition did not reveal any $Ni_{1-x}Al$ peaks. The KCl-affected sample did not show any peaks other than those of the as-coated sample.

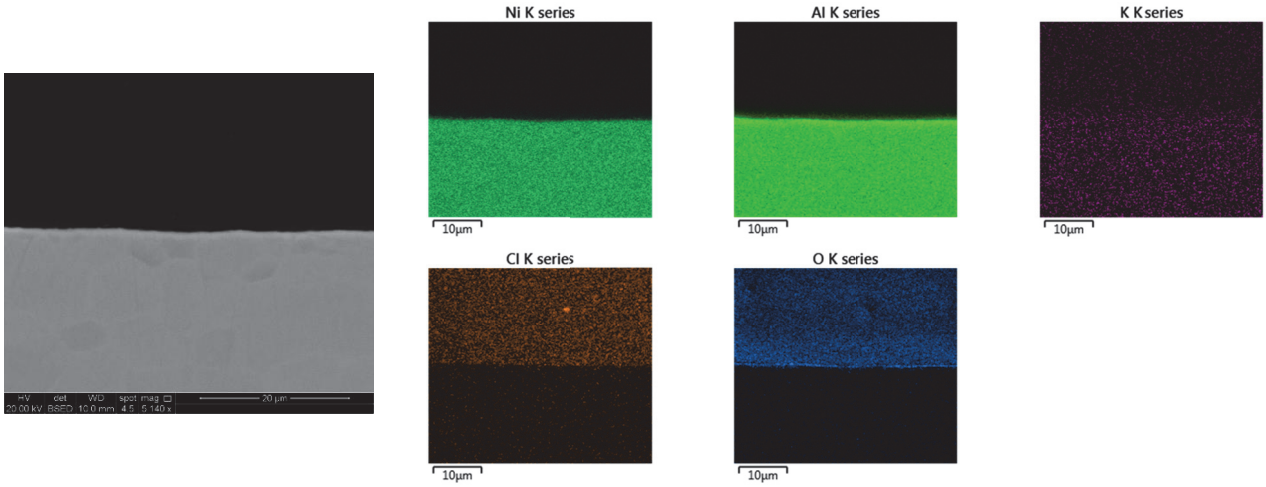

Figure 14: Distribution of the alloying elements throughout the corrosion product morphology on Ni_2Al_3-coated pure nickel. Note that the chlorine on the upper half of its map comes from the epoxy used for embedding the sample.

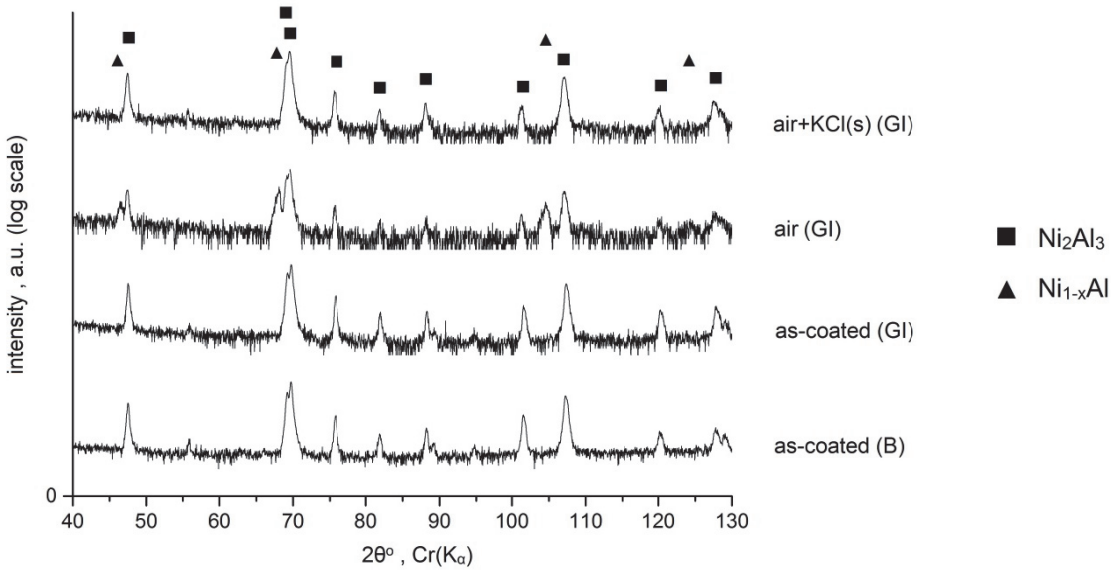

Figure 15: Phase composition of the Ni_2Al_3-coated pure nickel before and after the exposures. B denotes measurement in Bragg-Brentano configuration. The rest of the measurements have been performed in grazing-incidence (GI) configuration at an angle of 2^o.

4. Discussion

4.1 $Fe_{1-x}Al$ on P91

The observation that all the peaks on the diffractogram corresponding to the salt-free exposure (Figure 6) match those on the as-coated sample indicates that the oxide formed in the absence of the KCl is too thin to be detected with GI-XRD. This is consistent with the microstructure shown in Figure 2b and can be described by considering the aluminum concentration profile (Figure 2c) and the Fe-Al phase diagram (Figure 1). Although some depletion of aluminum has occurred due to interdiffusion, $Fe_{1-x}Al$ is still present after 168h of exposure. Wide range of non-stoichiometry in

the $Fe_{1-x}Al$ phase indicates that diffusion of aluminum in this phase is sufficiently fast. Apparently an aluminum-rich oxide could have been rapidly established and protect the alloy from further oxidation.

The failure of the alloy, although local, observed upon introduction of the salt means that the originally protective oxide is damaged. A close look at the mapping given in Figure 4 shows the presence of potassium (without chlorine) which matches those of aluminum and oxygen. Therefore a reaction between the KCl and the original aluminum oxide might have been possible which in turn paves the way for further corrosion. Referring to the commercial program FactSage [28] one finds that among the different possibilities for a reaction between KCl and Al_2O_3, formation of KAl_9O_{14} is the most thermodynamically favored:

$$KCl(s) + (9/2)Al_2O_3 + (1/4)O_2(g) = KAl_9O_{14} + (1/2)Cl_2(g) \quad ; \quad \Delta G^o(600^oC) = +48.5\ KJ \quad (1)$$
$$KCl(g) + (9/2)Al_2O_3 + (1/4)O_2(g) = KAl_9O_{14} + (1/2)Cl_2(g) \quad ; \quad \Delta G^o(600^oC) = -42.5\ KJ \quad (2)$$

Although the eq.1 has a positive ΔG^o and vapor pressure of KCl(s) at 600^oC is quite small (around $4*10^{-6}$ atm [29]), as the original Al_2O_3 formed on the alloy is very thin, the slightest reaction progress will damage the original oxide. A reaction between KCl and Al_2O_3 is opposite to a previous study [30] that evaluated KCl-Al_2O_3 reactivity with XRD. Such discrepancy can be attributed either to an electrochemical reaction releasing KOH(l,g) [31] or the limitations of XRD to detect amorphous and minor phases (less than 3wt.%).

Although the original Al_2O_3 can be damaged due to the presence of KCl, if the aluminum supply (concentration and diffusivity) after the initial attack is high enough the alloy can re-passivate. This is thought to be the situation shown in Figure 3a where the aluminum content is about 32at.% i.e. the $Fe_{1-x}Al$ is still stable. The presence of potassium without chlorine (mapping in Figure 4) has another implication as well. It indicates that chlorine has been released due to an interaction between the alloy and KCl. In the literature, it is reported that chlorine can cause selective removal of the more reactive alloying elements by volatilization [2], [32]–[36]. Therefore it is not surprising to detect significantly lower aluminum contents in the coating compared to the salt-free exposure. The morphology of the oxide shown in Figure 3b (formation of thick aluminum oxide out of the coating) and the content of residual aluminum (21at.%) strongly suggest that chlorine is involved in de-aluminizing of the coating. When the coating lacks sufficient aluminum to form a protective oxide a thick fast-growing oxide (see Figure 3c) and even internal nitrides (see Figure 5) will form. In summary, it appears that due to interdiffusion and the presence of KCl (both solid and vapor) aluminum content of the coating decreases. However, as long as it is within the stability range of $Fe_{1-x}Al$ the alloy can re-passivate and avoid significant material loss.

4.2 Fe_2Al_5 on P91

Considering the diffractogram corresponding to the salt-free exposure it is clear that no oxide peaks developed and that all peaks perfectly match the diffractogram of the sample before the exposure. This indicates that a protective oxide has formed and it is too thin to be detected with GI-

XRD. This is consistent with the sample's microstructure (Figure 8a) showing the absence of any fast-growing oxide. Apparently the only effect due to the salt-free exposure is the formation of interdiffusion zone between the coating and the alloy. The presence of a step in the concentration profile near 50at.% Al shown in Figure 8b indicates that $Fe_{1-x}Al$ has formed underneath the Fe_2Al_5. However, due to the wide range of non-stoichiometry in $Fe_{1-x}Al$ the step on the concentration profile is not flat.

The presence of KCl has a remarkable impact on Fe_2Al_5. Unlike $Fe_{1-x}Al$ which only showed local failures, surface of Fe_2Al_5 was entirely affected. Figure 9a and the mapping in Figure 10 show that aluminum has been selectively removed and iron/chromium have been enriched. In addition, it turns out that the removed aluminum can be found outside the original coating's surface matching the maps of oxygen and potassium. This is consistent with the Al_2O_3 peaks found in the diffractogram shown in Figure 12. The presence of a potassium-aluminum-oxygen compound could not be confirmed by XRD. A small spike near $71^o2\theta$ on the diffractogram could be attributed to a number of potassium-aluminum-oxygen compounds ($K_{1.6}Al_{11}O_{17}$, KAl_5O_8, $KAl_6O_{9.5}$, $K_2Al_2O_{14}$). However, all these phases have other peaks that cannot be found on the diffractogram. Other possibilities for the absence of the missing compound can be that it is formed in small amounts, it has an amorphous structure or it is obscured due to peak overlaps.

The microstructure in Figure 9a shows that aluminum removal is not limited to the coating surface as aluminum depleted areas can be found in the middle of the Fe_2Al_5 layer (see the light-contrast "islands" in the middle of the coating in Figure 9a). The depth and local nature of aluminum removal as well as morphology of the oxide strongly suggest that the mechanism of depletion is volatilization by chlorine (similar to what is shown in Figure 3b). On the other hand the coating is not completely corroded through. It appears that if the depleted area maintains a sufficient aluminum content (after an initial depletion) it has the possibility to re-passivate. EDS spot analysis on several aluminum-depleted areas similar to Figure 9a gave values around 51at.% for the residual aluminum. This is consistent with the detection of $Fe_{1-x}Al$ when the GI-XRD was performed at 5^o and describes why the corrosion does not continue on some parts of the Fe_2Al_5. Description of the corrosion morphology shown in Figure 9b is not as straight-forward as that in the Figure 9a. However, one can speculate a case where the de-aluminizing of Fe_2Al_5 is locally so severe that the residual aluminum content is less than what is needed to stabilize the $Fe_{1-x}Al$. In such case the alloy cannot re-passivate after the initial stages of the attack and eventually a double layer oxide rich in iron on top and aluminum at the bottom will form underneath the earlier corrosion products. Such description is of course tentative and proving it requires time-resolved exposures.

4.3 Ni_2Al_3 on Ni

The salt-free exposure did not lead to any visible degradation of the surface. In addition, lack of detection of oxide by GI-XRD indicates that it is very thin. This is consistent with the micrograph shown in Figure 13b that demonstrates a protective behavior. The only visible degradation effect is the interdiffusion between the coating and the nickel. The step on the concentration profile in Figure 13d (around 25 at.% Al) indicates that Ni_3Al has formed and the gradual decrease in aluminum

concentration between the Ni_2Al_3 and Ni_3Al is consistent with the non-stoichiometry in the $Ni_{1-x}Al$ formed between the two. Detection of $Ni_{1-x}Al$ with XRD on the surface of Ni_2Al_3 after the salt-free exposure is peculiar as it was not found when the measurement was done in Bragg-Brentano configuration. In addition no aluminum depletion was observed when EDS line scan was done on the cross section (see Figure 13b). This requires further investigation.

In contrast to what was observed for the $Fe_{1-x}Al$ and Fe_2Al_5 the presence of KCl did not lead to any significant effect on Ni_2Al_3. The diffractogram of the salt-affected sample perfectly matched that of the as-coated sample and no fast-growing oxide was observed on the sample when the cross section was studied with SEM. Considering the interaction between the KCl and the oxide formed on $Fe_{1-x}Al$ (see mapping in Figure 4) and the fact that the oxide-forming element in both cases of $Fe_{1-x}Al$ and Ni_2Al_3 is aluminum, a similar interaction could be expected with Ni_2Al_3 and KCl. However, the mapping in Figure 14 does not show any potassium enrichment and therefore it is not clear if an interaction has taken place or not. If an interaction has taken place, then it is on a scale that is not detectable with typical SEM analysis. All in all, it appears that even if the original oxide on Ni_2Al_3 has been damaged a re-passivation has taken place and has protected the coating from a continued attack. A number of argumentations can be put forward as to why such effect is not observed in case of Fe_2Al_5. One possibility can be the diffusivity of aluminum in that phase compared to that in Ni_2Al_3 and another one could be the presence of chromium-rich phases in the Fe_2Al_5 coating (see Figure 7a-b). Vokal et al. [10] attribute the KCl-induced attack on aluminide phases to the detection of α-Cr and/or $Cr_{23}C_6$ phases in the grain boundaries of the aluminide phases. This is consistent with the high affinity of chromium to react with alkali chlorides and form alkali chromates [37]–[43]. However, in this study no clear sign of chromium involvement could be observed and it was aluminum which was often associated with potassium.

Conclusions

The following conclusions can be drawn from what has been performed in this study:

1- Pack cementation process was employed to produce the $Fe_{1-x}Al$ and Fe_2Al_5 phases on the ferritic-martensitic stainless steel P91 and Ni_2Al_3 on pure Ni. These coatings showed excellent performance against air-oxidation at 600°C when KCl was absent.
2- $Fe_{1-x}Al$ coated on P91 formed a protective oxide on large parts of the surface when exposed to KCl. Local failures were observed on this coating which were always associated with depletion/dilution of aluminum.
3- Fe_2Al_5 coated on P91 was attacked all over the surface when KCl was present. The attack was generally in form of selective aluminum removal. On large parts of the surface the attack does not seem to have continued upon the formation of $Fe_{1-x}Al$. In a few cases, the coating was completely consumed and voluminous corrosion products had formed.
4- Ni_2Al_3 coated on pure Ni formed protective oxide all over the surface when exposed to KCl.

Acknowledgment

This work was performed within the framework of the project GREEN financed by the Danish Council for Strategic Research. John C. Troelsen, Flemming B. Grumsen and Peter J.S. Westermann are acknowledged for their help and technical support during this work.

References

[1] M. Montgomery, S. A. Jensen, U. Borg, O. Biede, and T. Vilhelmsen, "Experiences with high temperature corrosion at straw-firing power plants in Denmark," *Mater. Corros.*, vol. 62, no. 7, pp. 593–605, Jul. 2011.

[2] M. Montgomery and A. Karlsson, "In-situ corrosion investigation at Masnedù CHP plant - a straw-fired power plant," *Mater. Corros.*, vol. 50, pp. 579–584, 1999.

[3] M. Montgomery, A. Karlsson, and O. Larsen, "Field test corrosion experiments in Denmark with biomass fuels. Part 1: Straw-firing," *Mater. Corros.*, vol. 53, no. 2, pp. 121–131, 2002.

[4] P. Henderson, C. Davis, and M. Montgomery, "In-situ fireside corrosion testing of superheater materials with coal, wood and straw fuels for conventional and advanced steam temperatures," *VGB powertech*, vol. 6, pp. 53–59, 2005.

[5] M. Montgomery, O. Biede, and O. H. Larsen, "Experiences with Inconel 625 in Biomass and Waste Incineration Plants," *Mater. Sci. Forum*, vol. 522–523, pp. 523–530, 2006.

[6] M. Montgomery, S. A. Jensen, A. Hansson, O. Biede, and T. Vilhelmsen, "HIGH TEMPERATURE CORROSION TESTING AT MARIBOSAKSKØBING BIOMASS FIRING POWER PLANT," in *9th Liege Conference : Materials for Advanced Power Engineering*, 2010, pp. 1096–1105.

[7] Y. Li and M. Spiegel, "Internal Oxidation of Fe – Al Alloys in a KCl-Air Atmosphere at 650 ◦ C," *Oxid. Met.*, vol. 61, no. April, 2004.

[8] *Metals Handbook, Vol 3, Alloy Phase Diagrams*. ASM International, 1992.

[9] Y. S. Li, M. Spiegel, and S. Shimada, "Corrosion behaviour of various model alloys with NaCl–KCl coating," *Mater. Chem. Phys.*, vol. 93, no. 1, pp. 217–223, Sep. 2005.

[10] V. Vokál, V. Rohr, M. J. Pomeroy, and M. Schütze, "Corrosion of alloys and their diffusion aluminide coatings by KCl:K2SO4 deposits at 650 °C in air," *Mater. Corros.*, vol. 59, no. 5, pp. 374–379, May 2008.

[11] T. J. Pan, Y. S. Li, Q. Yang, R. F. Feng, and a. Hirose, "Internal oxidation and phase transformations of multi-phase Fe–Ni–Al and Fe–Ni–Al–Cr alloys induced by KCl corrosion," *Corros. Sci.*, vol. 53, no. 6, pp. 2115–2121, Jun. 2011.

[12] S. Enestam, D. Bankiewicz, J. Tuiremo, K. Mäkelä, and M. Hupa, “Are NaCl and KCl equally corrosive on superheater materials of steam boilers?,” *Fuel*, vol. 104, pp. 294–306, Feb. 2013.

[13] S. Karlsson, J. Pettersson, L.-G. Johansson, and J.-E. Svensson, “Alkali Induced High Temperature Corrosion of Stainless Steel: The Influence of NaCl, KCl and CaCl2,” *Oxid. Met.*, vol. 78, no. 1–2, pp. 83–102, Apr. 2012.

[14] D. W. Mckee, D. A. Shores, and K. L. Luthra, “The Effect of SO2 and NaCl on High Temperature Hot Corrosion,” *J. Electrochem. Soc.*, vol. 125, pp. 411–419, 1978.

[15] J. Smeggil and N. Bornstein, “The Effect of NaCl (g) on the Oxidation of NiAl,” *J. Electrochem. Soc.*, vol. 125, no. 8, pp. 1283–1290, 1978.

[16] A. Magdziarz and Z. Kalicka, “Hot corrosion behaviour of Ni3Al in sulphate–chloride mixtures in the atmosphere,” *Corros. Sci.*, vol. 49, no. 4, pp. 1869–1877, Apr. 2007.

[17] C. Schwalm and M. Schütze, “The corrosion behavior of several heat resistant materials in air+ 2% Cl2 at 300 to 800° C. Part 3–Alumina formers and intermetallics,” *Mater. Corros.*, vol. 172, pp. 161–172, 2000.

[18] J. Kalivodová, D. Baxter, M. Schütze, and V. Rohr, “Corrosion behaviour of boiler steels, coatings and welds in flue gas environments,” *Mater. Corros.*, vol. 59, no. 5, pp. 367–373, May 2008.

[19] G. Han and W. D. Cho, “The corrosion behavior of Fe3Al in gas mixtures of oxygen and chlorine at 700°C,” *Mater. Sci. Eng. A*, vol. 419, no. 1–2, pp. 76–85, Mar. 2006.

[20] G. Han and W. Cho, “High-Temperature Corrosion of Fe3Al in 1% Cl2/Ar,” *Oxid. Met.*, vol. 58, no. October, pp. 3–10, 2002.

[21] W. D. Cho and G. Han, “High-Temperature Corrosion of Y-Doped Fe₃ Al in Environments Containing Chlorine and Oxygen,” *J. Mater. Eng. Perform.*, vol. 15, no. 5, pp. 558–563, Oct. 2006.

[22] J. Klöwer, “High temperature Corrosion behaviour of iron aluminides and iron□aluminium□ chromium alloys,” *Mater. Corros.*, vol. 694, pp. 685–694, 1996.

[23] J. Klöwer, U. Brill, and U. Heubner, “High temperature corrosion behaviour of nickel aluminides: effects of chromium and zirconium,” *Intermetallics*, vol. 7, pp. 1183–1194, 1999.

[24] H. Latreche, S. Doublet, G. Tegeder, G. Wolf, P. Masset, T. Weber, and M. Schütze, “Behaviour of NiAl APS□coatings in chlorine□containing atmospheres,” *Mater. Corros.*, vol. 59, no. 7, pp. 573–583, Jul. 2008.

[25] M. C. Galetz, B. Rammer, and M. Schütze, “The Protection of Aluminides by Alloying with Molybdenum in High Chlorine Containing Atmospheres at 1,000 °C,” *Oxid. Met.*, vol. 81, no. 1–2, pp. 151–165, Dec. 2014.

[26] V. Rohr, M. Schütze, E. Fortuna, D. N. Tsipas, a. Milewska, and F. J. Pérez, “Development of novel diffusion coatings for 9-12 % Cr ferritic-martensitic steels,” *Mater. Corros.*, vol. 56, no. 12, pp. 874–881, Dec. 2005.

[27] B. Rammer, T. Weber, and M. Schütze, “Development of Diffusion Coatings on Nickel-base Alloys For The Use In Chlorine-Containg High Temperature Processes,” *Mater. Corros.*, vol. 39, no. 1, pp. 29–32, Jan. 2008.

[28] “FactSage 6.2, www.factsage.com.” .

[29] S. Kiamehr, K. V. Dahl, M. Montgomery, and M. A. J. Somers, “KCl-induced high temperature corrosion of selected commercial alloys part I: chromia-formers.”

[30] S. Kiamehr, K. V Dahl, T. N. Lomholt, T. L. Christiansen, and M. A. J. Somers, “High Temperature Corrosion due to Biomass Firing : A Study on the Reactivity between Potassium Chloride and Oxides,” in *International Symposium of High Temperature Oxidation and Corrosion*, 2014, vol. 2, no. Vi, pp. 144–147.

[31] N. Folkeson, T. Jonsson, M. Halvarsson, L.-G. Johansson, and J.-E. Svensson, “The influence of small amounts of KCl(s) on the high temperature corrosion of a Fe-2.25Cr-1Mo steel at 400 and 500°C,” *Mater. Corros.*, vol. 62, no. 7, pp. 606–615, Jul. 2011.

[32] J. Oh, M. McNallan, G. Lai, and M. Rothman, “High temperature corrosion of superalloys in an environment containing both oxygen and chlorine,” *Metall. Mater. ...*, vol. 17, no. 600, pp. 1087–1094, 1986.

[33] M. Rhee, M. McNallan, and M. Forthman, “Long term high temperature corrosion studies of high temperature alloys in chlorine contaminated environments,” *J. Mater. energy*, vol. 7, no. 4, pp. 294–301, 1986.

[34] A. Zahs, M. Spiegel, and H. Grabke, “The influence of alloying elements on the chlorineâ€ induced high temperature corrosion of Feâ€ Cr alloys in oxidizing atmospheres,” *Mater. Corros.*, 1999.

[35] A. Zahs, M. Spiegel, and H. J. Grabke, “Chloridation and oxidation of iron, chromium, nickel and their alloys in chloridizing and oxidizing atmospheres at 400 - 700C,” *Corros. Sci.*, vol. 42, pp. 1093–1122, 2000.

[36] A. Walter Hassel, L. Neelakantan, A. Zelenkevych, A. Ruh, and M. Spiegel, “Selective de-alloying of NiTi by oxochloridation,” *Corros. Sci.*, vol. 50, no. 5, pp. 1368–1375, May 2008.

[37] Y. Shinata and Y. Nishi, “NaCl-induced accelerated oxidation of chromium,” *Oxid. Met.*, vol. 26, pp. 201–212, 1986.

[38] Y. Shinata, “Accelerated oxidation rate of chromium induced by sodium chloride,” *Oxid. Met.*, vol. 27, pp. 315–332, 1987.

[39] Y. S. Li, M. Sanchez-Pasten, and M. Spiegel, “High Temperature Interaction of Pure Cr with KCl,” *Mater. Sci. Forum*, vol. 461–464, pp. 1047–1054, 2004.

[40] J. Lehmusto, P. Yrjas, B. J. Skrifvars, and M. Hupa, “Detailed Studies on the High Temperature Corrosion Reactions between Potassium Chloride and Metallic Chromium,” *Mater. Sci. Forum*, vol. 696, pp. 218–223, Sep. 2011.

[41] J. Lehmusto, D. Lindberg, P. Yrjas, B.-J. Skrifvars, and M. Hupa, “Studies on the Partial Reactions Between Potassium Chloride and Metallic Chromium Concerning Corrosion at Elevated Temperatures,” *Oxid. Met.*, Nov. 2011.

[42] J. Lehmusto, B.-J. Skrifvars, P. Yrjas, and M. Hupa, “High temperature oxidation of metallic chromium exposed to eight different metal chlorides,” *Corros. Sci.*, vol. 53, no. 10, pp. 3315–3323, Oct. 2011.

[43] J. Lehmusto, D. Lindberg, P. Yrjas, B.-J. Skrifvars, and M. Hupa, “Thermogravimetric studies of high temperature reactions between potassium salts and chromium,” *Corros. Sci.*, Mar. 2012.

9.6 Paper VI

T. Jonsson, A. Slomian, T. N. Lomholt, S. Kiamehr, K. V. Dahl

Microstructural investigations of pure Nickel exposed to KCl induced high temperature corrosion

Accepted for publication in Materials at High Temperatures

Microstructural investigations of pure Nickel exposed to KCl induced high temperature corrosion

T. Jonsson[*] A. Slomian[*] T. N. Lomholt[**], S. Kiamehr[**] K. V. Dahl[**]

[*)] Environmental Inorganic Chemistry, Department of Chemical and Biological Engineering, Chalmers University of Technology, S-412 96, Göteborg, Sweden

[**)] Department of Mechanical Engineering, Technical University of Denmark, Produktionstorvet building 425, DK-2800 Kgs. Lyngby, Denmark

Abstract

Oxidation of 99.99% pure Nickel was studied with and without 0.10 mg/cm^2 KCl(s) in an environment containing 5% O_2, 40% H_2O and 55% N_2 (vol.%) at 600 °C for up to 168 h. Oxide microstructure was investigated by XRD, FIB, BIB and SEM/EDX. Oxidized Nickel shows an approximately parabolic oxide growth rate. The oxide scale is dense with some pores at the oxide metal/interface. Adding small amounts of KCl does not result in a faster corrosion rate of Nickel. However, the surface morphology changes and small oxide crusts were observed in the vicinity of former KCl particles. This is proposed to be the result of a $NiCl_2$-KCl eutectic on top of the oxide scale formed above 514 °C. The oxide scale formed in the presence of KCl contains more and differently distributed voids than the scale formed without KCl.

Keywords: Nickel, KCl, high temperature corrosion, 600 °C, electron microscopy

Introduction

The fireside environment in power boilers may be quite corrosive, especially in boilers firing biomass, where the fireside environment is characterized by a combination of high levels of reactive alkali (NaCl and KCl), HCl and relatively low SO_2 concentrations. The corrosion problems shorten the lifetime of the waterwall and the steam superheater, limiting the maximum steam temperature to approximately 540°C when using state of the art chromia forming steels. An opportunity to increase the lifetime of the boiler is to apply Nickel based coatings or alloys that rely on Cr or Al for corrosion protection. However, for reference and in order to predict behaviour if an oxide scale spalls off or the coating becomes depleted in Al or Cr it is important to know how pure Nickel performs in the presence of KCl.

The literature reports a relatively inert behavior for pure Nickel against gaseous chlorine bearing species and solid alkali chlorides. However, this requires that temperature and $P_{Cl2(g)}/P_{O2(g)}$ ratio are not too high [1, 2]. Li et al. [3, 4] exposed pure Nickel at 650 °C for 48h in static lab air with a KCl deposit. After removal of corrosion products, they observed that the pure Ni showed a significantly lower mass loss compared to that of pure Fe, Cr, Fe-35Cr and Fe-25Cr-20Ni (wt%) alloys. Cha and Spiegel [5, 6] tested pure Nickel at 500 °C in an 79.95%N_2, 20%O_2 and 0.05%HCl (vol.%)

atmosphere with a KCl deposit. They report that the presence of KCl does not appear to cause an accelerated local oxidation. Shinata et al. [7] studied the performance of pure Nickel under an NaCl deposit and observed that when the temperature is below the melting point of the salt the extent of corrosion is quite small. The mechanism during the initial stages of corrosion of Nickel in the presence of small amounts of KCl(s) has however not been subjected to detailed microstructural studies.

The present study investigates the detailed microstructure of corroded Nickel samples after exposure in a KCl(s) containing environment. A detailed analysis is performed to investigate the oxide scales formed in the presence of KCl, in order to better understand the corrosive effect of alkali chloride on high temperature corrosion of pure Nickel. The detailed microstructural analysis is performed using a scanning electron microscope equipped with an energy dispersive X-ray (EDX) system and focused/broad ion beam (FIB and BIB) workstations. This made it possible to analyze the oxide scales and describe the microstructure in detail. The objective of this investigation is to link the microstructure of the formed oxide scales to the oxidation/corrosion mechanisms.

Experimental procedure

Pure Ni samples (99.99% purity), 2 mm thick half circular shaped (diameter 25 mm), were mounted on a sample holder and wet ground with SiC paper with increasing grit sizes: #80, #220, #320 and #1000 grits. The samples were in addition subsequently polished with 9, 3 and 1 μm diamond paste. The samples were rinsed with ethanol (99.5%) in-between every grinding and polishing step. The samples were dried in cool air, weighed in a Sartorius R 160 P scale and stored in a desiccator. KCl was applied to the samples prior to exposure by spraying a saturated solution of KCl in a 20:80 mixture of water and ethanol (99.5%) while continuously drying the sample with heated air. All samples were exposed at 600 °C in an environment containing 5% O_2, 40% H_2O and 55% N_2 (vol.%) in an electrically heated tube furnace with a gas flow of 1000 mL/min. The samples were exposed for 1, 24 and 168 hours, both with and without 0.10 mg/cm^2 KCl. After exposure, the samples were allowed to air cool followed by weighing. The exposed samples were examined in an FEI Quanta 200 FEG ESEM equipped with an Oxford Inca 300 EDX system for chemical analysis in high vacuum mode. X-ray diffraction was performed in a Siemens D5000 Powder Diffractometer. Ion milled sections were produced in Leica broad ion beam (BIB) workstation and a FEI Strata Dualbeam 235 focused ion beam (FIB) workstation. The thermodynamic calculations were performed using the software FactSage 6.4 and databases: Fact53, ELEM, BINS.

Results

Gravimetry

The corrosiveness of small amounts of KCl towards Nickel is illustrated in Fig. 1 showing the mass gain in 5% O_2, 55% N_2 with 40% H_2O (vol.%) with and without KCl(s) at 600 °C. The results indicate that the presence of small amounts of KCl does not result in a faster corrosion rate of Ni. Instead both the Ni without and Ni exposed in the presence of KCl follow a similar oxide growth rate. KCl is known to evaporate under these conditions [8], which could explain the smaller mass

gain of Nickel exposed with KCl. The mass gain of the Nickel sample exposed for 168 hours corresponds to a calculated oxide thickness of about 2 µm, using mass gain and NiO density.

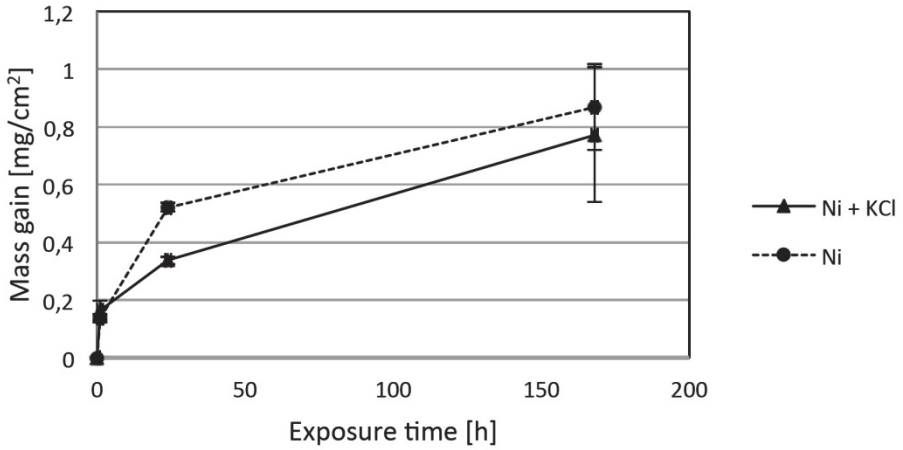

Figure 1: Mass gain of Nickel in the presence and absence of 0.10 mg/cm^2 KCl(s) in 5%O_2 + 40%H_2O at 600 ^{o}C

Morphology and microstructure in the absence of KCl

In the absence of KCl the scale formed on Nickel shows an approximately parabolic growth rate, see Fig. 1. XRD showed the presence of Nickel and NiO after all exposure times indicating a thickness below the penetration depth of the XRD (about 20 µm). After one hour of exposure the sample surface was covered with a smooth oxide scale, see Fig. 2. This type of morphology was present after all exposure times even though a small change in morphology could be observed with high magnification. The oxide scale morphology becomes more even with time (see Fig. 2). In Fig. 3 a FIB image shows one part of an ion-milled cross-section. The oxide scale was about 4 µm thick in the cross-section and contains few voids mainly at the metal/oxide interface. The oxide grains close to the oxide metal interface are about 500 nm wide while the oxide grains in the other parts of the oxide scale are columnar and much smaller (about 100 nm wide).

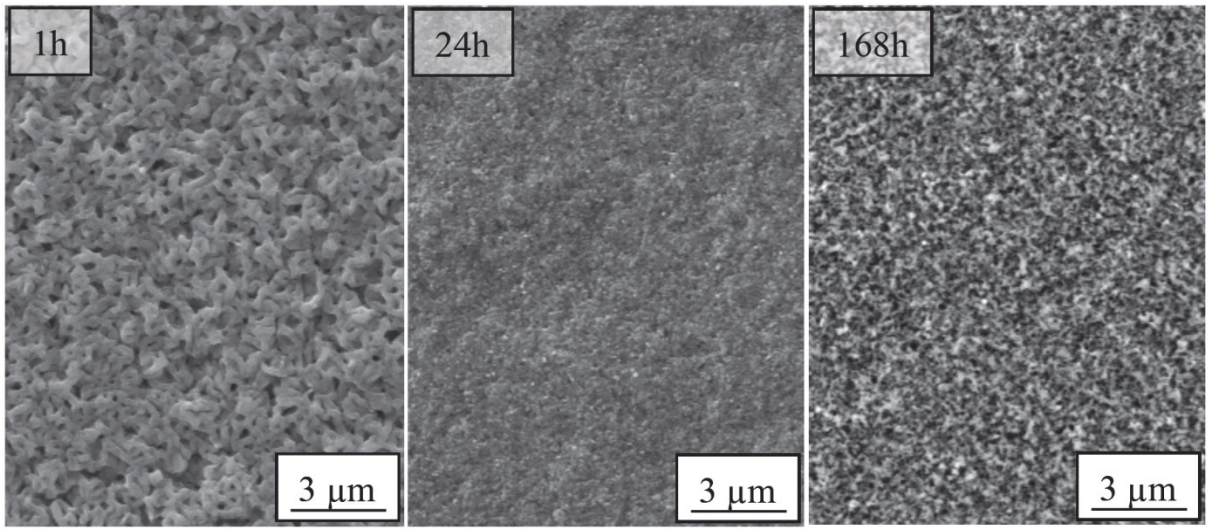

Figure 2: Plan view SE images of samples exposed for 1, 24, and 168 hours in 5%O_2 + 40%H_2O. The surface is very smooth after all exposure times.

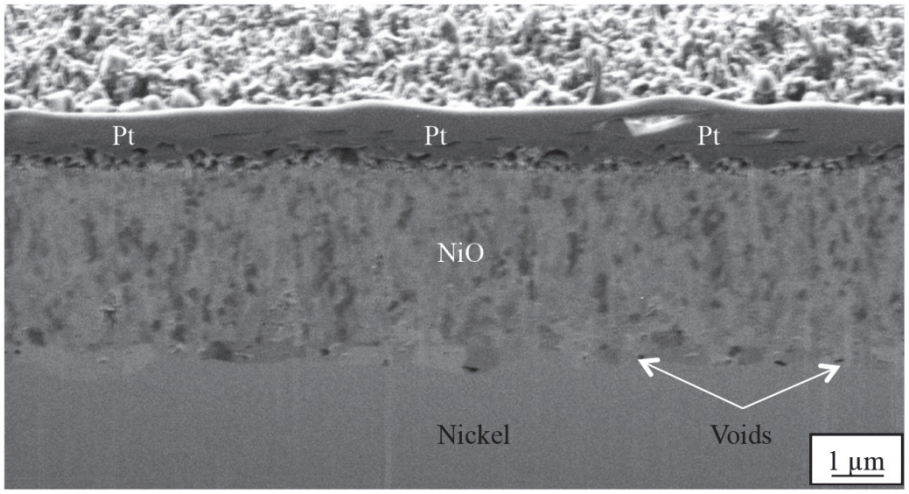

Figure 3: FIB image of an ion milled cross-section of the oxide scale formed after 168 hours exposure without KCl(s). The sample is tilted 52^{o} . The oxide scale is about 4µm thick in the cross-section and contains few voids mainly located at the metal/oxide interface.

Morphology and microstructure in the presence of KCl

In the presence of KCl the Nickel samples show a smaller mass gain, see Fig. 1. The smaller mass gain could be explained by the evaporation of KCl. This indicates that the oxide growth rate in presence of small amounts of KCl is similar to the reference exposure. XRD shows the presence of Ni and NiO on all samples while KCl is only detected after 1 hour of exposure. However, in contrast to the exposures in the absence of KCl, oxidation with KCl(s) gives rise to two different types of morphologies already after 1 hour of exposure, see Fig. 4. Thus, the low magnification

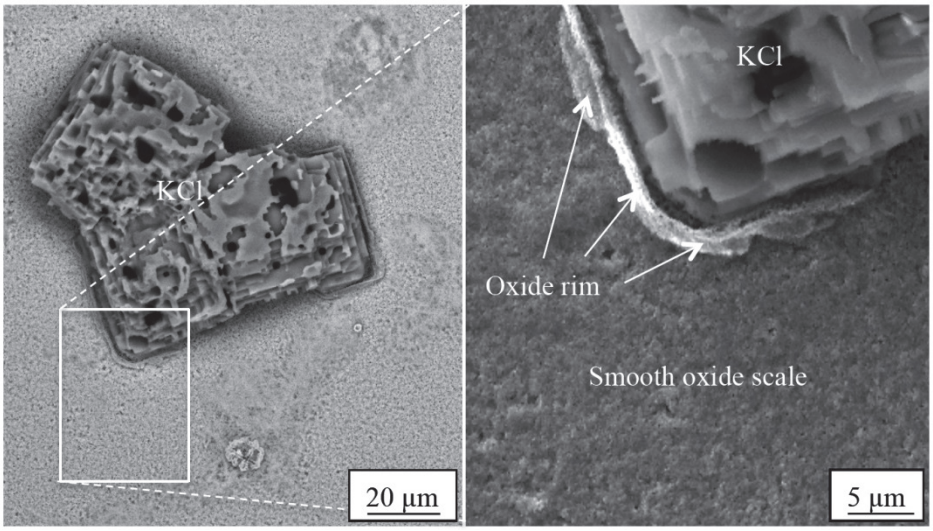

Figure 4: Low magnification SEM BSE image of the oxide scale and a KCl particle after one hours exposure (left image). The main part of the sample is covered with a smooth oxide scale. The marked region is shown with higher magnification (SEM SE image to the right). Close to the KCl particle an oxide rim could be observed.

image shows a smooth oxide on large parts of the surface while an oxide rim starts to form around KCl particles where KCl particles were deposited prior to the exposure. The high magnification SE image in Fig. 4 (image to the right) shows that an oxide rim has started to grow in the vicinity of the KCl particle. This phenomenon was observed around all KCl particles while the smooth oxide scale in between particles has the same type of morphology as the samples exposed without KCl. After longer exposure times (24 and 168h) most of the KCl has vanished, probably due to evaporation, leaving only the oxide rims indicating former KCl particles position, see Fig. 5. No indication of spallation was observed. The oxide rims are about 100 nm thick and have a similar height in all rims independent of distribution and particle size of the former KCl particles (see high magnification image in Fig. 5 after 24 hours exposure, bottom image).

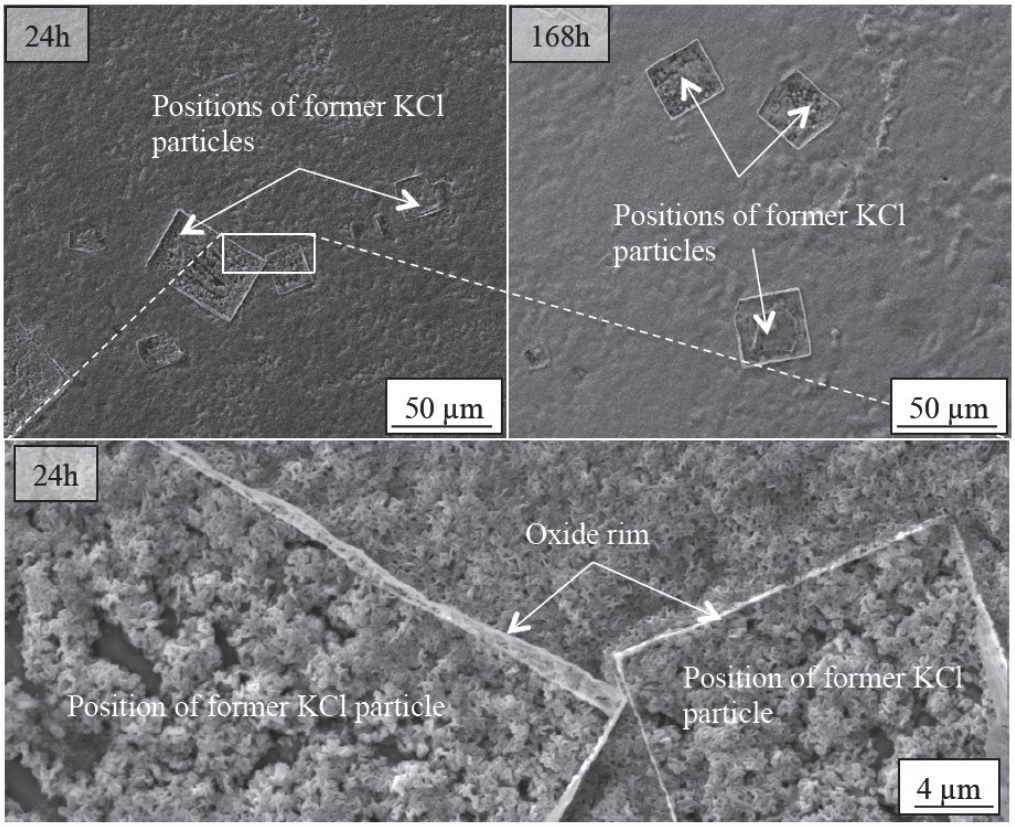

Figure 5: SEM SE images of the oxide scale formed after 24 and 168 hours exposure in the presence of KCl. The main part of the sample is covered with a smooth oxide scale while oxide rims have formed around former KCl particles, which has vanished already after 24 hours exposure. The oxide rim is shown with higher magnification, marked region.

A BIB cross-section was ion milled through the oxide scale and into the metal on a Nickel sample exposed for 168h in the presence of KCl. In Fig. 6 an SEM BSE image shows one part of the cross-section. The oxide scale was 3-7 µm thick in the cross-section and contained many voids. Some of the larger voids could be observed at the metal/oxide interface while the voids tend to be smaller closer to the oxide/gas interface. The oxide grains close to the oxide metal interface were columnar and 300-500 nm wide.

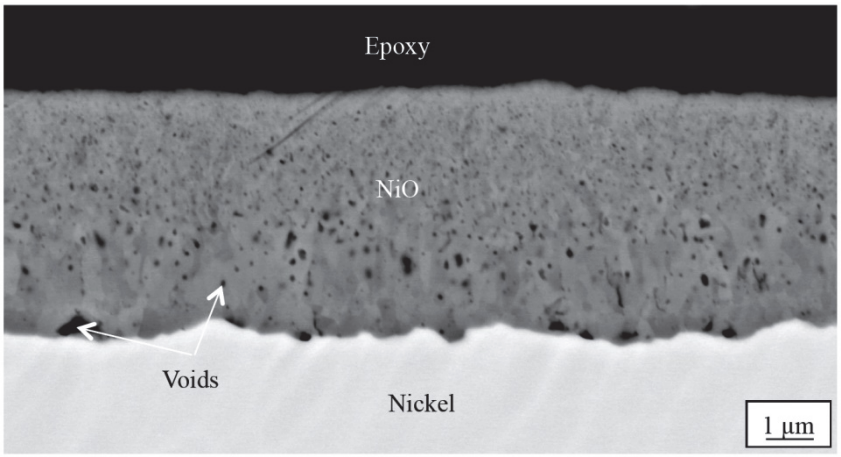

Figure 6: SEM BSE image of an ion milled cross-section of the oxide scale formed after 168h exposure in the presence of KCl. The oxide scale is about 4µm thick in the cross-section and contains many voids. Some of the larger voids could be observed at the metal/oxide interface while the voids tend to be smaller closer to the oxide/gas interface.

Discussion

The oxidation of Nickel results in a similar growth rate as observed for 18-8 stainless steel (304L) and the more highly alloyed stainless steel Sanicro28 in the presence of small amounts of KCl at 600 C up to 168 hours [8, 9]. In the case of the stainless steels the reaction between potassium and chromium in the protective scale results in breakdown of the protective chromium rich oxide scale. These alloys then behave as iron oxide forming alloys giving the fast oxide growth rate. A higher chromium content in the alloy results in a longer time to breakdown by supplying more chromium to the protective scale. However, the results in the present study indicate the addition of small amounts of KCl do not increase the growth rate on pure Nickel. Instead the gravimetric results present a smaller mass gain in the presence of KCl, see Fig. 1. The mass gain difference between the reference exposure and the exposure with KCl corresponds well with the amount of added salt (0.10 mg/cm^2), except after 24 hours where the difference is somewhat larger. If small amounts of KCl are deposited on the surface it is known to evaporate under the given exposure conditions [8, 9]. A comparison between oxide scale microstructure formed with and without KCl after 168 hours verifies that the difference in mass gain does not come as a result of different thickness of the scales (compare Figs 3 and 6). The larger difference found after 24 hours exposure could be explained by evaporation of $NiCl_2$ (see vapour pressure below) formed on the surface and especially the slower growth rate beneath the KCl particles, see Fig. 5. However, with time the KCl evaporates and the scale beneath the oxide grows giving a uniform thickness of the scale after longer exposure times. Thus, the present results suggest that the presence of small amounts of KCl does not change the oxide growth kinetics. This is in line with previous investigations of Nickel in the presence of KCl and Cl_2 [3].

Even though the gravimetric results and the microstructural investigation indicate that the oxide growth kinetics do not change by adding small amounts of KCl(s), the present study shows that the surface morphology changes around the KCl particles. This phenomenon is very similar to the build

up of oxide crust around KCl particles on low-alloyed steels and stainless steels even though it is not as pronounced as on the steels [8-10]. The formation of crusts around KCl particles has been explained by surface formation of an eutectic $FeCl_2$-KCl mixture, which has an eutectic temperature of 355 °C, [10]. Examining the thermodynamic properties of the $NiCl_2$-KCl system shows a similar eutectic, but at considerably higher temperature (at 514 °C), see Fig. 7. This difference in temperature may explain the much smaller crusts in the vicinity of the KCl particles on Nickel compared to the crusts formed on the low alloyed and stainless steels. An ESEM in-situ study of KCl particles on a low alloyed steel showed that a KCl particle becomes completely overgrown during 20 minutes of exposure at 400 °C on the low alloyed steel [10]. At 600 °C the stainless steel showed a similar behaviour [8] while only an approximately 100 nm high NiO oxide rim was observed on pure Nickel, see Fig 4. This comparison indicates that the surface transport and formation of crusts around KCl particles is a combination of oxide growth rate (diffusion of metal ions to the surface), vapour pressure of the metal chloride and eutectic temperature of the KCl-metal chloride mixture. The vapour pressure of $FeCl_2$ ($PFeCl_2$=0.001 atm at 600 °C) is higher than that of $NiCl_2$ ($PNiCl_2$=0.00012 atm at 600 °C). The results indicate that the formation of the eutectic on the surface does not strongly influence the growth rate of Nickel at 600 °C under the present conditions.

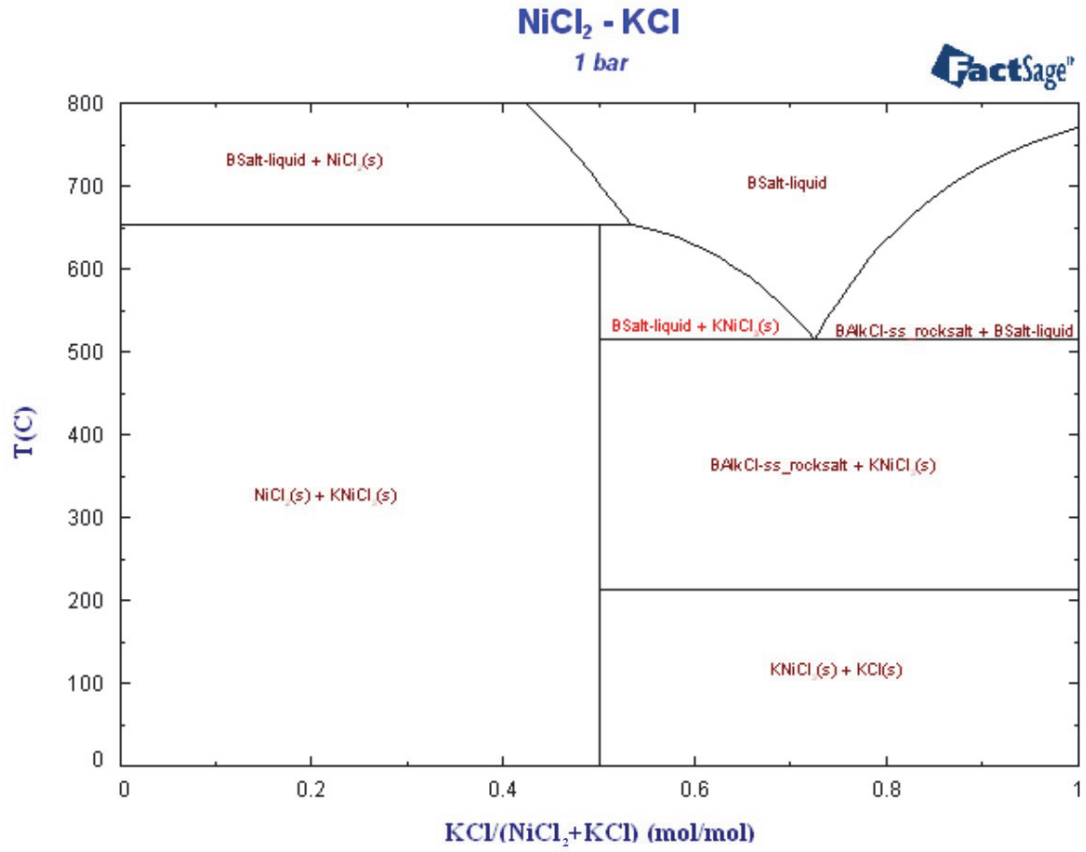

Figure 7: A KCl-NiCl2 phase diagram calculated with FactSage

No indications of the presence of potassium or chloride were found within the oxide scale. However, the oxide scale formed in the presence of KCl contains more pores after 168 hours

exposure, compare Figs. 3 and 6. These results also indicate that the oxide scale formed without KCl has larger grains close to the metal/oxide interface. It has previously been shown that iron oxide (magnetite) has an outward and an inward growing part [11-13]. Adding 100 ppm SO_2 changes the inward flux of oxygen ions and in addition the distribution of pores [11]. The mechanism of pore formation in Nickel oxide has been studied by Akiba et al. [14] using calculations of ion fluxes and their divergence in NiO scales at higher temperature. The annihilation of oxide, and thus void formation, was predicted based on the diffusivity of the ionic species and their potential gradients across the NiO scale, and were found to occur mostly in the vicinity of the metal/oxide interface. This is in good agreement with the pore formation observed on the sample exposed without KCl, see Fig. 3. Adding KCl indicates a change in the scale microstructure, i.e. forming a less defined inner layer, and with pore formation both at the metal/oxide interface and the interface between the columnar grained inwards growing oxide and the finer grained outwards growing oxide, which indicates a possible change in ion flux through the scale that could explain the different pore distributions. However, in order to better understand the mechanisms behind pore formation in the presence of small amounts of KCl, more time resolved information about the pore size and distribution is needed.

Conclusions

- 99.99% pure Nickel exposed at 600 °C in an environment containing 5% O_2, 40% H_2O and 55% N_2 (vol.%) shows an approximately parabolic oxide (NiO) growth rate. The oxide scale is dense with some pores at the oxide metal/interface.
- Adding small amounts of KCl does not result in a faster corrosion rate of Nickel. However, the surface morphology changes and a small oxide crust was observed in the vicinity of former KCl particles. This is proposed to be the result of a $NiCl_2$-KCl eutectic formed at 514 °C. The oxide scale formed in the presence of KCl contains more and differently distributed voids.

Acknowledgements

The project has been performed within the framework the fifth stage of the material technology research programme (KME, in kind contribution from Dong Energy A/S). The work is in addition a part of the Danish Strategic research center Power Generation from REnewable Energy (GREEN) and funded by the Danish Council for Strategic Research, grant no. 10-093956 and the Swedish High Temperature Corrosion centre (HTC).

References

1. Lee, Y.Y. and M.J. McNallan, *Ignition of Nickel in Environments Containing Oxygen and Chlorine.* Metallurgical Transactions a-Physical Metallurgy and Materials Science, 1987. **18**(6): p. 1099-1107.
2. Ihara, Y., et al., *The corrosion behaviour of nickel in hydrogen chloride gas and gas mixtures of hydrogen chloride and oxygen at high temperatures.* Corrosion Science, 1982. **22**(10): p. 901-912.

3. Li, Y.S. and M. Spiegel, *Internal oxidation of Fe-Al alloys in a KCl-air atmosphere at 650° C.* Oxidation of Metals, 2004. **61**(3-4): p. 303-322.
4. Li, Y.S., Y. Niu, and M. Spiegel, *High temperature interaction of Al/Si-modified Fe–Cr alloys with KCl.* Corrosion Science, 2007. **49**(4): p. 1799-1815.
5. Cha, S.C. and M. Spiegel, *Local reactions of KCl particles with iron, nickel and chromium surfaces.* Materials and Corrosion-Werkstoffe Und Korrosion, 2006. **57**(2): p. 159-164.
6. Cha S. C. , M.S., *Local reactions of KCl particles with iron, nickel and chromium surfaces.* Materials and Corrosion, 2006. **57**(2): p. 159-164.
7. Shinata, Y., *Accelerated Oxidation Rate of Chromium Induced by Sodium Chloride.* Oxidation of Metals, 1987. **27**: p. 315-332.
8. Jonsson, T., et al., *The influence of KCl on the corrosion of an austenitic stainless steel (304L) in oxidizing humid conditions at 600 ºC: A microstructural study.* Oxidation of Metals, 2009. **72**(3): p. 213-239.
9. Proff, C., et al., *Microstructural investigation of the KCl-induced Corrosion of the Austenitic alloy Sanicro 28 (35Fe27Cr31Ni) at 600°C.* Materials at High Temperature, 2009. **26**(2): p. 113-125.
10. Jonsson, T., et al., *An ESEM in situ investigation of initial stages of the KCl induced high temperature corrosion of a Fe-2.25Cr-1Mo steel at 400 °C.* Corrosion Science, 2011. **53**(6): p. 2233-2246.
11. Jonsson, T., et al., *The effect of traces of SO_2 on iron oxidation: A microstructural study.* Oxidation of Metals, 2007. **67**(3-4): p. 193-213.
12. Jonsson, T., et al., *An ESEM in situ investigation of the influence of H2O on iron oxidation at 500 degrees C.* Corrosion Science, 2009. **51**(9): p. 1914-1924.
13. Chen, R.Y. and W.Y.D. Yuen, *Review of the High-Temperature Oxidation of Iron and Carbon Steels in Air or Oxygen.* Oxidation of Metals, 2003. **59**: p. 433-468.
14. Akiba, K., et al., *Quantitative prediction of voids formation in a growing nickel oxide scale at 1373 K.* Materials Transactions, 2007. **48**(10): p. 2753-2761.

Appendices

Appendix I: *Chemical composition of the alloys (wt.%) mentioned in Chapter 2.*

Alloy	Fe	Cr	Ni	Mn	Si	Ti	Al	Mo	Cu	Co	C	N	other
AISI 310	bal.	25	19	1.5	0.5			0.3	0.2	0.1			
600	8.3	16.0	bal.										
625	2.5	21.5	bal.					9					3.7Nb
800	bal.	20.3	30.3										
214	2.5	16	bal.				4.5						0.01Y
602CA	9	25	bal.	0.1	0.05		2.08	0.04			0.172		Zr, 0.08Y
45TM	21.87	27.9	46.8	0.4	2.78		0.15				0.084		
HR160	0.2	27.9	37.6	0.46	2.70	0.46	0.15			30.7	0.05		
800H	bal.	20.55	30.65	0.7	0.4	0.35	0.3				0.069		
AISI 304L	bal.	18.5	10.2	1.41	0.55			0.49			0.027	0.075	
Sanicro 28	34.8	27	31	2	0.7			3.5					
P91		9.0	0.36	0.55	0.4		0.006	0.93					
153MA	bal.	18.5	9.5		1.3						0.05	0.15	
HK40	bal.	25	20										
X20CrMoV121	bal.	12	0.5	<1	<0.5			1			0.2		0.5V
AISI 430	bal.	16.37	0.14	0.6	0.22						0.04		0.027P, 0.006S
TP347	bal.	18	12	2	<0.75						0.07		<1.2Nb+Ta
825	30.7	22.4	bal.					3.2					1.9Cu
10CrMo910	bal.	2.49		0.55	0.11		0.007	0.99			0.1		
T22	bal.	2.19		0.43	0.26			0.93			0.095		0.014P, 0.01S
59	0.97	22.6	bal.	0.14	0.04		0.26	15.35			0.005		
Sandvik8LR30		18.0	10.5	1.0	0.5						0.04		Ti

Appendix 2:

This appendix provides complementary information regarding the investigations reported in the paper 1. This includes X-Ray Diffractograms, Scanning Electron Micrographs and Energy Dispersive X-Ray Spectroscopy (EDS) analysis performed on each oxide+KCl sample. Black diffractogram represents the unexposed sample and the green diffractogram represents the exposed one. Results of EDS analysis are all in atomic %.

Al_2O_3+KCl

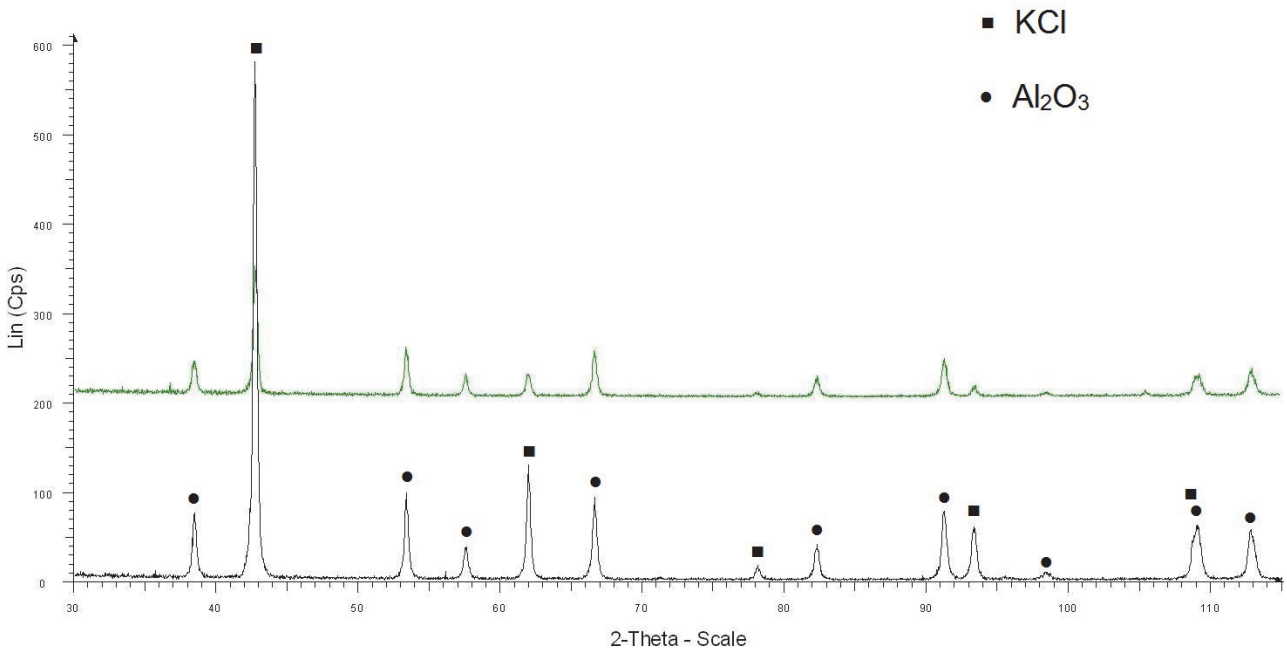

X-Ray diffractogram corresponding to the Al_2O_3+KCl sample.

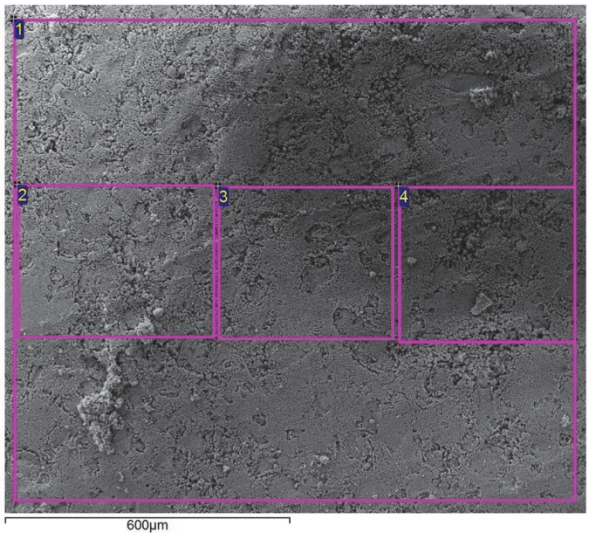

spot	Al	O	K	Cl	Si
1	32.48	63.61	1.87	1.41	0.63
2	32.64	63.87	1.54	1.43	0.52
3	32.25	64.09	1.74	1.33	0.60
4	32.54	64.47	1.61	1.38	

spot	Al	O	K	Cl	Si
1	40.40	59.60			
2	3.95	40.89	25.99	29.17	
3	32.34	62.69	2.95	2.02	

CeO_2+KCl

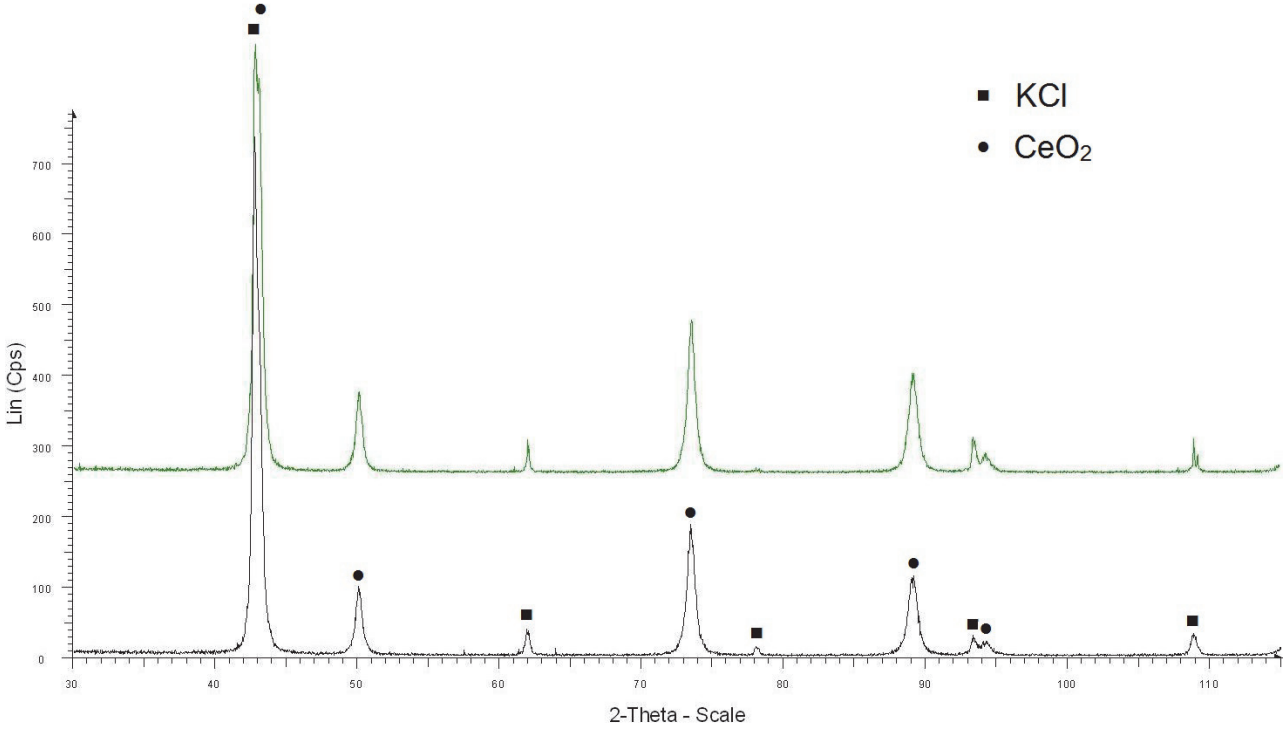

X-Ray diffractogram corresponding to the CeO_2+KCl sample.

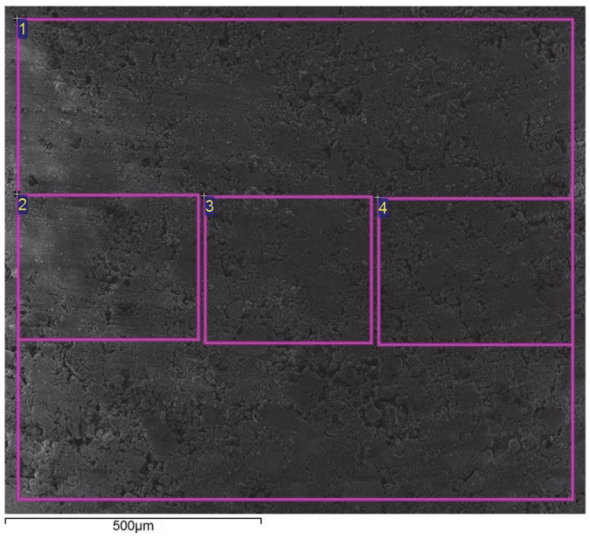

spot	Ce	O	K	Cl	Si
1	36.51	49.11	7.27	7.11	
2	36.00	50.08	6.24	6.21	1.47
3	35.14	51.42	5.99	5.92	1.53
4	34.51	51.20	5.77	6.94	1.58

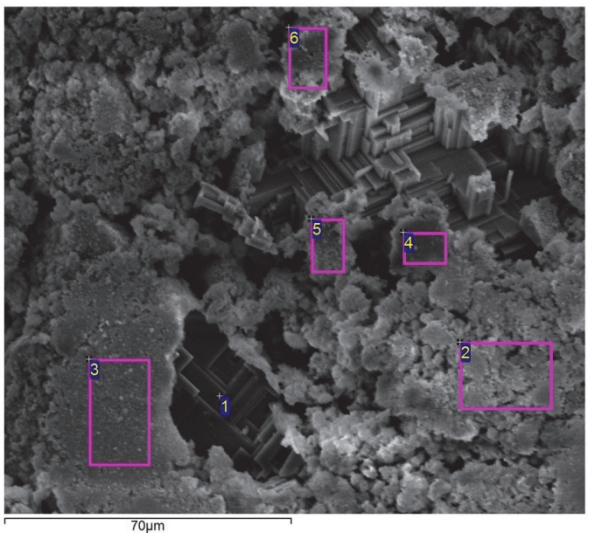

spot	Ce	O	K	Cl	Si
1	1.87	11.94	45.30	40.89	
2	47.44	48.99	2.05	1.53	
3	47.26	48.86	2.38	1.51	
4	3.92	23.89	35.22	36.97	
5	6.72	23.11	34.58	35.59	
6	4.70	26.45	33.08	35.77	

Co_3O_4+KCl

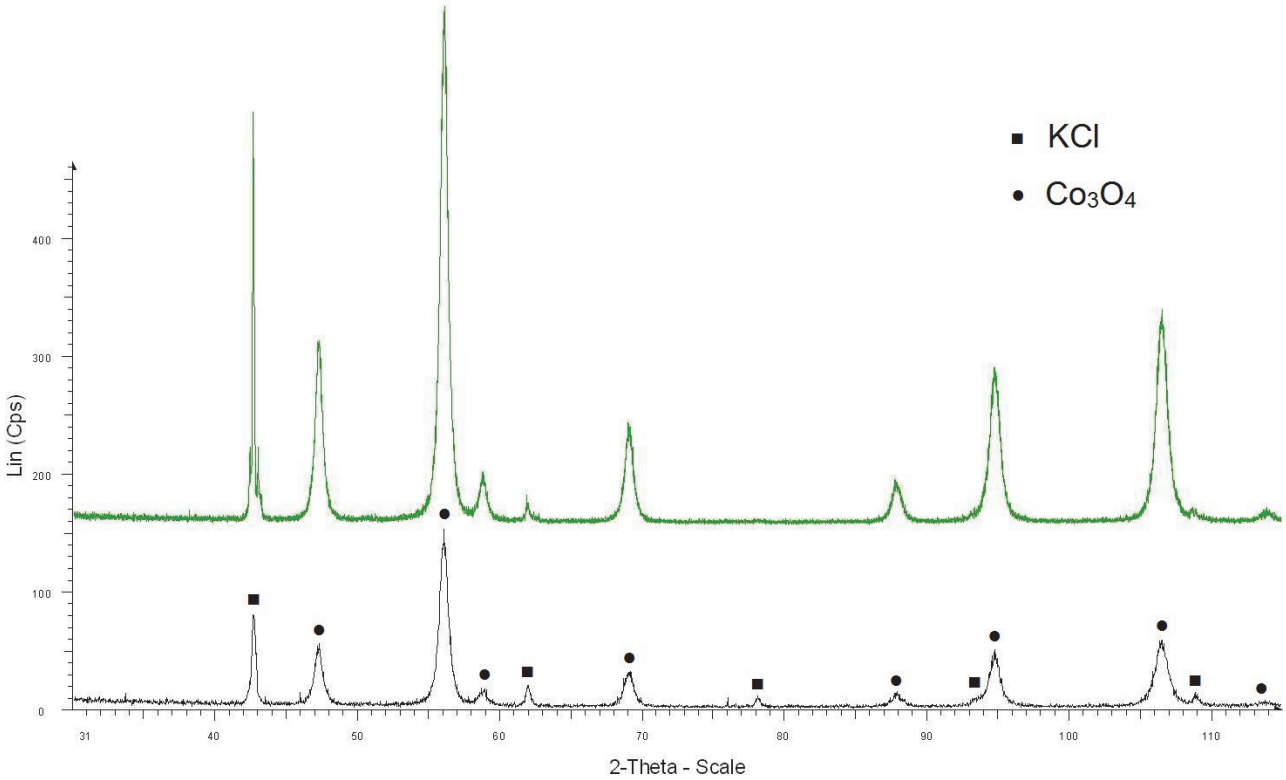

X-Ray diffractogram corresponding to the Co_3O_4+KCl sample.

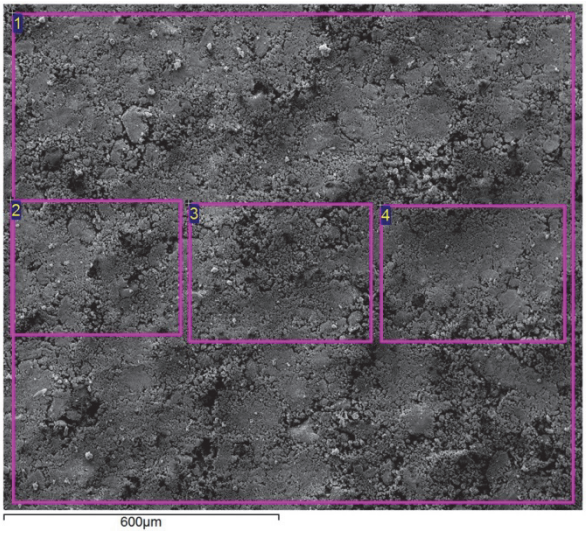

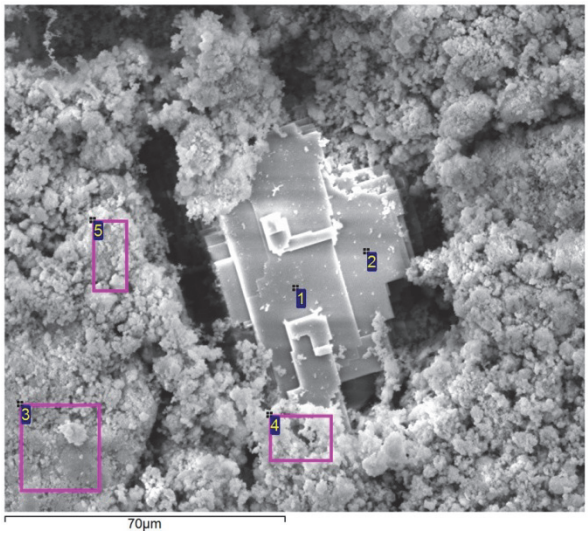

spot	Co	O	K	Cl	Si
1	55.49	38.42	1.97	1.31	2.81
2	56.52	38.36	1.62	0.86	2.64
3	53.64	39.52	2.25	1.78	2.80
4	55.78	38.48	1.62	0.87	3.25

spot	Co	O	K	Cl	Si
1	2.25	6.69	45.53	45.53	
2	3.84	6.15	45.40	44.61	
3	53.77	40.77	1.43	0.34	3.69
4	29.18	49.46	8.11	11.02	2.23
5	50.77	43.11	1.80	0.61	3.71

Cr_2O_3+KCl

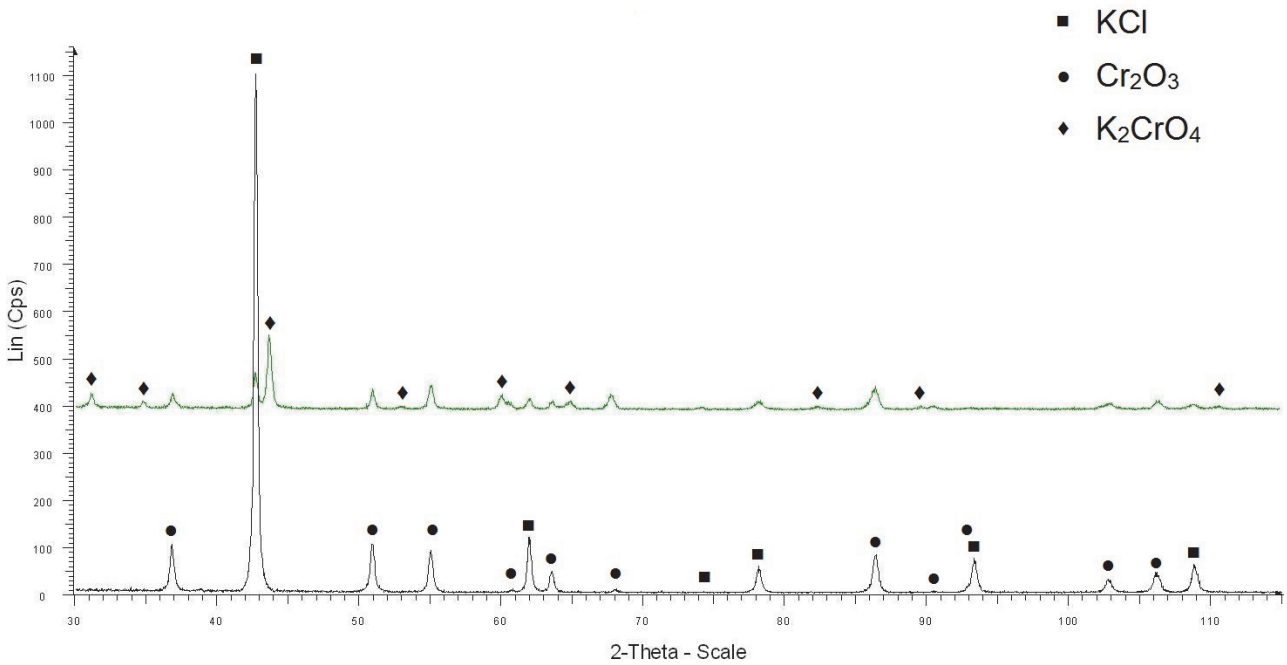

X-Ray diffractogram corresponding to the Cr_2O_3+KCl sample.

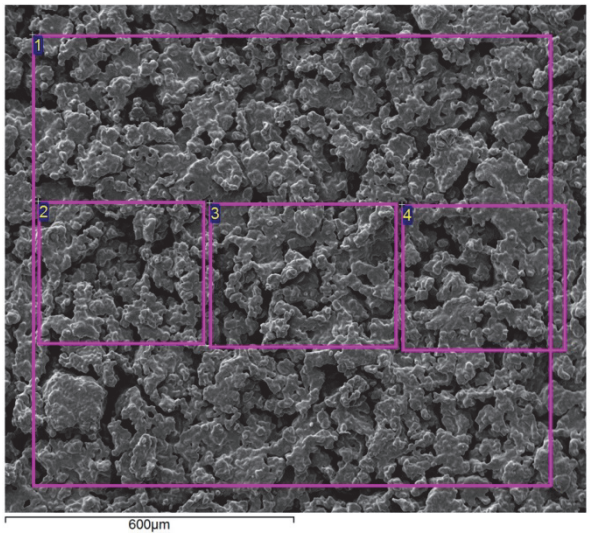

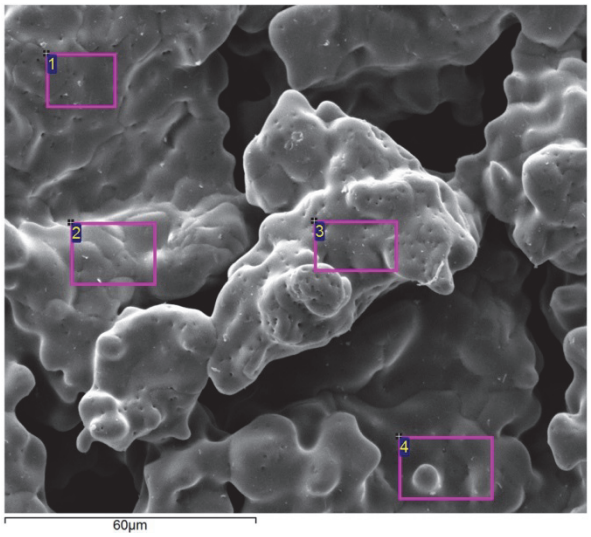

spot	Cr	O	K	Cl	Si
1	21.58	43.12	21.58	1.12	
2	21.65	43.81	21.65	1.37	
3	21.26	43.32	21.26	1.37	
4	21.72	42.54	21.72	1.41	

spot	Cr	O	K	Cl	Si
1	24.95	34.37	39.56	1.12	
2	16.34	54.06	28.20	1.39	
3	22.69	38.63	36.71	1.97	
4	21.63	45.78	32.10	0.48	

Fe_2O_3+KCl

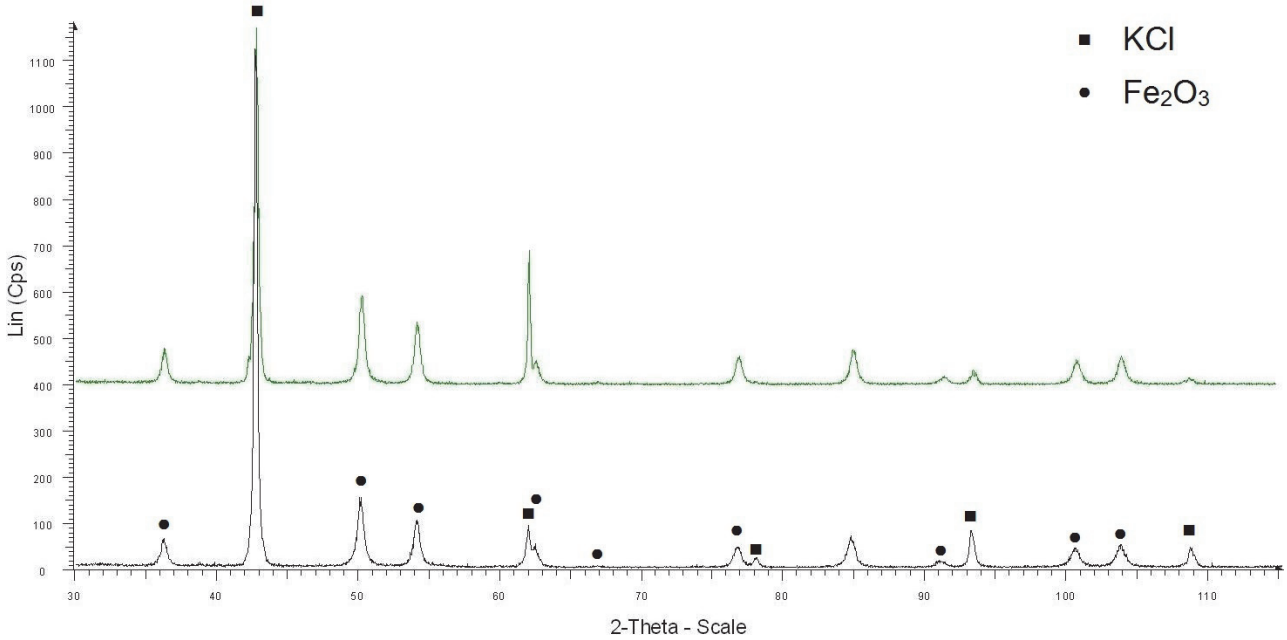

X-Ray diffractogram corresponding to the Fe_2O_3+KCl sample.

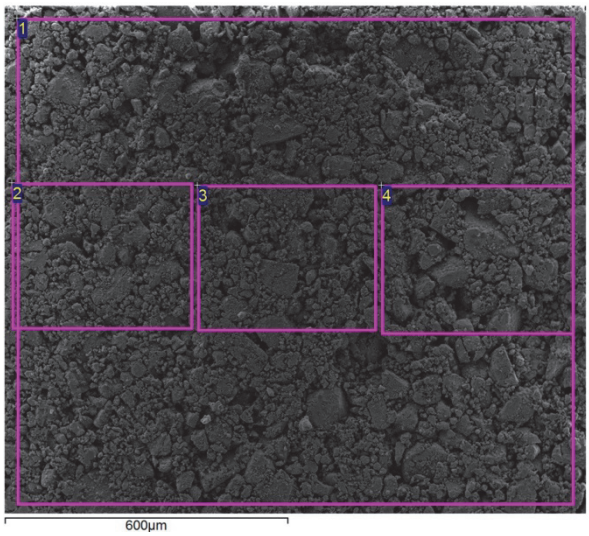

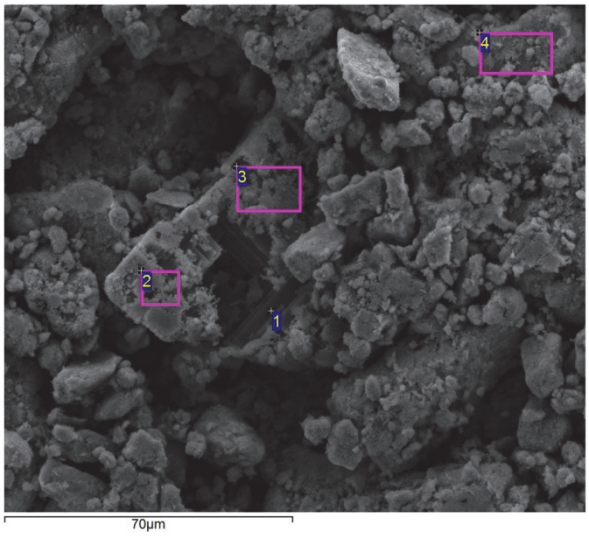

spot	Fe	O	K	Cl	Si
1	38.00	43.68	9.04	7.50	1.78
2	39.09	43.28	8.55	6.74	2.34
3	36.40	42.86	10.10	8.64	2.00
4	38.19	42.19	9.55	8.14	1.91

spot	Fe	O	K	Cl	Si
1	3.44	11.84	48.81	35.91	
2	3.31	22.29	36.83	36.88	0.69
3	12.24	38.93	25.37	22.01	1.44
4	14.60	43.70	20.21	20.02	1.47

HfO_2+KCl

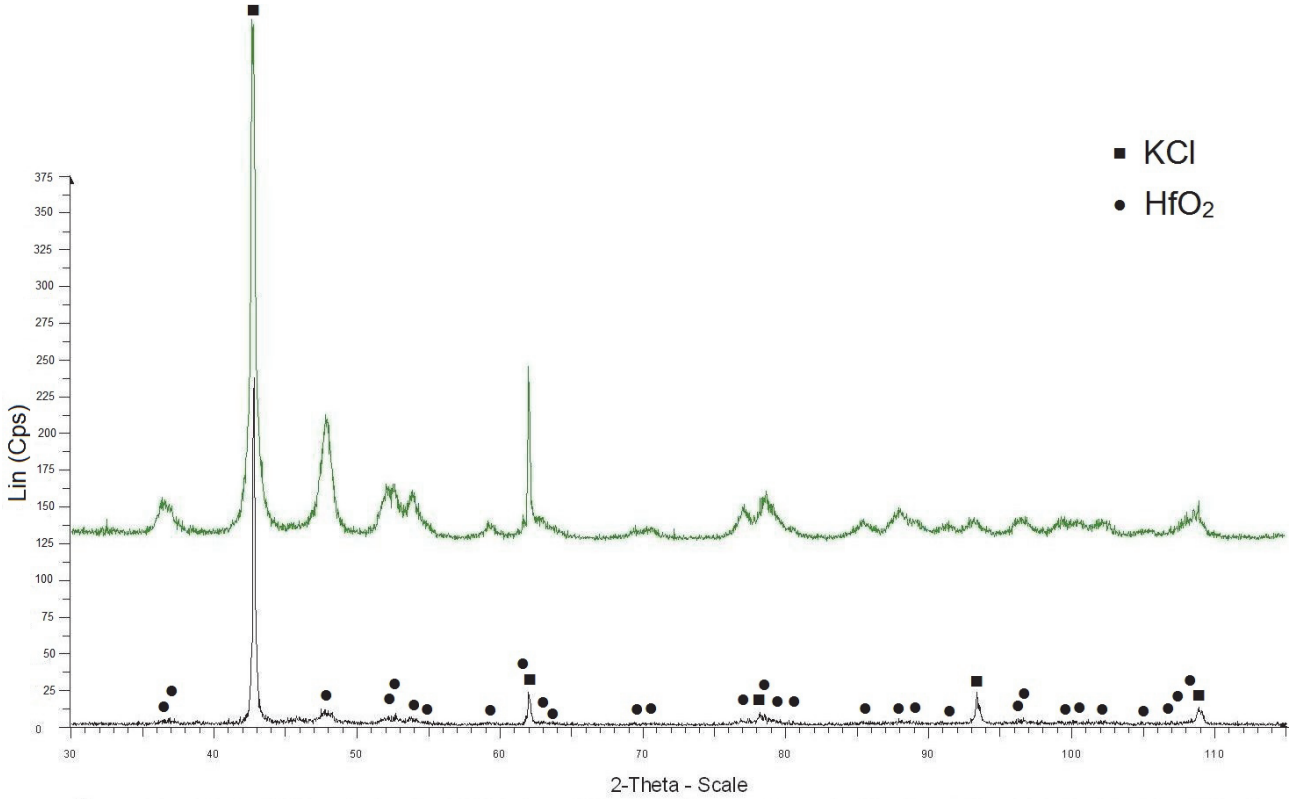

X-Ray diffractogram corresponding to the HfO_2+KCl sample.

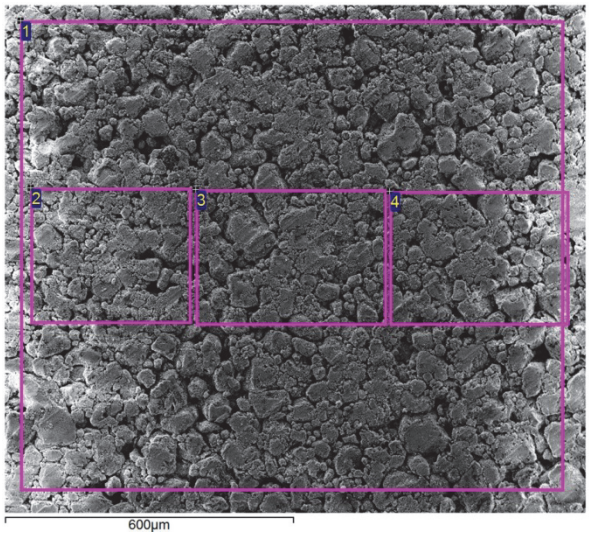

spot	Hf	O	K	Cl	Si
1	31.13	48.10	9.94	10.84	
2	30.06	50.09	9.01	10.84	
3	30.37	50.85	9.27	9.51	
4	30.06	49.18	9.39	11.37	

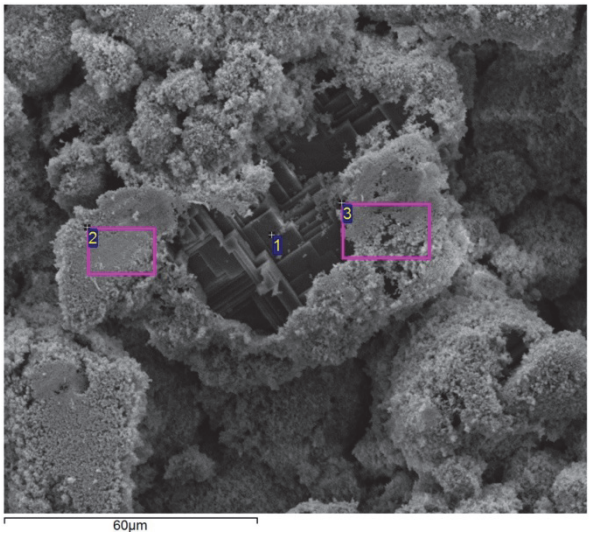

spot	Hf	O	K	Cl	Si
1	1.35	4.95	45.94	47.76	
2	38.80	52.91	3.81	4.48	
3	19.76	39.25	19.12	21.87	

Mn_3O_4+KCl

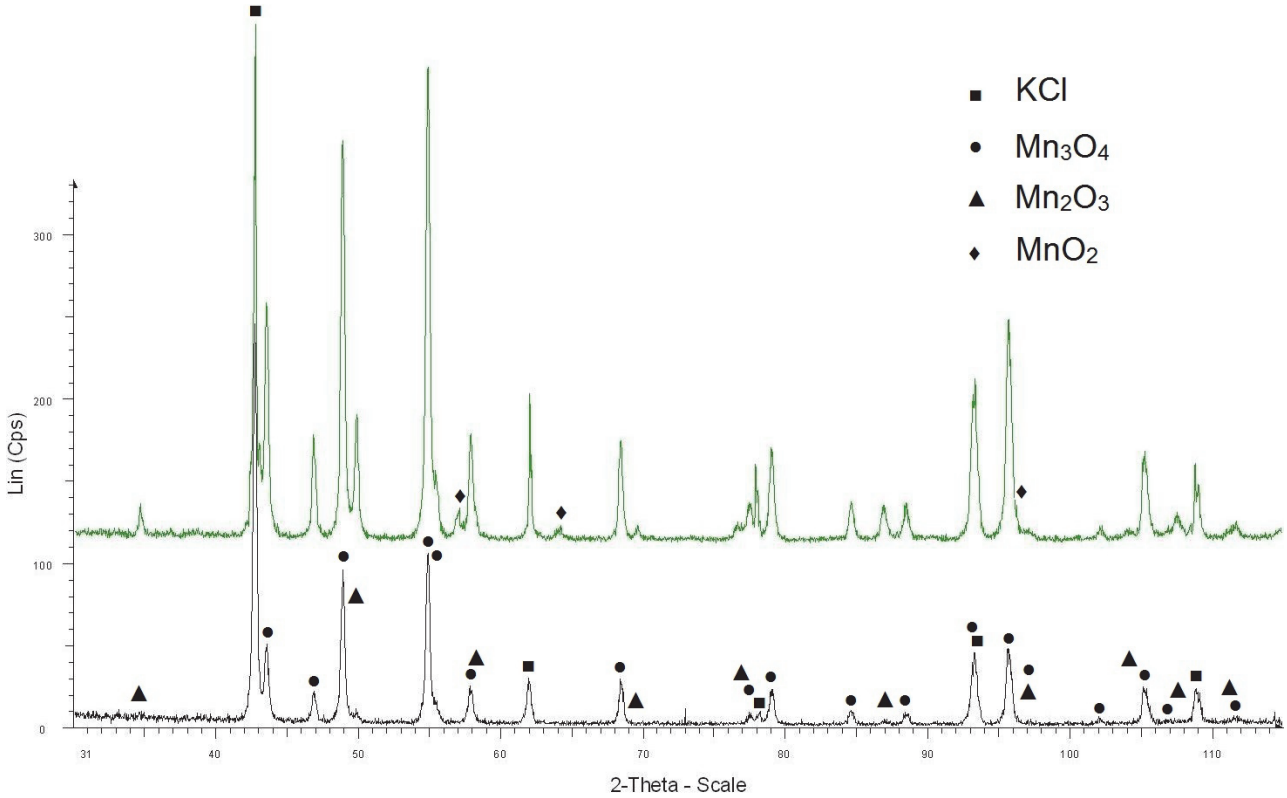

X-Ray diffractogram corresponding to the Mn_3O_4+KCl sample.

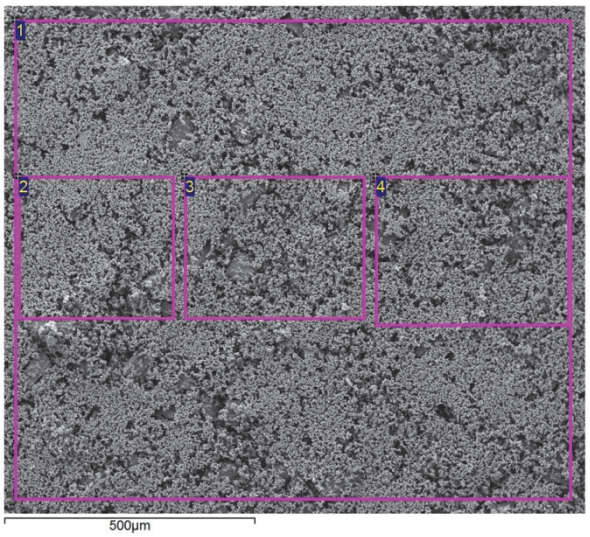

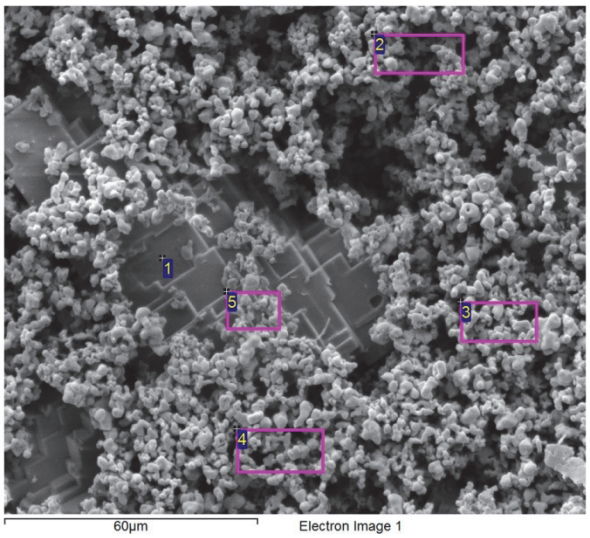

spot	Mn	O	K	Cl	Si
1	59.80	26.19	6.23	4.97	2.81
2	59.97	27.05	5.84	4.16	2.98
3	58.68	26.20	6.75	5.43	2.94
4	58.09	26.52	7.02	5.68	2.68

spot	Mn	O	K	Cl	Si
1	10.63	13.43	37.76	38.18	
2	61.19	21.45	8.03	4.38	4.96
3	66.50	24.81	2.41	0.68	5.61
4	63.91	25.89	4.27	2.05	3.88
5	28.49	27.04	20.13	20.13	4.22

NiO+KCl

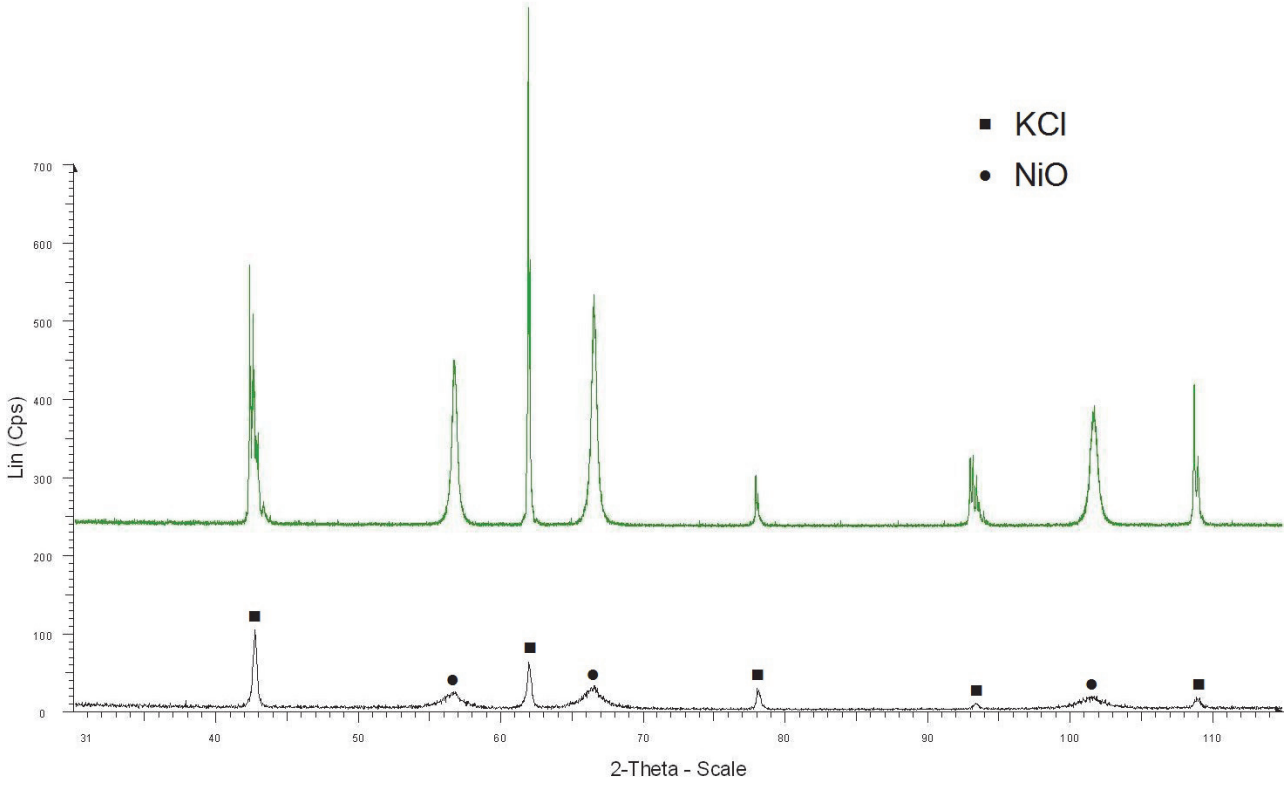

X-Ray diffractogram corresponding to the NiO+KCl sample.

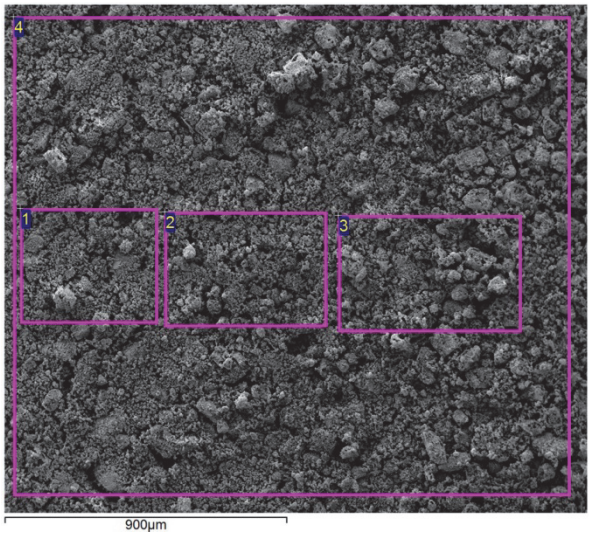

spot	Ni	O	K	Cl	Si
1	53.16	28.92	7.85	7.64	2.42
2	53.85	27.55	8.04	7.86	2.69
3	55.15	28.10	7.68	6.80	2.27
4	53.17	28.40	8.40	7.75	2.27

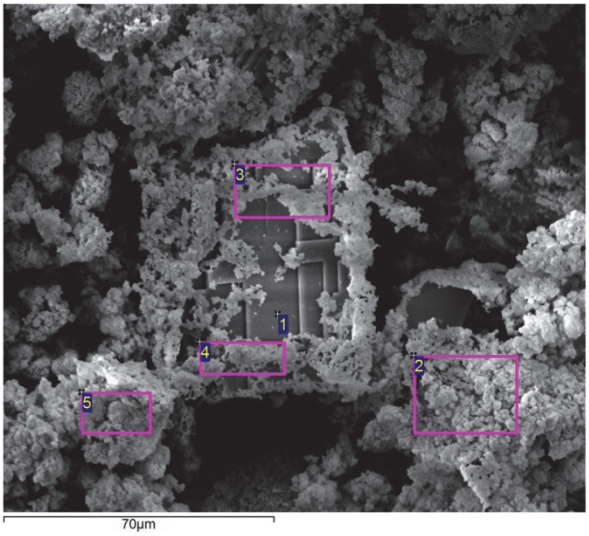

spot	Ni	O	K	Cl	Si
1	6.00	15.99	40.43	37.58	
2	42.00	35.45	9.66	7.36	5.52
3	14.00	34.57	24.33	24.44	2.67
4	19.53	37.10	19.96	20.05	3.36
5	52.30	33.43	5.15	1.06	8.07

SiO_2+KCl

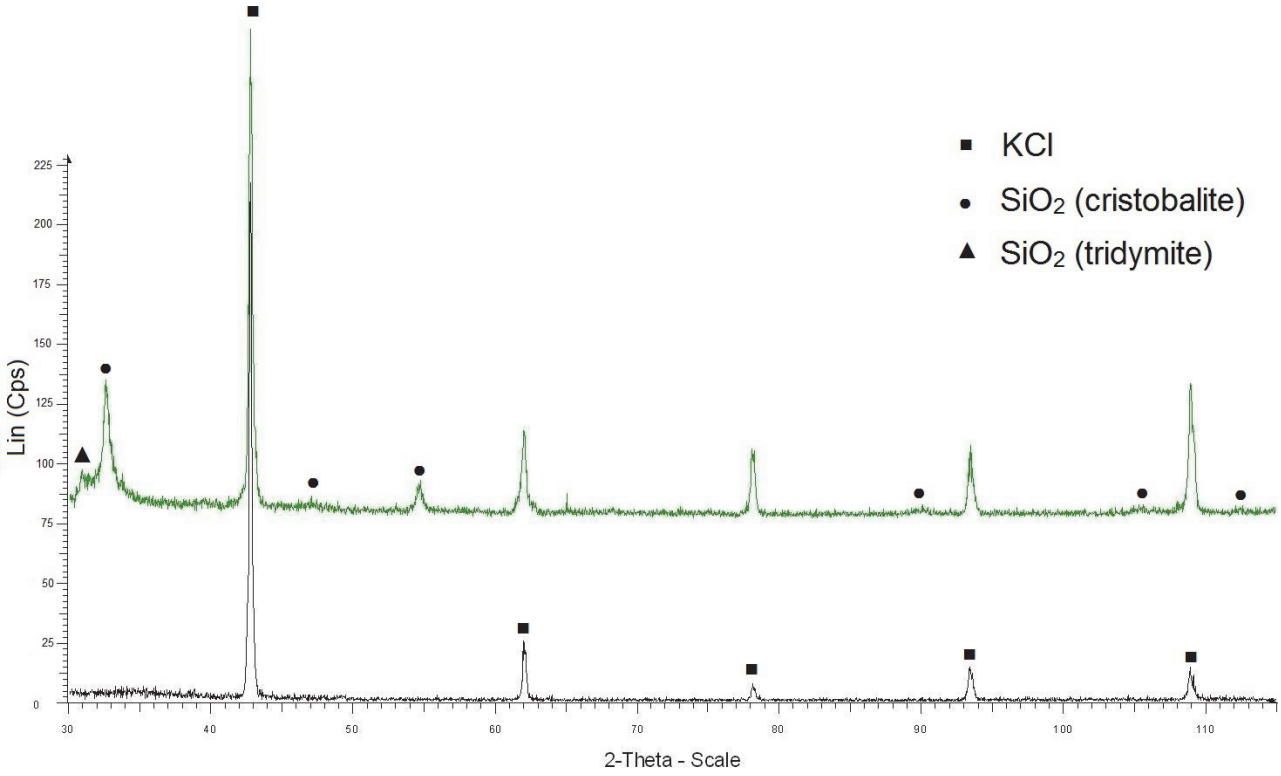

X-Ray diffractogram corresponding to the SiO_2+KCl sample.

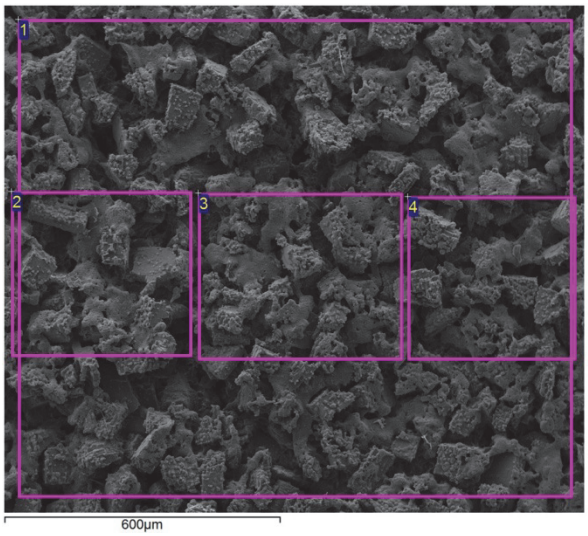

spot	Si	O	K	Cl
1	23.89	52.05	11.70	12.36
2	22.19	51.33	12.85	13.63
3	27.58	52.72	9.68	10.02
4	23.57	49.35	13.10	13.98

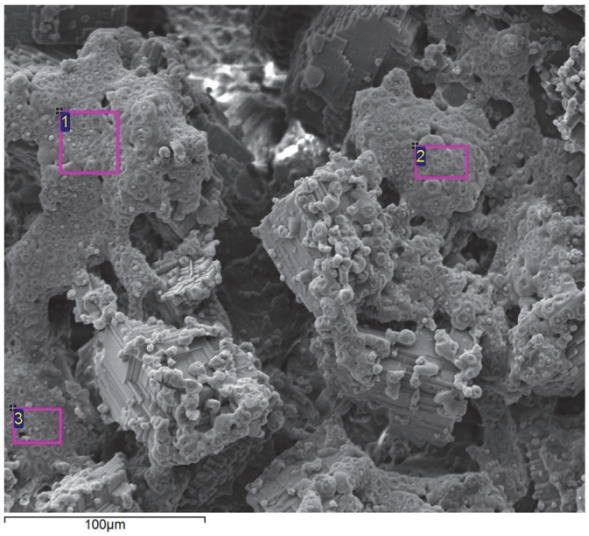

spot	Si	O	K	Cl
1	48.15	46.93	4.22	0.70
2	43.57	54.40	1.57	0.47
3	38.67	57.99	2.32	1.01

SiO_2+KCl (SEM image at higher magnification)

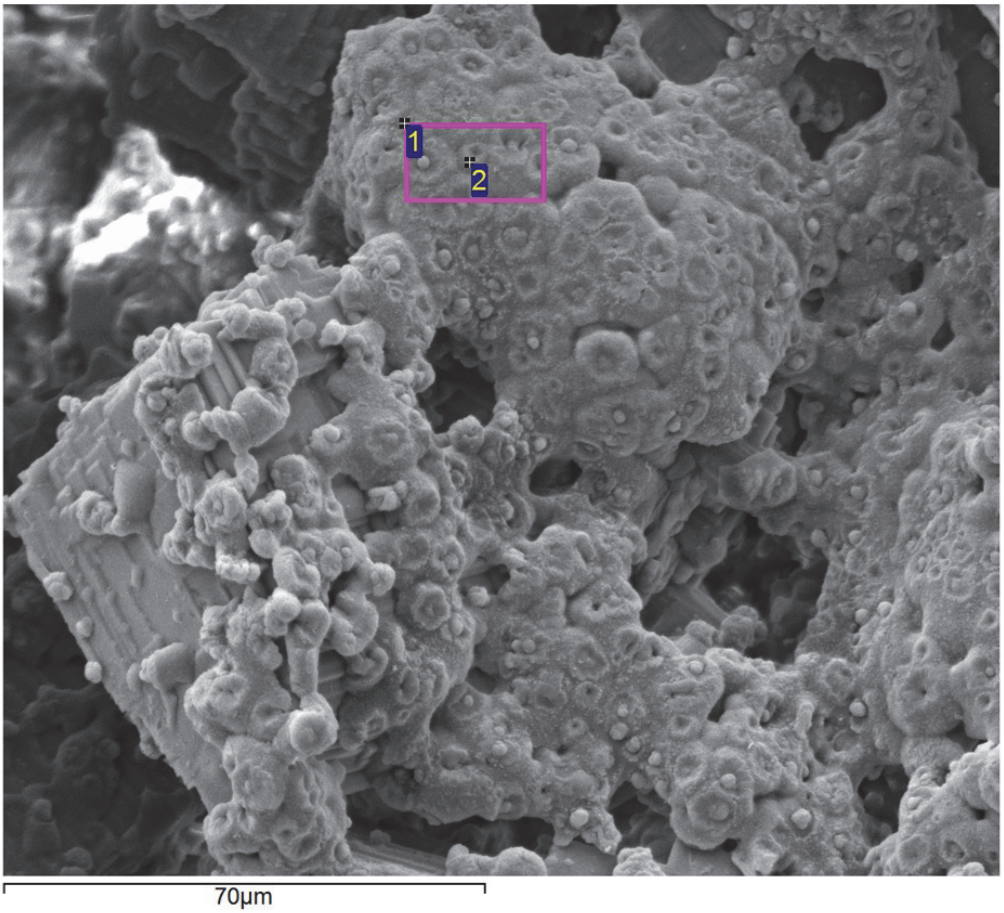

spot	Si	O	K	Cl
1	53.83	43.69	0.57	1.91
2	56.59	41.24	0.65	1.52

Ta_2O_5+KCl

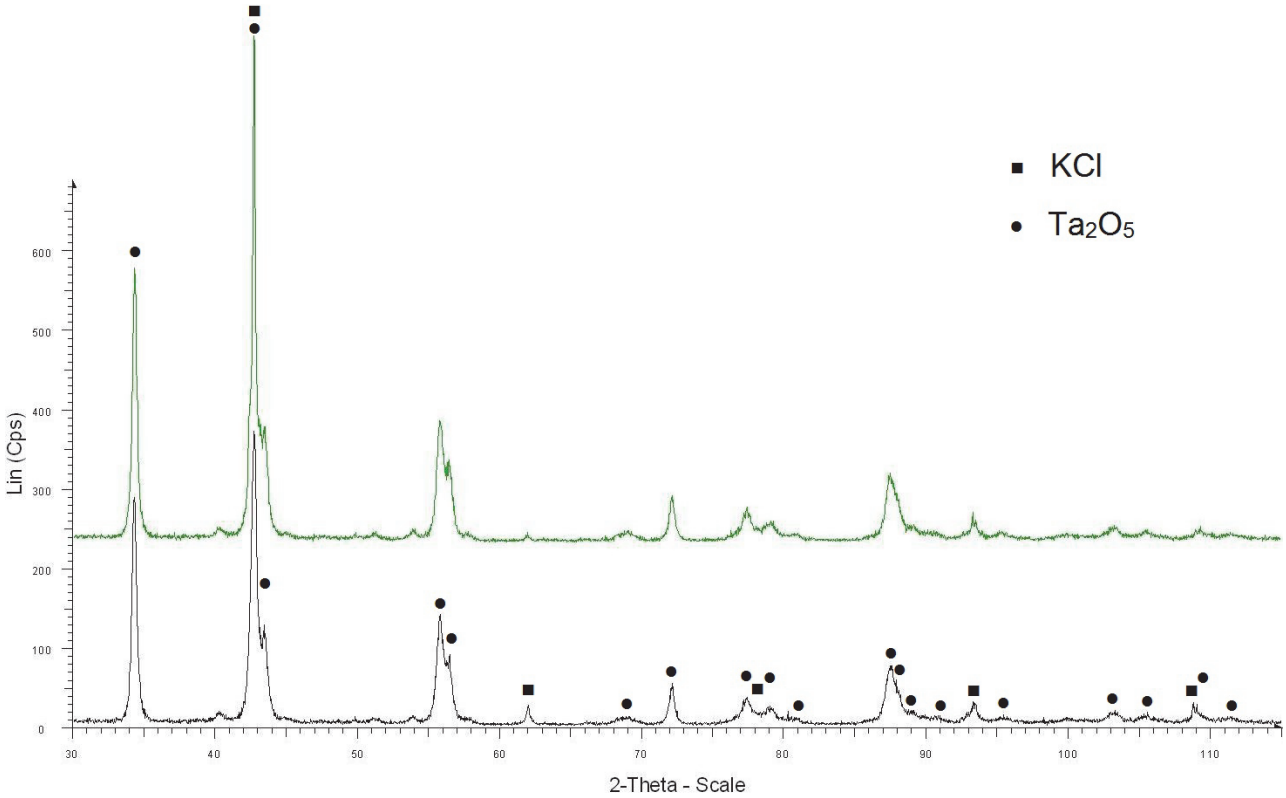

X-Ray diffractogram corresponding to the Ta_2O_5+KCl sample.

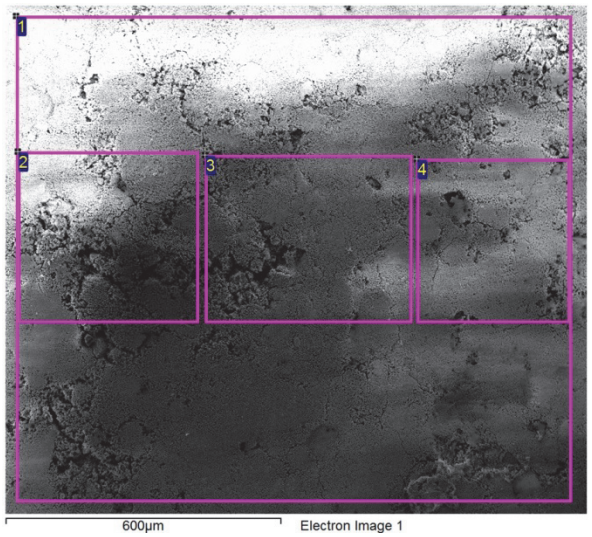

spot	Ta	O	K	Cl	Si
1	36.89	53.59	4.10	5.42	
2	35.27	52.54	5.61	6.58	
3	37.57	54.76	4.04	3.62	
4	39.22	55.94	2.24	2.59	

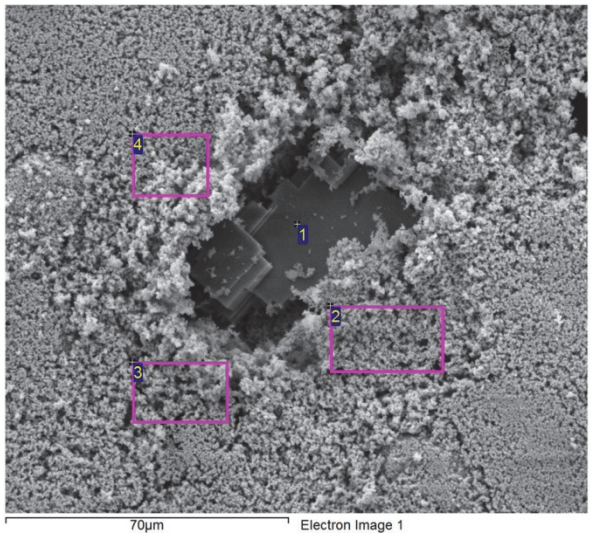

spot	Ta	O	K	Cl	Si
1	3.54	17.07	39.99	39.40	
2	38.78	59.93	0.69	0.60	
3	40.63	55.05	1.92	2.39	
4	39.97	58.12	1.37	0.55	

TiO_2(anatase)+KCl

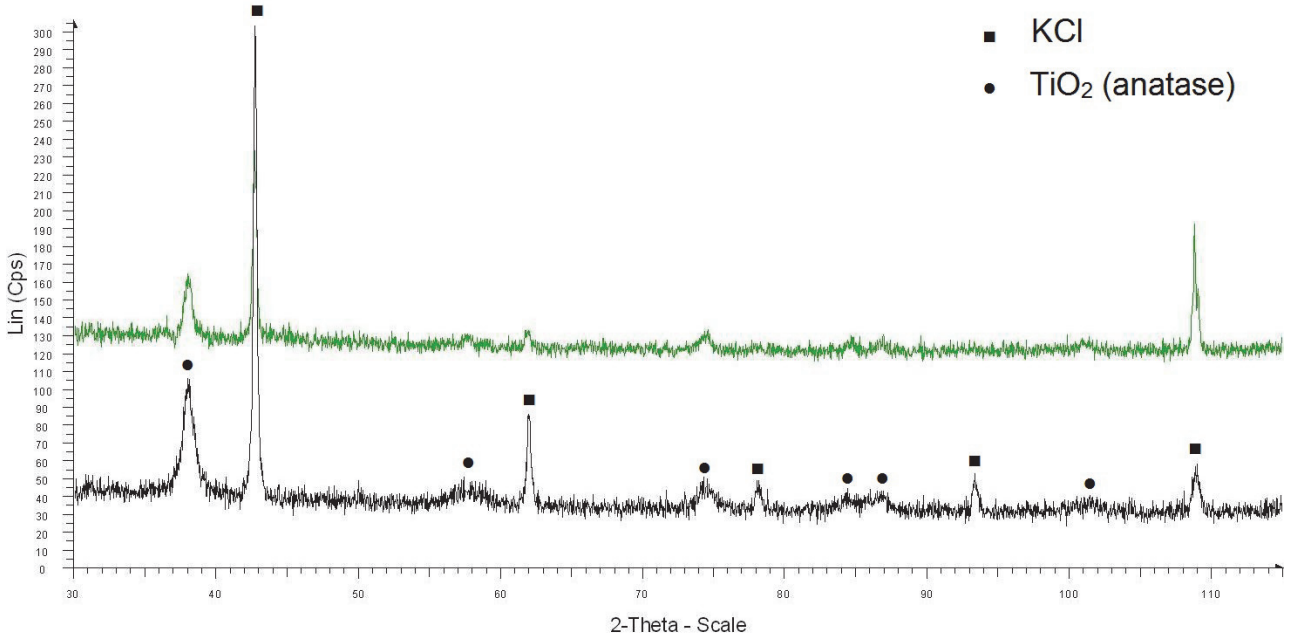

X-Ray diffractogram corresponding to the TiO_2(anatase)+KCl sample.

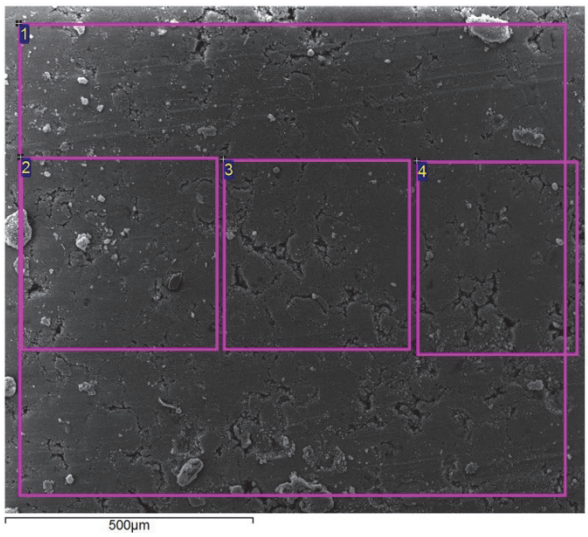

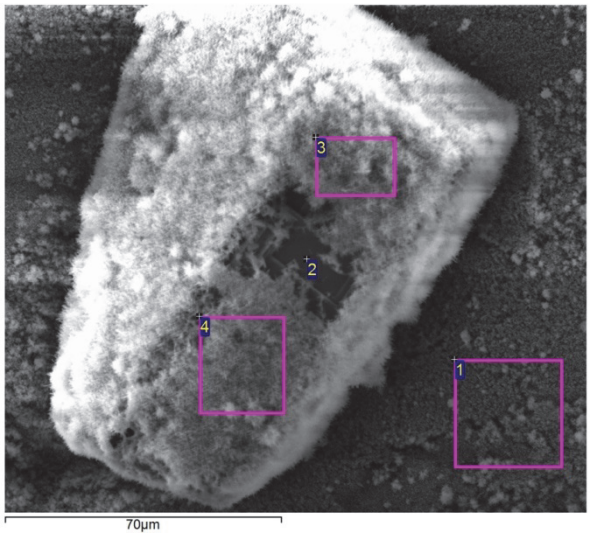

spot	Ti	O	K	Cl	Si
1	30.45	57.08	7.65	3.24	1.58
2	30.07	56.73	8.32	3.41	1.47
3	30.39	56.44	8.00	3.52	1.66
4	30.35	56.68	8.02	3.70	1.25

spot	Ti	O	K	Cl	Si
1	29.24	64.96	3.96	0.83	1.00
2	2.05	13.98	42.31	40.78	0.88
3	21.48	64.85	8.53	1.47	3.66
4	17.06	45.83	18.30	14.95	3.86

TiO_2(rutile)+KCl

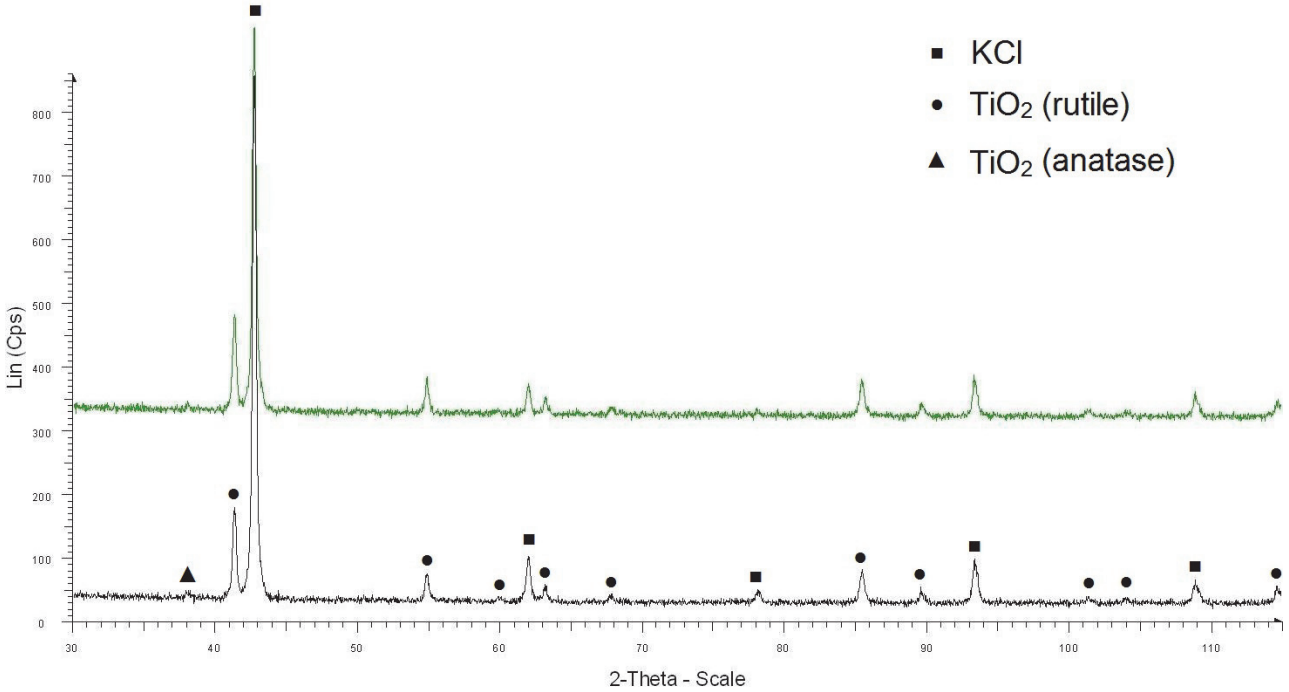

X-Ray diffractogram corresponding to the TiO_2(rutile)+KCl sample.

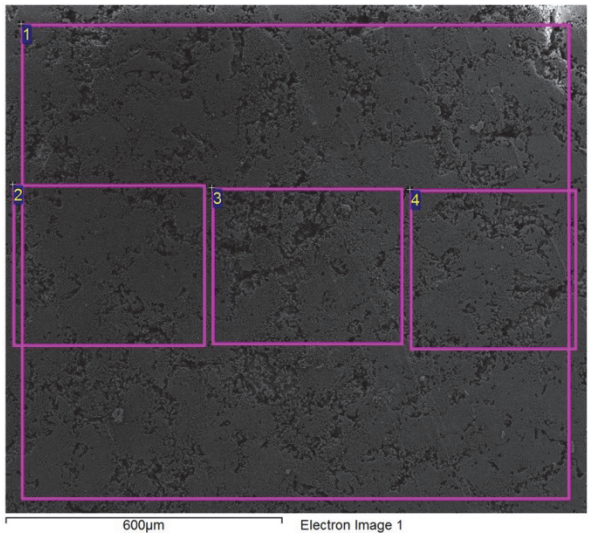

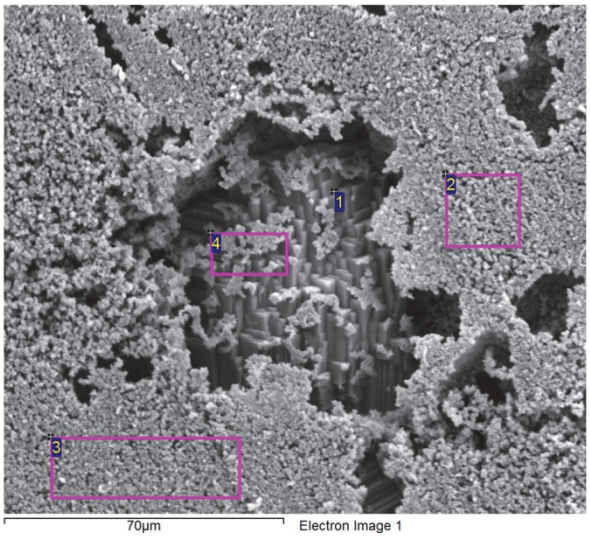

spot	Ti	O	K	Cl	Si
1	28.32	55.65	7.75	7.49	0.79
2	29.24	57.08	6.69	6.36	0.63
3	26.82	54.36	9.06	9.25	0.51
4	28.40	54.35	8.45	8.00	0.79

spot	Ti	O	K	Cl	Si
1	5.83	3.69	54.75	35.38	0.35
2	34.74	58.84	3.84	0.43	2.15
3	35.42	57.50	4.22	0.77	2.09
4	12.95	36.62	24.01	24.31	2.11

Y_2O_3+KCl

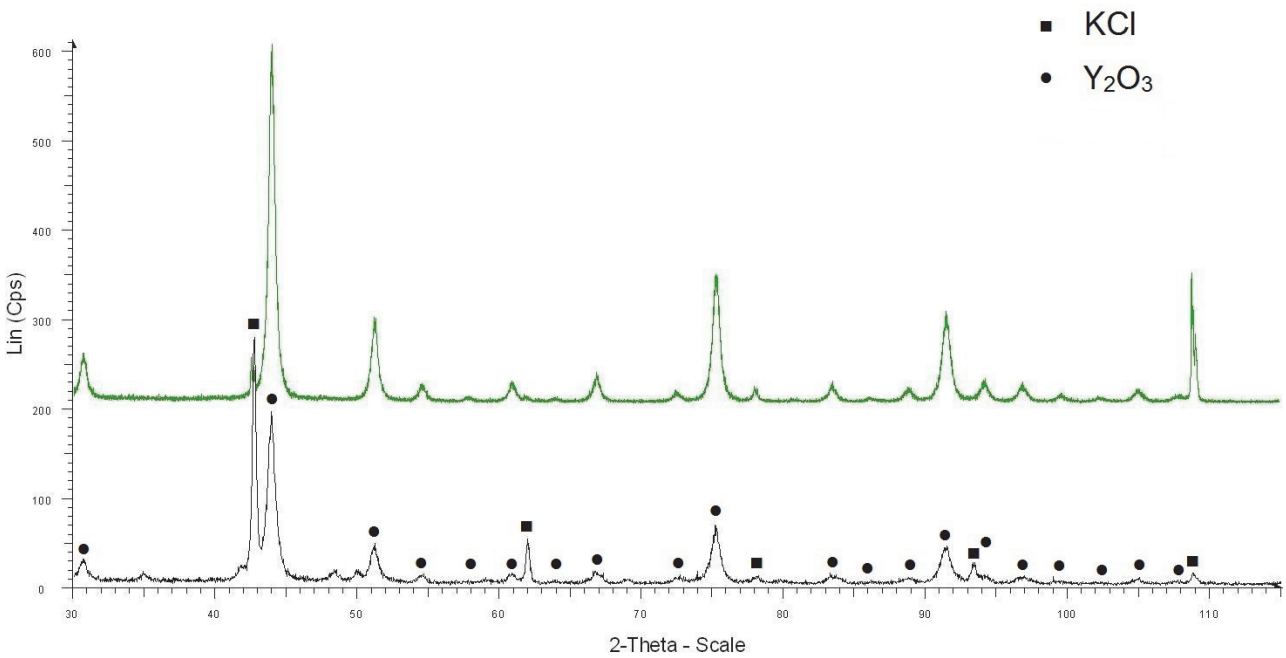

X-Ray diffractogram corresponding to the Y_2O_3+KCl sample.

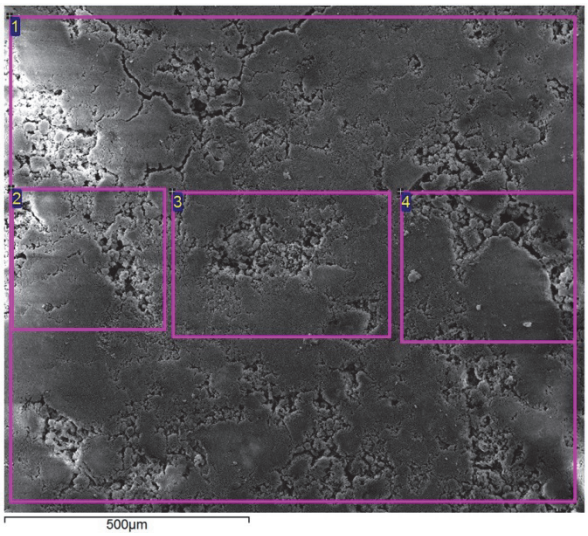

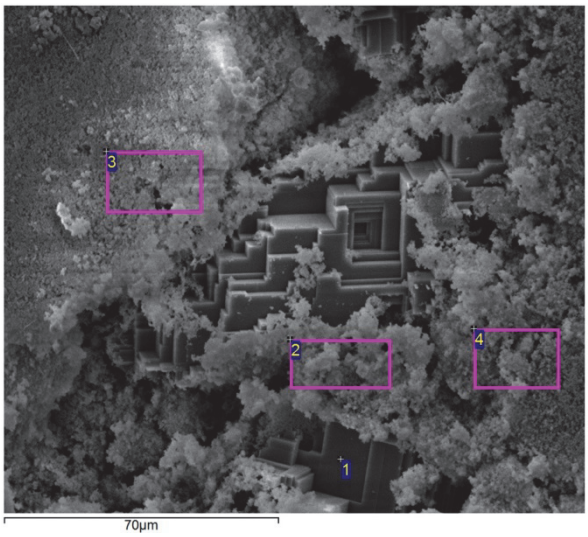

spot	Y	O	K	Cl	Si
1	43.07	46.85	4.74	5.34	
2	40.34	47.21	5.51	6.94	
3	41.13	48.09	4.96	5.82	
4	43.90	48.79	3.20	4.11	

spot	Y	O	K	Cl	Si
1	9.87	28.32	29.16	32.64	
2	31.71	54.31	4.17	5.49	4.32
3	48.50	46.33	2.28	2.89	
4	43.87	53.00	1.53	1.60	

ZrO_2+KCl

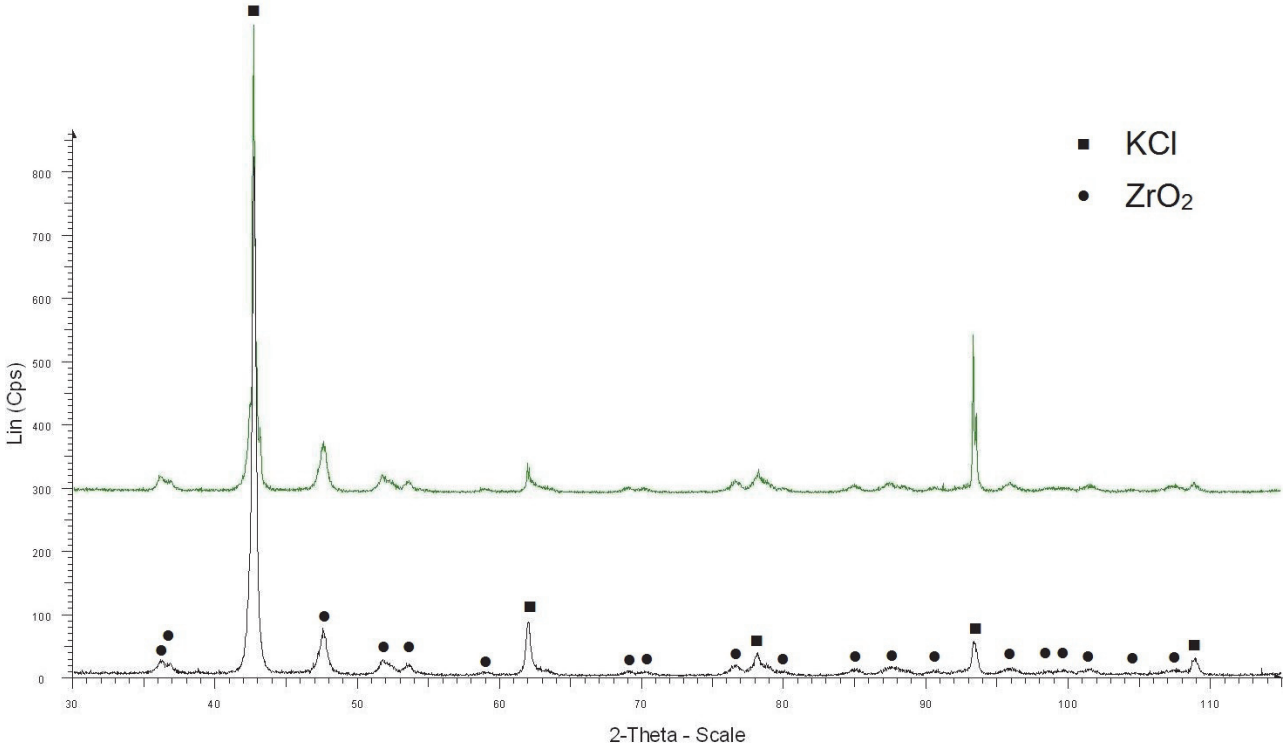

X-Ray diffractogram corresponding to the ZrO_2+KCl sample.

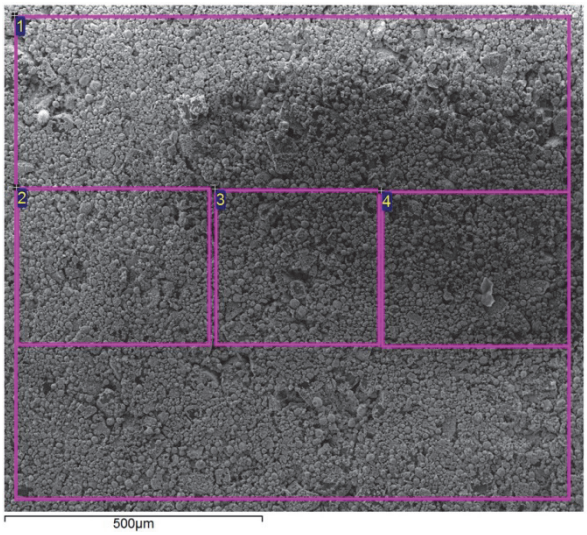

spot	Zr	O	K	Cl	Si
1	18.43	52.43	12.62	16.51	
2	18.27	58.83	10.13	12.76	
3	16.75	57.22	11.26	14.77	
4	16.12	55.40	12.38	16.10	

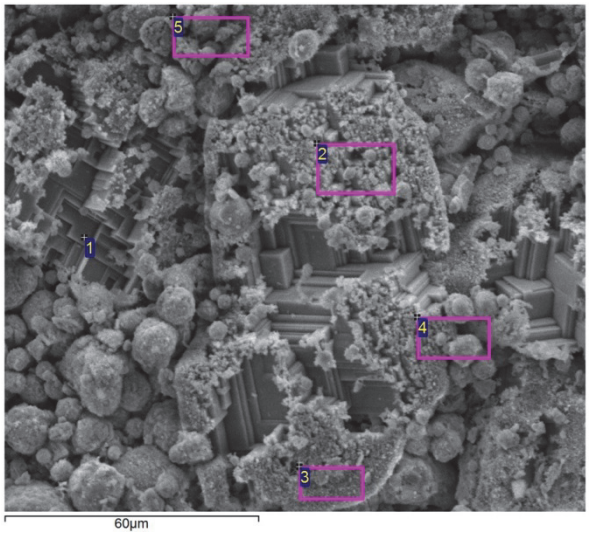

spot	Zr	O	K	Cl	Si
1		15.39	41.54	43.08	
2	1.89	28.57	33.40	36.14	
3	4.17	33.26	31.34	31.24	
4	14.88	45.17	18.37	21.58	

Appendix 3: ***A Concise Introduction to the Computational Thermodynamics***

Determination of equilibrium state for a system of defined size and components under a certain temperature and pressure is a fundamental issue in materials science. Since experimental investigations are often costly and time-consuming calculation of the equilibrium state has attracted much attention during the past decades. Thanks to the advances in computer science and computational methods, nowadays CALculation of PHase Diagrams (CALPHAD) is a widely practiced technic with regard to alloy design and development.

CALPHAD is based on modelling the Gibbs energy for all possible compound (stoichiometric phase) and solution phases for a certain set of chemical elements under known conditions of temperature and pressure. For pure species and compounds the Gibbs energy data is usually stored in form of polynomial functions in databases. As an example such polynomial function for case of Scientific Group Thermodata Europe (SGTE) database has the following form [1]:

$$G_m - H_m^{SER} = a + bT + cT\ln(T) + \sum_2^n d_n T^n \quad ; \quad 1$$

This equation gives the Gibbs energy relative to the Standard Element Reference (SER) state where H_m^{SER} represents the enthalpy of the pure element or compound in its defined (reference) state at 298.15K. In this formula a, b, c and d_n are element-specific constants. The exponent n usually takes the values of 2, 3 or -1. The Gibbs energy for solution phases is given by the general formula:

$$G = G^o + G_{mix}^{ideal} + G_{mix}^{xs} \quad ; \quad 2$$

Where G^o is the contribution from the pure components of the phase, G_{mix}^{ideal} is the change in the Gibbs energy assuming that the mixing is ideal (ideal mixing contribution) and G_{mix}^{xs} is the Gibbs energy change due to non-ideal mixing i.e. when there is interaction between the components of the phase [1]. The first two terms in eq. 2 can easily be calculated according to equations 3 and 4.

$$G^o = \sum_i x_i G_i^o \quad ; \quad 3$$

$$G_{mix}^{ideal} = RT\sum_i x_i \ln x_i \quad ; \quad 4$$

In these formula x_i is the mole fraction of the component i, G_i^o is the Gibbs energy for pure component i, R is the universal gas constant and T is the absolute temperature.

Unlike G^o and G_{mix}^{ideal}, calculation of G_{mix}^{xs} is not straightforward and several different models have been proposed for calculation of this quantity. In CALPHAD technic the first step is to provide as much experimental thermochemical data as possible for a certain phase from the literature (or perform complementary experiments). Subsequently a suitable model is employed to describe the phase i.e. to develop or adopt an equation that can explain the dependency of the G_{mix}^{xs} on the

composition of the system. Finally, with a curve-fitting mathematical procedure, constants of the model's equation are calculated to fit the experimental data. Repeating this procedure for all the possible phases makes it possible to perform equilibrium calculations. The process of finding the thermodynamic description for all the phases in the system is referred to as "thermodynamic assessment"[2]. Once the system is assessed, determination of the equilibrium state for a certain set of conditions is achieved by means of a suitable mathematical procedure which is able to find the exact combination of phases (along with their composition) that leads to the minimum Gibbs energy for the system. In other words the equilibrium state can be determined for conditions that have not been experimentally investigated.Thanks to the advances in computer programs and numerical methods, nowadays the abovementioned mathematical procedures, assessment and Gibbs energy minimization, can be performed easily. In fact, several computer programs are available whose databases contain the thermochemical data for a large number of compounds as well as solution phases. These softwares are often equipped with powerful and robust mathematical routines that can find the equilibrium state rapidly and accurately. In the current study commercial packages Thermo-Calc [3] (version S), FactSage [4] (version 6.2) and HSC Chemistry [5] (version 7) were widely used. The latter two softwares were only employed in calculations involving compounds (stoichiometric phases) and ideal gases. However, Thermo-Calc was employed for calculations involving the solid solutions as well as ideal gases and compounds. To model the Gibbs energy of condensed phases Thermo-Calc uses the "generalized multiple sublattice model" or Compound Energy Formalism (CEF). The details of this model can be found in [1], [6]. However, it is worth to mention that this model takes into account the crystal structure of solution and compound phases. In fact, the assumption that atoms in a solid solution can occupy any available site on the lattice is not always able to describe the ordered solid solutions and solid solutions with interstitials [1], [2].

References

[1] N. Saunders and A. P. Miodownik, *CALPHAD : Calculation of Phase Diagrams*. Pergamon, 1988.

[2] S. Hallström, "On High Temperature Corrosion Resistance : Towards the Materials Genome of High Temperature Alloys," Royal Institute of Technology (KTH), 2014.

[3] J. Andersson, T. Helander, and L. Höglund, "Thermo-Calc & DICTRA, computational tools for materials science," *Calphad*, vol. 26, no. 2, pp. 273–312, 2002.

[4] "FactSage 6.2, www.factsage.com." .

[5] "HSC Chemistry 7.00, www.hsc-chemistry.com." .

[6] H. L. Lukas, S. G. Fries, and B. Sundman, *Computational Thermodynamics : The Calphad method*. Cambridge University Press, 2007.

DTU Mechanical Engineering
Section of Materials and Surface Engineering
Technical University of Denmark

Produktionstorvet, Bld. 425
DK- 2800 Kgs. Lyngby
Denmark
Phone (+45) 4525 2205
Fax (+45) 4593 6213
www.mek.dtu.dk
ISBN: 978-87-7475-414-5